Growth and Characterization of Site-Controlled InAs(Sb) Nanowires for Use in Infrared Photodetectors

by

Aiyeshah Alhodaib

Department of Physics

Lancaster University

November 2017

This thesis is submitted in partial fulfilment of the requirements
for the degree of Doctor of Philosophy

Declaration

I declare that this thesis is the result of my own work which I carried out in Lancaster University between October 2013 and November 2017. To the best of my knowledge and belief, it contains no material previously published or produced by another party in fulfilment, partial or otherwise, of any other degree or diploma at another university or institute of higher learning, except where due acknowledgement and reference is made in the text. This thesis is not the same as any others I have already submitted, or in the process of submitting, for any degree at any university or institution. The word count on this thesis does not exceed the maximum limit of 80,000 words.

Aiyeshah Alhodaib
19 November 2017

Acknowledgements

I would first and foremost like to direct my sincere appreciation and gratitude to my supervisors, Professor Anthony Krier and Dr. Andrew R J Marshall for their excellent supervision, support, guidance and countless valuable conversations throughout my PhD. Thanks for giving me the opportunity to undertake a research project in your group, I have enjoyed the student experience with you and had a great research time working under your supervision.

I would like to thank Professor Anthony Krier for helping me in build the micro-PL and all the help he gave during m research time.

I would like also to thank Dr. Andrew R J Marshall for training me on the MBE and help me in the growth for my samples, also to give me the training I needed in the quantum technology centre and all the help he gave during m research time.

Many thanks also go to Dr. Atif Aziz for giving me the trainings I needed in the clean room and perform the EBL for some of my samples.

Many thanks also go Dr. Yasir Noori for performing the EBL and help me in doing the SEM for some of my samples.

Many thanks also go Dr. Michael Thompson for fabricating the pin InAsSb photodetector.

Many thanks also go Dr. Adam Craig for performing the spectra response measurments for the pin InAsSb photodetector, Dr. Alexander Robson for doing the AFM measurement for the substrate, Dr. Benjamin Robinson for performing the organic coating for the MQW NWs sample, and Dr. Peter Carrington for helping me with interrupting the PL results and calculate the band offset for my structures.

I would like to acknowledge Dr. Johannes Svensson from Lund University for performing the X-Ray and Dr. Ana Sanchez from Warwick University for performing the STEM analysis.

I would also like to acknowledge the Saudi Culture Bureau and Qassim University in Saudi Arabia for awarding me the studentship to undertake the PhD course in Lancaster University.

Thanks also to the members of my research group including, Manoj Kesaria, Lu Qi, Jonathan Hayton, Susan Krier, Denise Cardenes and Eva Menendez, Veronica Letka and Xiao Colin.

Finally, I would like to thank my parents, my brothers and sisters and my friends for all their help and encouragement during the past stressful period, your words of wisdom have and continues to be source of energy in my life. I love you all.

Thank you all

List of publications

1. Thompson, M., Alhodaib, A., Craig, A., Robson, A., Aziz, A., Krier, A., Svensson, J., Wernersson, L., Sanchez, A. and Marshall, A. Low Leakage-Current InAsSb Nanowire Photodetectors on Silicon. Nano Letters. 2016, 16(1), pp.182-187.

2. A. Alhodaib, Y. J. Noori, P. J. Carrington, Ana M. Sanchez, M. D. Thompson, M. C., A. Krier, A. R. J. Marshall. "Room temperature mid-infrared emission from faceted InAsSb multi quantum wells embedded in InAs nanowires" (Submitted to Nano letters, 2017).

Conference Presentation

1. Alhodaib, M.Thompson, A.Aziz, A. Marshall and A.Krier, Growth and Characterization of Site Controlled InAsSb Nanowires, Surface Science Day UCLAN 2015- poster presentation.

2. Alhodaib, M.Thompson, A.Aziz, A. Marshall and A.Krier, Photoluminescence, Photoresponse and Leakage Current in Site Controlled InAsSb Nanowires.

3. Alhodaib, M. Thompson, A. Marshall and A.Krier, Catalyst-Free Selective Area MBE Growth of InAsSb Nanowires on a Patterned Si Substrate, Nanowires 2015- Barcelona – poster presentation.

4. Alhodaib, A. Marshall and A. Krier, Nanowires growth and characterization, PROMIS workshop – Sheffield, Oral presentation 2015.

5. Alhodaib, A. Marshall and A. Krier, Growth and Characterisation of Site-controlled InAsSb Nanowires on Silicon for Photonic Devices, Lancaster University -Christmas Conference 2015 - poster presentation.

6. A. Alhodaib, A. Marshall and A. Krier, MBE growth of InAsSb Nanowires, UK MBE workshop 2016/ Cambridge University, Oral presentation.

7. Alhodaib, A. Marshall and A. Krier, MBE Growth of InAsSb Nanowires, SSC9 (Saudi student conference-Birmingham University) – proceeding paper submitted, Oral presentation 2016.

8. A. Alhodaib, M. Thompson, A. Marshall and A.Krier, MBE Grown InAsSb Nanowire Photodetectors, SPIE Photonics Europe, oral presentation.

Abstract

There is considerable interest in the development of InAs(Sb) nanowires for infrared photonics due to their high tunability across the infrared spectral range and integration with silicon electronics applications. The use of nanowires in IR photonics also promises transformational advantages. Site-controlled catalyst free epitaxial growth on silicon wafers was used in this work to enable exploitation of recent scientific understanding in the control of light matter interactions through geometry, while also offering practical integration advantages and strong, tuneable optical emission. However, optical emission is currently limited to low temperatures due to strong non-radiative Auger and surface recombination. Simple structures suffer from deleterious effects due to the high surface to volume ratio in nanowires which has limited emission to fixed wavelengths and low temperatures, until now.

In this thesis the growth of InAs(Sb) has been developed to realize high performance cost-effective optoelectronic structures for the development of emitters and photodetectors operating in the mid-infrared spectral range. In addition to characterizing the optical properties of the grown nanowires, this research has improved their optical efficiency by reducing nonradiative surface and Auger recombination.

The growth of advanced InAs nanowires containing embedded multiple quantum well (MQWs) and superlattices (SL) structures is reported for the first time. The MQWs and SL structures are based on type II InAsSb/InAs MQWs which exhibit bright mid-infrared photoluminescence up to room temperature. This unique geometry confines the electron-hole recombination to within the quantum wells which alleviates the problems associated with recombination via surface states, whilst the quantum confinement of carriers increases the radiative recombination rate and suppresses Auger recombination. This demonstration paves

the way for the development of new integrated quantum nano-light sources operating in the technologically important mid-infrared spectral range.

In this work we also realized the first InAsSb shortwave infrared nanowire photodetectors and the lowest leakage current density reported for any InAs(Sb) photodiode at 300 K. Using the same method of growth (site-controlled epitaxy), allowed for high quality shortwave nanowire infrared photodetectors to be grown on silicon substrates, while obtaining surprisingly low leakage current density. The unique design of these nanowire photodetectors also allows for electrical conduction through the substrate which simplifies many aspects of the fabrication and expands the opportunities for integration. Although the nanowires occupy only a small fraction of the light collection area, optimization of the length and diameter can significantly increase the absorbance up to that of planar films. Combined with the reduction in leakage current density over InAs(Sb), this should provide more than 2 orders of magnitude increase in signal-noise ratio over state-of-the-art InAs(Sb) devices. This represents a major step toward high-performance mid-infrared photodetectors compatible with silicon technologies and which can potentially be integrated with other photonic systems.

Table of Contents

Chapter 1

Introduction

1.1. Motivation

The integration of III−V semiconductors with silicon substrates targets the compelling goal of photonic devices combined with mature silicon technology.[1,2] However, the heteroepitaxy of bulk III−V materials on silicon substrates results in high defect levels which reduce the crystalline quality and performance of such devices.[3] InAs(Sb) nanowires (NWs) have great potential for technologically important applications in nanoscale and quantum devices[4,5,6]. These NWs are typically grown using metal−organic vapor phase epitaxy (MOVPE) and molecular beam epitaxy (MBE) using the vapor−liquid−solid (VLS)[9] growth mechanism which uses a metal droplet (either gold or indium) as the nanowire seed. In our work we used a catalyst free selective area epitaxy to produce high quality NWs in precise geometric arrangements. The advantages of this method are the avoidance of gold, which forms trap states in silicon,[2,11] and simpler growth as there is no need to optimize droplet deposition. The native oxide also prevents material deposition between the nanowires which is typical of growth on unpatterned Si substrates.[12] Although EBL is slow and costly, nanoimprint lithography[13,14] will allow for low cost patterning of large area devices. By controlling the site locations, nanowire groups can then be used as individual photonic devices such as pixels in focal plane arrays or ultrasmall detectors, which can be used for light-matter coupling and to tune optical properties[7,8] as well as facilitating scalable lithographic integration[9]. NWs have been shown to overcome this problem due to rapid strain reduction during growth leading to lower dislocation densities.3,[10] Significantly, this new technology has a much lower leakage than today's best InAs(Sb) photodiodes, which have reported leakage current densities around 100 mA/cm^2 at 300 K, despite their increased bandgap and homoepitaxial substrates.[11,12,13,14] In doing so it paves the way for lower noise III−V detectors, which can further benefit from intimate integration with silicon electronics technology. The novel

detector concept developed in this work has the potential to deliver a transformational increase in the performance of IR detectors. This can be translated into new IR imaging and detection systems with significant reductions in size, weight and power. However, in order to develop such novel detectors a study of the fundamental physics is required to develop these structures.

1.2. Introduction

Antimonide semiconductors have large lattice parameters relative to the other III-V semiconductors, ranging from GaSb at 6.10 Å to InSb at 6.49 Å, which leads consequently to narrow band gaps. In particular, InAsSb has the narrowest band gap among the III-V semiconductors, as low as 0.1 eV at room temperature, as shown inFigure 1.1, where the band gaps and relative band offsets are plotted against their crystal lattice parameter[15] for the most common semiconductors. Photodetectors operating in the mid- to long-wavelength infrared band in the range 3–14 μm are important for thermal imaging, gas analysis, and remote pollution monitoring at room temperature[16]. This is particularly important for applications in the military, industry, medical, and the scientific community. Examples of military and security applications include facilities security where surveillance, target detection, firefighting, and long-range monitoring are of strategic importance. The industrial quality assurance, equipment diagnostics, and pollution monitoring are some examples of industry applications. Medical applications include for instance blood glucose level monitoring and injury detection. Furthermore, some examples of scientific applications include measurement analysis and infrared astronomy16,[17,18] The InAsSb alloys are also very attractive for optical devices and considered to be a good alternative for the widely used

HgCdTe alloy due to the high thermal conductivity and mobility comparable to the more common HgCdTe detectors[19,20,17]. The tunable band gap of InAsSb alloy throughout most of the mid-IR spectrum enables sensing of gases that are of importance to the environment, such as CO_2, CO, CH_4, N_2O, and O_3.

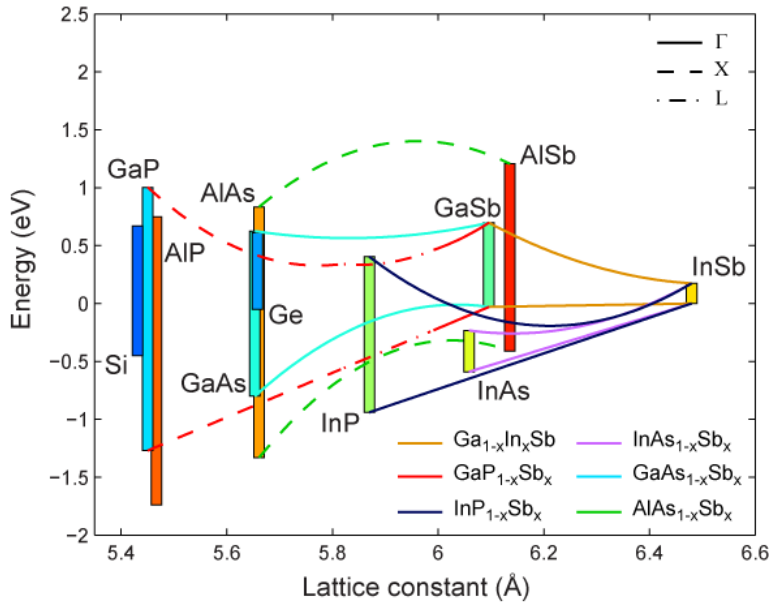

Figure 1.1. The band gaps and relative band offsets of the common semiconductors are plotted against their crystal lattice parameter[15].

The developments that took place in the past few decades in the semiconductor industry has allowed the realisation of III-V one-dimensional (1D) structures[21], such as NWs that has led to improved control of the size[22], higher flexibility in sample processes[23,24] and more freedom for bandgap engineering[25]. Bottom-up freestanding semiconductor NWs, in particular InAs(Sb) have been proven to function as electrical and optical devices[26]. This new technology has a much lower leakage current than today's best InAs(Sb) photodiodes[27,28,18], that paves the way of noise suppression for III−V detectors, while maintaining a high signal level. Even more, nanowires technology has allowed realising optoelectronic devices leading to nanoscale optical devices with small weight, power consumption and cooling

requirements[29,30]. The benefit of using cheap silicon substrates is also an attraction of this route[31], with the ultimate potential being the integration of the read-out IC (ROIC) into the substrate on which the mid-infrared absorbing nanowires (NWs) are grown[32].

In general, any lattice mismatching between the host substrate and the material could causes material quality degradation, thus, a common method to solve this is to grow nearly lattice-matched InAs/InAsSb, which realizes small effective band gaps via quantum confinement. However, these materials may suffer from rough hetero interfaces and weak light absorption due to a spatial separation of the carriers[33,34,35].In contrast, nanowires growth provides a good way to obtain high quality material despite the lattice-mismatch, while offering the possibility of material integration and the freedom to choose the alloy composition to form useful hetrostructure[35]. There are also some additional material properties which become important only when the structures are scaled down to nanometre dimensions.

1.3. Thesis outline

This contribution focuses on recent efforts towards exceptionally high quality InAs(Sb) NWs and InAs/InAsSb heterostructures multi quantum wells (MQWs) and super lattices (SLs) for use in quantum electronic and optoelectronic devices in particular based Sb photodetectors. This research has produced significant advances in nanowire growth by Molecular Beam Epitaxy (MBE) and in nanowire characterization by Scanning Electron Microscopy (SEM), Transmission Electron Microscopy (TEM) and X-Ray Diffraction (XRD). We also discuss major advances made using photoluminescence (PL) towards understanding of the nanowire electronic energy landscapes and the carriers transport in these nanowires. Chapter 1 provides a general introduction to the aim and the motivation of the work done in this thesis. Chapter 2

gives an overview of the theoretical concepts of nanowires. It firstly focuses on the physical properties and crystal structure of InAs(Sb) NWs, before discussing the possible recombination mechanisms. The advantage of quantum well active regions is then briefly discussed and finally the working principles of InAs(Sb) nanowire based photodetectors are explained. Chapter 3 gives a detailed review and comparison of different growth techniques and mechanisms of InAs(Sb) based NWs with a review of developments in the structures and the optical properties. Chapter 4 includes a description of the experimental tools and techniques that have been used to carry out the studies in this work. The experimental results of this work are divided into three chapters, the first results chapter, chapter 5, focuses on bulk InAs and InAsSb NWs grown on Si (111) substrates; the chapter will explain the growth process, the structural characterization and the optical properties for nanowires of both materials. The second results chapter is chapter 6, which focuses on InAs/InAsSb MQW and SL NWs. Chapter 6 will also describe the growth, the structural characterization and the optical properties for both wire structures. The third results chapter is chapter 7, which demonstrates the fabrication of pin InAsSb NW photodetectors, including the fabrication process and reports the results for the low leakage current and the photoresponse at room temperature. Finally, chapters 8 summarizes the work and draw overall conclusions, also discussing the possible future work that can be done to take this study a step further.

1.4. References

[1] Tomioka, K.; Tanaka, T.; Hara, S.; Hiruma, K.; Fukui, T. III-V Nanowires on Si Substrate: Selective-Area Growth and Device Applications. IEEE J. Sel. Top. Quantum Electron. **2011**, 17, 1112−1129.

[2] Sourribes, M. J. L.; Isakov, I.; Panfilova, M.; Liu, H.; Warburton, P. A. Mobility Enhancement by Sb-mediated Minimisation of Stacking Fault Density in InAs Nanowires Grown on Silicon. Nano Lett. **2014**, 14, 1643−1650. PMID: 24502770.

[3] Ertekin, E.; Greaney, P. A.; Chrzan, D. C.; Sands, T. D. Equilibrium limits of coherency in strained nanowire heterostructures. J. Appl. Phys. **2005**, 97, 114325.

[4] Joyce, H.; Gao, Q.; Hoe Tan, H.; Jagadish, C.; Kim, Y.; Zou, J.; Smith, L.; Jackson, H.; Yarrison-Rice, J.; Parkinson, P. et al. III–V Semiconductor Nanowires for Optoelectronic Device Applications. *Progress in Quantum Electronics* **2011**, *35*, 23-75.

[5] Thelander, C.; Björk, M.; Larsson, M.; Hansen, A.; Wallenberg, L.; Samuelson, L. Electron Transport in InAs Nanowires and Heterostructure Nanowire Devices. *Solid State Communications* **2004**, *131*, 573-579.

[6] Aharonovich, I.; Englund, D.; Toth, M. Solid-State Single-Photon Emitters. *Nat. Photon.* **2016**, *10*, 631-641.

[7] Svensson, J.; Anttu, N.; Vainorius, N.; Borg, B.; Wernersson, L. Diameter-Dependent Photocurrent in InAsSb Nanowire Infrared Photodetectors. *Nano Lett* **2013**, *13*, 1380-1385.

[8] Scofield, A.; Kim, S.; Shapiro, J.; Lin, A.; Liang, B.; Scherer, A.; Huffaker, D. Bottom-up Photonic Crystal Lasers. *Nano Lett.* **2011**, *11*, 5387-5390.

[9] Kim, H., Farrell, A., Senanayake, P., Lee, W. and Huffaker, D. Monolithically Integrated InGaAs Nanowires on 3D Structured Silicon-on-Insulator as a New Platform for Full Optical Links. *Nano Lett.* **2016**, 16**,** 1833-1839.

[10] Mandl, B.; Stangl, J.; Martensson, T.; Mikkelsen, A.; Eriksson, J.; Karlsson, L. S.; Bauer, G.; Samuelson, L.; Seifert, W. Au-Free Epitaxial Growth of InAs Nanowires. Nano Lett. **2006**, 6, 1817−1821. PMID: 16895379.

[11] Brotherton, S. D.; Lowther, J. E. Electron and Hole Capture at Au and Pt Centers in Silicon. Phys. Rev. Lett. **1980**, 44, 606−609.

[12] Anyebe, E.; Rajpalke, M.; Veal, T.; Jin, C.; Wang, Z.; Zhuang, Q. Surfactant effect of antimony addition to the morphology of selfcatalyzed InAsSb nanowires. Nano Res. **2015**, 8, 1309−1319.

[13] Austin, M. D.; Ge, H.; Wu, W.; Li, M.; Yu, Z.; Wasserman, D.; Lyon, S. A.; Chou, S. Y. Fabrication of 5nm linewidth and 14nm pitch features by nanoimprint lithography. Appl. Phys. Lett. **2004**, 84, 5299−5301.

[14] Munshi, A. M.; Dheeraj, D. L.; Fauske, V. T.; Kim, D. C.; Huh, J.; Reinertsen, J. F.; Ahtapodov, L.; Lee, K. D.; Heidari, B.; van Helvoort, A. T. J.; Fimland, B. O.; Weman, H. Position-Controlled Uniform GaAs Nanowires on Silicon using Nanoimprint Lithography.Nano Lett. **2014**, 14, 960−966. PMID: 24467394

[15] I. Vurgaftman, J.R. Meyer, J. Band parameters for III-V compound semiconductors and their alloys, Appl. Phys. 2001, 89, 5815.

[16] H. Schneider and H. C. Liu, Quantum Well Infrared Photodetectors: Physics and Applications, vol. 126 of Springer series in optical sciences (2007, Springer, New York).

[17] Karim, A.; Andersson, J. Infrared Detectors: Advances, Challenges and New Technologies. IOP Conference Series: Materials Science and Engineering 2013, 51, 012001.

[18] Shao, H.; Li, W.; Torfi, A.; Moscicka, D.; Wang, W. Room temperature InAsSb photovoltaic detectors for mid-infrared applications. IEEE Photonics Technol. Lett. 2006, 18, 1756−1758.

[19] Miao, J.; Hu, W.; Guo, N.; Lu, Z.; Zou, X.; Liao, L.; Shi, S.; Chen, P.; Fan, Z.; Ho, J. et al. Single InAs Nanowire Room-Temperature Near-Infrared Photodetectors. ACS Nano 2014, 8, 3628-3635.

[20] A. Rogalski, J. Antoszewski and L. Faraone, J. Third-generation photodetector arrays, Appl. Phys. 2009, 105, 09110.

[21] Tomioka, K.; Tanaka, T.; Hara, S.; Hiruma, K.; Fukui, T. III-V Nanowires on Si Substrate: Selective-Area Growth and Device Applications. IEEE J. Sel. Top. Quantum Electron. 2011, 17, 1112− 1129.

[22] Koblmüller, G.; Vizbaras, K.; Hertenberger, S.; Bolte, S.; Rudolph, D.; Becker, J.; Döblinger, M.; Amann, M.; Finley, J.; Abstreiter, G. Diameter Dependent Optical Emission Properties of InAs Nanowires Grown on Si. Applied Physics Letters 2012, 101, 053103.

[23] Naureen, S.; Sanatinia, R.; Shahid, N.; Anand, S. High Optical Quality InP-Based Nanopillars Fabricated By a Top-Down Approach. Nano Letters 2011, 11, 4805-4811.

[24] Thelander, C.; Björk, M.; Larsson, M.; Hansen, A.; Wallenberg, L.; Samuelson, L. Electron Transport in InAs Nanowires and Heterostructure Nanowire Devices. Solid State Communications 2004, 131, 573-579.

[25] B. Wang and P. W. Leu, "Tunable and selective resonant absorption in vertical nanowires,'' J. Optics Letters, 2012, Vol. 37, No. 18, 3756-3758, ().

[26] Dayeh, S.; Aplin, D.; Zhou, X.; Yu, P.; Yu, E.; Wang, D. High Electron Mobility Inas Nanowire Field-Effect Transistors. Small 2007, 3, 326-332.

[27] Ker, P.; Marshall, A.; Krysa, A. B.; David, J.; Tan, C. H.Temperature Dependence of Leakage Current in InAs Avalanche Photodiodes. IEEE J. Quantum Electron. 2011, 47, 1123−1128.

[28] Maddox, S. J.; Sun, W.; Lu, Z.; Nair, H. P.; Campbell, J. C.; Bank, S. R. Enhanced low-noise gain from InAs avalanche photodiodes with reduced dark current and background doping. Appl. Phys. Lett. 2012, 101, 151124.

[29] Yan, R.; Gargas, D.; Yang, P. Nanowire Photonics. Nature Photonics 2009, 3, 569-576.

[30] Dasgupta, N.; Sun, J.; Liu, C.; Brittman, S.; Andrews, S.; Lim, J.; Gao, H.; Yan, R.; Yang, P. 25Th Anniversary Article: Semiconductor Nanowires - Synthesis, Characterization, and Applications. Advanced Materials 2014, 26, 2137-2184.

[31] Ishiyama, T.; Nakagawa, S.; Wakamatsu, T. Growth of Epitaxial Silicon Nanowires on a Si Substrate by A Metal-Catalyst-Free Process. Scientific Reports 2016, 6.

[32] K., A.; K., N.; L., D.; Dubey, M.; Wijewarnasuriy, P. Nanostructured Detector Technology for Optical Sensing Applications (accessed Oct 12, 2017).

[33] D. Lackner, O. J. Pitts, S. Najami, P. Sandhu, K. L. Kavanagh, A. Yang, M. Steger, M. L. W. Thewalt, Y. Wang, D. W. McComb, C. R. Bolognesi, and S. P. Watkins,Growth of InAsSb/InAs MQWs on GaSb for mid-IR photodetector applications, J. Cryst. Growth 2009, 311, 3563.

[34] R. M. Feenstra, D. A. Collins, D. Z.-Y. Ting, M. W. Wang, and T. C. McGill, Antimonide-Related Strained-Layer Heterostructures, Phys. Rev. Lett. 1994, 72, 2749.

[35] Borg, B., Kimberly A., J. Eymery, and L.Wernersson, Enhanced Sb incorporation in InAsSb nanowires grown by metalorganic vapor phase epitaxy, Appl. Phys. Lett. 2011, 98, 113104.

Chapter 2

Background Theory

2.1. **Introduction**

This work concerns the growth and fabrication of III-V semiconductor NWs in the mid-infrared 2-5 μm spectral range. This chapter provides an overview on the theoretical concepts of nanowires. The chapter firstly focuses on the physical properties and crystal structure of InAs(Sb) NWs, before discussing the possible recombination mechanisms. The advantage of quantum well active regions is then briefly discussed and finally the working principles of photodetectors are explained.

2.2. **Energy bands in semiconductors**

Semiconductors are a particular state of the matter which shows a resistivity between metals and insulators, in the range between 10^{-3} Ω.cm and 10^{9} Ω.cm for metals and insulators respectively. They have a negative temperature coefficient of resistance and their electrical conductivity can be varied over several orders of magnitude with temperature, by the incorporation of impurities, the injection of excess charge carriers or by optical excitation[1]. Solid state semiconductor materials can be single crystalline, polycrystalline, or amorphous. In crystalline case, the atoms are arranged in a perfectly periodic structure in all three dimensions, where the polycrystalline are formed by many small regions of single crystalline materials that called grains and with amorphous there is no periodic structure. The semiconductors studied in this work are all single crystalline materials. In isolated free atoms, electrons can only exist in discreet energy levels. In bulk semiconductor materials, atoms are placed very close to each other in a periodic manner. The discreet energy levels develop into continuous energy bands. The majority of the electrons stay in the band with lower energy (valence band). While some of the electrons can be excited to the band with higher energy (conduction band). Between the conduction band and valence band, there is a band gap in

which there are no electron states. The differences in the energy bands between insulators, conductors and semiconductors are shown in Figure 2.1 below. In insulators, there is a wide energy gap between the conduction band and the valance band. The electrons can only stay in the valance band at any ordinary temperature. In semiconductors, the band gap is significantly narrower than insulators. A small number of electrons can be thermally excited to the conduction band. Under external excitations, the density of electrons on the conduction band can considerably increase, resulting in huge change of the physical properties for these semiconductor materials. In the conductors, both conduction band and valance band are overlap with each other. Large number of free electrons naturally exists in the material. Thus, the bandgap in semiconductors is a key factor of optical and electrical properties for any structures or devices[2].

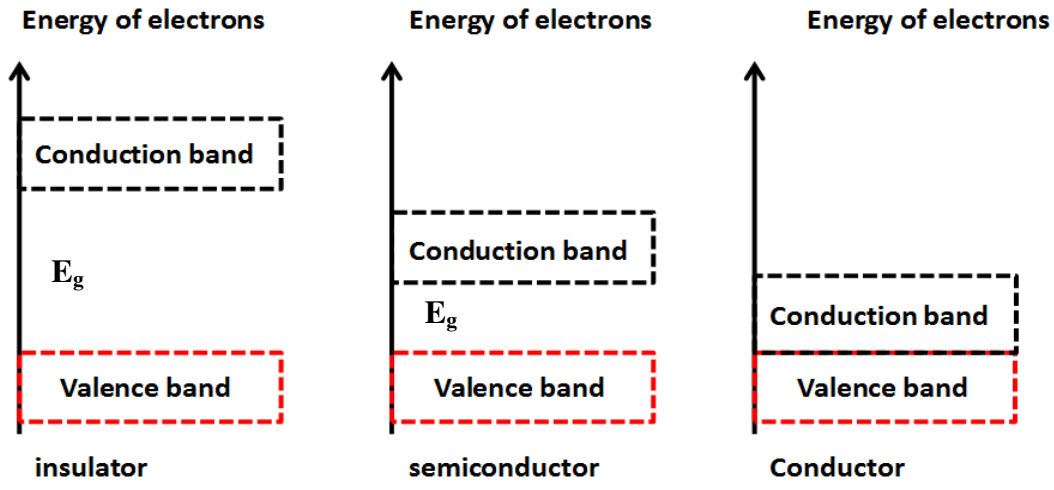

Figure 2.1.Illustration of energy bands in bulk solid materials, insulators with wide energy gap, semiconductors with narrower band gap than the insulators and conductors where there is an overlap between conduction and valence bands.

2.3. **Direct and indirect band semiconductors**

The band structure of a semiconductor is generally represented by an energy - wave vector relationship E - k: the upper and lower bands are respectively the conduction band (*CB* at energy E_C) and the valence band (*VB* at energy E_V), separated by a forbidden energy region where allowed states cannot exist[3].

The separation between the lowest conduction band and the highest valence band is the bandgap energy E_g. The wave vector k is related to a charge carrier's momentum by de Broglie's relation, p = ħk, and as such, these E-*k* diagrams demonstrate how energy states are distributed in momentum space[4]. Figure 2.2 (a) shows a simplified E-*k* diagram (for one-dimensional momentum space with wave number k), in which one can see the presence of a minimum in the conduction and a maximum in the valence band at $k = 0$[3]. Around these extrema, the bands appear approximately parabolic, similarly to the behaviour of free electrons, for which

$$E = \frac{\hbar^2 k^2}{2m_o} \tag{2.1}$$

where m_o =9.11 kg is the (free) electron mass[5]. Here, the curvature of the bands is dependent on the reciprocal electron mass $1/m_o$. For electrons in semiconductors, the curvature of the bands near to the minima can be far higher than the free electron case, and therefore it seems as though the semiconductor electron mass is much smaller than the free electron mass[5]. This mass the semiconductor electrons appear to have is called the effective mass and we can use it to re-write Equation 2.1 for the conduction and valence bands in Figure 2.2 (a):

$$E_c = E_g + \frac{2\hbar^2 k^2}{2m_o^*} \tag{2.2}$$

and

$$E_v = - \frac{2\hbar^2 k^2}{2m_h^*} \quad (2.3)$$

Here, m_e and m_h are the electron and hole effective masses, respectively[6]. Note that these energies are relative to E = 0 being at the valence band maximum, and unless otherwise stated, this convention shall be used throughout this thesis. For instance, it is common for there to be multiple valence bands, two of which are degenerate at $k = 0$: the heavy hole (hh) and light hole (*lh*) bands. These come with their own separate effective masses (m_{hh} and m_{lh}) and therefore Equation 2.3 can be replaced with[7]:

$$E_v = - \frac{2\hbar^2 k^2}{2m_{hh,lh}^*} \quad (2.4)$$

Semiconductor band structures are shown in Figure 2.2 for two different cases direct and indirect band structure semiconductors. In case (a) direct semiconductors, the conduction band minima and the valence band maxima are located at the same momentum value, so the transition between conduction and valence band can happen without any change of momentum. This kind of semiconductors is including for examples GaAs, InAs and InP. In direct semiconductors, the transition of electrons from the conduction band to the valence band can result in the emission of photons with energy equal to the band gap E_g. On the other hand, in case (b) indirect semiconductors, the conduction band minima and the valence band maxima do not have the same momentum value, thus, the recombination in indirect semiconductors is difficult to result in the emission of photons[8].

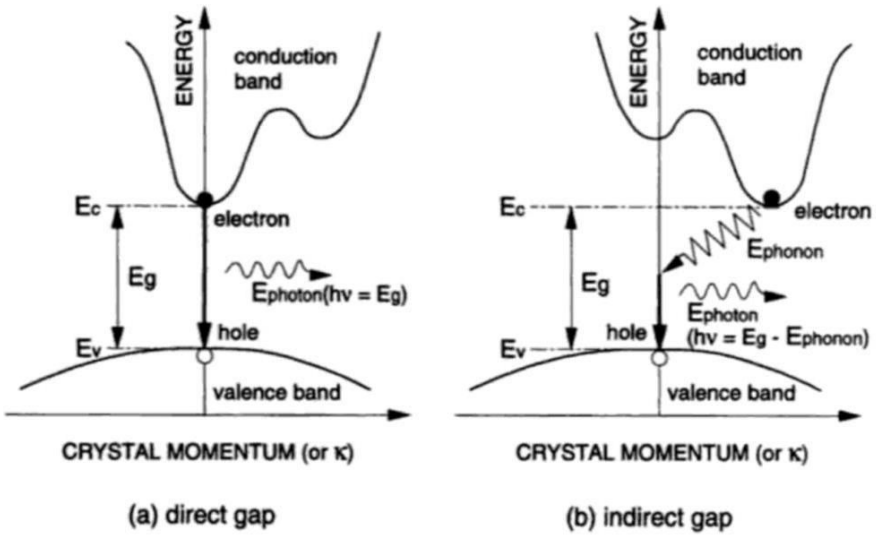

Figure 2.2.The electron energy versus momentum plot at the bottom of conduction band and the top of the valance band for two cases: (a) direct semiconductors and case (b) indirect semiconductor[3].

Thus a transition from the valance band to the conduction band requires not only an energy Eg but also momentum to change its momentum. Momentum is conserved via a phonon interaction. A phonon is a quantum lattice vibration and has a characteristic energy E_{phonon} (Long-wave Longitudinal- optical (LO) phonon energy $h\nu_{LO} \approx 29meV$ at 300K). So a transition from E_v to E_c involves either phonon emission or phonon absorption. If the transition is caused by optical excitation, the photon provides an energy hν but cannot provide a momentum. Therefore, if the photon energy $h\nu \leq E_g$, the transition will involve phonon absorption. If $h\nu > E_g$, the transition will involve phonon emission. Most III-V compounds semiconductors, such as GaAs, InP, InAs and InSb are a direct band gap semiconductors have a direct optical transition, small electron effective mass, and high electron mobility[9].

In a large crystal, the overall shape and size of the crystal make little or no difference to its internal properties. As we make a semiconductor crystal smaller and smaller, the effects of the surface become increasingly important and the physical properties change in many ways.

The size dependent structural effects are due to contributions from the surface energy of the nanocrystal as in this size regime the surface composes a substantial percentage of the crystal. As the fraction of atoms at the surface becomes larger, the arrangement of the nuclei changes in order to relax the energy of the system as a whole, causing the band gap to expand.

According to the quantum confinement theory, electrons in the conduction band and holes in the valence band are confined spatially by the potential barrier of the surface, or trapped by the potential well of the quantum box.

Because of the confinement of both electrons and holes, the lowest energy of the optical transition from the valence to the conduction band increases, effectively increasing the E_g. The sum of kinetic and potential energy of the freely moving carriers is responsible for the E_g expansion and therefore the width of the confined Eg grows as the characteristic dimensions of the crystallite decrease[10].

2.4. **Fermi Level, Electron Affinity and the Work Function**

The Fermi level E_F is defined as the energy of a state which has a 50% probability of being occupied, and as thermal excitation by higher temperatures means it is more likely that a higher energy state will be occupied, it is dependent on temperature. In semiconductors (and insulators), the Fermi level lies within the band gap and is hence a hypothetical energy level that no electron can actually occupy. In metals, it sits within the conduction band, availing free electrons that contribute towards a high conductance. The Fermi energy is discreetly different in definition; it is the highest occupied state at absolute zero and is therefore temperature-independent[9].

A quantity that is often used to compare different materials and one that is largely a material constant is the electron affinity, which in solid-state physics is defined as the energy required to move an electron from the conduction band edge to the vacuum level E_{vac}:

$$X = E_{vac} - E_C \quad (2.5)$$

The work function Φ is related to the electron affinity, but is the energy required to move an electron to the vacuum from the Fermi level, as opposed to from the conduction band edge:

$$\Phi = E_{vac} - E_f \quad (2.6)$$

2.5. **Electronic structure**

The crystal structure of a semiconductor is normally determined by the positions of the ions due to the larger mass compared to that of the electrons, the valence electrons and their interactions between each other determine the electrical properties of the material[11].

2.5.1. Density of States

In a solid, the atoms are close so their particular electric field allows for interaction with each other and then leads to a splitting of energy levels into a finite number of electronic states[4]. Thus, energy bands arise from the assembly of closely spaced sublevels were electrons occupied all the lower energy levels. An excited electron can reach the conduction band and thus take part in the conduction process, however, the absence from the valence band creates a local positive charge (hole). Electronic states can be populated or vacant, and the dependence on energy of states in the bands is described by the density of states[12]. Shrinking the dimensions of nanostructures alerts the confinement of the carriers within these structures and thereby the density of states of the material, as shown in Figure 2.3. A bulk layer is generally a thick layer and its thickness often varies between a few hundreds of nanometers

to a few micrometers. The carriers have three degrees of freedom (3D semiconductor) and the associated density of states has square-root dependence on energy.

Thinner planar structures can be grown in the tens of nanometers scale in so-called quantum wells, whether isolated in single quantum wells (SQW) or in the periodic structure of multiple quantum wells (MQW). The related density of states is constant as a function of the energy for this two-dimensional confinement (2D). Further confinement can be achieved in quantum wires and quantum dots (QD), where the degrees of freedom are reduced to 1 and 0 respectively, and the density of states has inverse square-root or dirac-function dependence on energy[13].

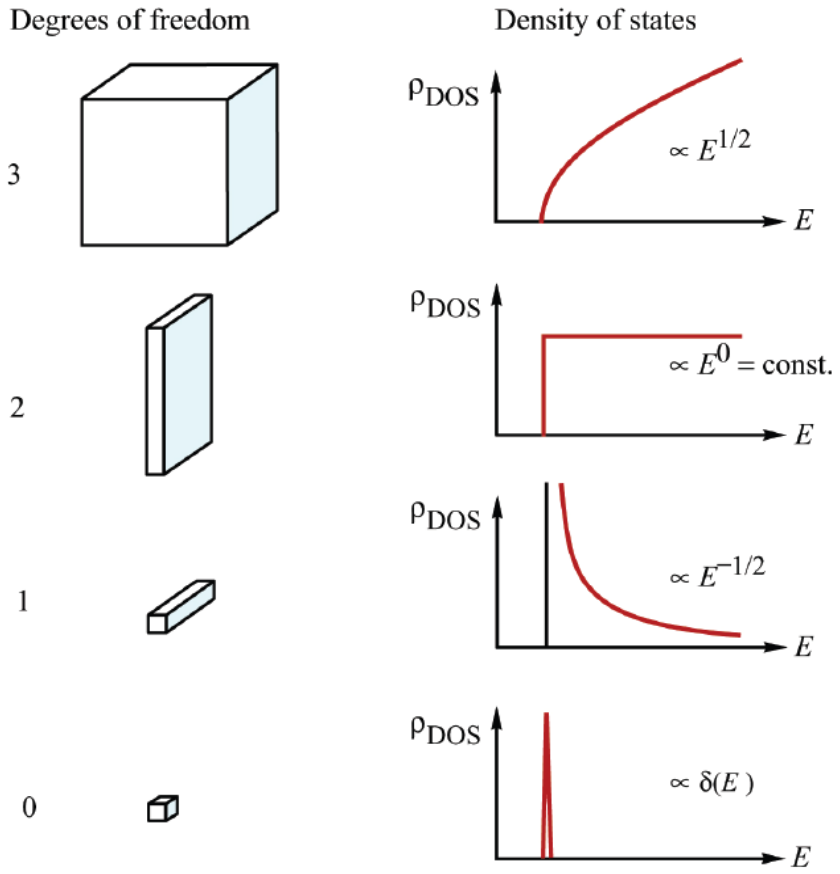

Figure 2.3.Schematic diagram showing the Density of electron states in bulk, 2D, 1D and 0D semiconductor structure[6].

2.6. **Band Gap Alignment for heterostructures**

A heterojunction can be formed by layers of two different semiconductors materials, e.g. a material of narrower bandgap can be placed between two layers of larger bandgap material. At the interface between the two materials, any changes to the electron affinities or Fermi level of the materials will leads to discontinuity in both or either of the valence and conduction bands. This causes offsets in the conduction band (ΔE_c) and in the valence band (ΔE_v). The relative bands alignment can be explained by considering two materials A and B, with narrower band gab and the wider bandgap respectively. In this case, ΔE_c is positive when the conduction band of B is higher than A and ΔE_v is positive when the valance band of B is lower than A. The signs of ΔE_c and ΔE_v can determined the band alignments of the materials as will be discussed below.

2.6.1. Type-I Alignment

Type-I alignment occurs when a narrow band gap material is placed between larger band gap material. In this structure, both band offsets (conduction and valence bands) are positive. Thus, the electrons and holes are confined in the narrow band gap semiconductor when the wider band gap material forms a barrier. A schematic of this structure is shown in Figure 2.4.

2.6.2. Type-II Alignment

Type-II alignment occurs when ΔE_c and ΔE_v have an opposite sign as shown in Figure 2.5. This type of alignment has a negative conduction band offset and positive valence-band offset. In this structure with this alignment the holes are trapped in the narrow gap region and

the electrons in the wide gap region. The material used in this work (InAsSb quantum wells with InAs barriers) has this alignment, including the MQWs and SLs structures.

2.6.3. Type-III Alignment

Type III band gap alignments occur in the cases when the valence band of the barriers is higher than the conduction band of the narrower band gap or in the case of vice versa. This alignment also called broken gap alignment and is shown in Figure 2.6.

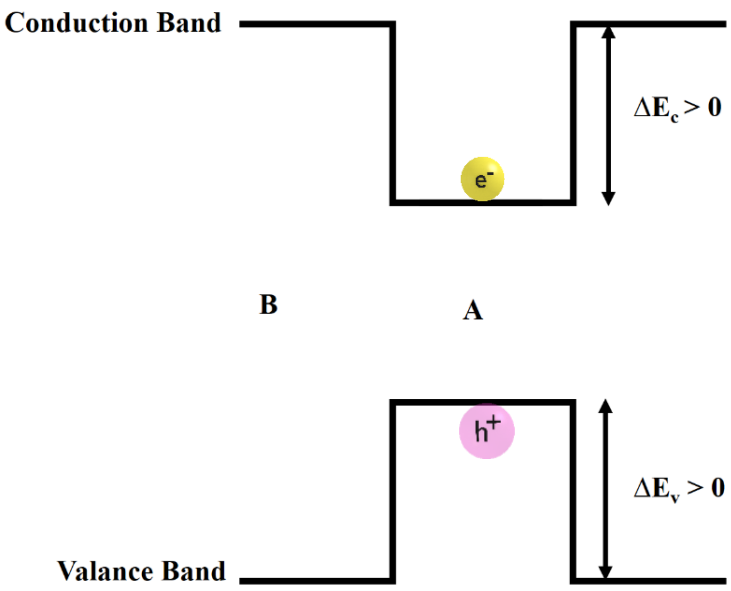

Figure 2.4.Type-I band alignment showing wide band gap (B) and narrow band gap (A) positions.

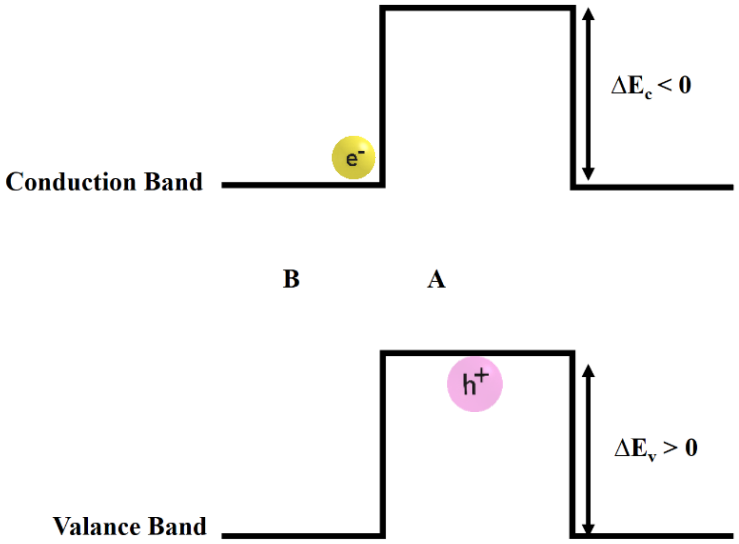

Figure 2.5.Type-II alignment, the holes are trapped in the narrow gap region and the electrons in the wide gap region.

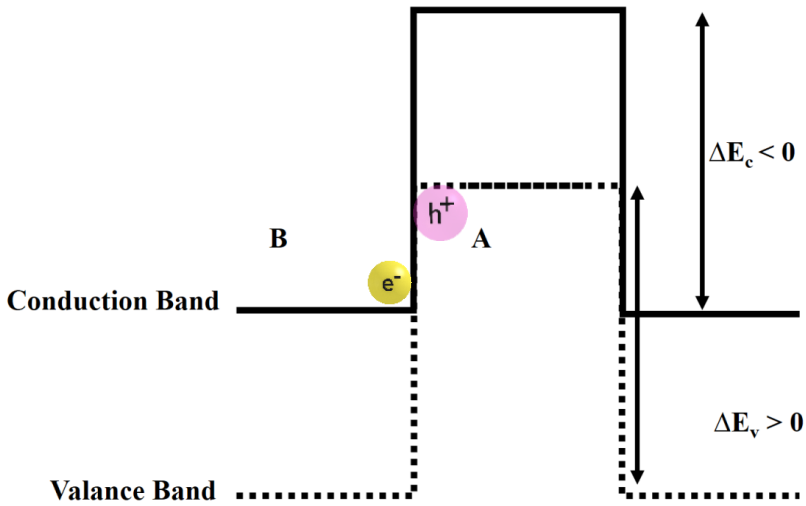

Figure 2.6.Type-III alignment which occurs when the valance band offset is higher than the narrow band gap semiconductor.

2.7. **Physical properties of III-V nanowires**

III–V compound semiconductor NWs has attracted much interest due to their exceptional physical properties. The antimonide materials in particular have large lattice parameters compared to the other III-V semiconductors, ranging from 6.10 Å for GaSb to 6.49 Å for InSb, which leads to relatively narrow band gaps[14]. The ternary semiconductor $InAs_{1-x}Sb_x$ has the narrowest band gap relatively to the other III-Vs semiconductors, as low as 0.084 eV when increasing the Sb content, along with the small electron effective masses and the high electron mobility. Consequently, these properties are required for high-performance and high speed optoelectronic devices in the mid- to long infrared wavelength range such as high-performance nanoelectronic[15], photodetectors[16], high-efficiency light-emitters, solar cells and photovoltaics, which cannot be easily achieved by using Si or other nanostructured materials[17].

2.8. **Crystalline structure**

A crystalline structure is a repeated unit of atoms with a fixed distance between the component parts in space[18]. A change in the atoms arrangements will thus change the crystal structure. The unit cell is the simplest case within a crystalline structure which consists of a single atom. These units are settled at the lattice points of what is known as a Bravais lattice. In three dimensions, there are 14 different Bravais lattices[19]. The NWs crystal structures most relevant to this work are formed in the cubic structures, (ZB), and the hexagonal structure (WZ). In some cases it is likely to grow a mixture of the two phases, depending on the stable structure of the bulk compound and the growth conditions, for example, NWs structure can be formed in a WZ or ZB, because of the fact that the WZ has lower surface energy than the

ZB crystalline orientations in the same material. In this case a WZ structure would be stabilized for very thin wires when the surface to volume ratio is high enough. However, an uncontrolled polytypism would be unfavourable for the device properties[20].Some research groups used this approach of controlling the crystal structure without the need to change the material[21] to open new possibilities for material engineering or even improving the devices properties[22].

To explain the structures Miller indices are used to indicate the crystal planes and crystal directions by the symbol (*hkl*) with the basis axes (a_1, a_2, a_3) for cubic system[12,23]. Crystal directions are given in the basis vectors with the relation:

$$[hkl] = ha_1 + ka_2 + la_3 \tag{2.7}$$

Many planes and directions are equal due to the symmetry of the crystal as shown in Figure 2.7 (b). A collective notation is then used for equivalent planes, {hkl}, and < hkl > for equivalent directions.

For example, the six sides of the fcc cubic unit are equivalent and form the set:

$$\{001\} = \{(001), (00\bar{1}), (010), (0\bar{1}0), (100), (\bar{1}00)\} \tag{2.8}$$

Normally nanowires are grown in the <111> growth direction for ZB as shown in Figure 2.7 (a), also the (111) and (001) planes of the cubic system are shown in the same figure.

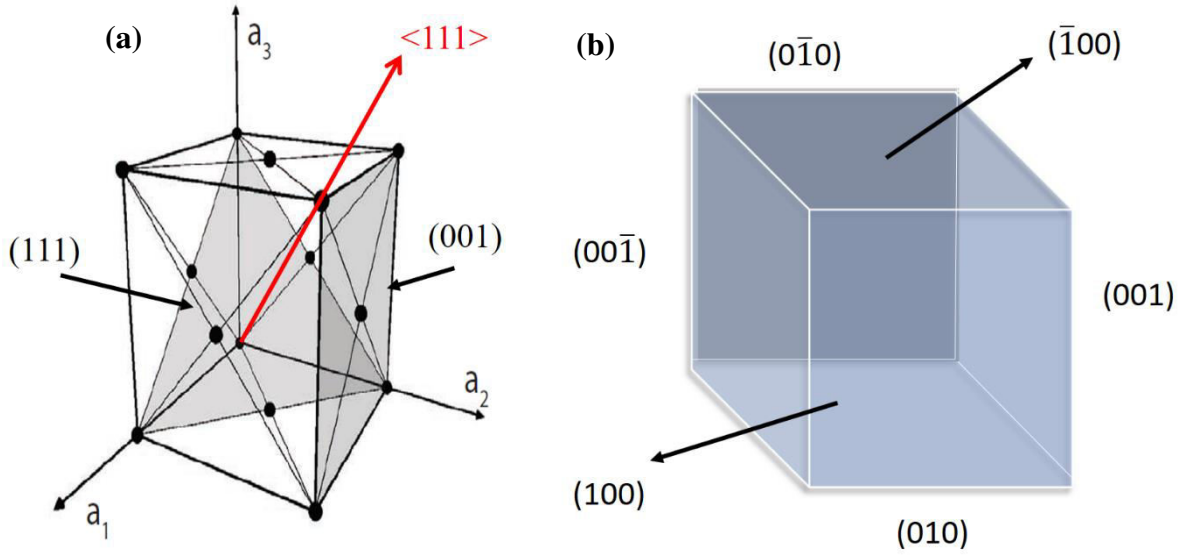

Figure 2.7.Schematic diagrams of the unit cell for the cubic system. (a) Showing the (111) and (001) planes of the cubic system and the crystal directions <111> in red, (b) The equivalent six sides of the ZB unit cell {(001), (00$\bar{1}$), (010), (0$\bar{1}$0), (100), ($\bar{1}$00)}.

For the hexagonal system, Miller–Bravais indices (*hkil*) are regularly used. These are labelled in the same way as referred to above for the cubic system Miller indices, since four basis axes are used, the first three indices are linearly dependent such that i = - (*k* + *l*). The advantage of using four indices is that equivalent planes have similar indices, which is not the case if three indices are used for the hexagonal system[16]. The indices of the six edge planes in Figure 2.8 (b) are, for example, constructed by permuting 1 and 1 over the first three indices. To simplify the labelling, a letter is often assigned to a certain set of equivalent planes. The six edge planes discussed above are the m planes:

m = {1$\bar{1}$00} = {(10$\bar{1}$0); ($\bar{1}$010); (0$\bar{1}$10); (1$\bar{1}$00); (10$\bar{1}$0); (01$\bar{1}$0)} (2.9)

Similar to the ZB structure the NWs are grown in the <0001> for WZ structure as shown in Figure 2.8 (a) with the two facets (1$\bar{1}$00) and ($\bar{1}$100).

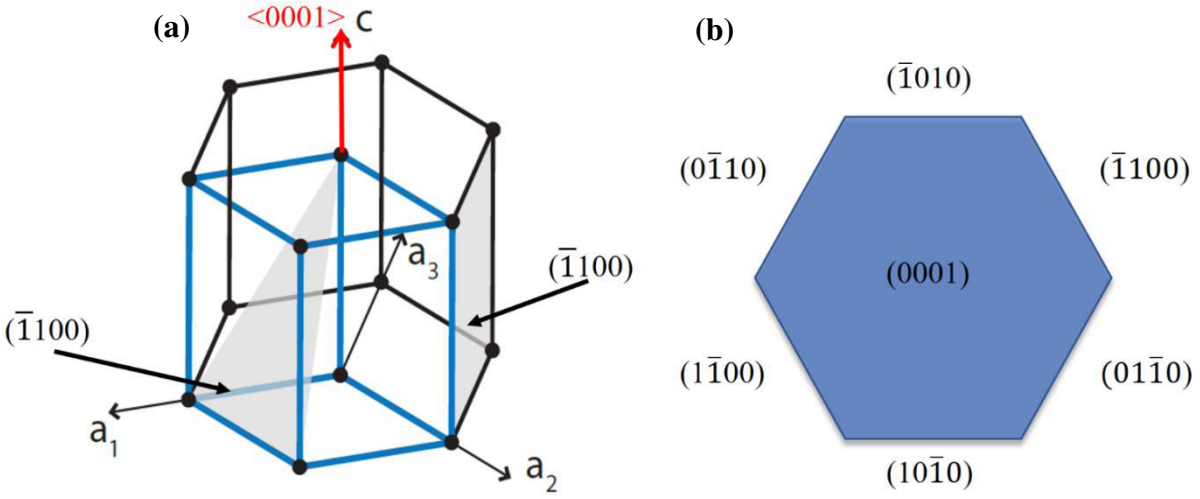

Figure 2.8.Schematic diagrams of the unit cell for the hexagonal system. Showing the $(\bar{1}100)$ and $(1\bar{1}01)$ planes and the crystal directions <0001> in red. (b) The equivalent six sides of the WZ unit cell $(10\bar{1}0)$; $(\bar{1}010)$; $(0\bar{1}10)$; $(1\bar{1}00)$; $(10\bar{1}0)$; $(01\bar{1}0)$.

Stacking faults are partial displacements affecting the regular sequence in the stacking of the lattice planes. Intrinsic stacking faults result from a vacant plane while extrinsic stacking faults are due to the insertion of an extra plane in the sequence. Depending on the stacking sequences, planar defects can be formed within the NWs such as: rotational twins, stacking faults (SF) and grain boundaries[16, 12].

2.9. **Different types of wires structures**

Epitaxial growth of free standing NWs offers more freedom in the design of complex structures and the possibility to grow heterostructures within the wires as compared to planar epitaxy heterostructures. Quantum structures can be formed in two different directions (axial

and radial) For example, axial quantum wells (QWs) or QDisks[24], radial QWs usually called as core-shell[25]or QDots[26].

As a consequence, mismatch strain can be relieved over a short distance from the interface of free-standing radial or axial heterostructures NWs[19,18]. The three types of NWs heterostructures are shown in Figure 2.9. The focus in this thesis will be mostly on axial QWs NWs heterostructures obtained by the selective area-MBE growth technique.

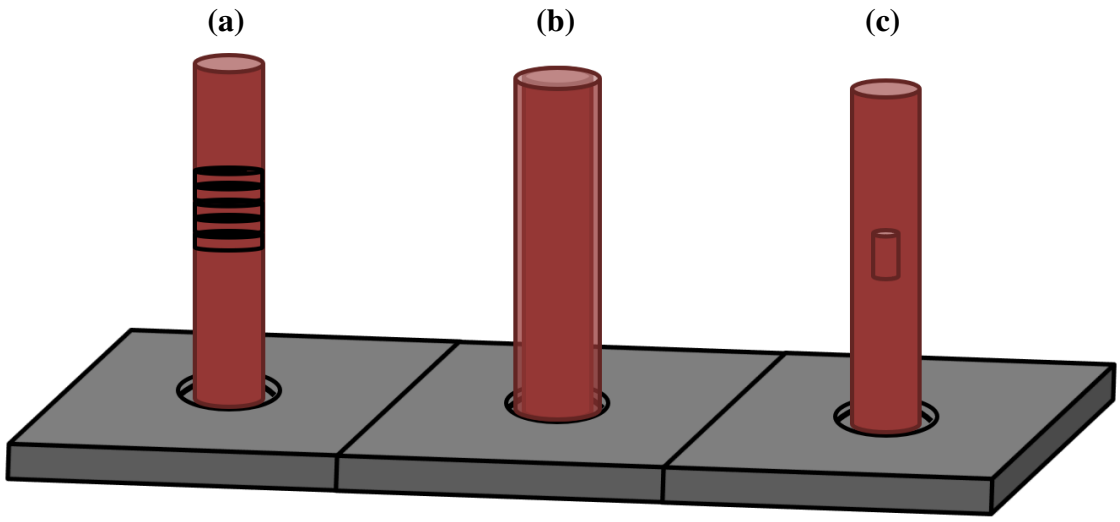

Figure 2.9.Schematic diagram showing different types of NWs Quantum structures, (a) axial quantum wells (QWs), (b) radial QWs (core-shell) and (c) QDots.

2.10. **Luminescence**

Luminescence in semiconductors describes light emission from radiative recombination of electron-hole pairs via application of extrinsic energy. Photoluminescence is the most common technique where luminescence is excited by photons usually a high energy laser, in

contrast to cathodoluminescence where carriers are generated by accelerated electrons or carrier injected (electroluminescence) and thermoluminescence when the carriers are excited thermally. The materials and devices fabricated in this work are characterised mainly by Photoluminescence.

2.11. **Photoluminescence**

Photoluminescence is non-destructive technique used for material characterisation. In this technique, light with energy greater than the band gap of the material is directed onto the surface of the sample. This energy is absorbed causing excitation and creation of electron hole pairs. The electrons return to their equilibrium state by recombining with holes. This results in emission of light (radiative) or instead a non-radiative emission. The emission from the radiative processes is used to study the material surface, interfaces, and the impurity levels and quantization effects within the material[27].

2.12. **Recombination Processes**

This process describes the electron-hole recombination mechanisms in direct bandgap semiconductors when free carries are excited in a semiconductor, either by light or current. There are two types of recombination, a preferred process which called radiative recombination, where emission of photon accompanies it and nonradiative recombination when the electron energy is converted to phonons. Nonradiative recombination is unwanted because it spoils the performance of long wavelength semiconductors, however, it can be minimized but never be reduced to zero. The Different types of the radiative and nonradiative process will be discussed below.

2.12.1. Radiative Recombination

In radiative recombination processes an electron from the conduction band recombines with an empty state (hole) in the valence band and emits photons with an energy approximately equal to the bandgap energy of the semiconductor. Figure 2.10 shows a summary of the radiative recombination processes that can happen in the material, (band to band recombination, band to donor/acceptor recombination, donor to acceptor recombination and exciton recombination).

2.12.2. Band to Band Recombination

Band to band recombination is one of the most important processes in semiconductors. This process happens when an electron in the conduction band recombines with a hole in the valence band which releases a photon. Normally the energy of the produced photon is the same as the band gap energy or greater than it in some cases which is an average of energy equal to:

$$h\nu = E_{ph} = E_g(T) + \frac{KT}{2} \tag{2.10}$$

Where $h\nu$ is the photon energy, $E_g(T)$ is the band gap energy and ½kT represents the thermal distribution of the carriers. ½kT is only a significant factor in narrow gap semiconductors where it accounts for several percent of the bandgap. This process is shown in Figure 2.10 (a).

2.12.3. Conduction Band to Acceptor/Donor to Valence Band Recombination

Donor and acceptor states are found when the grown material has impurities or defects. Discrete levels are then created within the band gap which makes it easy for electrons to recombine. This form of process can occur by two types of recombination. The first case is when an electron from the conduction band recombines with a hole from the acceptor level the energy of the produced photon is equivalent to that of the band gap energy less than the binding energy of the acceptor, thus producing a longer wavelength emission. The second process occurs when an electron from a donor site recombines with a hole from the valence band as shown in Figure 2.10 (b) and (c). Both two processes are described by the following equation:

$$h\nu = E_g(T) + \frac{KT}{2} - E_i \tag{2.11}$$

Where E_i is the binding energy of the acceptor or donor state, and ½kT is again the thermal distribution of carriers.

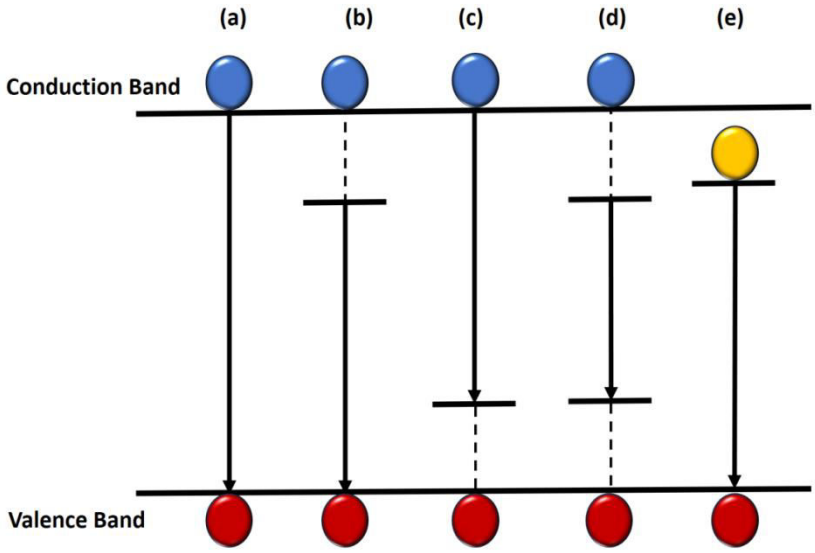

Figure 2.10.Summary of the radiative recombination processes that can happen in a semiconductor, (a) band to band recombination, (b) and (c) band to donor/acceptor recombination, (d) donor to acceptor recombination and (e) exciton recombination.

2.12.4. Donor to Acceptor Recombination

Transitions can happen between the donor and acceptor states, when large numbers of both donors and acceptors exist within the material as shown in Figure 2.10 (d). The emitted photons from this recombination have an energy that can be described by the following equation:

$$h\nu = E_g(T) - (E_D + E_A) + \frac{e^2}{4\pi\varepsilon_0\varepsilon_r r} \quad (2.12)$$

Where E_D *and* E_A are the binding energies of the donor and acceptor respectively. The last section in the equation describes the coulomb interaction between the donor and acceptor atoms on substitutional sites with ε_0 as the permittivity of free space, ε_r the relative permittivity of the material and r the spatial separation of the donor and acceptor. The transition of such cases happens mostly at low temperatures and this effect decreases with increasing temperature.

2.12.5. Excitonic Recombination

Excitonic recombination occurs when an electron and hole become bound via coulomb interaction. Excitons are generally formed in pure materials where the carrier concentration is low; this is required as a large concentration of free carriers results in screened coulomb interaction between carriers, which perturbs the band edge and induces a "tail" of the band states into the energy gap would screen the interaction. Another condition for the formation of an exciton is a low enough temperature such that the thermal energy is lower than the exciton binding energy[28]. Excitons can be formed by either free excitons or bound excitons as shown in Figure 2.10 (e). Free exciton has photon energy in the following form:

$$h\nu = E_g(T) - E_f \quad (2.13)$$

Where E_f is the binding energy of the exciton and is usually only a few meV. Bound excitons occur when an exciton is bonded to a defect or impurity state that gives a photon with energy:

$$h\nu = E_g(T) - E_f - E_b \quad (2.14)$$

Where E_b is the binding energy of the exciton to the impurity states.

2.13. Nonradiative Recombination

In nonradiative recombination electron and holes are recombined and the energy is emitted as phonons, thus, the electron energy is converted to heat instead of producing a photon. These non-radiative processes are responsible for limiting the operating temperature and intensity of light emission from a device. The non-radiative recombinations that affect long wavelength semiconductors are surface recombination, Auger recombination and Shockley-Read-Hall recombination, all of which will be explained below.

2.13.1. Auger Recombination

Auger recombination processes involve electron- hole pairs recombined in a band to band transition giving up the released energy to another electron or hole that is excited to higher states, from where the energy is lost in nonradiative emission. In Auger recombination both wave vector and energy must be conserved at the same time, thus the transition energy would be larger than the energy gap, and the difference between the two depends on the band structure. Normally wide band gap materials have a large effective mass, in such case the Auger recombination needs a large change in momentum (holes occupying high *k* states) to

occur which is not so likely. However, in narrow gap semiconductors (e.g. InAs) the small effective mass in the conduction band and heavy hole mass in the valence band readily enables the momentum changes that are required for Auger to happen. Auger recombination has a large effect on the quantum efficiency and the performance of the device especially as the temperature increases, see Figure 2.11. The rate at which the recombination takes place is proportional to Cn^3 with the cubic dependence of the carrier density (n) arising from the three carriers involved and C is the Auger coefficient which is determined by:

$$C = \sum_i C_i e^{\left(-\frac{E_{ai}}{KT}\right)} \tag{2.15}$$

Where C_i is the rate for each Auger process at zero kelvin, and E_{ai} the activation energy associated with that process depending on the type of Auger recombination. There are several types of Auger recombination responsible for non-radiative recombination in narrow gap semiconductors, as shown in Figure 2.11, the most common types of Auger recombination are:

(a) CHCC: Involves two electrons and a heavy hole. Two electrons collide: one combines with a hole and the energy released excites the other electron up the conduction band. This process is dominant where there is an excess of electrons (see Figure 2.11 (a)).

(b) CHLH: An electron recombines with a heavy hole and the energy released lifts a hole from the light hole to the heavy hole band (see Figure 2.11(b)).

(c) CHSH: Electron recombines with a heavy hole and the recombination energy lifts a hole from the split off band to the heavy hole band (see Figure 2.11 (c)).

CHCC process is dominant in n-type material. Other processes involve two holes and one electron and are dominant in p-type material. In CHCC the recombination happened by giving the energy for another electron to be excited higher up in the conduction band, the activation energy for this process is[29]:

$$E_a^{CHCC} = \left(\frac{m_c}{m_c + m_h}\right) E_g \tag{2.16}$$

Where m_c is the electron effective mass, m_h is the heavy hole effective mass and E_g is the transition energy. It can be seen that the activation energy decreases with increasing wavelength (as E_g α $\frac{1}{\lambda}$) which correspond to an increase in CHCC recombination in longer wavelength devices.

In CHSH the recombination excites a carrier from the SO band into the heavy hole band with an activation energy of:

$$E_a^{CHSH} = \left(\frac{m_c}{2m_h + m_c - m_s}\right)\left(E_g - \Delta_{so}\right) \tag{2.17}$$

Where m_c is the electron effective mass, of SO band holes, and Δ_{so} is the energy gap between the heavy hole and SO bands. In particle terms, this means that if $\Delta_{so} > E_g$ than the CHSH process is effectively suppressed but when $\Delta_{so} = E_g$ resonance is achieved and the CHSH rate is greatly increased.

2.13.2. Shockley-Read-Hall Recombination (SRH)

The recombination of free carriers through deep states in the band gap mainly caused by native lattice defects, dislocations or impurities, the rate of SRH at which the carriers can recombine via such a centre can be obtained from:

$$R = nA_{SRH} \tag{2.18}$$

Where n is the carrier concentration and A_{SRH} is the SRH coefficient and were given by:

$$A_{SRH} = \frac{1}{2\tau_0} \tag{2.19}$$

Where τ_0 is the carrier lifetime. Usually in the case of deep-level transitions were the electron is trapped long enough to recombine with other carriers by multi-phonon emission[30].

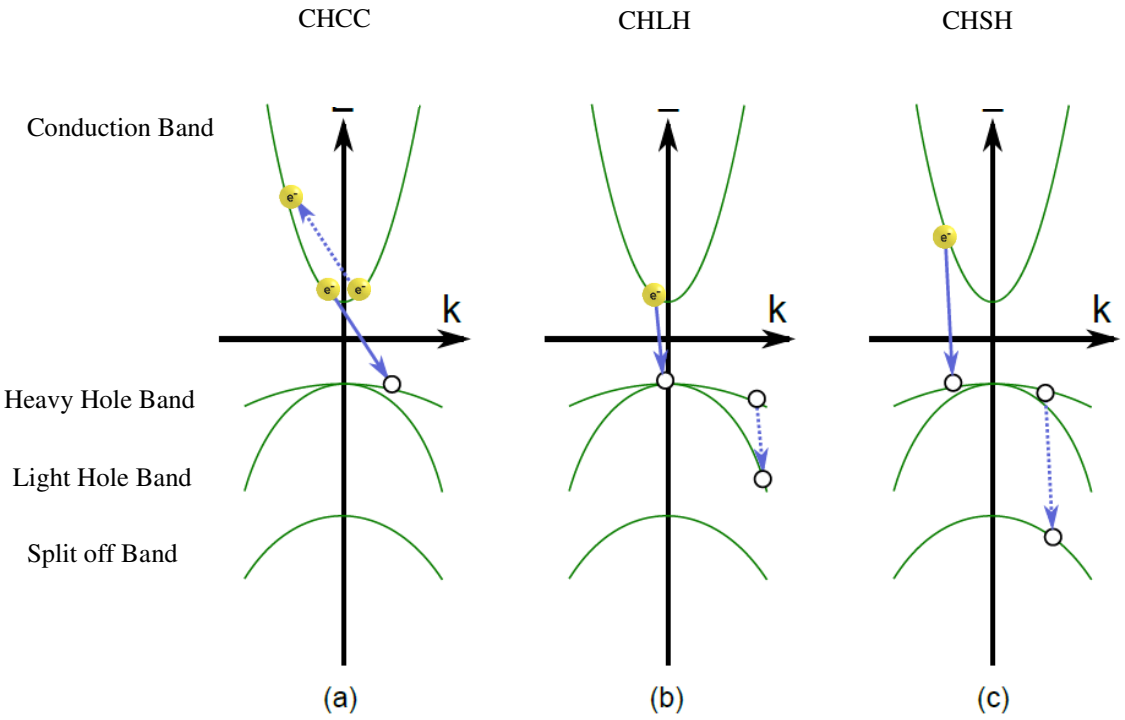

Figure 2.11. Types of Auger recombination responsible for non-radiative recombination in narrow gap semiconductors (a) CHCC, where an electron is excited higher in the conduction band (b) CHLH where the recombination excites a hole from the heavy hole band into the SO band, and (c) CHSH where the electrons recombines with a heavy hole and the recombination energy lifts a hole from the split off band to the heavy hole band.

2.13.3. Surface Recombination

Non-radiative recombination can occur at the semiconductor's surface or the interface between two layers which create regions of strain leading to the formation of dangling bonds. These bonds are a strong perturbation to the crystal lattice and are able to attract impurities into the structure during growth which may lead to surface states being produced across the band gap. Surface states plays an important role in NWs because of the large surface to volume ratio and the fact that they can act as radiation recombination centers, which may create dangling bonds that can adsorb impurities. Dangling bonds can act as donor-like or acceptor-like states depending on their charge state. The bonds may also rearrange themselves and form bonds between neighboring atoms in the same surface plane which can lead to a new atomic structure with state energies different from bulk atomic states. These surface states can lie above or below the bandgap where they can compete with band-edge emission, which greatly reduces the luminescence efficiency. The surface recombination is limited by the rate at which the carriers arrive at the surface. This parameter is known as the surface recombination velocity[31], given units of (cm/s). In general the very high surface recombination always reduces the luminescence efficiency, thus, a passivation is needed to remove the unwanted surface states, decrease surface recombination velocity and also stop any new formation of surface states. The passivation process can be done by introducing the semiconductor surface to an additional material which bonds to the dangling bonds. Joyce et al[32] extracts the surface recombination velocities of 5.4x 10^5, 3.0 x10^3 and 170 cm s^{-1} for GaAs, InAs and InP surfaces, respectively. These values are consistent with results obtained for bulk GaAs[33], InAs[34] and InP[35]. In this study, the surface recombination velocity of GaAs nanowires is higher than the InAs which could be a case of a single study. However, surface

passivation has been shown to increase the carrier lifetime in GaAs nanowires[36] and improve band-edge PL emission from InAs nanowires[37].

2.14. Temperature dependence of the band gap:

When the temperature is increased the band gap of a semiconductor tends to decrease, this is because the inter-atomic bond spacing expands leading to slightly weaker bonds between the atoms. This weakening of the bonds means that less energy is required to break a bond and push an electron into the conduction band as such reducing the band gap. The temperature dependence of the band gap was found to obey the Varshni equation:

$$E_g\,(T) = E_g(0) - \frac{\alpha\, T^2}{\beta + T} \tag{2.20}$$

where $E_g(0)$ is the band gap of the material at zero Kelvin, α and β are two empirical parameters relating to the material with α in the order of 0.5 meV/K and β in the order of the Debye Temperature respectively. Typically, low temperature deviations from this equation gives information about states below the band gap[38].

2.15. K value for PL emission Power Dependent

Analysis of excitation-power dependent PL is commonly performed to investigate the emissions in narrow gap semiconductors[39,40,41,42]. Schmitt et al [43] describes a calculation of the excitation power dependence of near-band-edge photoluminescence (NBEPL) lines. The calculation is based on a set of rate equations for the free-exciton, bound-exciton, free-to-bound, and donor-acceptor recombinations. No further assumption on nonradiative processes

is made on this paper. The steady-state solutions of the rate equations are obtained by a method presented by Zulehner[44]. With this model they explained the features of the NBEPL which were observed in experiment. The model yields the power dependence of all NBEPL lines. Deviations from the I~L behavior, which are observed in experiments when L is varied by more than two orders of magnitude, are also reproduced by our model. Furthermore, the variation of k for the free-exciton line which was observed when the wavelength of the excitation laser light is varied from above-band-gap to resonant excitation of excitons can also be understood in the framework of their calculation. They also present analytical relations between the k's of the free exciton, the bound exciton, and the free-to-bound emission. These relations can be used for the unambiguous identification of PL lines from their power dependence.

For the calculation of the power dependence of the NBEPL, they take into account a number of transitions which are shown schematically in Figure 2.12. Assuming that photoexcited electron-hole pairs can recombine by the following transitions: (A) free-exciton (FE) recombination, (B) and (C) radiative recombination of donor- and acceptor-bound excitons (D^0 X, A^0 X), (D) donor acceptor pair recombination (D^0A^0), (E) radiative recombination of a free electron and a neutral acceptor (eA^0), (F) radiative recombination of a free hole and a neutral donor (hD^0), and (G) and (H) nonradiative transitions of free electrons and holes to ionized donors and acceptors, respectively. Also included in Figure 1 are the excitations processes (I) ~ (L): (I) is the excitation of electron-hole pairs by above-band-gap laser light, hν) Eg, (J) stands for resonant formation of free excitons when the laser energy $h\nu \approx E_s$, and (K) and (L) are the excitation of electrons from neutral donors or ionized acceptors by the laser radiation, respectively.

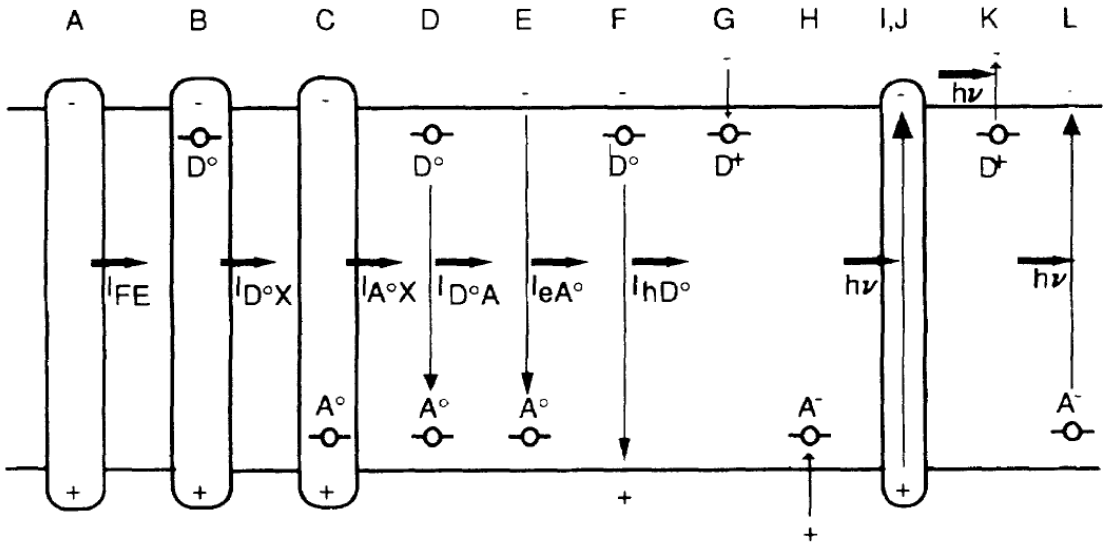

Figure 2.12.: Radiative and nonradiative transitions which are included in the model calculation of the near-band-edge photoluminescence. (A) Free-exciton recombination, (B) and (C) radiative recombination of donor- and acceptor-bound excitons (D^0X, A^0X), (D) donor-acceptor pair recombination (D^0A^0), (E) radiative recombination of a free electron and a neutral acceptor (eA^0), (F) radiative recombination of a free hole and a neutral donor (hD^0), and (G) and (H) are nonradiative transitions of free electrons and holes to ionized donors and acceptors, respectively. Also included in the figure are the excitation processes (I)~(L): (I) is the excitation of electron-hole pairs by above-band-gap laser light, hν & E_g, (J) stands for resonant formation of the free excitons with hν ≈ Eg, and (K) and (L) are the excitation of electrons from neutral donors or ionized acceptors by the laser radiation, respectively[43].

From the above some fundamental recombination mechanisms can be identified from excitation-intensity- dependent PL measurements. The power-dependent PL intensity can be described by the empirical formula[22]:

$$I \sim L^K \tag{2.21}$$

K is the power index and can be extracted by a simple measurement of gradient upon y = mx + c with the use of logarithmic scaling. I, L and K are related by

$$\text{Log}(I) = K \log(L) + C \tag{2.22}$$

where I is the luminescence intensity, L is excitation laser intensity, and k is the scaling index, (L is varied over a range of less than two orders of magnitude), usually $1 < k < 2$ for

the free- and bound-exciton emissions (close to the bandgap), when excitation laser has energy exceeding bandgap of the material; k < 1 for free-to-bound transitions (donor-hole hD, electron-acceptor eA) and donor-acceptor pairs (DAP) in near-band-edge photoluminescence studies. We use this approach to compare InAs to InAsSb; k is equal to 1 for the free exciton emission when excitation laser has the same energy with bandgap. The nonlinear behavior of the bound-exciton emission intensity is due to the increase of the population of neutral impurities by photo-excited carriers, so it often suggests an impurity related origin. A rapid quenching of the peak intensity with the increase of temperature and the rapid saturation with the increase of excitation density imply a transition involving an impurity or defect. In the case of free electrons recombining with acceptors, such dramatic temperature dependence cannot be expected. To conclude, the near band edge PL has been described in a series of connecting rate equations and concludes by stating explicitly that the extraction of sub-linear K parameters (K<1) indicates the influence of free to bound and donor to acceptor recombination, where such recombination takes the ideal form of K=0.5. Samples not subject to intentional doping with large densities of defect centres are likely then to exhibit luminescence involving sub-gap states. The author then reports the experimental verification of this technique, citing extracted K parameters from known sub-gap recombination in comparison to known free exciton recombination. The results of free exciton recombination consistently yielded K parameters of 1 and above, the lower energy sub-gap luminescence gave K<1 conversely. For detailed mathematical treatment of recombination characteristics the reader is referred to the cited source[45].

2.16. **Activation energy measurement from double Arrhenius Plot**

Different processes might contribute to the changes of the PL features versus the increase of temperature such as thermal release of trapped carriers, followed by capture in a nonradiative recombination. Temperature dependence of the integrated intensity I of PL peaks is often described using the Arrhenius equation. The Arrhenius equation method was originally developed to extract the dependence of reaction rates via thermally induced processes to temperature. The Arrhenius equation in relation to charge carriers within a semiconductor is given by

$$K = A \exp(-E_a/K_bT) \tag{2.23}$$

Where A is the pre-exponential factor or frequency factor, Ea the activation energy which is the threshold energy that the reactants must acquire before reaching the transition state, K is the Boltzmann constant and T is the absolute temperature at which the reaction take place. In the case of photoluminescence, the activation energy (E_a) represents the required minimum energy for transformation of the reactants, and the reaction is the transformation of particles from radiative states to non-radiative states. E_a then gives the threshold energy for the dominant mechanism responsible for the reduction in luminescence at any given temperature. The temperature dependence of the integrated PL intensity is expressed as the temperature dependence of the integrated PL intensity is expressed as

$$I = \frac{I_0}{1+A \exp -E_a/K_BT+B \exp -E_b/K_BT} \tag{2.24}$$

The activation energy is extracted by log plot to give

$$\text{Log (I)} = \log(\text{constant}) + (E_a/kT + E_b/kT) \tag{2.25}$$

By fitting to an inverse temperature scale, E_a then is extracted by gradient similar to $y = mx + c$, where I is the integrated PL intensity at T K, I_0 the integrated PL intensity at 0 K, k the Boltzmann constant and E_A and E_B are the acquired activation energy[46]. Narrow gap materials have a lower electron mass than wider gap materials which makes Auger recombination a dominant factor in limiting their performance. In addition to this, the activation energy of Auger processes has a dependence on the band gap which gives narrow gap materials lower activation energy.

2.17. **Band bending**

The interface between two regions can form an electric field caused by the diffusion of carriers to the lower energy side of the interface. This field bends the band which leads to strong localised confinement of carriers at low temperatures similar to a quantum wells. Carrier transport can be blocked because of the interface potentials, this can be reduced by replacing abrupt interfaces with graded ones.

2.18. **Triangular Quantum well**

In type II quantum well structures holes are confined in the quantum well and the electrons are attracted toward the interface. An increase in excitation intensity will produce additional charges which raise the steepness of the confining potential for electrons and create a triangular quantum well (with electron quantization energies) as shown in Figure 2.12. The flat-band energy of the quantum well can then be extracted from the power dependence of the PL.

The triangular quantum well originates from an electric field *F*, which is proportional to the charge carrier density n_w and the integrated PL intensity *L* is proportional to the integrated spontaneous emission rate which is proportional to n_w squared, as we can see from equation (2.6). The strongly localized holes form a charged plane and produce an approximately triangular quantum well with electric-field strength of *F*

$$F = \frac{2\pi e n_W}{\varepsilon_0} \tag{2.26}$$

Where n_w is the charge carrier density in the triangular well.

The integrated PL intensity *L* is proportional to the integrated spontaneous emission rate as described in the following formula:

$$L = \gamma B n_w^{\,2} \tag{2.27}$$

B is the radiative recombination coefficient and γ is the collection efficiency.

n_w will be proportional to the square root of L. The ground electron state energy is given by this equation and will be proportional to n to the power of 2 divided by 3 and will be in proportional to the cubic root of L. The electron charge carrier density n_w is:

$$n_w = \sqrt{\frac{L}{\gamma B}} \propto L^{1/2} \tag{2.28}$$

The ground electron state in such a well is given by:

$$E_e = \left(\frac{9\pi}{8}\right)^{2/3}\left(\frac{\eta^2}{2m_e}\right)^{1/3} F^{2/3} \propto n^{2/3} \propto L^{1/3} \tag{2.29}$$

Thus, an increase in excitation intensity will raise the steepness of the confining potential and consequently the electron quantization energy E, with a typical $\Delta E \sim L^{1/3}$ behavior where L is integrated PL intensity[47].

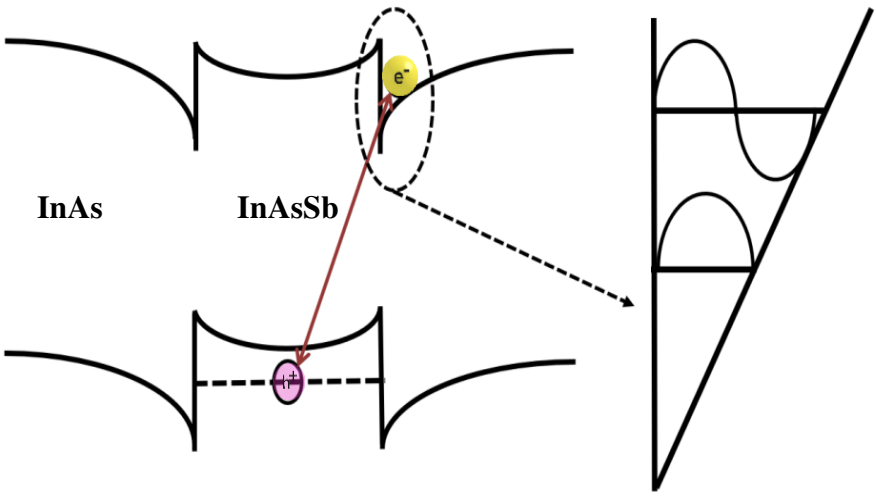

Figure 2.13. A schematic diagram showing the triangular quantum well (with electron quantization energies) created by an increase in the excitation intensity which produces additional charges that raise the steepness of the confining potential for electrons.

2.19. **P-n junction**

Joining two semiconductors together with n- and p- type doping at zero bias makes a p-n junction. This structure is very useful for many optoelectronic applications including photodetectors, which is the main use of these junction structures in this work. The electrons and holes in the *N* and *p* type regions respectively diffuse to the opposite side of the Interface and recombine which leaves behind regions containing the charged immobile acceptors and donors as shown in Figure 2.13. These depleted regions at the interface constitute the space-charge region. This region creates a built-in field that opposes the carrier diffusion and modifies the energy diagram the resulting band diagram is shown in Figure 2.13, the potential barrier is called the built-in field and is equal to:

$$V_D = \frac{K_T}{e} \ln \frac{N_{A+}\, N_D}{n_i^2} \tag{2.30}$$

Were n_i is the intrinsic carrier concentrations of semiconductors, N_A is the acceptor concentration, N_D is the donor concentration. However, the Fermi level should be constant throughout the n- and p- type regions, including the junction region, as the junction considered as single semiconductor. Since the majority carrier hole density on the *p*-side is much greater than the minority carrier hole concentration on the *N*-side, there will be a hole diffusion current. The degree of band bending is dependent on the composition of the two materials, the carrier concentration, the Fermi level position (which is affected by impurity concentration), operating temperature and any applied bias which modifies the built-in potential[48].

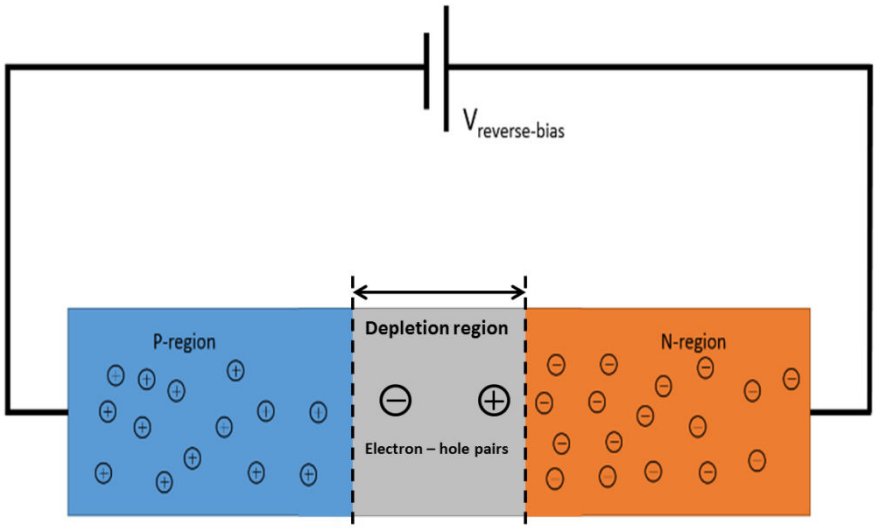

Figure 2.14.A schematic diagram showing the pn junction, where the electrons and holes diffuses to the opposite side of the interface forming an electron and hole depletion region at the interface.

2.20. **P-i-n Photodiodes**

A p-i-n structure can be described as an intrinsic layer normally undoped, i-region or depletion region surrounded by two doped regions respectively p- and n-type as shown in Figure 2.14 (a). The main benefit of such structures is in the ability of tailoring the

depletion region thickness to allow an optimization of the quantum efficiency and frequency response[49]. The structure is called a homojunction, if the n-, i- and p-regions are made of the same semiconductor, or heterojunctions when the junctions are made of semiconductors with different bandgaps However, for low leakage current, the lattice constants should be closely matched for the two materials. The mechanisms involved in the generation of a photocurrent are illustrated in Figure 2.14 (b). In a p-i-n, the light is absorbed and produces hole-electron pairs. The pairs produced in the depletion region and within the diffusion length ($1/\alpha$) are separated by the electric field[30]. The drift of the carriers across the structure generates a current. In a reverse-biased depletion region, assuming that the thermal generation current can be neglected and that the width of the p-region W_p verifies $W_p << 1/\alpha$, the total photogenerated current density J_p is:

$$J_p = J_{drift} + J_{diff} \tag{2.31}$$

where J_{drift} is the drift current density due to carriers generated inside the intrinsic region W and J_{diff} the diffusion current density from carriers outside W diffusing into the junction. The hole-electron generation rate *G(x)* as a function of the distance within the semiconductor is:

$$G(x) = \Phi_0 \alpha \exp(-\alpha x) \tag{2.32}$$

where α is the absorption coefficient, Φ_0 the incident photon flux described by $\Phi_0 = \frac{P_{opt}(1-R)}{Ah\nu}$, R the reflection coefficient at the air-photodetector interface, A the area of the illuminated surface[30]. The drift current density J_{drift} is proportional to the integral of *G(x)* over the intrinsic region width W:

$$J_{drift} = -q\int_0^W G(x)dx = q\Phi_0(1-e^{-\alpha W}) \tag{2.33}$$

and the diffusion current density J_{diff}, also a function of the absorption coefficient, can be expressed in an analogous way. The total current in a diode is the contribution of the photogenerated current, due to the absorption, and the dark current, due to the thermal generation-recombination of electron-hole pairs in the depletion region. The current I for an ideal diode under illumination is expressed for a current-voltage (I-V) characteristic in the form:

$$I = I_0\left(\exp\left(\frac{qV}{k_B T}\right) - 1\right) - I_p \tag{2.34}$$

where I_0 is the reverse-bias saturation current, V the applied voltage, T the absolute temperature, and I_p is the photogenerated current in the relation:

$$I_P = J_P A \tag{2.35}$$

where J_p the total photogenerated current density and A the area of the device[30].

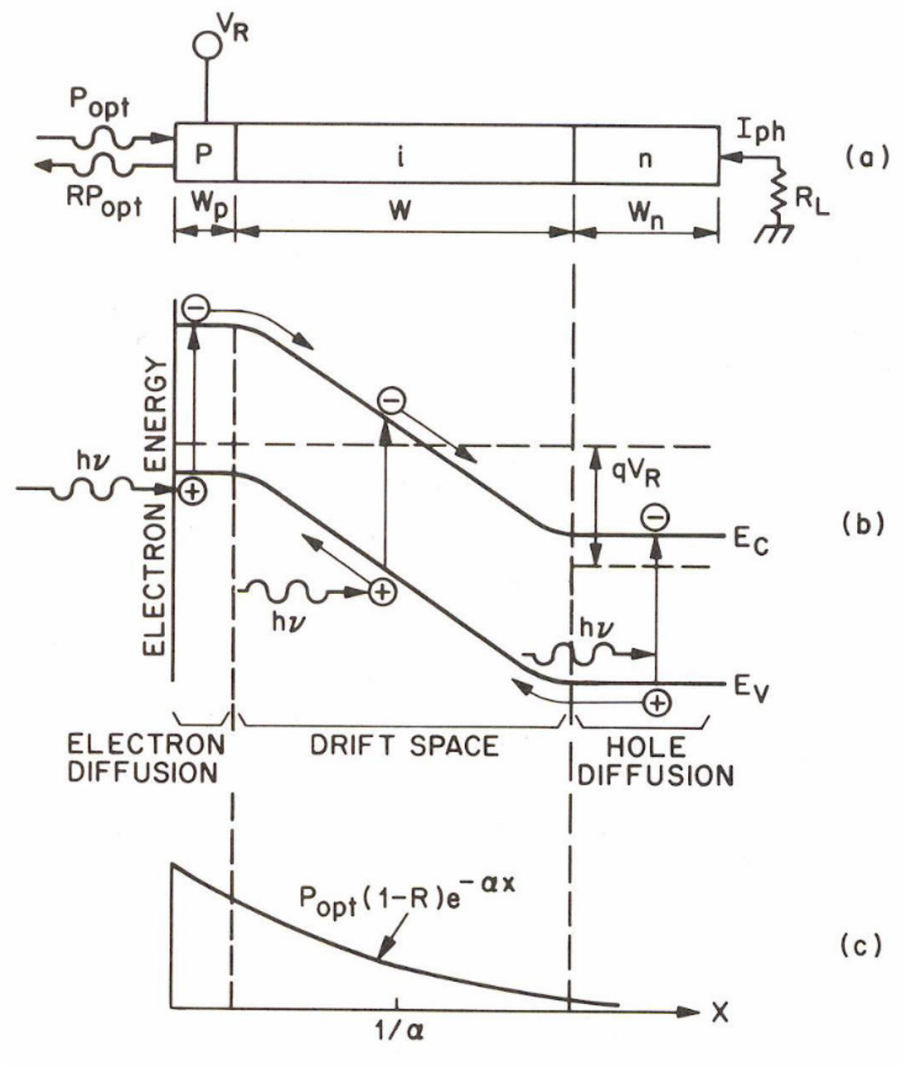

Figure 2.15. Homojunction p-i-n diode: (a) cross-sectional view; (b) energy-band diagram under reverse bias; (c) generation-recombination characteristics[30].

2.21. **References**

[1] N. Dasgupta and A. Dasgupta, Semiconductor devices: modelling and technology. New Delhi: Prentice-Hall of India, 2004, p. 9.

[2] Brus LE. Electron-electron and electron-hole interactions in small semiconductor crystallites – the size dependence of the lowest excited electronic state. J. Chem. Phys 1984, 80:4403–4409.

[3] W. Lin and K. E. Benson. Silicon crystal growth. In Microelectronic Materials and Processes, Nato Science Series E, chapter 1. Springer Netherlands, 1986.

[4] J. I. Pankove. Optical Processes in Semiconductors. Dover Books on Physics. Dover Publications, New York, 1971.

[5] C. Kittel. Introduction to Solid State Physics. John Wiley & Sons, New York, USA, 6th edition, 2004.

[6] J. I. Pankove. Optical Processes in Semiconductors. Dover Books on Physics. Dover Publications, New York, 1971.

[7] C. Kittel. Introduction to Solid State Physics. John Wiley & Sons, New York, USA, 6th edition, 2004.
[8] M. Fukuda, Optical semiconductor devices. New York: John Wiley & Sons, 1999, p. 7.

[9] Dielectric Phenomena in Solids: With Emphasis on Physical Concepts of , Kwan-Chi Kao.

[10] Hafaiedh, A.; Bouarissa, N. Quantum Confinement Effects on Energy GaPs and Electron and Hole Effective Masses of Quantum Well AlN. Physica E: Low-dimensional Systems and Nanostructures 2011, 43, 1638-1641.

[11] Alivisatos AP. Perspectives on the physical chemistry of semiconductor nanocrystals. J. Phys. Chem 1996;100:13226–13239.

[12] A. Yariv and P. Yeh, Photonics: optical electronics in modern communications, 6th ed. Oxford University Press, 2007, p. 678.

[13] E. F. Schubert Physical Foundations of Solid-State Devices 2009 Ed.

[14] Borg, B., Kimberly A., J. Eymery, and L.Wernersson, Enhanced Sb incorporation in InAsSb nanowires grown by metalorganic vapor phase epitaxy, Appl. Phys. Lett. 2011, 98, 113104.

[15] S. Johansson, M. Egard, S. Gorji Ghalamestani, B.M. Borg, M. Berg, L.-E. Wernersson, E. Lind, RF Characterization of Vertical InAs Nanowire Wrap-Gate Transistors Integrated on Si Substrates, IEEE Trans. Microwave Theory Tech. 2011, 59.

[16] Svensson, J., Anttu, N., Vainorius, N., Borg, B. and Wernersson, L. Diameter-Dependent Photocurrent in InAsSb Nanowire Infrared Photodetectors. Nano Lett. 2013, 13**,** 1380-1385.

[17] T.-W. Yeh, Y-T. Lin, L.S. Stewart, P.D. Dapkus, R. Sarkissian, J.D. O'Brien, B. Ahn, S.R. Nutt, InGaN/GaN Multiple Quantum Wells Grown on Nonpolar Facets of Vertical GaN Nanorod Arrays, Nano Lett. 2012, 12, 3257-3262.

[18] Salfi, J.; Roddaro, S.; Ercolani, D.; Sorba, L.; Savelyev, I.; Blumin, M.; Ruda, H.; Beltram, F. Electronic Properties Of Quantum Dot Systems Realized In Semiconductor Nanowires. Semiconductor Science and Technology 2010, 25, 024007.

[19] C. dang, \Cristal densite surface." Website, 2009. [Online; accessed 2017-09-20].

[20] Murayama, M.; Nakayama, T. Chemical trend of band offsets at wurtzite/zinc-blende heterocrystalline semiconductor interfaces. Phys. Rev. B: Condens. Matter Mater. Phys. 1994, 49, 4710−4724.

[21] Bolinsson, J.; Caroff, P.; Mandl, B.; Dick, K. Wurtzite–Zincblende Superlattices in InAs Nanowires Using a Supply Interruption Method. Nanotechnology 2011, 22, 265606.

[22] Caroff, P, Dick, KA, Johansson, Jonas, Messing, Maria, Deppert, K, Samuelson, L. Controlled polytypic and twin-plane superlattices in III-V nanowires. Nature nanotechnology. 2009, 4. 50-5. 10.1038/nnano.2008.359.

[23] Kriegner, D.; Panse, C.; Mandl, B.; Dick, K.; Keplinger, M.; Persson, J.; Caroff, P.; Ercolani, D.; Sorba, L.; Bechstedt, F. et al. Unit Cell Structure of Crystal Polytypes in InAs and InSb Nanowires. Nano Letters 2011, 11, 1483-1489.

[24] Arbiol, J.; de la Mata, M.; Eickhoff, M.; Morral, A. Bandgap Engineering in a Nanowire: Self-Assembled 0, 1 And 2D Quantum Structures. Materials Today 2013, 16, 213-219.

[25] Treu, J.; Bormann, M.; Schmeiduch, H.; Döblinger, M.; Morkötter, S.; Matich, S.; Wiecha, P.; Saller, K.; Mayer, B.; Bichler, M. et al. Enhanced Luminescence Properties of InAs–InAsP Core–Shell Nanowires. Nano Lett. 2013**,** 13, 6070-6077.

[26] Heiss, M.; Fontana, Y.; Gustafsson, A.; Wüst, G.; Magen, C.; O'Regan, D.; Luo, J.; Ketterer, B.; Conesa-Boj, S.; Kuhlmann, A. et al. Self-Assembled Quantum Dots in a Nanowire System for Quantum Photonics. Nature Materials 2013, 12, 439-444.

[27] Schubert F. E. Light Emitting Diodes, Cambridge University Press (2003).

[28] R. S. Knox, Theory of excitons, Solid state physics (Ed. by Seitz and Turnbul, Academic, NY), v. 5, 1963.

[29] Pidgeon, C.; Ciesla, C.; Murdin, B. Suppression of Non-Radiative Processes in Semiconductor Mid-Infrared Emitters And Detectors. Progress in Quantum Electronics 1997, 21, 361-419.

[30] Mani, H, PhD Thesis, Montpellier University, 1989.

[31] Van Opdorp, C.; Werkhoven, C.; Vink, A. A Method to Determine Bulk Lifetime and Diffusion Coefficient of Minority Carriers; Application Ton-Type LPE Gap. Applied Physics Letters 1977, 30, 40-42.

[32] Joyce, H.; Docherty, C.; Gao, Q.; Tan, H.; Jagadish, C.; Lloyd-Hughes, J.; Herz, L.; Johnston, M. Electronic Properties of GaAs, InAs and InP Nanowires Studied by Terahertz Spectroscopy. *Nanotechnology* 2013, *24*, 214006.

[33] Dmitruk N L, Lyashenko V I, Tereshenko A K and Spektor S A 1973 Investigation of surface recombination on epitaxial GaAs films Phys. Status Solidi a 20 53–62.

[34] Mikhailova M P, Nasledov D N and Slobodchikov S V 1965 Spectral response of the photoeffects in InAs Phys. Status Solidi b 11 529–34.

[35] Casey H C and Buehler E 1977 Evidence for low surface recombination velocity on n-type InP Appl. Phys. Lett.
30 247–9.

[36] Parkinson P, Joyce H J, Gao Q, Tan H H, Zhang X, Zou J, Jagadish C, Herz L M and Johnston M B 2009 Carrier lifetime and mobility enhancement in nearly defect-free core–shell nanowires measured using time-resolved terahertz spectroscopy Nano Lett. 9 3349–53.

[37] Sun M H, Joyce H J, Gao Q, Tan H H, Jagadish C and Ning C Z 2012 Removal of surface states and recovery of band-edge emission in InAs nanowires through surface passivation Nano Lett. 12 3378–84.

[38] Nepal, N.; Li, J.; Nakarmi, M.; Lin, J.; Jiang, H. Temperature and Compositional Dependence of the Energy Band Gap of Algan Alloys. Applied Physics Letters 2005, 87, 242104.

[39] A photoluminescence study of polycrystalline thin-film CdTe/CdS solar cells, D.P. HALLIDAY, J.M. EGGLESTON, K. DUROSE, Journal of Crystal Growth 186, 543-549 (1998)

[40] Midinfrared photoluminescence of InAsSb quantum dots grown by liquid phase epitaxy, A. KRIER, X.L. HUANG, A. HAMMICHE, Applied Physics Letters volume 77 number 23, 3791-3793 (2000).

[41] Low-temperature photoluminescence of epitaxial InAs, Y. LACROIX, C.A. TRAN, S.P. WATKINS, M.L.W. THEWALT, Journal of Applied Physics volume 80 number 11, 6416-6424 (1996).

[42] Excitonic photoluminescence in high-purity InAs MBE epilayers on GaAs substrates, P.J.P. TANG, C.C. PHILLIPS, R.A. STRADLING, Semiconductor Science and Technology 8, 2135-2142 (1993).

[43] Schmidt, T.; Lischka, K.; Zulehner, W. Excitation-Power Dependence of the Near-Band-Edge Photoluminescence of Semiconductors. Physical Review B 1992, 45, 8989-8994.

[44] W. Zulehner, Math. Comput. 50, 167 (1988).

[45] Theory of semiconductor heterostructures for infrared applications, M.R. KITCHIN, doctoral thesis, University of Newcastle upon Tyne, 12-17 (1999).

[46] Laider.K.J Chemical Kinetics,Third Edition, New York: Harper & Row,(1987).

[47] Ledentsov, N.; Böhrer, J.; Beer, M.; Heinrichsdorff, F.; Grundmann, M.; Bimberg, D.; Ivanov, S.; Meltser, B.; Shaposhnikov, S.; Yassievich, I. et al. Radiative States in Type-II GaSb/GaAs Quantum Wells. Physical Review B 1995, 52, 14058-14066.

[48]C. Van Opdorp and J. Vrakking, Solid State Electron, Appl. Phys. Lett. 1977, 30, p40.

[49] Shockley, W. The Theory of p-n junctions in semiconductors and p-n junction transistors. Bell Syst. Tech. J. 1949, 28, 435–489.

Chapter 3

Literature Review

3.1. Introduction

III-V semiconductors nanowires have many interesting physical and optical properties, such as the narrow band gap, the small electron effective mass and the very high electron mobility, along with a great potential for realising nanoscale devices[1]. The unique geometry for such structures offers new photodetector architectures for sensing, operating in the mid-infrared spectral range as mentioned in the previous chapter. In particular InAs- based nanowires have been extensively investigated and successfully used to fabricate nanoscale devices including field-effect transistors[2], solar cells[3], sensor applications[4], lasers[5] and photodetectors[6], and until today it is attracting many researchers for further developments of optoelectronic devices and nanoscale photonic applications[7]. Giving further insight into the optical emission and related energy band gap would lead to improvements in the use of these materials, especially for infrared detectors and emitters.

3.2. Fabrication methods of III-V NWs

Semiconductor nanowires in nanotechnology can be synthesized with two main approaches, one is called top-down and bottom-up approaches. The idea behind the top-down approach is to etch out and remove the crystal planes of the material from larger pieces which already present on the substrate to form the nanowires, this approach mostly dominates in industry for large scale fabrication. Few researches have been used successfully to produce NWs using this approach, for example InP and InGaAsP/InP structures[8,9]. To the best of our knowledge, until today, there has not been any report of InAsSb fabricated using top down approach; this approach shows to some extent the ability to be producing NWs for some III-V materials. However, it this method suffers from drawbacks such as wires surface contamination or damages after etching treatment, especially in the case of optical studies. In the bottom-up

approach, the nanostructures are built up on the substrate by adding atoms layer by layer in an ordered manner, offering crystal structures growth of very high uniformity, with a higher relative controllability in the NWs growth rate. There are two methods within the bottom-up fabrication of nanowire growth techniques: the template directed and the free- standing methods. Most of the reported NWs have been fabricated using the second approach by random or site control growth. The work in this thesis will focus on the patterned template method, full details of the fabrication of the nanowire sites will be explained in more details in next section. Figure 4Figure 3.1 shows SEM images for InAs NWs growing by the bottom-up approach (a) represent a free-standing method[5], and (b) controlled method[6].

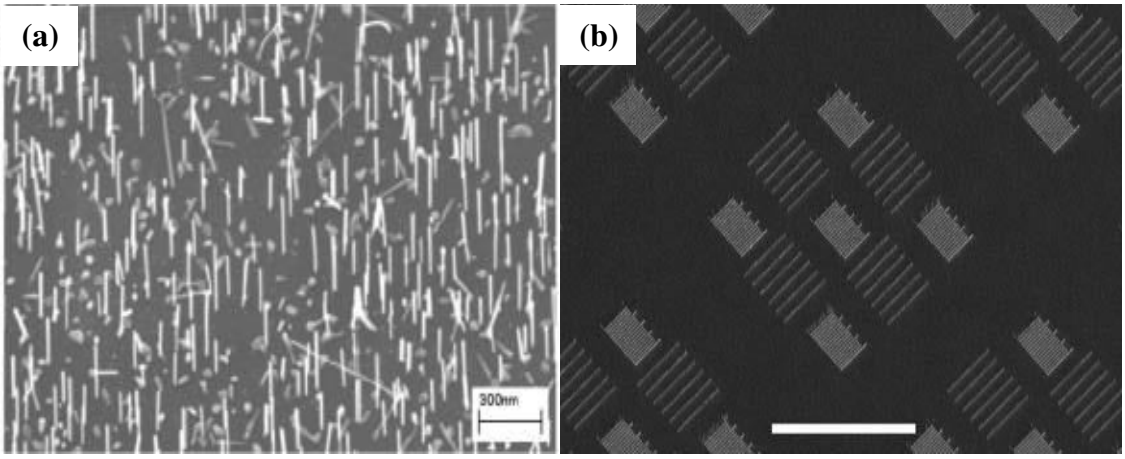

Figure 3.1. SEM images of InAs NW growing by the bottom-up approach (a) represent a free standing method[5], and (b) controlled method[6].

3.3. Nanowires growth mechanism and growth techniques

The field of InAs(Sb) NWs growth has been evolving rapidly over the last decade. Most of the reported growths mechanisms were governed by the famous vapor-liquid-solid (VLS) mechanism. In this approach, metal droplets are deposited on the growth substrate either through self-induced for example In for InAs(Sb) or foreign metal catalyst such as Au

followed by subsequent nanowire synthesis. Alternatively, the growth can be described by vapor solid (VS) mechanism, which we believe is the mechanism for our growth. In the VS growth mechanism, the material starts in vapor form in the chamber and the layer over layer growth over the substrate is done epitaxially in the solid phase. This mechanism can be companied with catalyst assistant or without any catalyst. Furthermore, such processes can be lithographically patterned or self-assembled. In the case of catalyst is self-assembled the NWs are grown randomly on the surface and have a variation of diameter and length. However, this kind of growth may lead to unintentional kinking in the grown NWs. Thus, controlling over position and size (diameter and length) of the NWs are required to fabricate efficient nanowire- based devices, hence allow their applications into large-scale. As more progress is made towards realizing efficient optoelectronic devices, many methods are adapted for NWs growth, such as pulsed laser deposition, chemical beam epitaxy, metal organic chemical vapor deposition MOCVD and molecular beam epitaxy (MBE). However, in particular for III-V based InAs nanowires on Si, the most popular method to grow NWs are (MOCVD)[10,11] and (MBE)[12,13]. MOCVD system and related gas phase techniques are used in the production of commercial large scale product, due to the higher surface diffusion, faster growth rates and higher throughput. However, in comparison to MOCVD, solid-source MBE offer several advantages in low impurity incorporation from the ultrahigh vacuum environment and highly pure elemental growth species, very accurate composition of the monolayer deposition and doping control and the ability to grow advanced radial and axial core-shell heterostructures via sophisticated in situ growth monitoring methods. Although InAs- based NWs have been grown successfully using both methods, the focus in this work will be up to the MBE growth, and it will be discussed in detail in the following chapter.

However, the growth of device quality nanowires should be achieved by avoiding the common growth process that employs a foreign catalyst such as gold to nucleate the wires. Au is well known to introduce deep level traps in the material band gap as contaminations[14,15], which then limits the performance of the devices functionality on Si. Therefore, using lithographically predefined SiO_2 templet is an additional benefit besides avoiding catalysts which enables an accurate control over positions and diameters of NWs allowing homogenous arrays by selective-area epitaxy (SAE) without any catalysts. In this technique, the growth substrates are patterned with a lithographically defined mask that determines where the growth occurs.

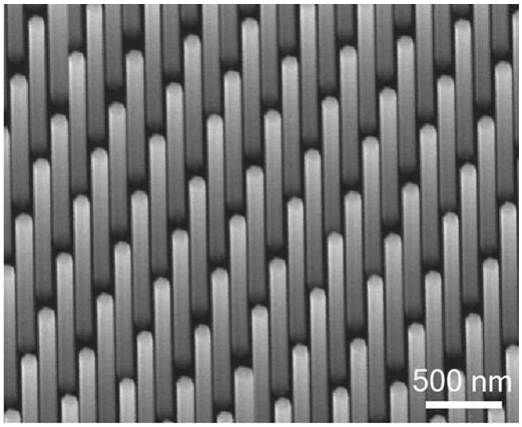

Figure 3.2. SEM images of InAs NWs arrays growing by selective-area epitaxy (SAE) without any catalysts[14].

To meet all these demands, there has been only a limited amount of success by growing InAs(Sb) nanowires on Si, mainly using SA- MBE growth. There are few groups reported a SA growth for InAs NWs, for instance, G. Koblmüller et al. from Walter Schottky Institute established the growth for InAs NWs using SA-MBE, and published few researches about the growth kinetics for the InAs NWs and the optical properties, see Figure 3.2 for example of InAs NWs grown by SA-MBE[16]. For InAsSb NWs, apart from our work only one study by

Farrell et al. demonstrated the first growth of $InAs_{1-x}Sb_x$ nanowires grown by catalyst-free selective-area using metal−organic chemical vapor deposition (SA-MOCVD). Figure 3.3 shows SEM images for this work. However, there are other groups that have reported growths of InAsSb NWs using gold catalyst or self-seeding. Marion J. L. Sourribes et al. demonstrated the growth of InAsSb NWs using catalyst free MBE growth on Si (111) with up to 15% Sb contents. By increasing the Sb content in wires, they observed a sharp decrease of the stacking fault density in the NWs[14] see Figure 3.4. Even more, Q. D. Zhuang et al. reported InAsSb NWs growth using In droplet as shown in Figure 3.5, and tried to control the phase structure by tuning the Sb composition[17]. Heidi Potts et al. has gone further and increased the Sb content in free standing MBE grown InAsSb NWs up 35%. They also found that increasing the Sb reduces the stacking fault in the NWs while enhancing the nanowire conductivity and mobility[18].

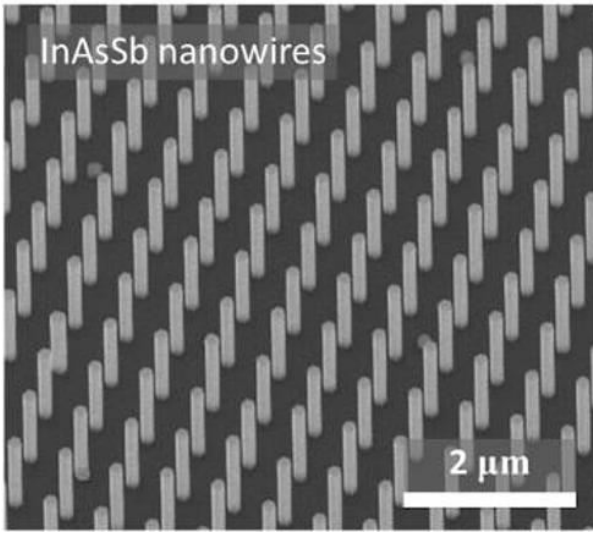

Figure 3.3. SEM images of InAsSb NWs growing by selective-area epitaxy (SAE) without any catalysts[19].

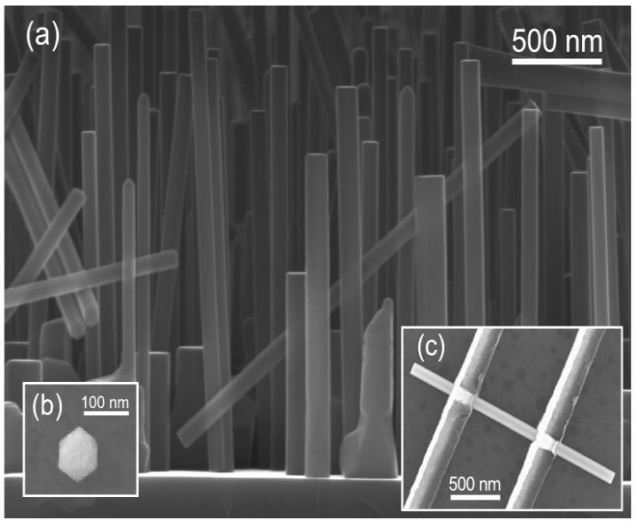

Figure 3.4. SEM images of InAsSb NWs growing directly on the Si substrate without any catalysts[14].

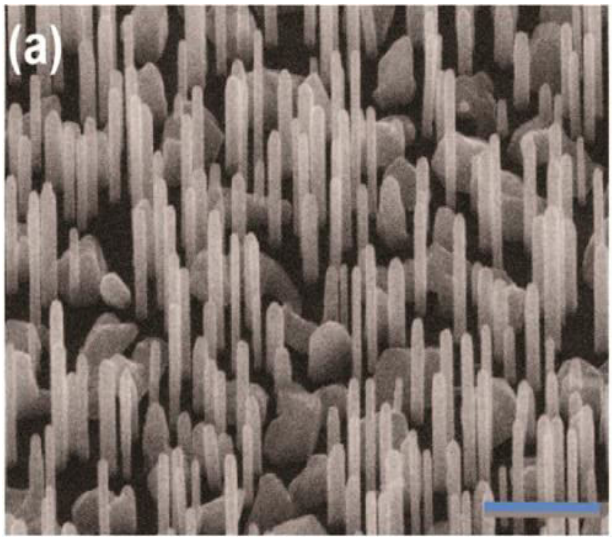

Figure 3.5. SEM images of InAsSb NWs growing using In droplet[17]. Scale bar is 500 nm.

3.4. Crystal structure studies

Control the difference or the change in crystal structure in NWs is a very important for both the fundamental understanding of the nanowire growth mechanism, and also for enabling the practical application of nanowires. It is evident that the growth parameters strongly influence

whether WZ or ZB will be the preferential structure in nanowire growth for InAs - based NWs in particular[20]. Although both WZ and ZB crystal phase have been observed in InAs NWs, the majority of InAs NWs have mainly WZ phase structure[21,22,23]. This case has been observed for any grown InAs wires at any growth methods with foreign or self-catalyzed. However, there are different bandgaps for the two phases. Tragardh et al. predicted a WZ bandgap of 0.54 eV from extrapolation fitted photocurrent measurments on InAsP NWs[1]. Sun et al. reported pure WZ InAs NWs with E_g=0.406 eV [2]. The formation of the WZ phase is elucidated by a lower surface energy of specific sidewall facets of the WZ NWs depending on the specific growth properties of thin NWs such as the nucleation. Even more, Bernhard Mandl et al. reported InAs NWs grown by MOCVD without Au catalyst. They found that the dominate phase structure is WZ rather than zinc blende ZB, although different growth temperature were investigated, with large density of stacking faults in the nanowires[24]. Kimberly A. Dick et al. have gone further in controlling the structure by adjusting the growth parameters to design a WZ-ZB heterostructures superlattice in InAs NWs with high accurate placement of atomic layers, where composition is varied for further improvement of the optical, electrical, thermal effects of structure variation and structural defects and for feasibility studies of devices utilizing these effects. However, incorporating Sb into the InAs NWs leads to a shift towards preferential ZB crystal structure formation, even a small amount of Sb (around 4%) is enough to switch the crystal structure towards ZB[19]. The transition towards ZB been explained in literature due to different reasons, Guo et al. explained this by the lower ionicity of the bonds in GaSb and InSb compared to the other III-Vs[25]. Additionally, the Sb surfactant effect could also play a role at changing the crystal structure[26]. Further investigation by Marion J. L. Sourribes et al. reported a drastic change in the crystal structure in both polytype and wurtzite-dominant to almost pure zinc-blende in the $InAs_{0.85}Sb_{0.15}$ (99% ZB) [14]. It is been reported that for stems wires structures (for example

InAs stems with InAsSb NWs), the InAs bottom segment of the NW has a WZ or polytype structure with few stacking faults, as typically found in pure InAs NWs, grown in these conditions[27,18]. The InAs/$InAs_{1-x}Sb_x$ interface is nearly abrupt, with a complete change of contrast from a WZ to a ZB structure after two to three atomic layers (0.7–1.05 nm). The $InAs_{1-x}Sb_x$ part reported to has a ZB structure with a regular growth, with twinning or stacking faults defect observed in the structures[28]. For example, Xu et al. has studied the Au-seeded MBE growth of InAs/$InAs_{1-x}Sb_x$ nanowires. They conclude that only small amounts of Sb is enough to change the crystal structure from WZ (x=0) to twinned ZB (x=0.05), and further to defect-free ZB (x>0.08)[29]. This result agrees with that of Borg et al. results that investigated InAs/$InAs_{1-x}Sb_x$ nanowires with compositions above x=0.13, were they found defect-free ZB nanowires[30]. In this thesis the reported NWs structures are in very good agreement with previously reported results were it was concluded that the addition of 6 % Sb into the InAs leads to changing the phase from WZ to ZB with twining planes[30].

3.5. Heterostructures nanowires

Continuous progress in synthesizing nanowires leads to produced novel axial and radial nanowire heterostructures with accomplishment in materials characterization and device fabrication have led to advanced optoelectronic and electronic devices. The ternary antimonide NWs have fascinating applications, as it enables a freedom to choose the energy of the band gap and to tune the band alignments in heterostructures. Several groups have taken the advantage of introducing radial or axial core shells geometry in enhancing the carrier confinement, waveguide capabilities, and suppressed surface recombination process to enhance the optical properties for these materials[31,32].

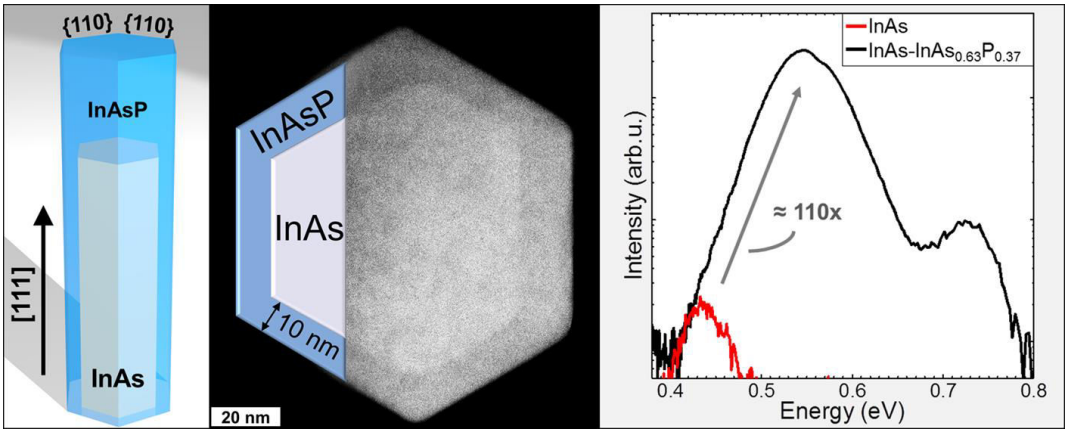

Figure 3.6. SEM images of InAs- InAsP core-shell NWs, (b) PL emission for the wires showing the enhancement in the PL intensity when adding the core shell[32].

In particular for InAs NWs due to the strong non-radiative surface and Auger recombinations. Consequently, the axial and radial NWs core-shell have been extensively investigated, for instance, axial InAs/GaAs, InAs/GaSb, InAs/InP, GaAs/InAs, GaAsSb/InAs, GaAs/InGaAs, and more advanced InAs- $Al_XIn_{1-X}AsP$ hetrostructure. However, these reports focused on the structure properties, and only a few have investigated the optical properties for such heterostructures. For instance, Julian Treu et al. demonstrated PL emission intensities enhancements of InAs NWs by growing an InAsP shell, as shown in Figure 3.6[32].

3.6. Band gaps and band alignments

The optical properties of InAs and InAsSb NWs in this work have been estimated by PL measurements. As mentioned previously that the InAs can form in either the ZB or WZ phases; this will affect the band alignments in heterostructures for such structures. A variety of methods have been used to theoretically estimate the difference between the energy gap of the InAs WZ and ZB phases, ΔEg. ***Local density approximations (LDA)***[33], with Generalised Gradient Approximations (GGA) which were employed extensively by solid state physicists in ab-initio DFT studies to interpret electronic and magnetic interactions in

semiconductor materials including semiconducting oxides and Spintronics. By disregarding the spin−orbit (s−o) interaction, ab initio first-principle pseudopotential methods they can found the Eg. ***Dynamically screened exchange***[34] (the screened exchange (sX) hybrid functional has been widely used in computational material science. Although it has widely been studied in bulk systems, less is known about its functional behavior in surface systems which are crucial to many technologies such as materials synthesis and nano-electronic devices). ***GW approximation***[35] (the calculations are performed in the GW approximation based on a model dielectric function using plane waves and pseudopotentials)[36]. In the latter work[37], the energy gap of all different InAs polytypes has been estimated (0.411, 0.431, 0.440, and 0.481 eV for the 3C, 6H, 4H, and 2H polytypes, in order of increasing percentage of hexagonally), which results in an energy gap of WZ InAs being (50-70) meV greater than that of ZB InAs[22]. However, in the case of the InAsSb NWs which have ZB crystal structure, the band gaps should be close to the bulk semiconductor values contain the same Sb content. Even more, the NWs have a diameter dependent and consequently a blue-shift was observed with decreasing the diameter from 80 to 60 nm, and was attributed to confinement effects[38].

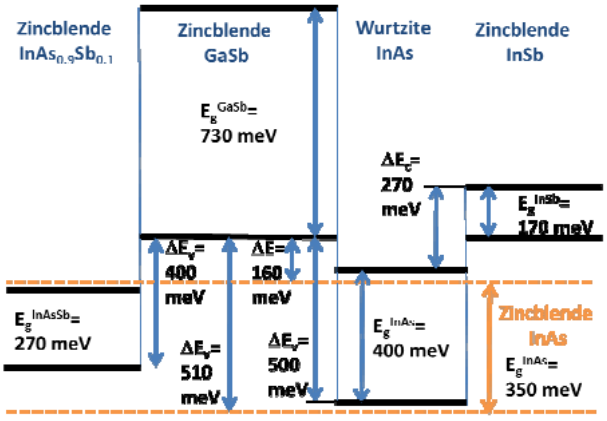

Figure 3.7. Shows the band structure alignment of various heterostructure combinations, where the provided off-sets have been evaluated from temperature-dependent current voltage measurements across MOVPE-grown heterojunctions using WZ InAs as reference[30].

Thus for device applications it is very important to determine the band off-sets between these materials. Figure 3.7 shows the band structure alignment of various heterostructure combinations, where the provided off-sets have been evaluated from temperature-dependent current voltage measurements across MOVPE-grown heterojunctions using WZ InAs as reference[30].

3.7. Optical properties of InAs Nanowires

InAs(Sb) NWs has been an attractive topic for many research groups. The focus in earliest studies has been on optimizing the growth conditions, analyse or control the crystal structure for such wires. However, the crystal phase is particularly relevant to PL studies because the bandgap and hence emission wavelength are phase dependent. In general, bulk InAs grown by conventional epitaxial techniques has a zinc-Blende phase, hence its bandgap ($Eg_{InAs\ (ZB)}$) is well characterized at 0.415 eV. However, in contrast a consensus has not yet been reached around a single bandgap for Wurtzite InAs ($Eg_{InAs\ (Wz)}$). While low temperature studies build initial understanding, only a few optical emission studies have been reported, due to the very poor optical efficiency of these materials, very strong nonradiative surface and difficulties of performing spectroscopy in the IR spectral region[39]. For instance, the first low temperature PL of InAs NWs was reported by Sun et al. for InAs NWs on Si having both pure WZ and ZB crystal phase, with band energy (0.41- 0.425 eV) corresponding to above band edge surface state related recombination, with a slight shift at increasing the temperature. They also noticed a blue shift due to quantum confinement depending on the wires diameter not on the structure changes. Furthermore, Tragardh et al. predicted a WZ bandgap of 0.54 eV from extrapolation fitted photocurrent measurements at 5 K on single InAs NWs with a centrally placed $InAs_{1-x}P_x$ segment of the composition $0.14< x <0.48$. M Moller et al. reported

temperature-dependent PL studies that enable them to estimate the wurtzite band gap to be 0.458 ± 0.010 eV at low temperatures. Koblmuller et al. have gone further to report PL temperature dependence of InAs NWs having a WZ phase structure and a peak position 0.411eV at 15k. Despite the strong PL emission at low temperatures, the emission was only reaching 130K before the signal quenched[38]. The wires show a 25 meV blue shift due to confinement by reducing the wire diameters from (100-40 nm) with respect to bulk InAs bulk due to quantum confinement and dominant surface effect which limits PL efficiencies. The non-radiative recombination causing this quenching could originate from lattice defects, surface states or Auger recombination[38]. Recently, Rota et al. estimated the energy gap for InAs WZ nanowires at energy of 0.477 ± 0.003 eV, 59± 3 meV higher than the ZB bandgap by 59 meV, and does not depend on the nanowires size and carrier confinement. The spread of results that ranges from 0.41 eV to 0.54 eV, may originate from the polytypism, with a further complication being atmospheric absorption in the commensurate spectral range. However, whilst low temperature PL measurements have supported initial studies confirming the crystal structure, emission at room temperature will be required for most practical applications. A common route to suppressing non-radiative recombination at the surfaces is the in-situ growth of a wider bandgap shell and this has been employed to InAs wires by Treu et al. using an InAsP shell where they demonstrated 10^2 times enhancement of the PL emission up to room temperature[40](see Figure 3.6). Also, GaAs/AlGaAs core-shell NWs improved the PL intensity compared to bulk GaAs NWs, because of the reduction in the surface states, which found to be effective enhancing the PL emission intensity to persist up to room temperature. In addition to suppressing loss through non-radiative recombination, PL intensities and quenching temperatures can be increased by acting to raise the radiative recombination rate. Also in a very recent study Pamela Jurczak et al. demonstrated a ten-fold enhancement of InAs NWs PL emission using an InP core-shell layer that passivate the

surface states and reduced the rate of nonradiative recombination[41]. Xiren Chen et al. reported PL emission of up to 290K from InAs NWs growing on n- and p- type Si (111) substrate, showing that the type of doping leads to carriers assembling near the WZ-ZB interface, assuming they have a type II radiative recombination near the WZ –ZB InAs interfaces[42].

However, in this work, we have taken the approach of adding InAsSb multi-quantum-wells (MQWs) and superlattices (SLs) to InAs wires, to exploit quantum confinement and enhance PL emission. Also other methods have been employed in this work, for example, organic coating. The energy gap for our InAs NWs is in the range assigned for the WZ InAs NWs reported in literature; the addition of the Sb will be discussed in the next section.

3.8. Optical properties of InAsSb NWs

Continues progress has been done to overcome the InAs nanowires poor efficiency by incorporate Sb to improve the crystal quality and reduce the staking fault density. However, many groups focused on InAsSb NWs due to the unique properties for these wires, Lund University for example, studied InAsSb extensively by means of structure and fabricating devices. And it is being concluded that the addition of small Sb fractions has been shown to suppress certain defects in InAsSb wires, twinning and stacking faults in particular. Even more, for instance, Marion J. L. et al. observed a sharp decrease of stacking fault density with increasing the Sb content up to 15% with more than three times increase in the field effect mobility compared to InAs nanowires as mentioned earlier[14]. Despite the development in growing these wires and improvement in the crystal structures, the reported PL quenching behavior for InAsSb wires is slightly improved[27]. There are three reports of InAsSb PL that

appears to be a reasonable conclusion since the band-edge perturbations introduced by these defects will not strongly influence the non-radiative recombination rate[11, 19, 27]. Furthermore, the influence of the catalyst may affect the optical properties for the InAsSb NWs. For example, using In droplet assisted growth with 4% Sb have been reported by Zhuang et al., which showed a band to band edge emission from WZ phase structure without the presence of type II QW emission indicating the quasi- pure WZ phase structure in the InAsSb nanowires[17]. Farrell et al. reported the first catalyst free selective area InAsSb nanowires up to 15% Sb where PL studies at 77K for the wires with pure ZB phase structure have shown two peaks that correspond to InAs substrate at 0.4 eV and the InAsSb nanowires at 0.35 eV, without any defect emission[19]. Thompson et al. fabricated a pin InAsSb nanowires for shortwave infrared detection, the overall PL peak consist of two sections InAs at 0.435 eV and InAsSb section at 0.382eV[27]. The emission from the InAs is blue shifted due to wire diameter confinement[27]. A recent study by Q D Zhuang et al. reported a PL emission of InAsSb NWs with PL emission up to 5μm with 15% Sb[43]. The reported PL measurments for the InAsSb NWs are in good agreement with the PL results presented in this thesis.

3.9. Based-Sb nanowires optoelectronic devices photodetectors

Developing new materials is essential for photodetectors operating at room temperature. InAsSb-based photodetectors are important in obtaining a sufficiently narrow band gap which enables detection in the wavelength range between 3 and 14 μm. However, it is also considered an alternative to the traditional HgCdTe based detectors, due to the importance regarding stability, uniformity and toxicity problems[4]. Even more, the high thermal conductivity, mobility and weak dependence of band gap on composition are useful to form heterostructures with other III−V semiconductors were the band gap can be tuned by varying the relative composition to reach the narrowest room temperature band gap. However, bulk

InAs or InAsSb photodetectors have limitations that include high dark current and cryogenic temperatures operation requirements. These problems could be solved by using InAsSb NWs based photodetectors. In such way, the dark current will be significantly reduced with higher functioning temperature due to quantum confinement effect (According to the quantum confinement theory, electrons in the conduction band and holes in the valence band are confined spatially by the potential barrier of the surface, or trapped by the potential well of the quantum box, which excited many electrons to the conduction band that are free to contribute to current. This makes many electrons contribute to the reverse bias current hence higher dark current). Photon scattering suppression in in such structures affects the efficiency of the detector, higher photons scattered (not absorbed) means lower number of electrons and holes created, i.e. the signal to noise ratio of the detector will reduced. In addition, much high signal to noise ratio means higher probability of photons being absorbed by the system, which will increase the sensitivity of the detector and hence its efficiency. This can be achieved together with long photocarriers lifetime and shorter carrier transit time in InAsSb-based photodetectors due to their high surface to volume ratio. Improving the photoresponse of InAsSb NWs-based detectors is of great interest to applications in defence, fire detection, communication, and astronomy. However, previous work on nanowire photodetectors have mostly focused on the visible spectral region with only a few reports on detection of mid-infrared radiation. Prior studies have reported InAsSb nanowires with higher Sb fractions, configured for infrared photodetection. Without any type of junction these photoconductive wires showed some response; however, despite cooling to 5 K, leakage remained in the mA range for ~8000 wires[44]. The measured dark current for the fabricated photodetector in this work is significantly below the best results reported for large area InAs photodiodes, which typically suffer from high levels of surface leakage and exhibit ~100mA/cm^2. This paves the

way towards realizing efficient nanowire based photodetectors in the mid infrared range at room temperatures, and will be discussed in detail in chapter 7.

3.10. Conclusion

An overview of the different techniques used to fabricate InAs(Sb) NWs in the mid-infrared (2-5 μm) has been mentioned in this chapter. Most applications in this wavelength range require operation at room temperature. The main goal in this thesis is to grow nanowires with high crystalline quality. InAs(Sb) NWs have been studied extensively in literature, by means of structure, fabricating devices and also incorporating Sb into the InAs NWs. However, it is being concluded that the addition of small Sb fractions has been shown to suppress certain defects in InAsSb wires and increasing the field effect mobility compared to InAs nanowires. Few groups have investigated the optical properties for the InAs and InAsSb at low temperatures, however, giving further insight into the optical emission and related energy band gap would lead to improvements in the use of these materials. Finally, developing new materials is extremely essential for photodetectors operating at room temperatures, hence development in this filed is growing at a very fast pace to achieve these goals.

3.11. References

[1]Tomioka, K.; Tanaka, T.; Hara, S.; Hiruma, K.; Fukui, T. III-V Nanowires on Si Substrate: Selective-Area Growth and Device Applications. IEEE J. Sel. Top. Quantum Electron. 2011, 17, 1112− 1129.

[2] Dayeh, S.; Aplin, D.; Zhou, X.; Yu, P.; Yu, E.; Wang, D. High Electron Mobility InAs Nanowire Field-Effect Transistors. Small 2007, 3, 326-332.

[3] Foldyna, M.; Yu, L.; Roca i Cabarrocas, P. Theoretical shortcircuit current density for different geometries and organizations of silicon nanowires in solar cells. Sol. Energy Mater. Sol. Cells 2013, 117, 645−651.

[4] Du, J.; Liang, D.; Tang, H.; Gao, X. InAs Nanowire Transistors As Gas Sensor and The Response Mechanism. Nano Letters 2009, 9, 4348-4351.

[5] Thelander, C.; Björk, M.; Larsson, M.; Hansen, A.; Wallenberg, L.; Samuelson, L. Electron Transport in InAs Nanowires and Heterostructure Nanowire Devices. Solid State Communications 2004, 131, 573-579.

[6] Miao, J.; Hu, W.; Guo, N.; Lu, Z.; Zou, X.; Liao, L.; Shi, S.; Chen, P.; Fan, Z.; Ho, J. et al. Single InAs Nanowire Room-Temperature Near-Infrared Photodetectors. ACS Nano 2014, 8, 3628-3635.

[7] B. Wang and P. W. Leu, "Tunable and selective resonant absorption in vertical nanowires,'' J. Optics Letters, 2012, 37, No. 18, 3756-3758.

[8] Naureen, S.; Sanatinia, R.; Shahid, N.; Anand, S. High Optical Quality InP-Based Nanopillars Fabricated by a Top-Down Approach. Nano Letters 2011, 11, 4805-4811.

[9] Wang, H.; Sun, M.; Ding, K.; Hill, M.; Ning, C. A Top-Down Approach to Fabrication of High Quality Vertical Heterostructure Nanowire Arrays. Nano Letters 2011, 11, 1646-1650.

[10] S. A. Dayeh, E. T. Yu, and D. Wang, "Growth of InAs nanowires on SiO_2 Substrates: nucleation, evolution, and the role of Au nanoparticles", J. Phys. Chem. C. 2007, 111, 13331.

[11] X. Zhang, J. Zou, M. Paladugu, Y. Guo, Y. Wang, Y. Kim, H. J. Joyce, Q. Gao, H. H. Tan, and C. Jagadish, "Evolution of epitaxial InAs nanowires on GaAs (111)B", Small. 2009, 5, 366-369.

[12] M. Tchernycheva, L. Travers, G. Patriarche, F. Glas, J. C. Harmand, G. E. Cirlin, and V. G. Dubrovskii, "Au-assisted molecular beam epitaxy of InAs nanowires: growth and theoretical analysis", J. Appl. Phys. 2007, 102, 094313.

[13] S. G. Ihn and J. I. Song, "InAs nanowires on Si substrates grown by solid source molecular beam epitaxy", Nanotechnology. 2007, 18, 355603.

[14] Sourribes, M. J. L.; Isakov, I.; Panfilova, M.; Liu, H.; Warburton, P. A. Mobility Enhancement by Sb-mediated Minimisation of Stacking Fault Density in InAs Nanowires Grown on Silicon. Nano Lett. 2014, 14, 1643−1650. PMID: 24502770.

[15] Brotherton, S. D.; Lowther, J. E. Electron and Hole Capture at Au and Pt Centers in Silicon. Phys. Rev. Lett. 1980, 44, 606−609.

[16] Tomioka, K.; Izhizaka, F.; Fukui, T. Selective-Area Growth of InAs Nanowires on Ge And Vertical Transistor Application. Nano Letters 2015, 15, 7253-7257.

[17] Zhuang, Q. D., Anyebe, E. A., R. Chen, H. Liu, Ana M. Sanchez, Mohana K. Rajpalke, Tim D. Veal[#], Z. M. Wang, Y. Z. Huang, and H. D. Sun," Sb-Induced Phase Control of InAsSb Nanowires Grown by Molecular Beam Epitaxy" Nano Lett. 2015, 15 (2), 1109−1116.

[18] Potts, H., Friedl, M, Amaduzzi, F., Tang, K., Tütüncüoglu, G., Matteini, F., Alarcon L. E., Paul C. l., and Morral, A." From Twinning to Pure Zincblende Catalyst-Free InAs(Sb) Nanowires" Nano Lett. 2016, 16 637−643.

[19] Farrell, A.; Lee, W.; Senanayake, P.; Haddad, M.; Prikhodko, S.; Huffaker, D. High-Quality InAsSb Nanowires Grown by Catalyst-Free Selective-Area Metal–Organic Chemical Vapor Deposition. Nano Letters 2015, 15, 6614-6619.

[20] Johansson, J.; Bolinsson, J.; Ek, M.; Caroff, P.; Dick, K. A. Combinatorial Approaches to Understanding Polytypism in IIIV Nanowires. ACS Nano. 2012, 6, 6142−6149. PMID: 22681568.

[21] Möller, M.; de Lima Jr, M.; Cantarero, A.; Chiaramonte, T.; Cotta, M.; Iikawa, F. Optical Emission of InAs Nanowires. Nanotechnology 2012, 23, 375704.

[22] Rota, M.; Ameruddin, A.; Fonseka, H.; Gao, Q.; Mura, F.; Polimeni, A.; Miriametro, A.; Tan, H.; Jagadish, C.; Capizzi, M. Bandgap Energy of Wurtzite InAs Nanowires. Nano Letters 2016, 16, 5197-5203.

[23] Trägårdh, J.; Persson, A.; Wagner, J.; Hessman, D.; Samuelson, L. Measurements of The Band Gap of Wurtzite $InAs_{1-X}P_X$ Nanowires Using Photocurrent Spectroscopy. Journal of Applied Physics 2007, 101, 123701.

[24] Mandl B, Stangl J, Martensson T, Mikkelsen A, Eriksson J, Karlsson LS et al. Au-free epitaxial growth of InAs nanowires. Nano Letters. 2006 Aug 9;6(8):1817-1821. Available from, DOI: 10.1021/nl060452v.

[25] J.C. Phillips. Ionicity of the Chemical Bond in Crystals. Reviews of Modern Physics 1970, 42, 317-356.

[26] Portavoce, A., Berbezier, I.; Ronda, A. Effect of Sb on Si/Si and Ge/Si Growth Process. Materials Science and Engineering: B 2003, 101, 181-185.

[27] Thompson, M., Alhodaib, A., Craig, A., Robson, A., Aziz, A., Krier, A., Svensson, J., Wernersson, L., Sanchez, A. and Marshall, A. Low Leakage-Current InAsSb Nanowire Photodetectors on Silicon. Nano Letters. 2016, 16(1), pp.182-187.

[28] Caroff, P.; Dick, K.; Johansson, J.; Messing, M.; Deppert, K.; Samuelson, L. Controlled Polytypic And Twin-Plane Superlattices In III–V Nanowires. Nature Nanotechnology 2008, 4, 50-55.

[29] Xu, T.; Dick, K.; Plissard, S.; Nguyen, T.; Makoudi, Y.; Berthe, M.; Nys, J.; Wallart, X.; Grandidier, B.; Caroff, P. Faceting, Composition and Crystal Phase Evolution In III–V Antimonide Nanowire Heterostructures Revealed by Combining Microscopy Techniques. Nanotechnology 2012, 23, 095702.

[30] Borg, B., Kimberly A., J. Eymery, and L.Wernersson, Enhanced Sb incorporation in InAsSb nanowires grown by metalorganic vapor phase epitaxy, Appl. Phys. Lett. 2011, 98, 113104.

[31] Fabrication of III–V semiconductor core-shell nanowires by SA-MOVPE and their device applications - IEEE Conference Publication http://ieeexplore.ieee.org/stamp/stamp.jsp, arnumber=5699743 (accessed Sep 25, 2017).

[32] Treu, J.; Bormann, M.; Schmeiduch, H.; Döblinger, M.; Morkötter, S.; Matich, S.; Wiecha, P.; Saller, K.; Mayer, B.; Bichler, M. et al. Enhanced Luminescence Properties of InAs–InAsP Core–Shell Nanowires. Nano Letters 2013, 13, 6070-6077.

[33] Murayama, M.; Nakayama, T. Phys. Rev. B: Condens. Matter Mater. Phys. 1994, 49, 4710−4724.

[34] Ferreira, L. G.; Marques, M.; Teles, L. K. Phys. Rev. B: Condens. Matter Mater. Phys. 2008, 78, 125116.

[35] Zanolli, Z.; Fuchs, F.; Furthmüller, J.; von Barth, U.; Bechstedt, F. Phys. Rev. B: Condens. Matter Mater. Phys. 2007, 75, 245121.

[36] De, A.; Pryor, C. E. Phys. Rev. B: Condens. Matter Mater. Phys. 2010, 81, 155210.

[37] Bechstedt, F.; Belabbes, A. J. Phys.: Condens. Matter 2013, 25, 273201.

[38] Koblmüller, G.; Vizbaras, K.; Hertenberger, S.; Bolte, S.; Rudolph, D.; Becker, J.; Döblinger, M.; Amann, M.; Finley, J.; Abstreiter, G. Diameter Dependent Optical Emission Properties of InAs Nanowires Grown on Si. Applied Physics Letters 2012, 101, 053103.

[39] Sun, M.; Leong, E.; Chin, A.; Ning, C.; Cirlin, G.; Samsonenko, Y.; Dubrovskii, V.; Chuang, L.; Chang-Hasnain, C. Photoluminescence Properties of InAs Nanowires Grown on GaAs and Si Substrates. Nanotechnology 2010, 21, 335705.

[40] Treu, J.; Bormann, M.; Schmeiduch, H.; Döblinger, M.; Morkötter, S.; Matich, S.; Wiecha, P.; Saller, K.; Mayer, B.; Bichler, M. et al. Enhanced Luminescence Properties of InAs–InAsP Core–Shell Nanowires. Nano Letters 2013, 13, 6070-6077.

[41] Jurczak, P.; Zhang, Y.; Wu, J.; Sanchez, A.; Aagesen, M.; Liu, H. Ten-Fold Enhancement of InAs Nanowire Photoluminescence Emission With an InP Passivation Layer. Nano Letters 2017, 17, 3629-3633.

[42] Chen, X.; Zhuang, Q.; Alradhi, H.; Jin, Z.; Zhu, L.; Chen, X.; Shao, J. Midinfrared Photoluminescence up to 290 K Reveals Radiative Mechanisms and Substrate Doping-Type Effects of InAs Nanowires. Nano Letters 2017, 17, 1545-1551.

[43] Zhuang, Q.; Alradhi, H.; Jin, Z.; Chen, X.; Shao, J.; Chen, X.; Sanchez, A.; Cao, Y.; Liu, J.; Yates, P. et al. Optically Efficient InAsSb Nanowires for Silicon-Based Mid-Wavelength Infrared Optoelectronics. Nanotechnology 2017, 28, 105710.

[44] Svensson, J.; Anttu, N.; Vainorius, N.; Borg, B. M.; Wernersson, L.-E. Diameter-Dependent Photocurrent in InAsSb Nanowire Infrared Photodetectors. Nano Lett. 2013, 13, 1380−1385. PMID: 23464650.

Chapter 4

Experimental Procedures

4.1. Molecular Beam Epitaxy (MBE)

Molecular Beam Epitaxy (MBE) is an epitaxial growth technique used to produce high quality semiconductor crystals structures by relatively heated up precise solid sources materials. MBE growth requires ultra-high vacuum, typically 10^{-10} mbar, to ensure a free path for the evaporated atomic beams traveling to the substrate, with a slight scattering of particles between source material and substrate[1]. A shutter in front of each source allows the beams to be shuttered in a fraction of a second from one material to another. In comparison to other techniques such as Metal-Organic Vapour Phase Epitaxy (MOCVD), MBE enables slow growth rate around 1ML/s (a few Å/s)[2]. Thus, researchers can access complex structures requiring ultra-thin quantum structures with very abrupt interfaces and precise control of the thickness, doping and compositional accuracy[3].

4.1.1. Growth Apparatus

The MBE apparatus used to grow the samples in this work is a VG-V80H MBE system. A typical MBE system, it consisted of three sections, the entry lock, preparation chamber and growth chamber. The wafers were loaded into the MBE and transferred through the entry lock which should be pumped down after the wafers were loaded. Then the wafers was moved by a mechanically controlled wafer trolley to the preparation chamber were it can be stored or outgassed to ensure a clean substrate surface from water vapour or hydrocarbons. The preparation chamber is pumped by an Ion pump to a vacuum of 10^{-10} mbar, while the load lock was pumped from atmosphere using a roughing pump, turbo pump and ion pump to a vacuum of 10^{-7} mbar. A diagram of the MBE growth chamber is shown in Figure 4.1. A cryopump, ion pump and turbopump are used to maintain UHV. A liquid nitrogen cryopanel surround the growth chamber to provide thermal isolation between the different cells and

greatly reduces the background pressure to 10^{-11} mbar. Substrates are mounted onto molybdenum blocks loaded inside the growth chamber into a substrate manipulator positioned in the centre of the chamber. This substrate manipulator rotates the substrate during growth for more uniformity across the wafer. A reflection high energy electron diffraction (RHEED) system is used to monitor the surface atomic reconstruction on the substrate during the growth, on a fluorescent screen. This allowed the growth rate for each material to be accurately determined. Samples in this work were grown on quarters of 2-inch diameter Si (111) substrates. The substrates were mounted onto three-inch molybdenum holders between two thin molybdenum disks with quarter circle cut-outs. This allowed the front and back of the substrate to be exposed to the growth flux and substrate heater respectively. Before growth, wafers were outgassed in the MBE's preparation chamber at 250 ºC.

Group III fluxes were supplied by thermal effusion K-cells which consists of the solid material held in an inert crucible heated by a resistance heated source. To accurately control the temperature, a thermocouple is used. A dual element cell was used to supply indium which consisted of a tip heater for the crucible lip, and a base heater for the crucible body which was set to 700-790 ºC. Two Veeco valved cracker cells were used to provide the antimony and arsenic fluxes. In these cells, the material is first thermally evaporated in the form of tetramers (As_4 and Sb_4) and is passed through a hotter cracking zone where the molecules are then dimerised into As_2 and Sb_2. The cracker temperature is set at 950 ºC and the base temperatures are set between 360-380 ºC and 580-590 ºC for As and Sb respectively. The flux from the cracker cells can be changed rapidly and are controlled by a mechanical needle valve. The use of dimers results in better crystal growth since the incorporation mechanism is simpler than for tetramers[4].

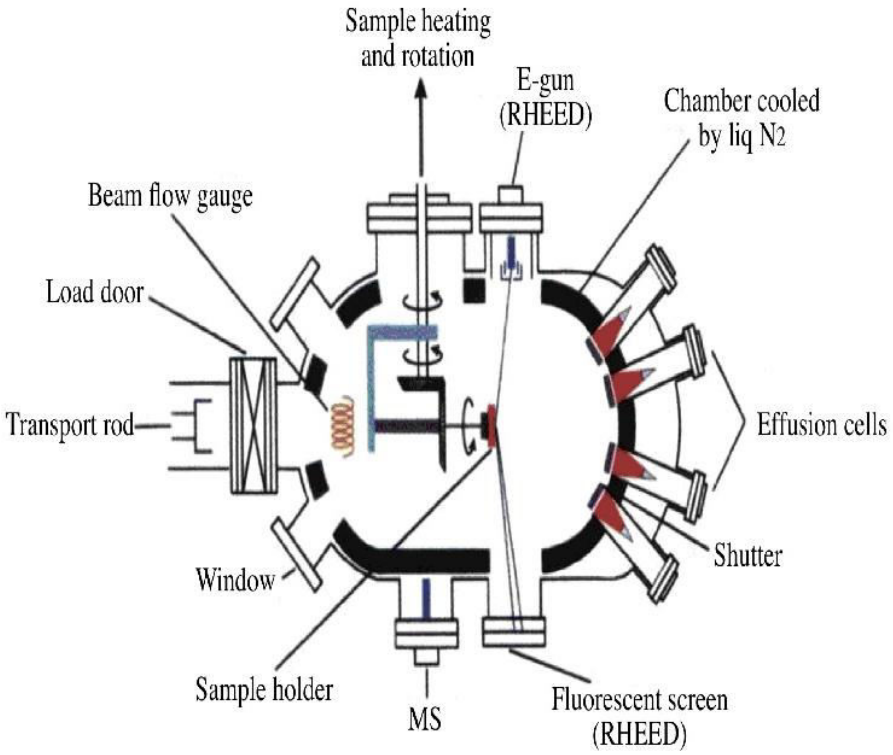

Figure 4.1. Diagram of MBE growth chamber showing the layout of the effusion cells, RHEED gun and screen, sample manipulator and gate valve between growth chamber and preparation chamber[4].

4.1.2. Reflection high energy electron diffraction (RHEED)

Reflection high energy electron diffraction (RHEED) is a growth technique monitoring the surface of semiconductor materials during the growth process. RHEED works by directing a narrow electron beam at the sample surface at a glancing angle of 0.5 to 2 degrees[5]. The reflected electrons from the surface are then collected on a phosphor screen forming a diffraction pattern for revealing the surface crystallography (Figure 4.2). The RHEED system contains an electron gun operated at a current of ~1.4 A and a beam voltage of ~14 kV. The diffraction pattern is corresponding to the surface structure, crystal orientation, and the roughness or smoothness of the surface[6]. For growth mode monitoring any changes in the RHEED pattern indicates a change to the surface. Thus, a smooth surface when a full layer of

atoms is formed gives high reflection intensity, while a rough surface gives a lower intensity when a new layer begins to grow and clusters formed on the surface, see Figure 4.2. Growth rates can be measured for group III and V elements by measuring the time taken for the RHEED intensity oscillation during the growth without rotating the sample. However, the NWs in this work haven't shown any RHEED patterns, thus the growth rates were calculated based on 2D growth layer. Ga and As growth rates were measured on GaAs, the In growth rate as measured using InAs and the Sb growth rate was measured using InSb. In this work, 2D layer growth rates were employed of 0.08 ML/s for In, 1.59 ML/s for As and 0.36 ML/s for Sb. These growth rates were calibrated for 2D ZB growth on (001) InAs, GaAs and InSb substrates respectively as mention previously.

4.1.3. Temperature Calibration

The substrate temperature inside the growth chamber, is controlled using a set point temperature and closed loop electronics. The set point temperature is measured using a thermocouple in direct contact with a complementary molybdenum block placed behind the heater and designed to mimic the wafer holder in front of the heater. However, the temperature specified by the thermocouple does not exactly match the actual substrate temperature. Thus, to determine the actual temperatures, measurements are made of the set point were the real temperature can be known from RHEED pattern transitions, such as a known oxide desorption temperature.

4.2. Selective Area Epitaxy of nanowires growth:

Selective area epitaxy (SAE) on patterned substrates is very important to control the nucleation position and the size for homogenous NWs[7]. In the SAE method, the substrate is

masked with a patterned dielectric layer, normally a SiO_2 layer with thickness below 100 nm. In this work, selective area molecular beam epitaxy (SA-MBE) of InAs(Sb) NWs on Si substrates was achieved with nano-hole patterns produced by EBL.

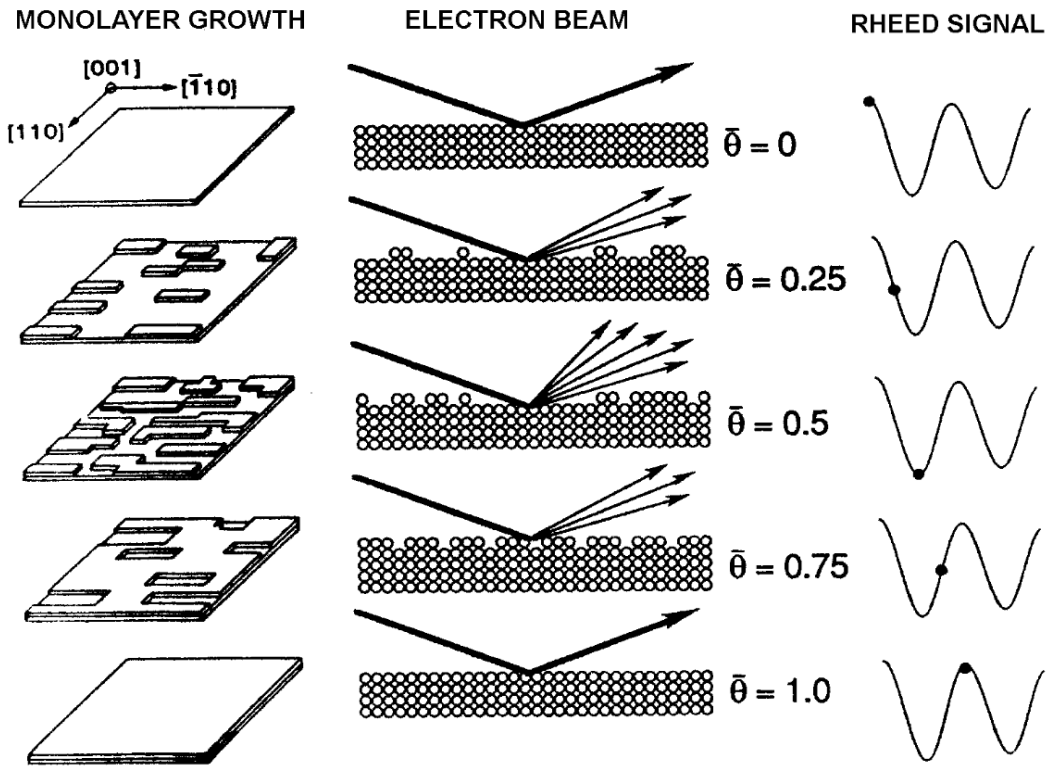

Figure 4.2. Diagram showing the growth of a single layer and how the RHEED intensity oscillations due to scattering of electron beam during growth of a monolayer[5].

Figure 4.3 explains the process of selective area growth of NWs. The NW growth starts when the As and In adatoms starts to form critical nuclei of certain sizes on the surface inside the patterned holes. After being deposited on the substrate, the impinging species spread laterally on the substrate allowing higher sticking coefficient of the growth, followed by an axial growth. Critical nuclei are formed when the impinging In adatoms diffuse on the surface until being restricted in the holes, in the same time the As_2 gets incorporated to the In in the opening holes. In these processes, the NW growth is influenced by the diffusion rate of adatoms, the direct incorporation of the impinging species on the growing NWs, and the

incorporated diffusing atom. Diffusivity is enhanced whereas the sticking coefficient is reduced by increasing the growth temperature[8]. To achieve optimal selectivity, growth parameters especially growth temperature should be optimized. The effect of the growth temperature on the NWs geometry, growth selectivity and the effect of introducing the Sb will discussed in chapter 5.

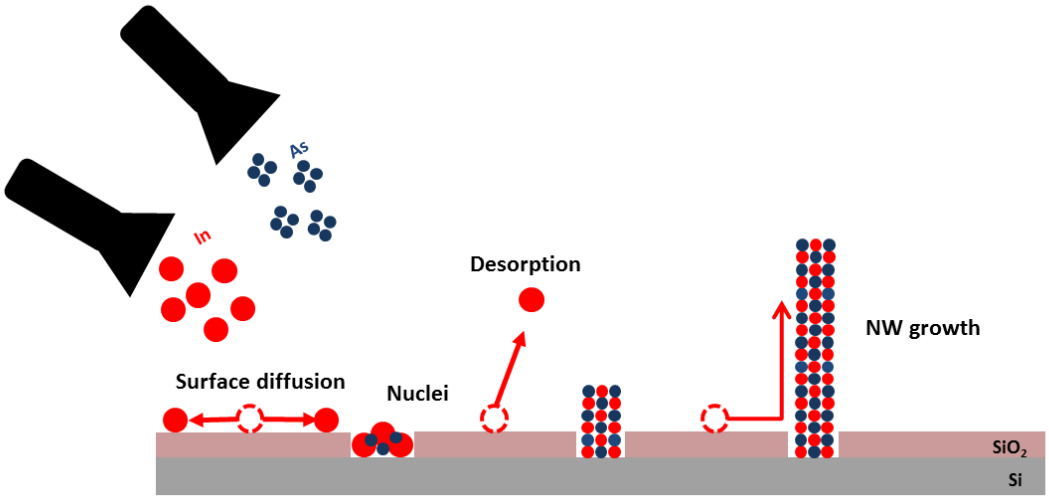

Figure 4.3. Diagram showing the selective area growth on Si substrate with holes in the oxide layer, started by the nucleation of specific nuclei and finished by the NWs growth.

4.3. Substrate preparation

4.3.1. The substrate

The NW growth developed through selective area molecular beam epitaxy (SA-MBE) on silicon (Si) wafers. All the Si wafers used in this work have been manufactured commercially by Virginia semiconductor, with specifications as follows: single side polished, backside etched, 2 inches in diameter (50 mm ± 0.3mm), ~275µm central thickness, boron doped (p-type) in the <111> orientation, and a resistivity between 0.044 – 0.066 Ω cm. The Si

substrates have a grown thermal oxidation layer, SiO_2, of 25 nm thickness. Growth experiments were performed using two different doping concentration of the Si substrates from the same manufacturer, $1x10^{15}$ cm^{-3} and $1x10^{18}$ cm^{-3}.

4.3.2 Design the mask template:

The wires were grown with different diameters and spacing based on a nano pattern template designed using DraftSight software. The first template drawing used in this work is called pattern I as shown in Figure 4.4. This template design was simply one layer defining a pattern within a 1x1 mm square area. Each corner of the big square contains four plus signs (+) to be used as alignment marks. The big square is divided into small subsection squares; the small squares are 100 X 100 µm. Each small square contained a grid of 50 x 50 circles with constant diameter and pitch. Along the x and y directions of the mask, the squares are arranged to increase the pitch and the diameter of the circles respectively.

In the small squares, the diameter is a sequence arranged starting at 200 nm, 150 nm, 125 nm, 100 nm, 80 nm, 60 nm and 40 nm. The pitches are started from 200 nm, 400 nm, 500 nm, 600 nm, 700 nm, 800 nm, 1000 nm and 2000 nm. For example, if we look at the first row in the x direction, the first square will contain circles repeated 50X50 times having diameter of 200 nm with pitch of 200 nm. The following square in the same x direction will contain circles having diameter of 200 nm and pitch of 400 nm. A series of samples have been grown with varying growth temperature using pattern 1 to map out the temperature range and identify the optimal wires growth. However, from the SEM images, it was found that the wires typically have a diameter less than that of the hole. Therefore, a new pattern design has been developed using a big square in the middle with densely packed array of smaller holes (50 nm diameter

with 300 nm pitch), called pattern II. Figure 4.5 shows the mask design for pattern II with the different sections labelled.

The pattern is one layer with maximum extent of around 1mm x 3mm along with 6 alignment marks in each corner of the patterns. At the centre, there is a 300 x 300 µm square for PL studies, the square has circles of 50 nm diameter and 300 nm pitches. To the left of the PL square there are 4 sections as labelled in Figure 4.5. The first section to left is 7 rows of squares contained circles repeated 25x25 times, the circles in the squares have a diameter of 50 nm, with a changed spacing distance, each row represent different pitches arranged from 80 nm, 100 nm, 130 nm, 150 nm, 180 nm, 200 nm and 230 nm. Below this section a row of squares have circles repeated 10x10 times, the distance between the holes is constant 1000 nm, with a changed diameter ranging at 500 nm, 400 nm, 300 nm, 250 nm, 200 nm, 150 nm, 125 nm, 100 nm and 75 nm for each block at this row. The last row in the left side consists of two sections as clear in Figure 4.5. The first section under the PL square contained circles with constant diameter of 50 nm and constant pitch of 300 nm, but the circles repeats times are varying and starting by 5x5, 10x10, 25x25, 50x50 and 100x100. Next to this section a row of squares has circles repeated 10x10 times, the diameter for these holes is constant 50 nm, with changed pitches ranging at 5000 nm, 3000 nm, 2000 nm, 1500 nm, 1000 nm, 900 nm, 800 nm, 700 nm, 600 nm, 500 nm, 400 nm and 200 nm for each block at this row. To the right of the PL square there are repeats of single and twin squares. The top and the bottom rows contain repeats of single circles with constant diameter of 50 nm. In the middle between these two rows there are 7 rows with twin circles, the diameter for the holes are constant of 50 nm, and the pitches are varied for each row starting from 80 nm, 100 nm, 130 nm, 150 nm, 180 nm, 200 nm and ending at 230 nm. The addition of the single and twin holes arrays was

in order to allow further studies for single and twin wire. Figure 4.5 showing a simple draw for the mask.

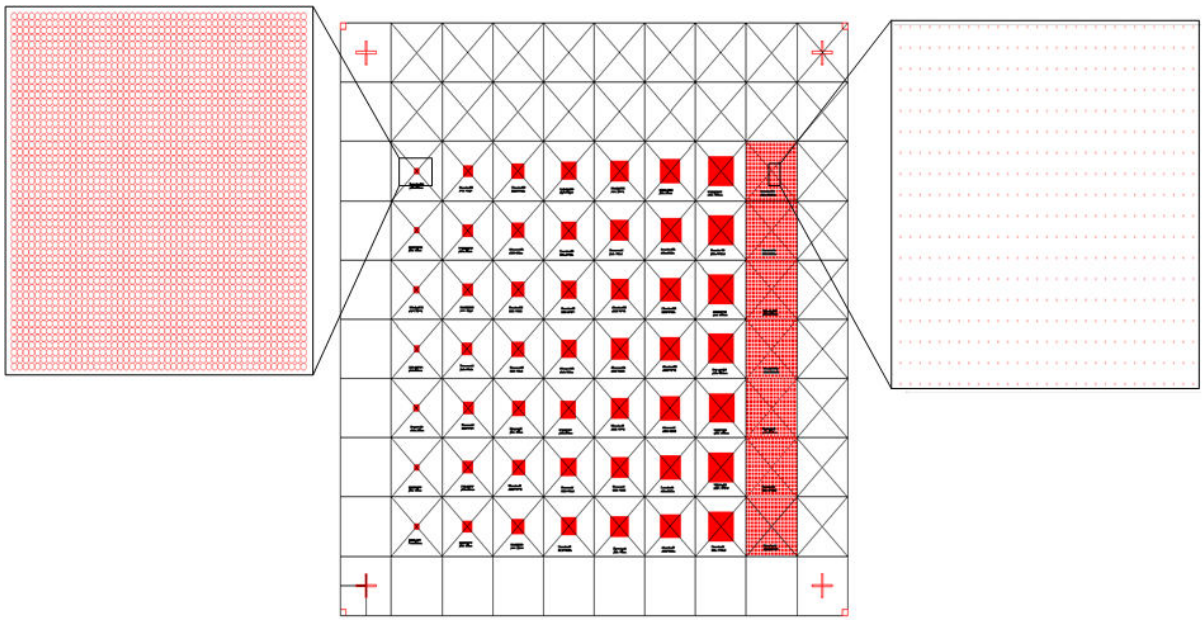

Figure 4.4. A screenshot of the mask for pattern I showing the holes used to grow the NWs. The pattern consists of big square 1x1 mm, with100 x 100 µm small squares inside it. Each small square contained repeated circulars in the x and the y direction; the repeats time is constant for all the features in the squares 50x50 repeats times, with different diameters and pitches.

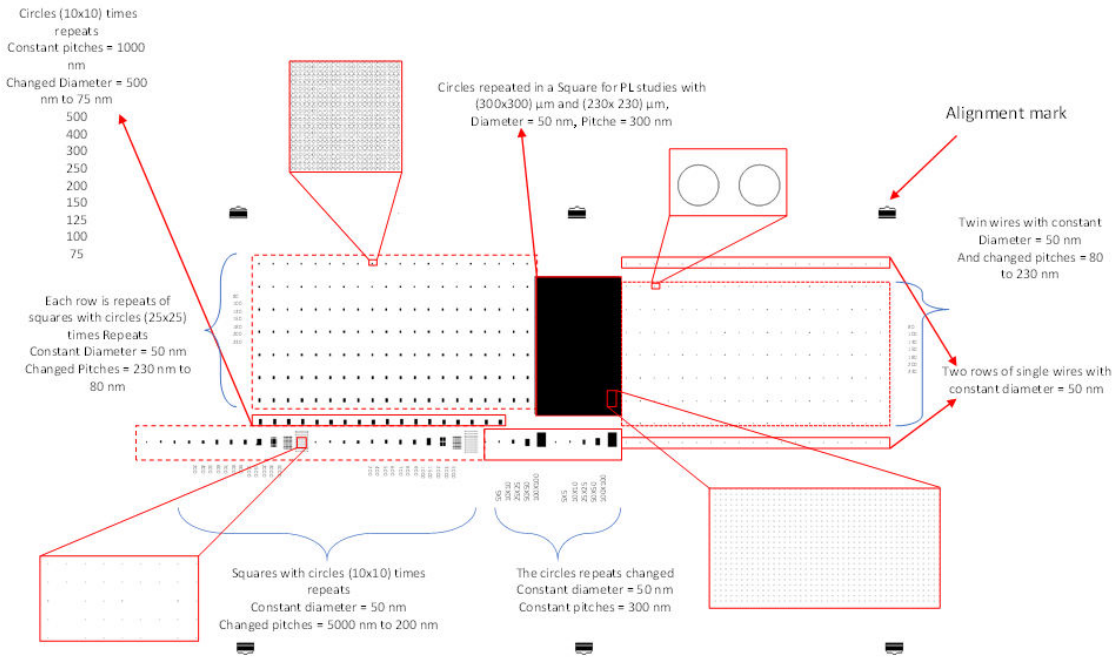

Figure 4.5. A screenshot of the mask for pattern II showing the holes that used to grow the NWs. The pattern consists of big square around 1mm x 3mm along with 6 alignment mark surrounding the patterns. At the center there is a 300 x 300 µm square for PL studies, the square has a circles with 50 nm diameter and 300 nm pitches.to the right of the PL square there are 4 sections as labelled in the figure with different diameters and pitches, to the left there is a section for twin and single holes

4.4. Electron Beam Lithography (EBL)

Electron beam lithography is a very common lithography technique that is widely used in semiconductor research[9]. E-beam lithography involves scanning an e-beam sensitive resist with an electron beam to pattern a desired structure[10]. Compared to photolithography, e-beam lithography can have a patterning resolution that is smaller than 10nm[11]. This is due to the small electron De-Broglie wavelength in comparison to photolithography that uses light of much longer wavelengths. The electron beam writer used in all of this work is a 50 kV Jeol (model 5500DZ) that has an addressed line resolution of 0.5nm and spot size of 2 nm. The e-beam current used in the fabrication of the holes array is 50 pA with an exposure dosage of 115 µC/cm^2. In this work EBL was used to pattern hole arrays that were used as sites for

deterministic spatial growth of NWs on Si. The e-beam resist used together with details will be discussed in the next section. Figure 4.6 shows a simple schematic of the steps used to fabricate the nanowire sites.

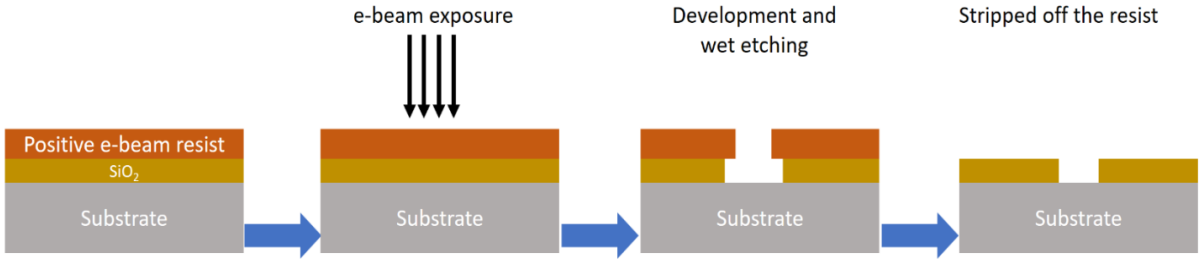

Figure 4.6. Schematic drawing of EBL process shows the e-beam exposure, development and the wet etch and finally strip off the resist.

4.5. Substrate preparation prior to growth

To begin the preparation process, the Si substrate cleaned using an ultrasonic cleaning with acetone and Isopropyl alcohol (IPA) before an e-beam resist is spin-coated on the substrate. The wires arrays were patterned using a JEOL JBX-5500FS e-beam writer with two positive e-beam resists namely; Poly (methyl methacrylate) (PMMA) and AR-P 6200 (CSAR-62) to perform the electron beam lithography (EBL) used in this experiment; details of both resists will be explained later. After development, the underlying SiO_2 layer was etched using buffered hydrofluoric acid oxide etcher (BOE) solution, before the resist was removed using resist stripper with ultrasonic cleaning. Immediately before loading to the MBE reactor, the sample was given an additional, unmasked, dip in BHF. This ensures the presence of an oxide free, hydrogen terminated silicon surface within the hole. The final hole diameter was ~80 nm due to the lateral etching. All the samples in this study have the same diameter and spacing between the wires. In the first growth attempts where we used pattern I, the substrates were spin coated using the PMMA e-beam resist with a hole diameter of 50 nm.

PMMA resist can offer extremely high-resolution, ease of handling and wide process latitude, however, it requires high dosages to completely develop the resist to expose the substrate completely. SEM inspections have been performed on the pattern template to make sure that the holes are patterned successfully and the resist is stripped off before the growth. One of the main problems we noticed with pattern I is that the holes were not etched completely. This means that the resist has not been fully removed after developing from the etched holes which affected the growth seeding. Although most of the wires were seeded in the holes, the nucleation began near the edge of the holes, which is probably due to some resist left in the holes, thus the adatoms are restricted to be nucleated at the edge were the resist is completely removed. Figure 4.7 (a) and (b) shows SEM images for the patterned holes, and we can see clearly some of the resist left in holes or maybe some SiO_2 particles which formed after the etching. Consequently, to improve the EBL pattern process, we turned to use pattern II with dense arrays. However, initial growths using this pattern failed due to incorrect focus on the e-beam writer leading to an overexposure of the resist between the holes. After development and etching we found that the holes in the oxide layer were much larger than expected and the remaining oxide was only a few nanometres thick. After making corrections to the e-beam writer, new substrates were patterned and we measured the diameter of the holes in the resist prior to etching. Figure 4.8 shows atomic force microscope (AFM) image of the holes arrays in the resist with a pitch of 300 nm and a diameter of 50 nm, the resist is covered with a 10 nm thick layer of gold which has slightly reduced the hole diameter). Note that the sample is rotated by approximately 45 degrees. For further development to the pattern, positive e-beam resist AR-P 6200 (CSAR-62) used to coat the substrate to perform the EBL with the same hole diameter of 50 nm. As the high dosage sensitivity of CSAR62 allows the fabrication of patterns with a lower exposure dosage, hence reducing the exposure time, and improving contrast of the exposed patterns due to reduced electron forward scattering. As

shown in Figure 4.9 the holes are almost clean without any resist left which improve the wire seeding and hence the growth.

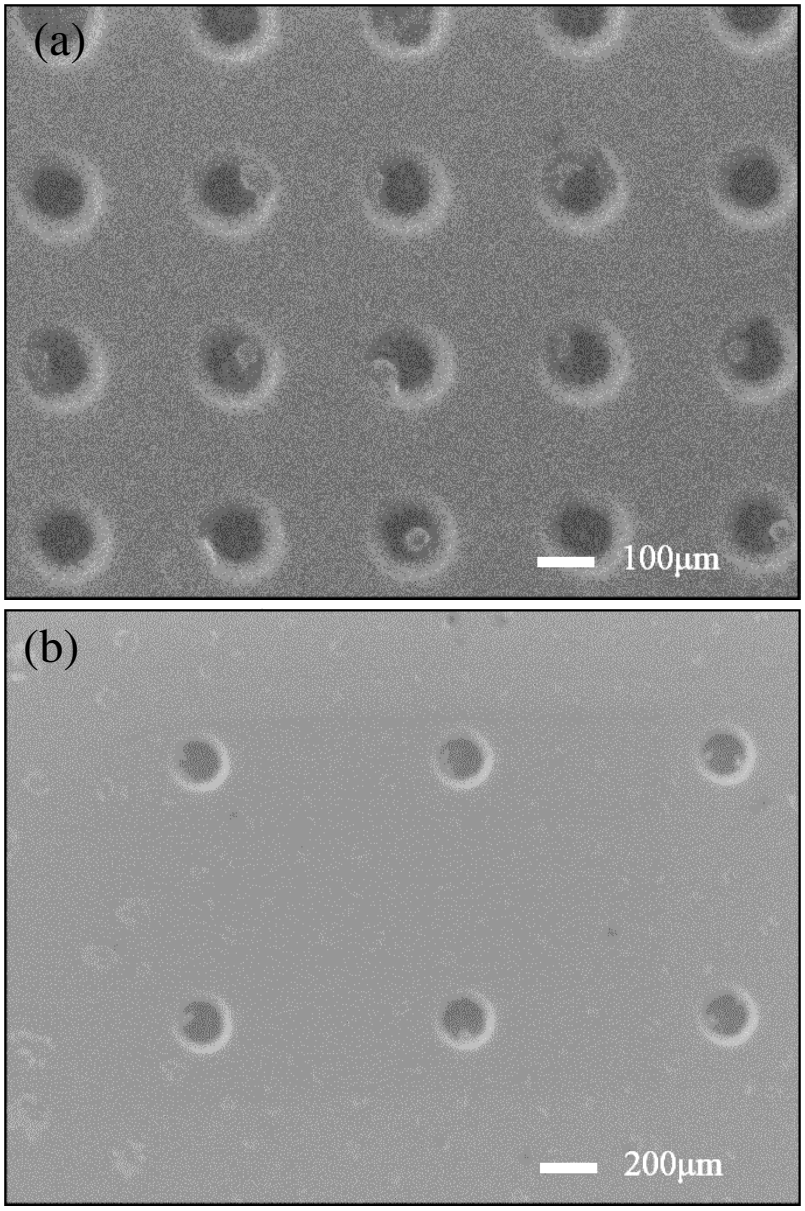

Figure 4.7. SEM images of patterned holes showing some of the resist left in holes or maybe some SiO_2 particles which formed after the etching in the holes (a) and (b) shows two different areas from the sample

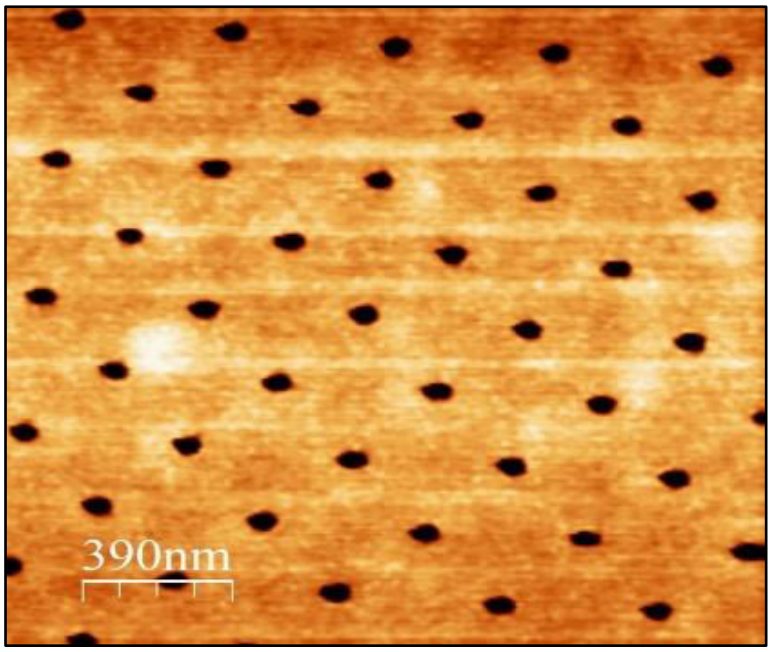

Figure 4.8. Atomic force microscope (AFM) image of the etched holes in the oxide layer on the substrate. Scale bar: 390 nm.

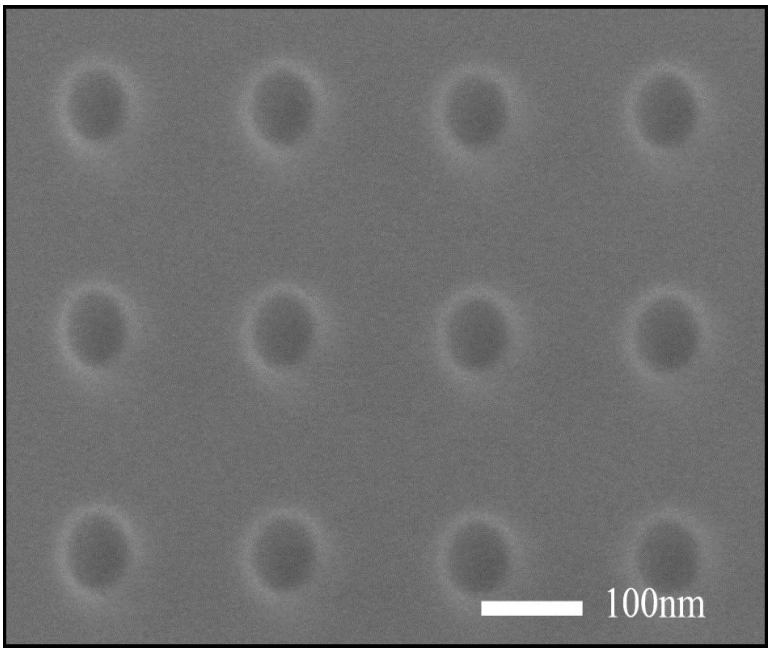

Figure 4.9. SEM image of the patterned holes using CSAR62 showing that the holes are almost clean without any resist left.

4.6. X-Ray Diffraction

X-Ray Diffraction is a widely used technique that reveals structural characteristics of semiconductor epitaxial layers. It provides information about the lattice constant of a crystal which is used to determine the composition, thickness and strain of the layer as well as being useful in making a qualitative assessment of the crystal uniformity. The technique utilises Bragg's Law for the scattering of X-rays by a crystal lattice,

$$n\lambda = 2\, d_{hkl} \sin\theta \qquad (4.1)$$

where λ is the emission wavelength of the X-rays incident beam, d_{hkl} is the lattice plane spacing atomic layers, θ is the Bragg angle between the incident beam and the scattering planes and n is an integer. Materials with different lattice plane spacing will exhibit constructive diffraction of X-rays at different angles. A lab-setup XRD system was used to determine the composition of the $InAs_{1-x}Sb_x$ nanowires by performing a $2\theta-\omega$ scan of the 111 reflections of the as-grown sample (see Figure 4.10). To ensure that the XRD peak originates from nanowires and not surface growth, several scans with different θ offsets have been performed showing only a slight decrease in intensity. Due to the small diameter of the nanowires, their diffraction peaks have a larger in-plane broadening compared to surface growth for which only a small θ offset is sufficient to decrease the intensity considerably. The XRD measurements for the sample QA399 have been performed in collaboration with Lund University. XRD measurements have been performed at Lancaster for both the MQW and the SL samples, but haven't been interpreted in detail for this work due to the limited time.

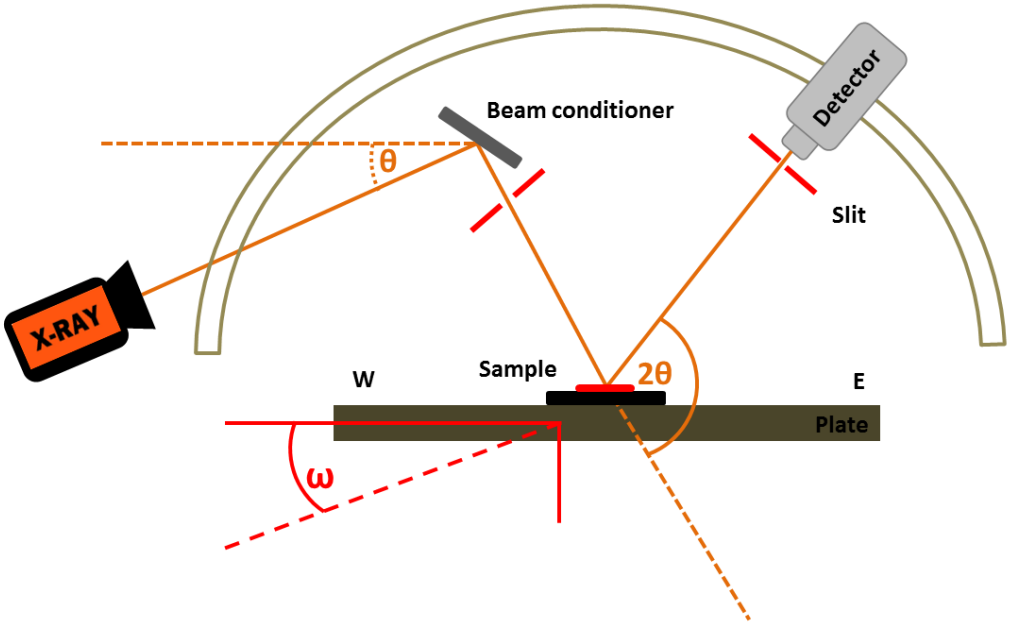

Figure 4.10. Schematic of a typical XRD lab-setup system showing the θ and ω axis. The set up was used to determine the composition of the $InAs_{1-x}Sb_x$ nanowires by performing a 2θ−ω scan of the 111 reflections of the as-grown sample.

4.7. Atomic Force Microscopy (AFM)

Atomic Force Microscopy (AFM) is a very high-resolution technique used for samples surface imaging at the nanoscale level. AFM images were used to study the surface of a patterned sample to obtain information about the hole diameter and the spacing between the wires. The AFM images were taken with a Bruker Multi Mode 8 scanning probe microscope in Tapping Mode using Budget Sensors Tap300Al-G probes type, non-contacted with 5nm tip radius.

The AFM in principle consists of a silicon cantilever with sharp probe to scan across a sample surface. The sample is mounting on an x-y-z piezo stage and moving it upwards until the tip contact the sample surface. An external voltage is applied across the piezo stage to allow the scanning under the probe to investigate the surface of the sample. A laser is calibrated to be reflected from the cantilever toward the centre of a four-quadrant photodiode.

When the surface of a sample is scanned, the probe is deflected based on the topography of the sample, causing the reflected laser spot to shift from the centre of the photodiode. This shift is registered with time and a correlation between the topography and probe position is recorded to output a topography map. Basically, the AFM relies on the forces between the tip and sample; these forces define an AFM image.

4.8. Scanning Electron Microscopy (SEM)

SEM is a powerful high magnification imaging technique which used focused beams of high energy electron (~30 keV) to construct an image of the sample surface. Generally, the beam is directed through a column of microscope which includes electromagnetic lenses that focused the electron beam directly on the sample[12]. The SEM used in in this thesis is a SEM - JEOL JSM-7800F. In the JEOL system, the e-beam is generated from a cold field emission electron gun, and the e-beam is attracted by an anode that is normally at a potential of 50 kV. The gun is made of a crystalline tungsten tip that is very sharp, typically less than 0.1 μm at its end, hence creating a strong electric field at the tip. The beam is then passed through a series of electromagnetic condensing lenses that reduce the diameter of the beam. The beam is then passed through a beam limiting aperture, where the aperture size used in the JEOL system is normally 40μm. Finally, the beam diameter is focused on the sample by an objective lens where the diameter size of the beam typically reaches <1 nm. During the writing and alignment process, the scanning coils are used to scan the beam on the sample and pattern the desired structure. The backscattered and secondary electrons detectors are used to image the surface by detecting electrons scattered and those emitted by the sample, respectively. The system is typically operated under high vacuum to prevent electron scattering and losses as they travel through the column.

The samples have to be conductive, otherwise the electrons accumulate, which leads to charging effects (for example incoming electrons are deflected). When the electrons interact with atoms in the sample, other electrons are produced from the sample either backscattered and secondary electrons or x-ray photons. Secondary electrons come from areas close to the surface and the backscattered electrons from deeper regions. However, secondary electrons give mainly information on the structure, since they only escape from regions close to the surface because of their low energies. Backscattered electrons provide information on the composition, as heavier elements scatter electrons more than lighter elements. The electrons are then detected by a detector, and sent as signals to be viewed in a screen. In this work, imaging was conducted with secondary electrons (SE), as we investigated the structure of the wires only.

To characterize NWs in this work, the NWs were imaged as grown without any metal layer on the surface with a very small working distance (WD) of 15 mm was used in combination with acceleration voltages ranging from 3 to 15 Kv. Higher acceleration voltages results in higher resolution images in case of metal specimen and conductive surfaces. However, lower acceleration voltages are more suitable for non-conductive samples due to the surface charging. Figure 4.11 shows a schematic diagram of a typical scanning electron microscope (SEM). The figure shows the electron beam path as it travels through the anode, magnetic lens, scanning coils before exposing the sample. The figure also shows the secondary and backscattered electron detectors used for imaging and calibration.

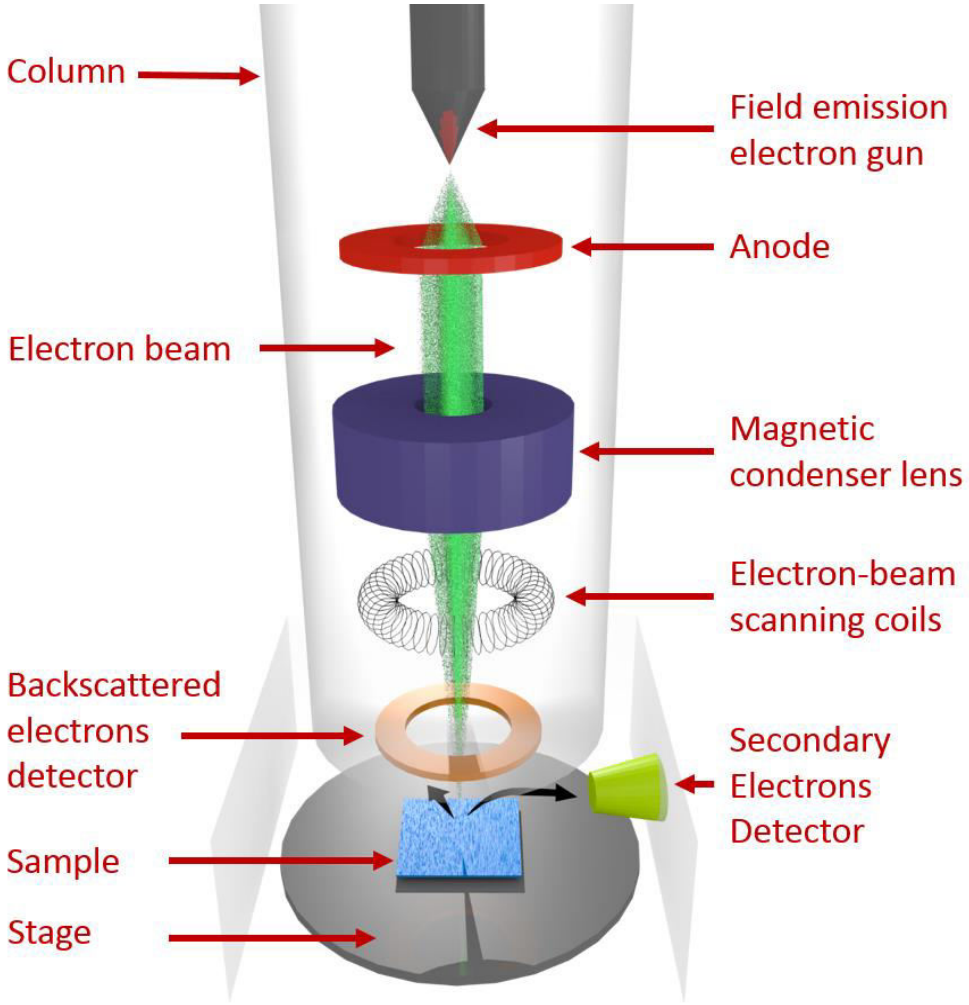

Figure 4.11. A simplified schematic illustration of a typical scanning electron microscope. The figure shows the electron beam path as it travels through the anode, magnetic lens, scanning coils before exposing the sample. The figure also shows the secondary and backscattered electron detectors used for imaging and calibration.

4.9. Transition Electron Microscopy (TEM)

TEM is a useful microscope technique that used to study the material crystal structure. A very high energy beam of electrons is directed toward the sample. The interaction between the electrons and the atoms can be used effectively to study the growth of layer, the composition and defects in semiconductors[13]. Also, the high resolution enables analysis of the quality, shape, size and density of quantum wells, wires and dots. In this work, the morphology of the wires, including the diameter and height was studied using Scanning Transmission Electron

Microscopy (STEM), images were taken in an aberration-corrected JEOL ARM-200F microscope working at 200 Kv at Warwick University. The TEM consist of electron source, electromagnetic lens system, sample holder and imaging system. The electron source contains cathode and anode. The cathode is usually a tungsten filament which is heated until electrons are emitted. A negative cap then directs the electrons into a loosely focused beam. Then the positive anode accelerated the beam towards the specimen. Electrons at the edge of the beam will fall onto the anode while the others at the center will pass through the small hole of the anode. After leaving the electron source, the electron beam is tightly focused using electromagnetic lens and metal apertures. The system only allows electrons within a small energy range to pass through, so the electrons in the electron beam will have a well-defined energy. The sample is placed on a holder equipped with an arm holder that hold the specimen and control the position of the sample. The imaging system consists of another electromagnetic lens system and a screen. The electromagnetic lens system contains two lens systems, for refocusing the electrons after they pass through the specimen, and to enlarging the image and projecting it onto the screen. The screen has a phosphorescent plate which glows when being hit by electrons. The transmission of electron beam is highly dependent on the properties of material being examined. Such properties include density, composition, etc. For example, absorbent material will allow more electrons to pass through while dense material will allow less.

As a result, a specimen with a non-uniform density can be examined by this technique. Whatever part is transmitted is projected onto a phosphor screen for the user to see. Figure 4.12 show a typical TEM experiment apparatus with the sections that a TEM consist of: electron source, electromagnetic lens system, the sample holder and the imaging system. Normally TEM images can be conducted in real space corresponds to bright field (BF) images and in reciprocal space corresponds to dark field (DF) images. The two terms

basically describe the shade of the vacuum in the image, bright or dark. Images in reciprocal space are formed by electron diffraction at the lattice planes (it can also be seen as the Fourier transformation of the real image), called Bragg diffraction scattering at a set of crystal planes gives maxima only at certain angles related to the crystal orientation. These maxima appear as spots; if the sample is tilted such that a zone axis 3 is oriented parallel to the beam, a regular pattern appears. This diffraction pattern gives information about crystallinity, crystal structure and lattice plane spacing. The diffraction pattern appears in the back focal plane of the objective lens, close to the objective aperture. The spots are displayed on the screen, if the image plane is moved to the plane of the objective aperture by changing the focus of the intermediate lens, and the selective area aperture is inserted to choose the contributing part of the image. In practice, this happens automatically at the microscope when switching to diffraction mode. It should be noted that site specific specimen preparation for analysing the nanowire/substrate interface by electron microscopy was achieved using focused ion beam (FIB) lift-out. In this work three samples have been sent for TEM studies, InAsSb NWs sample (QA392), InAsSb/InAs MQWs NWs (QA608) and InAsSb/InAs SLs (QA396), the results of these analyses will be discussed in detail in the next chapters.

Site specific specimen preparation was used to analyze the nanowire/substrate interface by electron microscopy which was achieved using Focused Ion Beam (FIB) lift-out. FIB systems can be used to cut out specimens from specific regions of a sample for further studies. The process involves milling the sample using the focused ion beam, whilst it is under observation so that identified areas of the sample can be removed. In some cases, the ion beam itself can be used to image the region of interest before the machining begins. A better method involves using a dual beam instrument in which a scanning electron microscope is used for continuous observations whilst the machining is accomplished with the ion beam. In

the FIB lift-out technique, thin membranes are extracted from bulk samples for studies using transmission microscopy after lift out.

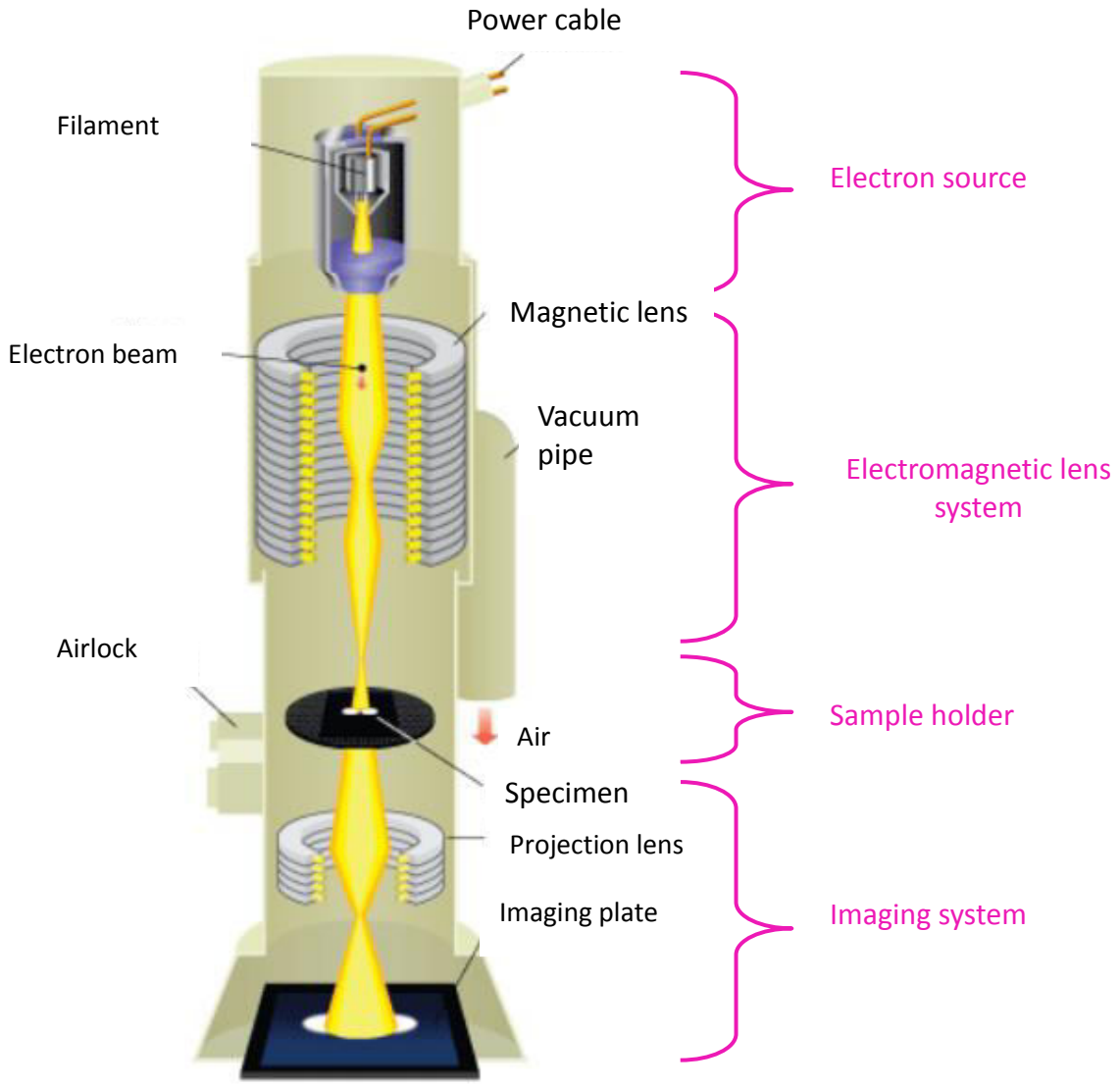

Figure 4.12. Schematic of TEM experiment apparatus, showing the sections that a TEM consist of: electron source, electromagnetic lens system, the sample holder and the imaging system[13].

4.10. Photoluminescence (PL) Spectroscopy

A schematic diagram of a confocal optical configuration micro-PL system is shown in Figure 4.13. The experiment employed using a class 4 GaAs Diode laser (fiber pigtailed) source that generates an output light power of ~ 25W, which connects to a confocal microscope with an optical fiber. The beam is attenuated at the fiber output to 1.5W, and emits invisible light composed of lines at 808 nm with 5nm spectral width (FWHM) and a ±10 nm wavelength tolerance. The laser beam is operated with a pulsed current chopped at a frequency f ~ 1 kHz (500 μs pulse width, 1.0 ms pulse period, 10s time limit and a peak radiant power of 78 mW). The laser beam is then directed on the sample located within the He cryostat. The laser is contained within an optical table which consists of a variable temperature cryostat, a monochromator, a detector, a CCD camera and a computer controlled detection and recording system. The samples were placed in an Oxford Instruments continuous flow He cryostat which enabled temperature selection in the range 4-300 K. The sample space in the cryostat was evacuated to 10^{-1} mbar using a rotary pump and then filled with helium gas prior to cooling. A diaphragm pump was used to transfer liquid helium around the system. The helium was pumped from a dewar to the outer chamber of the cryostat via a transfer arm. Within the cryostat the helium is passed over heat exchangers before returning back along the transfer arm and through the temperature controller to the return line for recycling.

The temperature was adjusted using a temperature controller which controlled the heaters inside the cryostat until the desired temperature was reached. The emitted photoluminescence was collected using a Bentham 0.3 m monochromator before been focused by two of CaF2 lenses (L1 L2). A liquid N_2 cooled InSb photodetector was used to collect the light out from the monochromator. The monochromator grating was set at 3.5 μm (300 lines/mm), (with

blaze wavelength at 3 μm), the monochromator has a dispersion of 10.8 nm/mm (related to the slit width) and a resolution of 1.2 nm and can discriminate light up to ~ 5.5 μm wavelength. The width of its slits can be adjusted to increase details in the PL spectrum if needed. Filters (F) with cut-off wavelengths in the mid infrared spectral range are automatically inserted to eliminate the orders of the laser. At the exit of the monochromator, a J10D Series 77K photodiode Indium Antimonide (InSb) photodetector (PD) was used for the PL which provides an excellent performance in the 1 to 5.5 μm wavelength region. 808 nm laser wavelength pulsed at 1 KHz and 50:50 duty cycles, 2 mm-diameter window (for detection between 1.5 μm and 5.5 μm), cooled to 77 K with liquid nitrogen to improve its performance, detects the discriminated radiation. The output of the detector is connected to a pre-amplifier (A) and the output signal was amplified and then sent to a Stanford SR830 DSP lock-in-amplifier (which has a reference signal from the chopper, the LIA can recover the signal from the noise). A Labview program drives the monochromator through a stepper motor controller (SMC) and collects the signal passing through a voltmeter (V) to record the PL spectrum. The laser and beam before the sample are enclosed for safety reasons.

Positions of the lenses must be slightly adjusted for every sample since the cryogenic high vacuum grease (Apiezon N grease) used to stick the sample on the cold finger can induce a minor tilt. From experience, the lenses can initially be arranged to allow the laser beam reach the sample (with the monochromator at the zero position); a slight horizontal translation of the photodetector (PD) perpendicularly to the beam should allow the detection of the mid-infrared signal. After an initial scan over a wide range with a large monochromator step, the signal should be optimised at the peak emission wavelength by further adjustment of (L_2, L_3) and (PD). The noise of the detected signal is reduced by the choice of an adapted sensitivity

of the voltmeter and a time constant of 1 s on the lock-in amplifier helps smoothing the measured spectrum.

Samples were typically tested using 14 mW laser power which was set on the laser power/current controller. This corresponded to an incident power density, I of 10W/cm^2 since the intensity of the laser beam decreased by approximately 10 times along the optical path and was focused down to a spot size of a 40 μm. The carrier concentration can be estimated from

$$n = \frac{I\alpha\tau}{h\gamma} \tag{4.2}$$

where α is the absorption coefficient of InAs equal to 65.6x10^3 cm^{-1} [14] of InAs at a laser of 1.56 eV with a spot size of 40 μm and a power density of 10^4 W.cm^{-2} the induced excess carrier concentration is approximately 1.7x10^{17} cm^{-3}.

A monochromator can use either the phenomenon of optical dispersion in a prism, or that of diffraction using a diffraction grating, to spatially separate the colors of light. It usually has a mechanism for directing the selected color to an exit slit. Usually the grating or the prism is used in a reflective mode. A reflective prism is made by making a right triangle prism (typically, half of an equilateral prism) with one side mirrored. The light enters through the hypotenuse face and is reflected back through it, being refracted twice at the same surface. The total refraction, and the total dispersion, is the same as would occur if an equilateral prism were used in transmission mode. The dispersion or diffraction is only controllable if the light is collimated, that is if all the rays of light are parallel, or practically so. A source, like the sun, which is very far away, provides collimated light. Newton used sunlight in his famous experiments. In a practical monochromator, however, the light source is close by, and an optical system in the monochromator converts the diverging light of the source to

collimated light. Although some monochromator designs do use focusing gratings that do not need separate collimators, most use collimating mirrors. Reflective optics are preferred because they do not introduce dispersive effects of their own.

The Indium Antimonide detectors (InSb) offered by Infrared Associates Inc. are p-n junctions formed by mesa techniques using single crystal material. This process yields the highest quality photodiodes which exhibit excellent electro-optical performance in the 1μm to 5.5μm wavelength region. These diodes are background limited detectors and their performance can be enhanced by spatial (cooled FOV stops) or spectral (cooled interference filters) reduction of the background.

A lock-in amplifier is a type of amplifier that can extract a signal with a known carrier wave from an extremely noisy environment. Depending on the dynamic reserve of the instrument, signals up to 1 million times smaller than noise components, potentially fairly close by in frequency, can still be reliably detected. It is essentially a homodyne detector followed by low-pass filter that is often adjustable in cut-off frequency and filter order. Whereas traditional lock-in amplifiers use analog frequency mixers and RC filters for the demodulation, state-of-the-art instruments have both steps implemented by fast digital signal processing, for example, on an FPGA. Usually sine and cosine demodulation are performed simultaneously, which is sometimes also referred to as dual-phase demodulation. This allows the extraction of the in-phase and the quadrature component that can then be transferred into polar coordinates, i.e. amplitude and phase, or further processed as real and imaginary part of a complex number (e.g. for complex FFT analysis). The device is often used to measure phase shift, even when the signals are large and of high signal-to-noise ratio and do not need further improvement. Recovering signals at low signal-to-noise ratios requires a strong, clean reference signal with the same frequency as the received signal. This is not the case in many

experiments, so the instrument can recover signals buried in the noise only in a limited set of circumstances.

The setup is not corrected for spectra response, and this is because of the range of interest in the spectra for my samples are very narrow between 2.5 and 3.5 μm. The grating response at 3 μm blaze wavelength is flat in the range of my samples. The spectra response for the photodotors is flat in this range of interest for my samples, and the total transmition of the sapphire window is covering wide range from 150nm to 6μ and again flat in the range of my samples.

4.11. Photodetector Processing

Following MBE growth, the fabrication process of the photodetectors was performed by setting the wires into 2 μm thick of negative photoresist SU-8 and then etching back around 500 nm from the top of the SU-8 using reactive ion etching in CF_4 and O_2 to expose the tips of the wires. The samples were then held by a vacuum chuck in a Commax Precima photoresist spinner and two drops of resist spun on at 3800 rpm for 30 seconds to achieve a thickness of ~ 1.3 μm. To define the spot contacts the sample was exposed to ultra violet radiation for ~2 seconds through a positive mask using a Suss MJB4 mask aligner. The photoresist was then developed for 90 s using MFCD-26 positive developer to remove the photoresist which had been exposed to the ultra violet radiation. The wires were then contacted on top using an optically opaque Ti/Au (30 nm Ti and 100 nm Au) evaporated contact. The excess gold was removed by leaving the samples in a beaker of 1165 resist remover. Finally, 200 nm of Al was deposited on the back of the substrate, forming the back contact. As shown in Figure 4.14.

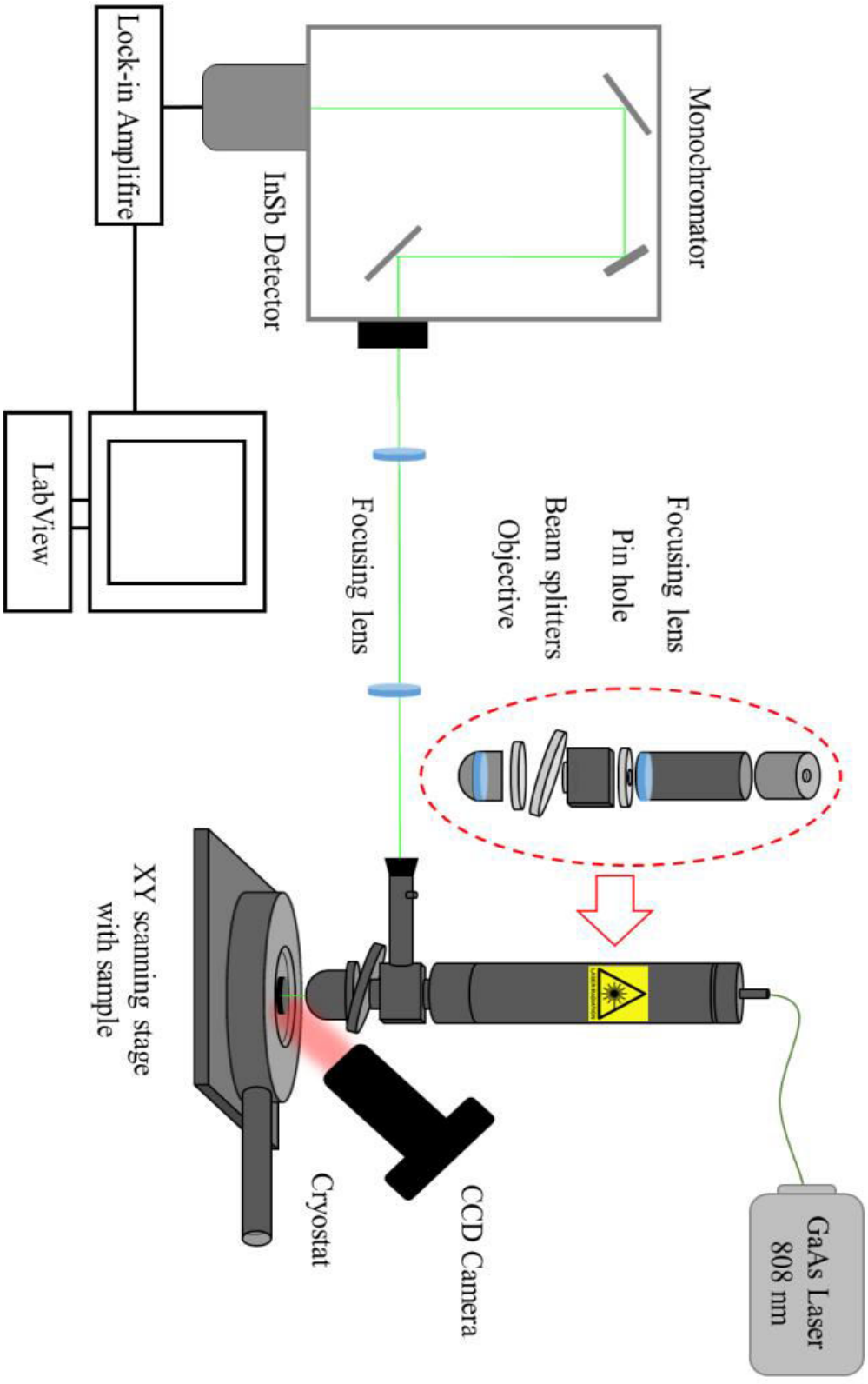

Figure 4.13. Schematic of confocal micro -PL experiment apparatus. The green line represents the laser beam

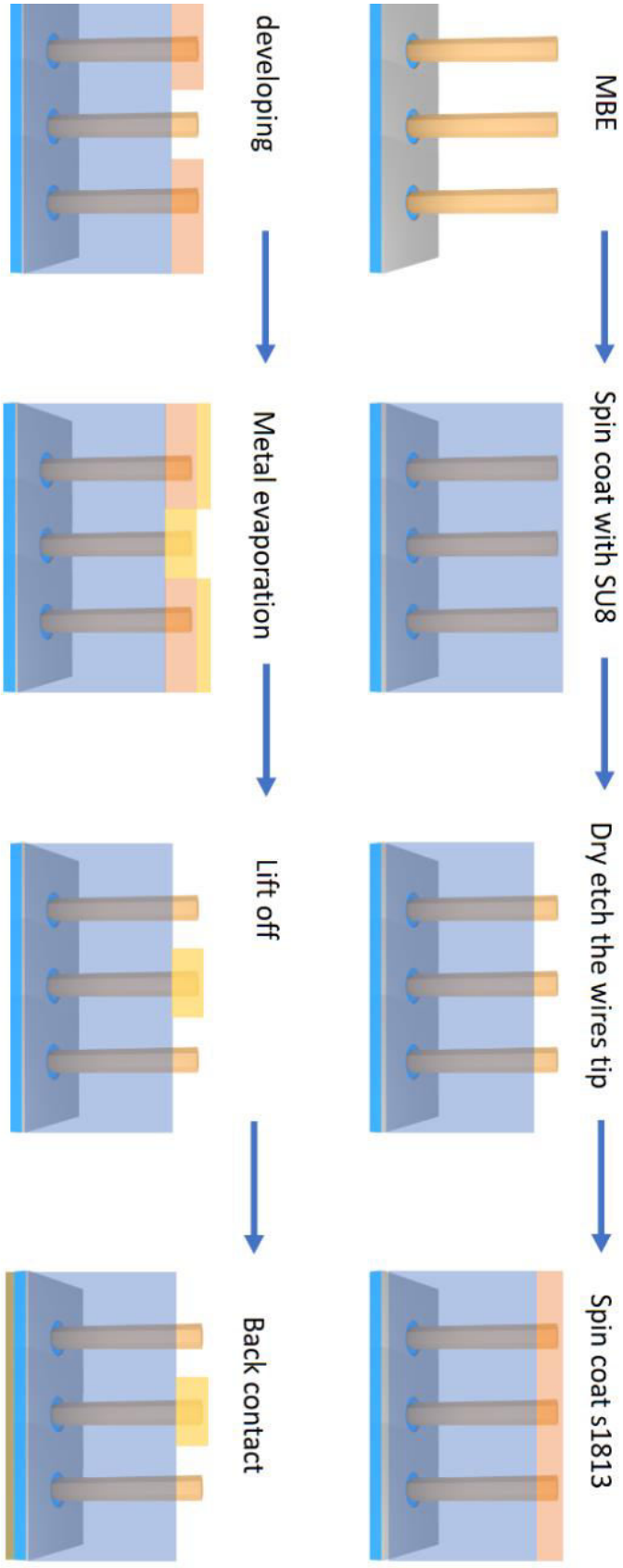

Figure 4.14. The steps for the photodetector fabrication process. The nanowire is encapsulated by cross-linked SU-8, with Ti/Au forming the top contact and Al on the back of the substrate forming the back contact.

4.12. Current-voltage (I-V) measurements

For the fabricated nanowire photodetector, current voltage (IV) measurements were carried out to determine the reverse current leakage. The I-Vs measurments for the device of interest was conducted using a Lakeshore TTPX probe station basic source-measurement unit with guarded triaxial connectors with a low-noise sourcemeter (Keithley 6430 Sourcemeter) and an external preamplifier. The Keithley 6430 meter provides good sensitivity to small currents, there is in practice a requirement for a long source delay (>5 s) to allow the reading to stabilise, the measurements were recorded using Labview software. For this work, the scans were typically current limited to avoid damage of the device and the voltage range was set at a typical operational bias of (18 pA), with a source delay of 10 s between data points used to minimize the effect of transient triboelectric or piezoelectric effects. I-V measurements could be done over a range of temperatures by making use l the TTPX probe stations cryostat capability.

4.13. Fourier Transform Infrared Spectroscopy (FTIR)

Fourier Transform Infrared Spectrometry (FTIR) is a technique used to obtain an infrared spectrum of absorption or emission of a material over a wide spectral range. Spectral response measurements were performed in a Bruker Vertex V70 FTIR spectrometer coupled to the TTPX probe station along with a typical operation bias for the devices of -0.1 V. The front-side illumination would result in reflection by the metal top contact, thus the NWs were back-side illuminated through the Si substrate. A black body source operating at a temperature of 1360 K was used for the optical characterization, with a beam splitter made from KBr. An additional benefit of the back-side illumination is that light passes through the

wires twice due to the highly reflecting top contact, and thus absorption is further increased. The top contact was biased, and the current from the substrate contact converted to a voltage using a current-to-voltage amplifier with a 100 Hz high-pass filter, then sent to an SRS SR830 Lock in amplifier before the signal was routed into the FTIR spectrometer. The FTIR was placed into (SS) mode due to the very low signal that is generated by the effective area of the nanowires. Figure 4.15 shows a schematic diagram for the FTIR. All spectral photocurrent measurements were performed at 300 K, measurements at lower temperatures would further reduce the noise imposed by the large dark current. Photocurrent was measured under illumination by a 14 mW 1.55 μm laser; however, due to the continuous, optically opaque top contact covering the nanowire array, this was not directly incident on the nanowires. Instead it was fibre coupled onto an area adjacent to the edge of the contact, where a small fraction was coupled into the wires through scattering and interface reflections.

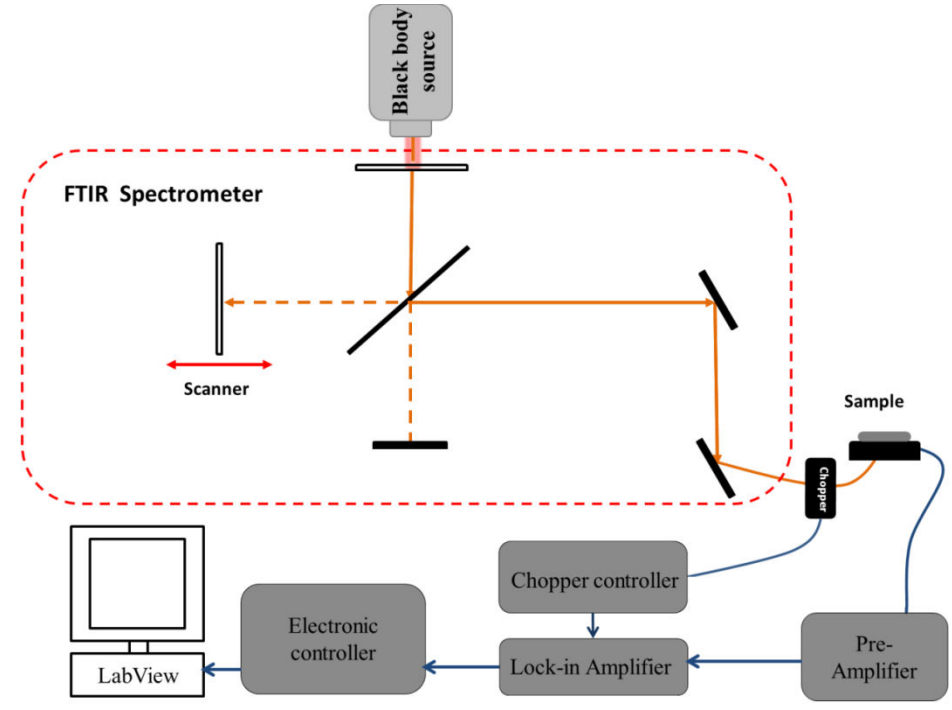

Figure 4.15. Schematic of the FTIR experiment apparatus, were the spectral responses measurements were carried out using the FTIR with a bias of -0.1 V, which is the typical operation bias of the devices. The beam splitter is made from KBr and the source of the light is a black body source operating at a temperature of 1360 K.

4.14. FTIR principle

The mechanism of FTIR spectroscopy is based on the Michelson interferometer. The structure of a Michelson interferometer is sketched in Figure 4.16. Broadband infrared light originates from the light source L, and impinges upon a beam splitter BS. The BS transmits 50% of the light to the mirror M2 and reflects the other 50% light to the mirror M1. The light reflected off the two mirrors is passed/reflected by the BS again, and the two beams (E1 and E2) recombine on the other side of the BS. Finally the recombined beam hits onto the detector D. In FTIR spectroscopy, one mirror (M1) is held in a fixed position relative to the BS during the measurement. The other mirror (M2) scans back and forth relative to the BS.

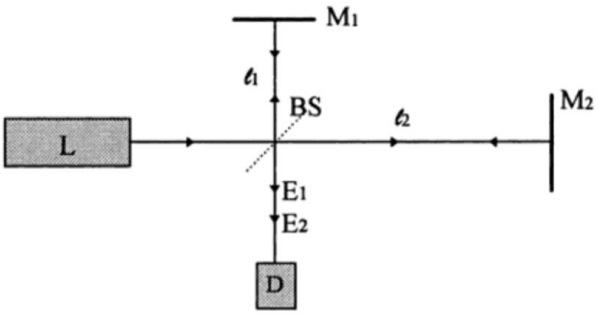

Figure 4.16. The Michelson interferometer: L is the light source, BS is the beam splitter D is the photo detector and M are mirrors[15].

At each position of the moving mirror, the detector collects the interfered light of the two beams for the whole wavelength range. The interference is dependent on the optical path difference of the two light beams, which is determined by the position of the moving mirror. So the intensity registered at the detector is a function of the moving mirror positon. This relation can be translated through a Fourier transform to extract the spectrum of the light source[15].

4.15. References

[1] Parker, E. H. C. 'The Technology and Physics of Molecular Beam Epitaxy', Kluwer Academic/Plenum Publishers (1985).

[2] Tsang, W. T. Applied Physics Letters. 1987, 38: 587.

[3] Rinaldi, F. Basics of Molecular Beam Epitaxy (MBE) Annual Report, Optoelectronics Department, University of Ulm (2002).

[4] Foxon C. T., J. Vac. Sci. and Tech. B, 1983, 1, No. 2, pp.293-297.

[5] Ohring M., The Material Science of Thin Films, Academic Press, 1992.

[6] Patanè, A. Physical Review B, 2009, 80: 115207.

[7] Joyce, H.; Gao, Q.; Hoe Tan, H.; Jagadish, C.; Kim, Y.; Zou, J.; Smith, L.; Jackson, H.; Yarrison-Rice, J.; Parkinson, P. et al. III–V Semiconductor Nanowires For Optoelectronic Device Applications. Progress in Quantum Electronics 2011, 35, 23-75.

[8] E. Fadaly. Molecular Beam Epitaxy of Catalyst-Free InAs Nanowires on Si (111). PhD thesis, Chalmers University of Technology Gothenburg, Sweden 2015.

[9] M. A. Mohammad, M. Muhammad, S. K. Dew, M. Stepanova. Fundamentals of electron beam exposure and development. Nanofabrication, ch.2. Springer (2012).

[10] M. J. Madou. Fundamentals of Microfabrication: The science of Miniturization, second edition. Lithography, ch.1. CRC press (2002).

[11] R. Garcia, A. W. Knoll, E. Riedo. Advanced scanning probe lithography. Nature Nanotechnol.2014, 9 577-587.

[12] A. Heuberger. X-ray lithography. Journal of Vacuum Science & Technology B, Nanotechnology and Microelectronics: Materials, Processing, Measurement, and Phenomena 1988, 6, 107-121.

[13]Atomic World, Transmission electron microscope (TEM), Principle of TEM http://www.hk-phy.org/atomic world/tem/tem02_e.html (accessed Sep 25, 2017).

[14] Aspnes, D.; Studna, A. Dielectric Functions and Optical Parameters of Si, Ge, Gap, GaAs, GaSb, InP, InAs, and InSb From 1.5 to 6.0 Ev. Physical Review B 1983, 27, 985-1009.

[15] J. Shamir, Optical Systems and Processes. Bellingham: SPIE, 1999, p. 163.

Chapter 5

Growth, Structural and Optical Analysis of Bulk NWs InAs & InAsSb NWs

5.1. Introduction

The development of NWs synthesis is certainly an important first goal to achieve the fabrication of a NW based device. This chapter focuses on the growth, structural and optical characterization of InAs and InAsSb NWs. Thanks to their unique optical properties, they can have great potential for the development of emitters and photodetectors operating in the mid-infrared spectral range. In particular, InAs-based NWs on Si are an attractive technology to realize high performance and low cost optoelectronic devices. As discussed in chapter three, InAs NWs have been widely investigated in literature regarding the physical properties and crystal structure, but only few researches overcome the difficulties of poor optical efficiency of InAs NWs in the spectral range 2- 3.5 μm [1,2, 3,4,5] by achieving low temperature PL up to 130K. However, in this work we developed the growth process of InAs(Sb) NWs and report the optical properties for the grown wires, while mainly aiming at improving their poor optical efficiency by reducing nonradiative surface and Auger recombination. Thus, our challenge was in achieving emission at room temperature for realising practical applications. The next step was in introducing the Sb to the InAs NWs, as it was reported that the addition of small amounts of Sb has been shown to suppress lattice defects, including twinning and stacking faults in InAsSb NWs, in agreement with our recent findings. However, the PL quenching behaviour is only marginally improved[6] since the band-edge perturbations introduced by these defects do not strongly influence non-radiative recombination. In this thesis, the main motives for the study is to realise InAsSb nanowire based photodetector. The final goal of realising proof of principle InAsSb nanowire based photodetectors is achieved and will be discussed in more details in chapter 7.

5.2. InAs NWs: MBE growth

Four undoped samples were grown by selective area MBE growth technique on Si (111) substrate for PL studies, using an array of etched holes in SiO_2 with a diameter of 50 nm and an array pitch of 330 nm. After preparing the samples and the treatment in HF prior to growth, the substrates were loaded into the MBE chamber and underwent 10 minutes of annealing at 600 ºC to remove any contaminants. The growth was initiated by impinging As flux on the substrate for 3 min to ensure excess As is available within the chamber prior to expose the sample to the In flux. The In/As flux ratio was kept constant for all the samples at an As beam equivalent pressure of 2.5X 10^{-6} torr. The NWs were not characterized using in situ RHEED during the growth. The growth temperatures for the NWs were investigated in the range of 473 -509 ºC to initiate the InAs NW growth. Finally, the growth was terminated by closing the In flux followed by the As flux after few minutes. In our samples, the optimal conditions are found to be at T_S= 494 °C with fluxes at 0.08 ML/s 1.59 ML/s for In, As respectively. The As flux was estimated from two-dimensional equivalent growth rate on GaAs (001) surface as mentioned in chapter four. All the four samples in this work commenced with bulk InAs, in addition to a planar bulk InAs sample was also grown on an InAs substrate, as a further reference. For the optimal sample, 1hour growth of bulk InAs at growth temperature of 494 ºC is expected to form around 800 nm long InAs NWs, however, from the SEM images the wires obtained were on average 760 nm in length and 80 nm in diameter. As the samples are growing using selective area growth, the nucleation of the wires formed when the (In/As) adatoms diffuse on the surface until they get trapped in the holes within the oxide layer. The effect of the diffusion growth rate and the direct incorporation of the impinging species on the growth will be explained in detail later. The nanowires had a regular hexagonal cross-section and the absences of a droplet on the NWs tip is confirming

that the wires were grown with the VS mechanism[7]. Table 1 summarized the InAs NW samples used in this work with growth temperature and the wire length.

Sample no.	Pattern	Wire length	Growth temperature (Tg ºC)
QA 250	1	300 nm	473
QA 612	2	750 nm	494
QA 336	1	400 nm	501
QA 251	1	100 nm	509

Table 1: Summary of the grown InAs NWs samples using different growth temperatures in the range 473 – 509 ºC, and two different growth templates 1 and 2 (see experimental chapter).

5.3. Temperature dependence of InAs NWs growth

Different growth temperatures (T_g) were used in an attempt to optimise the growth for the site control InAs NWs. It is clear that T_g strongly influenced the uniformity and the seeding of the nanowires. For T_g = 473 ºC, the InAs NWs growth was uniform but the wires height was considerably low, as shown in the SEM images in Figure 5.1. In addition, InAs clusters also grew by VS deposition between the holes onto the oxide surface on the Si substrate. This can be explained by the surface migration length of In adatoms on SiO_x/Si (111) which is rather low resulting in higher sticking coefficient and extensive cluster formation[8]. With gradually increasing T, the selective growth was enhanced at T_g= 494 ^oC, due to the longer surface migration lengths and the probability of incorporation into the top of the NWs growth is also

enhanced, which results in longer NWs. Polycrystalline growth is observed between the wires, which seems to be separated by roughly the diffusion length of In adatoms on the Si surface (~ 1 um), or due to the roughness of the substrate surface and the low temperature that causes the adatoms to diffuse along the surface surrounding the NWs (see Figure 5.2). Further increase of the temperature to T_g= 501 ^oC, results in a subsequent decrease in NW length and a clean surface between the wires, which could be related to a significant loss of In, since parasitic clusters are also much less and competitive incorporation processes can be neglected as shown in Figure 5.3. At a higher temperature, T_g= 509 ^oC, crystallites are no longer formed on the oxide layer, however, In droplets are formed on the holes instead of a wire, as shown in Figure 5.4, hence the desorption of As and In is enhanced with increasing temperature. Thus, 494 ^oC is concluded to be the optimal growth temperature for well controlled uniformity and successful selective growth of the InAs NWs array as shown in Figure 5.5.

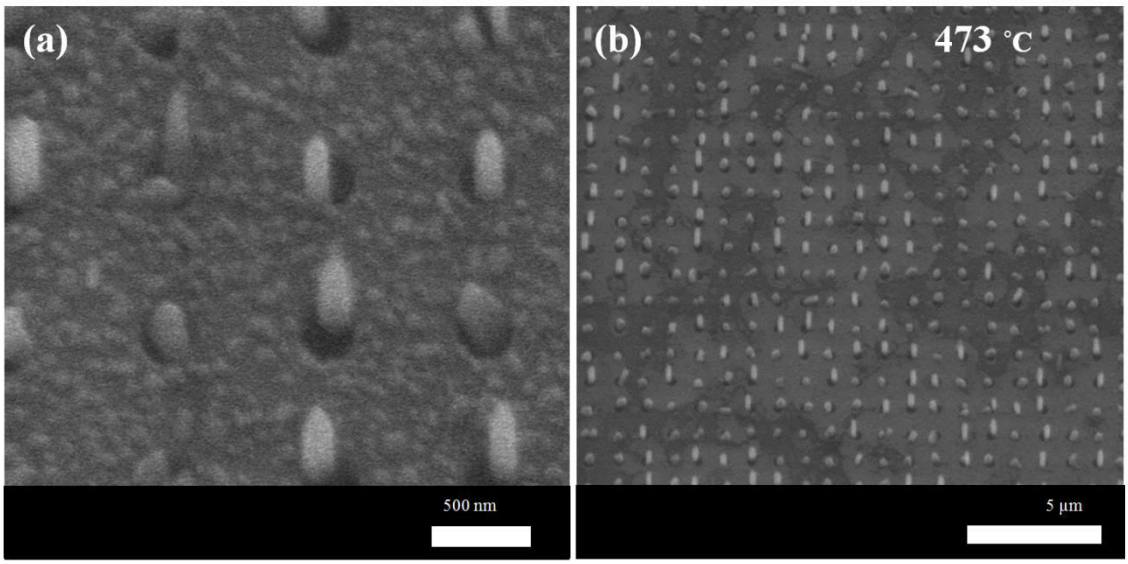

Figure 5.1. InAs NWs at growth temperature of 473°C with 300 nm wire length, (a) 30° tilted SEM images, (b) top view SEM images.

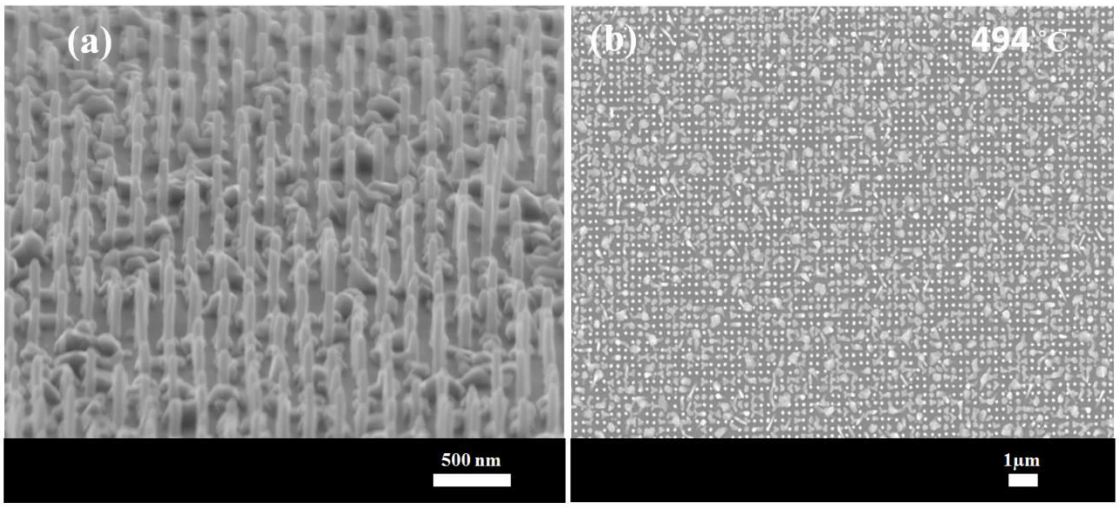

Figure 5.2. InAs NWs at growth temperature of 494 °C with 750 nm wire length, (a) 30° tilted SEM images, (b) top view SEM images.

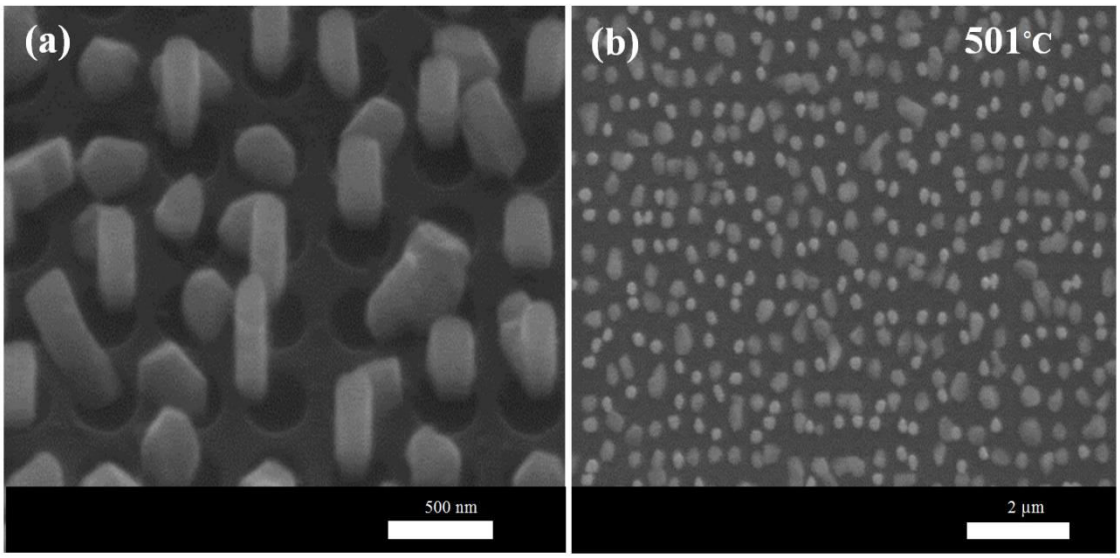

Figure 5.3. InAs NWs at different growth temperature of 501 °C with 400 nm wire length, (a) 30° tilted SEM images, (b) top view SEM images.

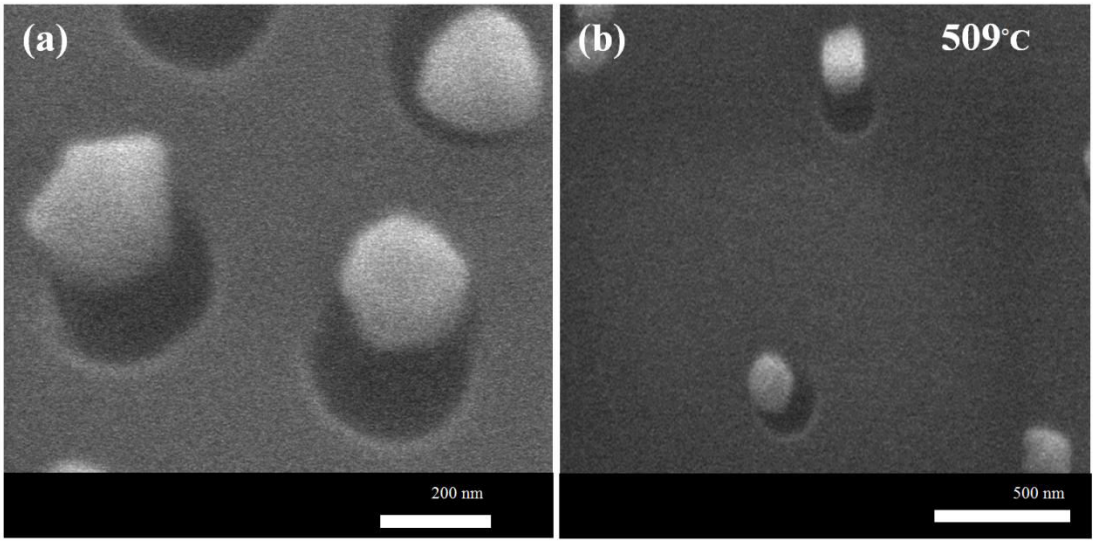

Figure 5.4. InAs NWs at different growth temperature of 509 °C with 100 nm wire length, (a) 30° tilted SEM images, (b) top view SEM images.

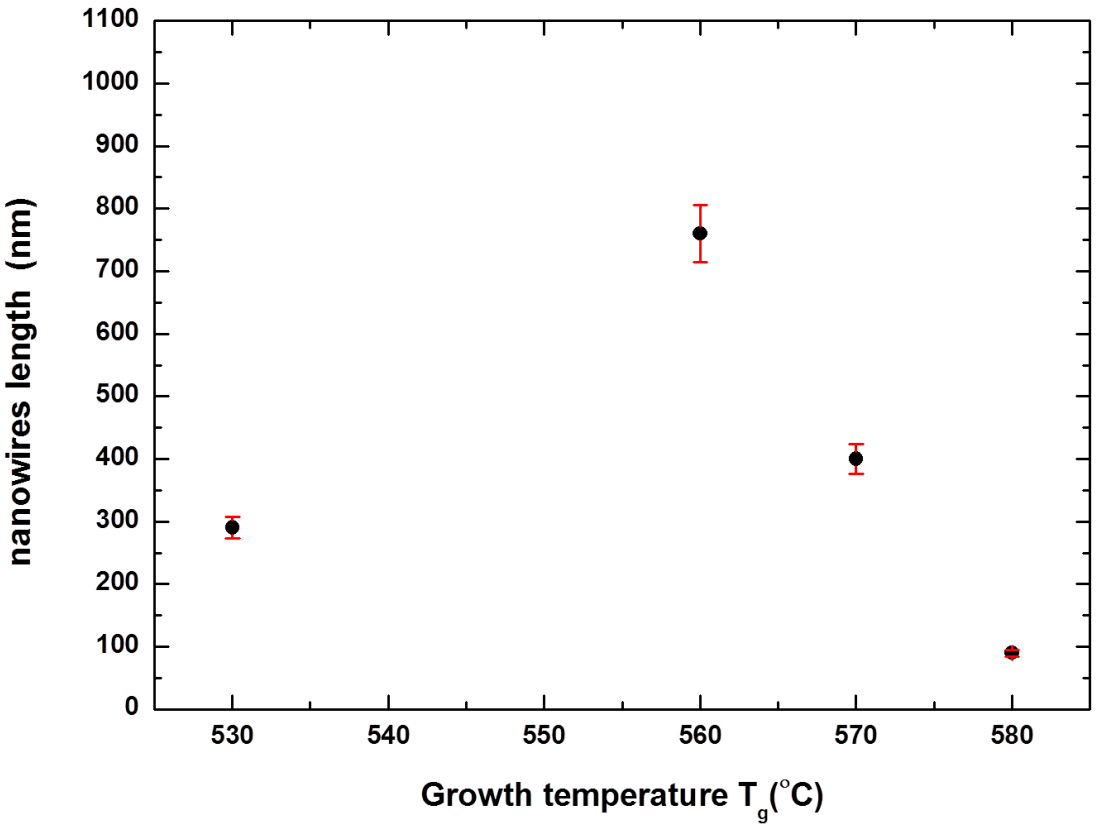

Figure 5.5. Average InAs NWs length at different growth temperatures at 473C° with 300 nm wire length, 494 °C with 750 nm wire length, 501 °C with 400 nm wire length, 509 °C with 100 nm wire length.

5.4. Structural analysis

TEM analysis have not been performed for bulk InAs NWs sample, however, it was performed on samples contained InAs section at the first stage of the growth (namely InAsSb/InAs SLs (QA396)). All the InAs NWs used in this work were grown under the same growth conditions with growth temperature of 494 ºC, thus, the STEM analysis should be the same for the InAs wires presented here. Figure 5.6 shows high magnification STEM images of 80 nm diameter NW sample. The area in red square shows a sharp interface between the NW and the Si substrate which demonstrates that the NW grown directly on the Si substrate.

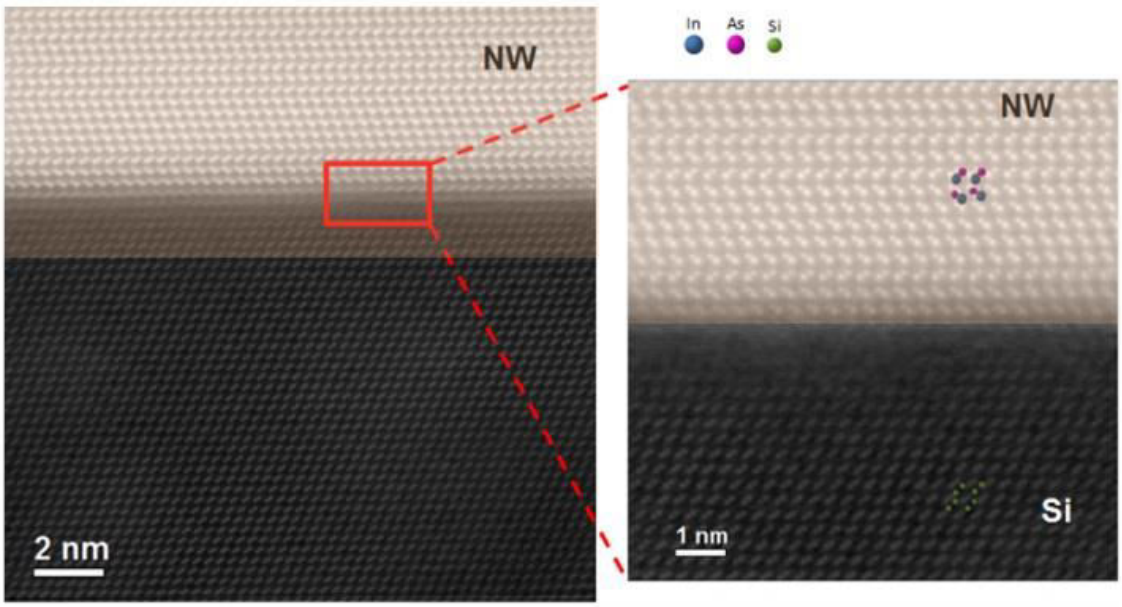

Figure 5.6. Structural characterization of InAs NWs. High magnification STEM images corresponding to the InAs nanowire/Si interface shows that the nanowires have grown directly onto the substrate and the InAs section shows a mix of WZ and ZB regions.

The InAs NWs are formed by predominantly a pure wurtzite phase with a few stacking faults and a few monolayers of ZB phase as commonly observed for InAs NWs[9]. The ZB section is at the bottom region of the NW which formed at the first stage of the growth, it should be noted that the sample used for the TEM is not a bulk InAs NW as mentioned previously. Figure 5.7 shows a zoomed-in view of the high-resolution STEM image for the

InAs NWs structure, were the different sections of both ZB and WZ can be clearly identified. The NWs grew perpendicular to the (111) surface of the substrate along the <111> growth direction for the ZB section and <0001> growth direction for the WZ structure phase. In this section, the total atomic layers are 30 layers, the bottom10 layers of the total area are formed by ZB section and the other 20 layers are WZ with staking faults and ZB segments within the WZ section. Switching from the ZB to the WZ phase was observed after 9 atomic layers (~ 9 nm), with a 60º rotation of the lattice around the (111) axis switches the growth to WZ and the NW continues to grow along the (0001) axis.

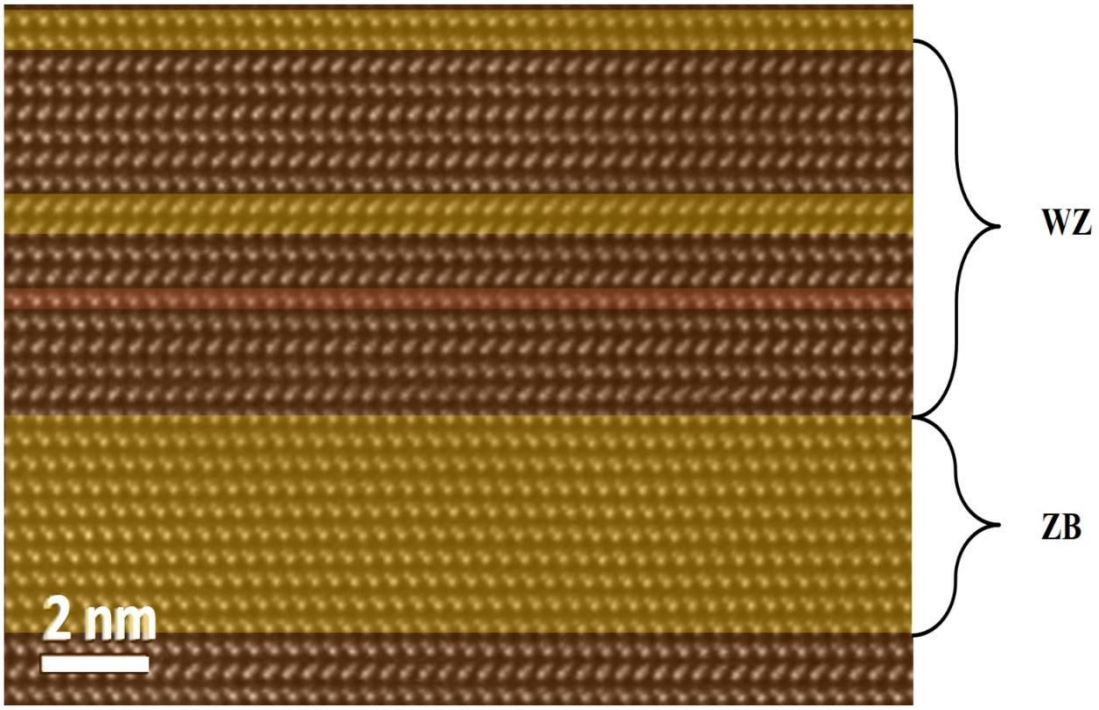

Figure 5.7. Structural characterization of InAs NWs. A zoomed-in view of the high magnification STEM images shows both ZB and WZ structures within the InAs NWs. The NWs grown along the <111> growth direction for the ZB section and <0001> growth direction for the WZ structure phase with multiple stacking faults on both crystal structures.

5.5. Micro- PL measurements

The optical properties of the NWs were studied using temperature dependent micro-photoluminescence spectroscopy for the four grown samples. No PL emission was obtained from the first two samples QA250 and QA251, and a very weak signal was obtained from QA336, however, maximum PL emission was detected from the sample QA612. At low excitation $1.1x10^3$ Wcm^{-2}, a comparison of the spectra measured at 4 K from the InAs NWs and bulk alloy InAs sample is shown in Figure 5.8. Normally, under low excitation conditions, bulk ZB InAs at 4 K exhibits characteristic emission due to bound exciton and donor-acceptor transitions around at 0.417 eV and 0.374 eV respectively[10]. The InAs NWs emission is deconvoluted into two Gaussian fits consist of a main peak at 0.473 eV with a dominant WZ phase, the atmospheric water vapour absorption is evident on this peak between 0.445 eV and 0.485 eV^2. A shoulder on the lower energy side from the main peak originating from ZB InAs appears as the dominant phase in the early stage of our NW growths[11] at 0.429 eV. The spectra can be scaled (as shown in Figure 5.8) to account for the reduced cross-sectional area of the nanowire samples, where only 7% of the surface area is covered by the NWs, assuming a 100% nucleation yield in the mask sites. Accounting for the reduction in active area allows best direct comparison of emission intensity. We observed that at $1.1x10^3$ Wcm^{-2} excitation, the InAs NW emission intensity is 1.6-fold enhanced with respect to a bulk InAs reference sample. The higher excitation intensity (~ 10^4 Wcm^{-2}) in our micro-PL experiments results in state filling so that a single InAs peak is observed at 0.425 eV as shown in Figure 5.8. In the present case, the InAs NW emission is further blue-shifted 55meV with respect to the bulk ZB reference sample due to the WZ crystal structure of the NW where the bandgap of WZ InAs is known to be higher than that of ZB InAs by 50 – 60 meV[12]. Our result is consistent with earlier studies of WZ InAs NWs which reported

bandgaps in the range 0.477 eV to 0.540 eV[13]. In addition, quantum confinement induced blue-shifts have also been observed as the diameter of InAs NWs are reduced[2], however in our case, for 80 nm diameter wires, the shift is rather small ~ 6 - 7meV (see Figure 5.8).

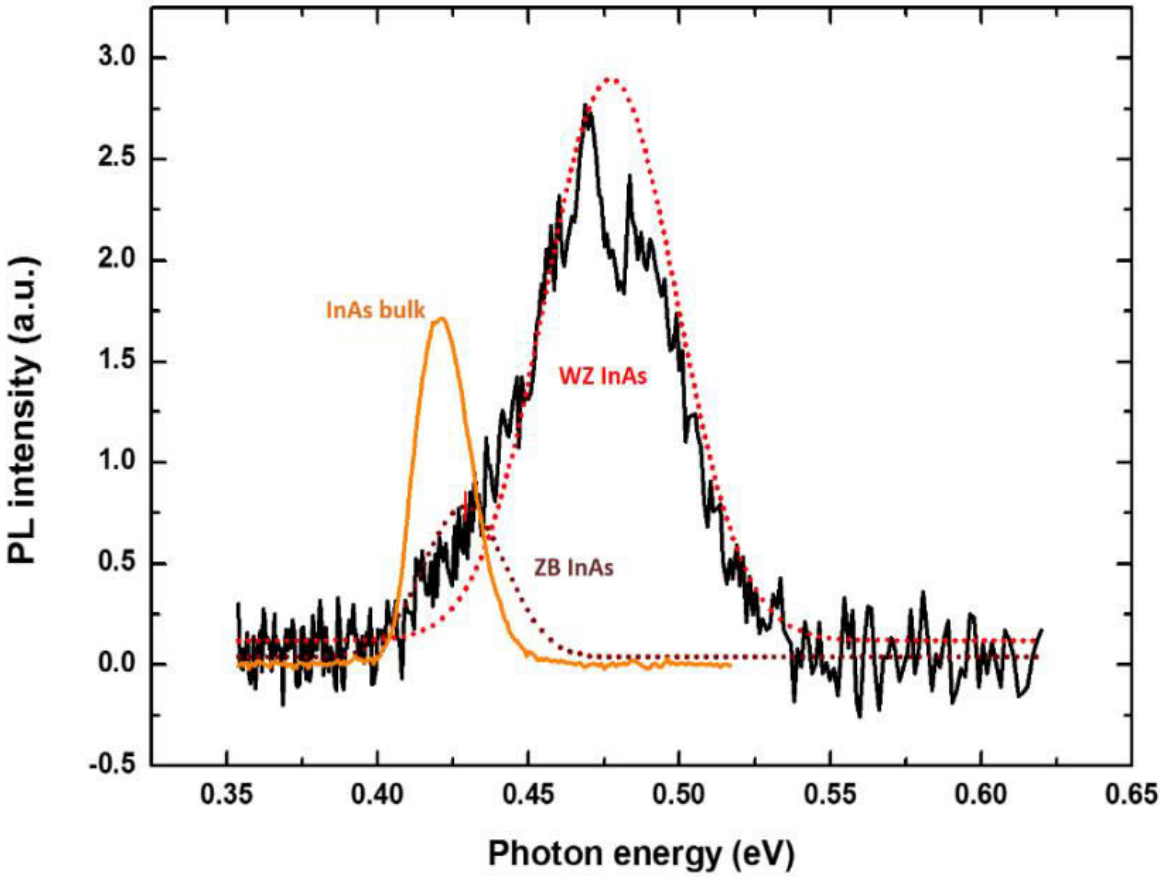

Figure 5.8. The 4K PL emission spectrum for InAs NWs, dotted curve showing the Gaussian fit of the main peak at 0.473eV with a dominant WZ phase, and a shoulder on the lower energy side originating from ZB InAs at 0.429 eV, at $1.1x10^3$ Wcm^{-2} excitation power. The InAs bulk emission is shown for comparison.

5.6. PL Power dependence

Figure 5.9 shows the PL excitation power dependence of the InAs NWs (QA612) at 4 K. The intensity was found to increase linearly with increasing laser power. Peak emission energy ranges from 0.473 eV ($1.1x10^3$ Wcm^{-2} excitation) to 0.494 eV ($3.8x10^4$ Wcm^{-2} excitation).

The PL emission energy from the InAs NWs blue shifted by 21 meV over the range of pump powers used in our experiments, as shown clearly in Figure 5.10, similar to that obtained by Koblmüller et al and which is associated with band filling[2]. The PL linewidth (full width at half maximum-FWHM) increased from 61 meV at low power to 85 meV at high power. This is boarder than the bulk InAs reference used in the experiment with a FWHM of 21 meV at low power and 33 meV at high power. In the literature, the FWHM is varied in the range between 40 meV and 60 meV[2,12 ,14]. Our results are clearly in the range previously reported for WZ InAs NWs.

Analysis of excitation-power dependent PL is commonly performed to investigate the emissions in narrow gap semiconductors[15,16,17,18]. The PL intensity I_{PL} shows a variation with increasing excitation L modelled by[19,15] the relation (2.15) in chapter two[20], where k is an exponent verifying $1 \leq k \leq 2$ for exciton-like transitions (close to the bandgap) and $k < 1$ for free-to-bound transitions (donor-hole hD, electron-acceptor eA) and donor-acceptor pairs (DAP) in near-band-edge photoluminescence studies. We use this approach to compare InAs to InAsSb.

Thus, in order to determine the type of recombination, the k value was calculated from plotting the integrated intensity and laser power, as shown in Figure 5.11. The InAs peak had a k value of less than 1 (0.78) which is believed to be free to bound transitions and donor-acceptor pair recombination. This value suggests that impurity-like recombination processes are involved, as observed by Moller et al for WZ InAs NWs[14], and as previously reported for donor–acceptor pair and band-to-acceptor transitions in bulk InAs[21,22]. Electron accumulation in such low-gap materials is commonly attributed to large densities of donor-type surface states, thus due to formation of an electron accumulation layer in the near-interface region, i.e., a peculiar tendency of InAs to adjust its energy bands in such a way that

the Fermi level (E_F) becomes located above the conduction band minimum (CBM) at the surface and thus create strong surface band bending in InAs nanowires[23,24]. It is well known that the surface of bulk InAs contains a large number of states that lie above the conduction band minimum and can cause electrons to form a surface accumulation layer. Because of the large surface charge density, the Fermi level for InAs is pinned in the conduction band. The surface Fermi level pinning and associated band bending at the surface may result in spatially separated electrons and holes confined near the surface rather in the centre of the NW.

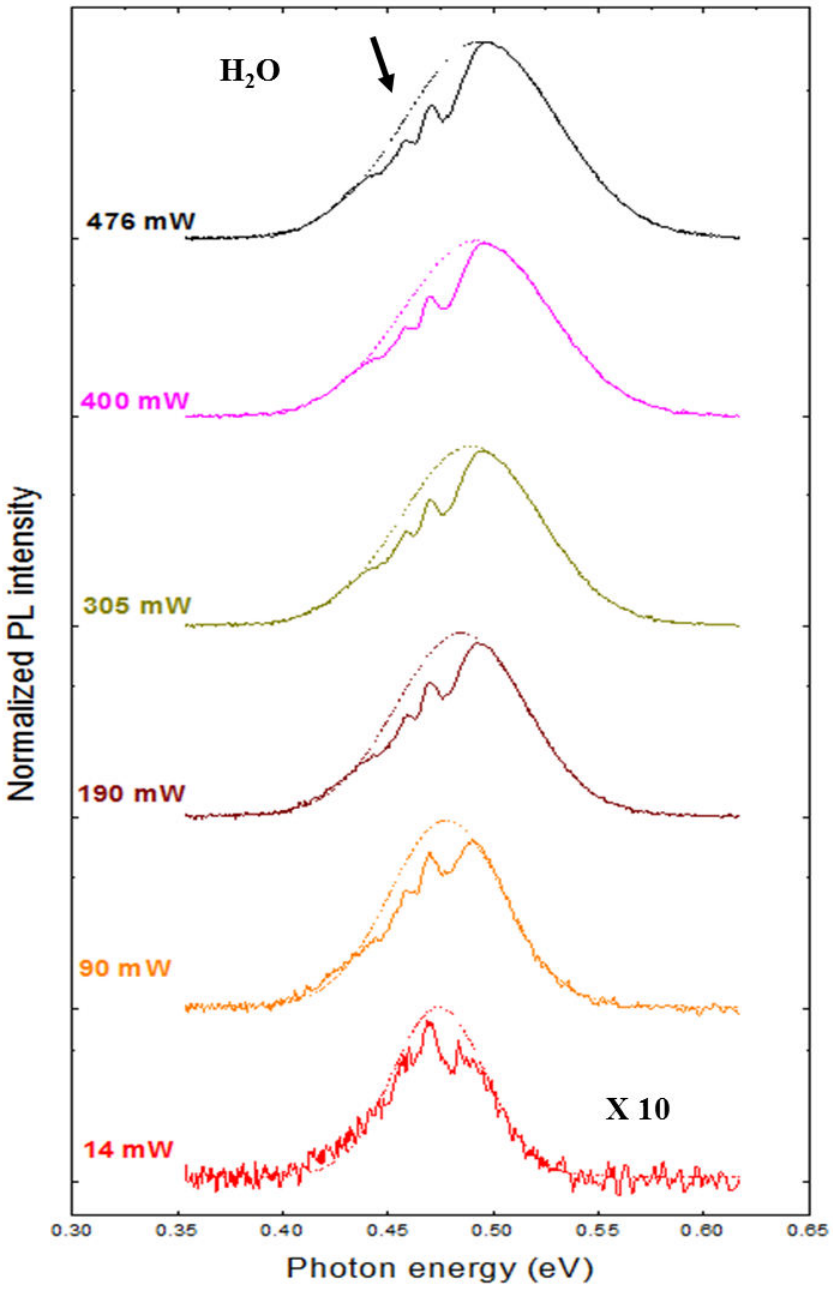

Figure 5.9. Excitation power dependence for the PL of InAs NWs in the range of ($1.1x10^3$ Wcm^{-2} – $3.8x10^4$ Wcm^{-2} excitation.

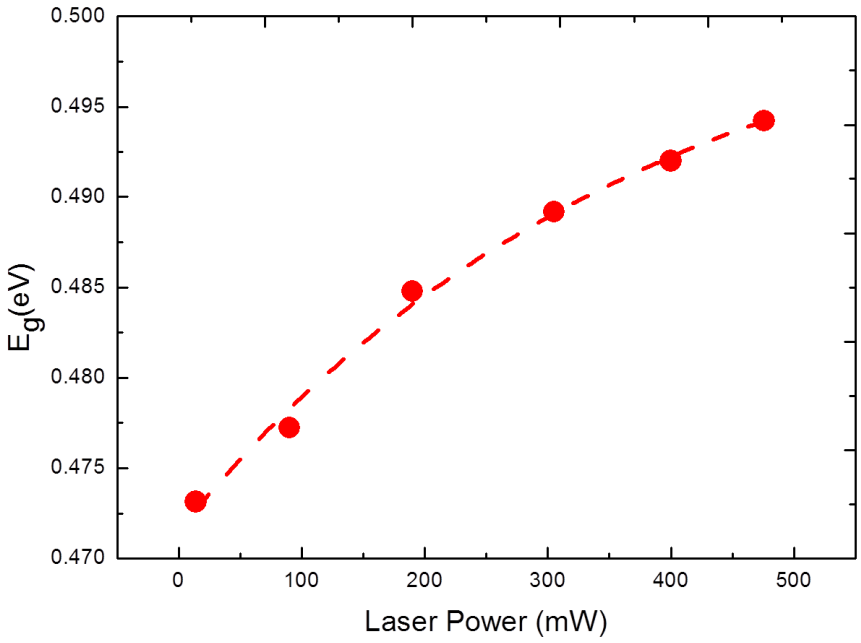

Figure 5.10. The energy gap as a function of the laser power with a 21 meV shift between low and high powers for InAs NWs in the range of $1.1x10^3$ Wcm^{-2}– $3.8x10^4$ Wcm^{-2}.

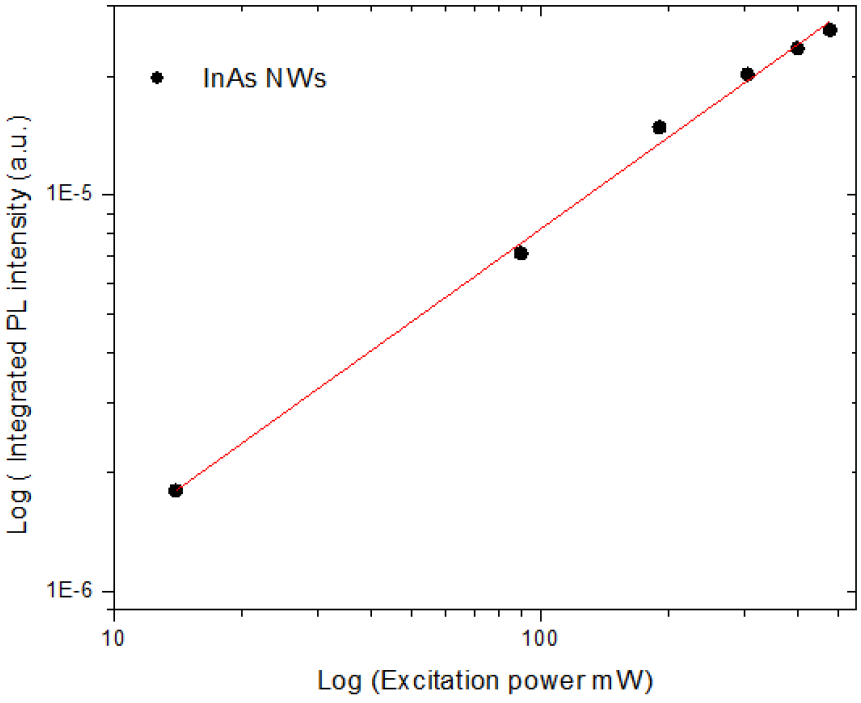

Figure 5.11. Analysis of the excitation power dependent PL spectra recorded at 4K for the InAs NWs, showing a K value of 0.78 for the InAs NWs.

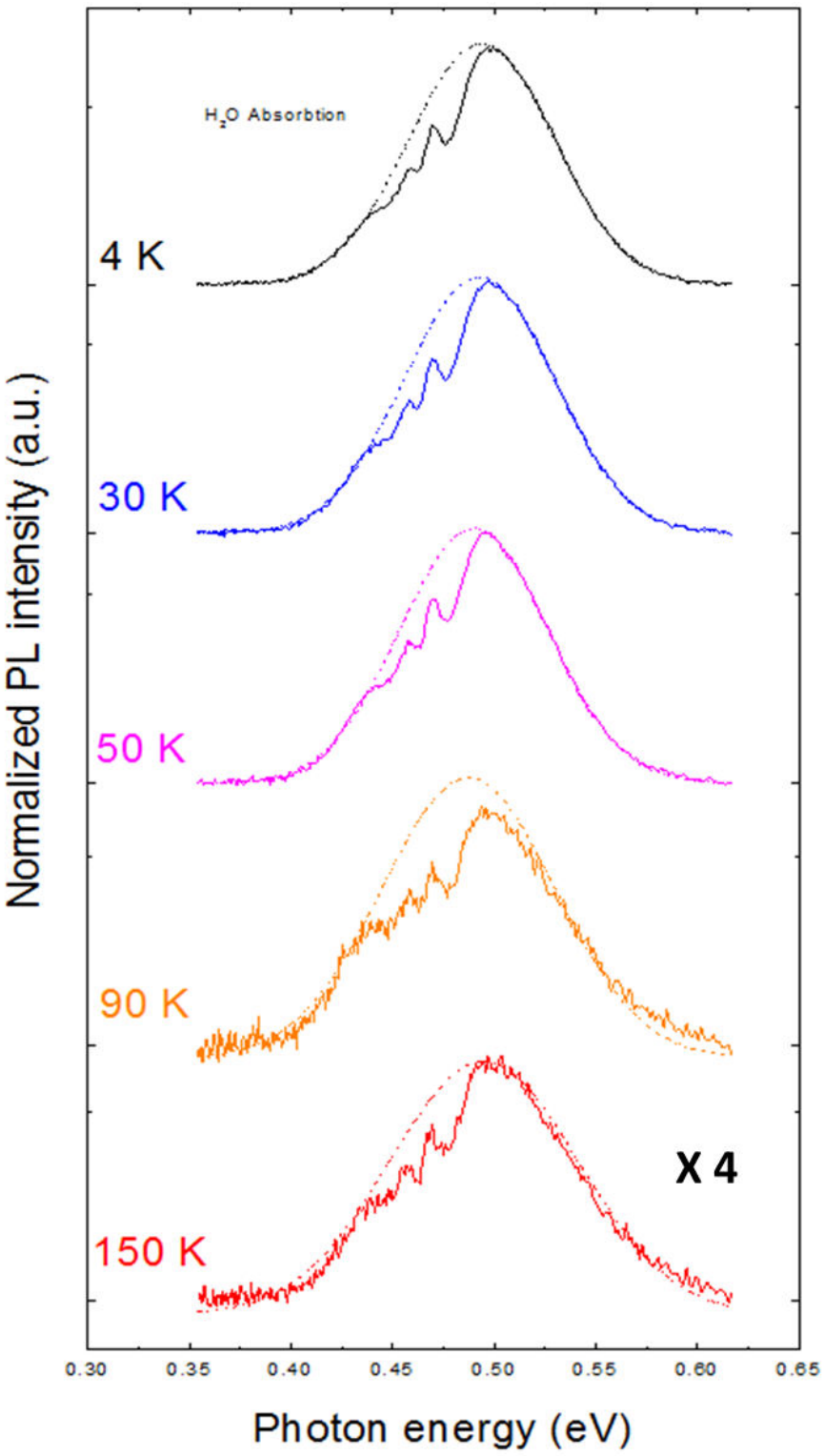

Figure 5.12. Temperature dependence of the PL emission from InAs NWs. Emission spectra measured over the range 4-150 K. (Above 150 K the emission intensities fell below our measurement noise floor).

5.7. PL temperature dependence

PL spectra obtained at different temperatures for QA612 are shown in Figure 5.12. The wires exhibit strong PL emission at 4 K before quenching at 150 K. This indicates that radiative recombination occurs near the surface regions, where InAs NWs are known to be accumulated due to Fermi level pinning resulting in a low efficiency for radiative emission[25], which is in a good agreement with reported results for InAs NWs. The PL spectra are inhomogeneously broadened as mentioned before resulting in broad PL emission maybe as a result of the length variations in the NWs.

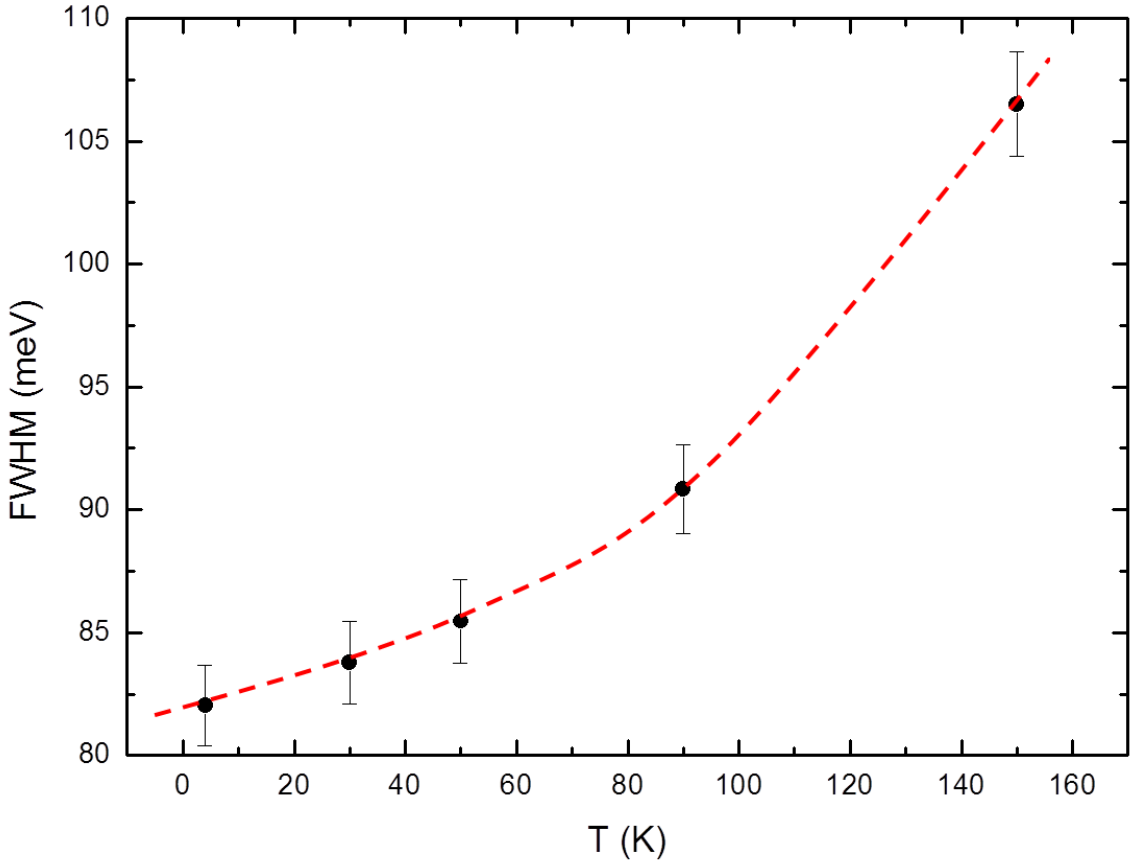

Figure 5.13. The FWHM of the PL peaks from InAs NWs as a function the temperature dependence measured over the range 4-150 K.

The FWHM as a function of temperature is shown in Figure 5.13 for the InAs NWs. The FWHM was significantly increased with increasing the temperature in the range 4 to150 K from around 80 meV to 105 meV respectively. Figure 5.14 shows the temperature quenching behaviour of InAs NWs. The figure shows no PL emission detected from InAs NWs above 150 K. This quenching is a result of the non-radiative surface states which can affect the band edge emission, hence reducing luminescence efficiency. The temperature dependence of the peak energies (including a correction of $K_BT/2$) for the NWs is further shown in Figure 5.15. The dotted lines represent fitting of the results using the empirical Varshni equation. The values obtained for the fitting parameters E_g (0) (the bandgap at absolute zero), α (gives indication of temperature sensitivity) and β is (related to the Debye temperature) are given in table 2 along with reference values for bulk InAs and InSb.

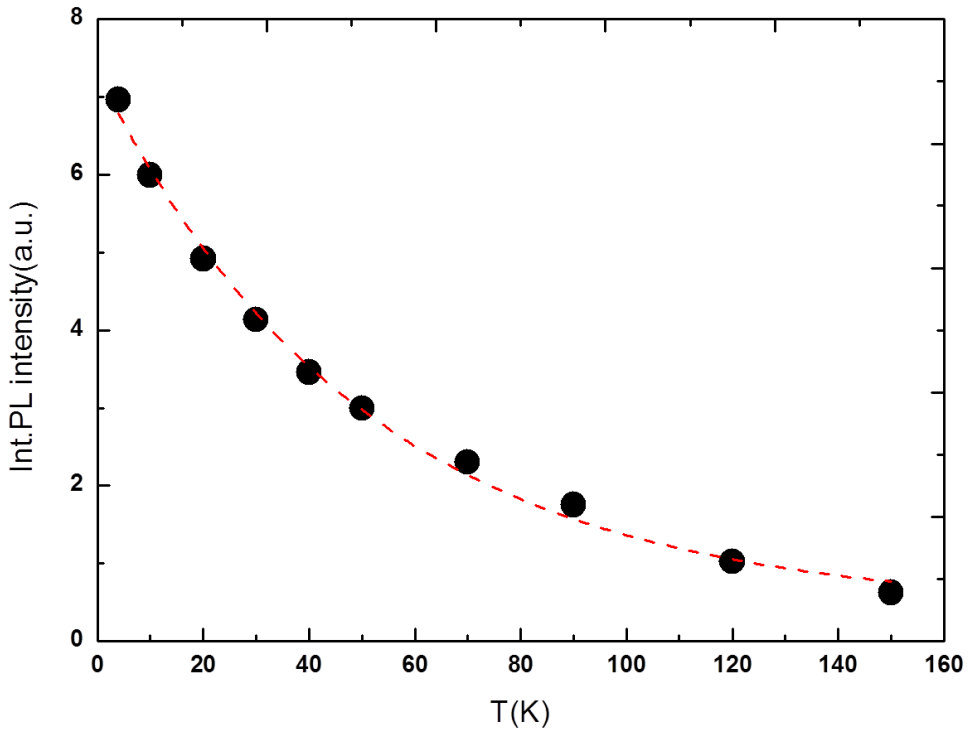

Figure 5.14. Temperature dependent analysis of PL data from the InAs NWs showing the PL intergradient intensity as a function of the temperature in the rang (4-150K).

The InAs NWs have a WZ crystal structure and consequently have a weaker dependence of bandgap on temperature (lower value of α) than the corresponding bulk ZB materials.

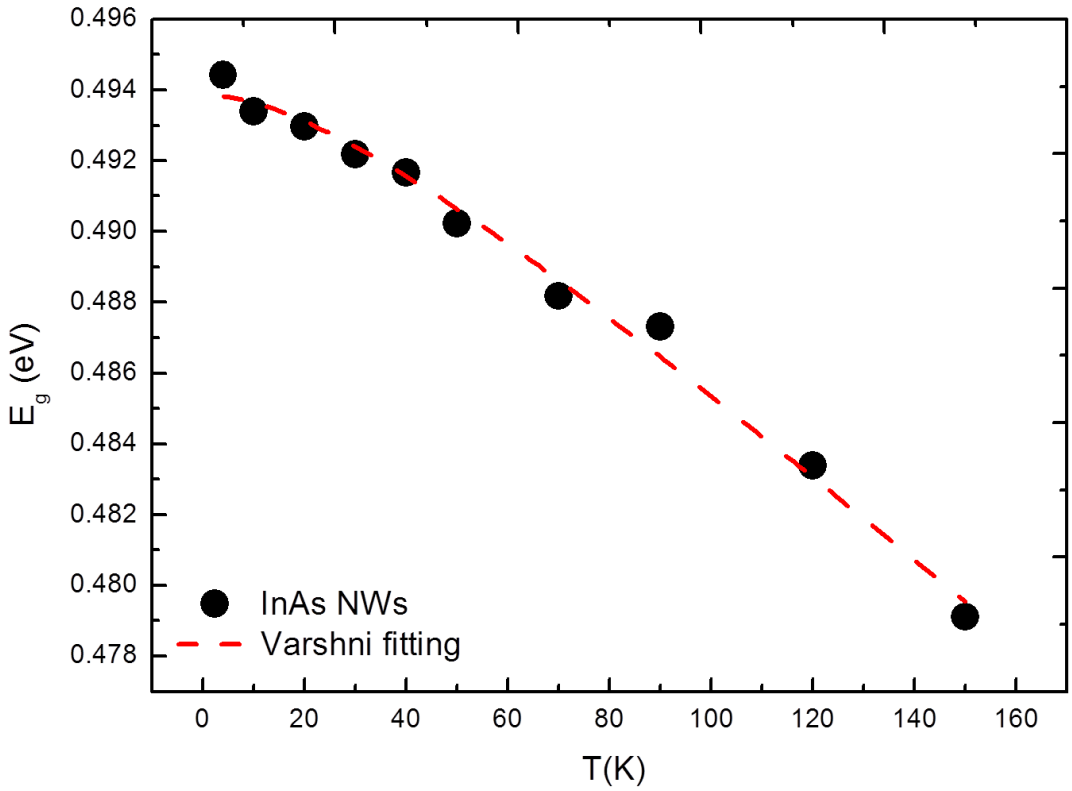

Figure 5.15. Temperature dependent analysis of PL data from the InAs NWs, The temperature dependence of the PL peak emissions (points), used to fit the Varshni relationships (solid lines) and extract the associated coefficients, for the NW sample.

To determine the dominant quenching process, the integrated intensity of photoluminescence emission was plotted against 1/kT where k is the Boltzmann constant and T is the temperature. The activation energy can be determined using the Arrhenius equation (2.18) mentioned in chapter 2, the Arrhenius fitting function is shown in Figure 5.16. The Arrhenius plot for NW gives an activation energy of 27 meV from the high temperature region and ~2.2 meV for the low temperature region, which would suggest it to be a defect related process. These values are very similar to those reported by G. Koblmuller[2] with E_a= 24.6 meV and E_b= 6.2 meV for the high and low temperatures respectively. These values are very similar to

the bulk reference, E_a=27 meV and E_b=6.2 meV for the high and low temperatures respectively[2]. The similar thermal activation energies suggest that the luminescence quenching mechanisms for InAs NWs is very similar to the ZB bulk[2].

	E_0 (eV)	α (meV/K)	β (K)
InAs NWs	0.494	0.126	47
InAs bulk	0.417	0.276	93
InSb bulk	0.235	0.320	170

Table 2**:** Table showing the extracted Varshni fitting parameters E_0, α and β from Varshni fits for InAs NWs (QA612), compared with published parameters for bulk InAs and InSb[26].

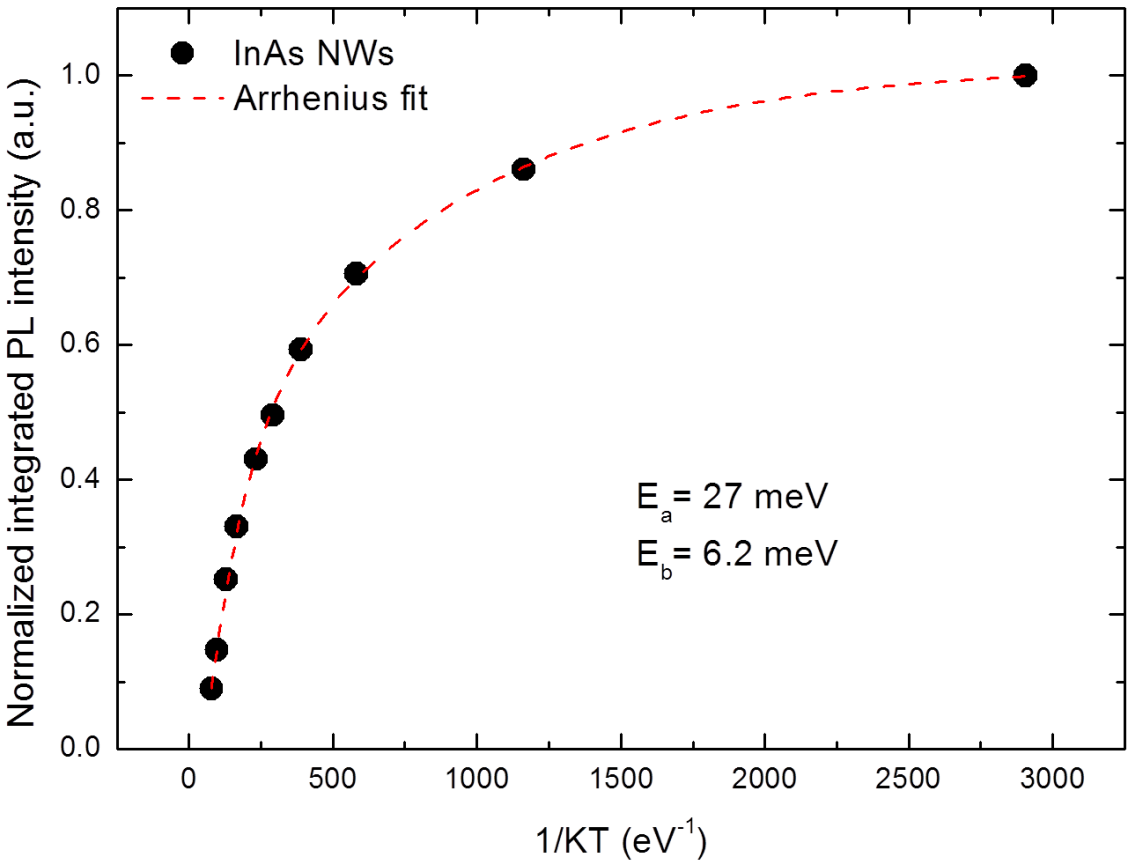

Figure 5.16. An Arrhenius plot of integrated PL intensity as a function of inverse temperature for the InAs NWs, used to extract activation energies for the mechanisms driving thermal quenching.

5.8. InAsSb NWs: MBE growth

A series of nanowire samples were grown on boron-doped (111) orientated Si substrates by MBE growth techniques, using the dense pattern which is called pattern II (see experimental details chapter 4). For this study, the holes are around 50 nm in diameter before the etching and patterned into a 300 nm pitch square array. The same growth conditions mentioned in the previous section for the InAs NWs were kept constant for all the samples used in this work. Similar to the InAs NWs the in situ RHEED were not used to characterize the NWs during the growth. The substrate was initially heated to 600 °C without any group V flux before being cooled down to the desire growth temperature in the range between (494-501 ºC) to grow the InAsSb NWs. The optimal conditions are found to be with fluxes at 0.08 ML/s 1.59 ML/s for In, As respectively and Sb at 0.36 ML/s which gives a V−III ratio of 42:1. The As growth rate was measured for two-dimensional equivalent growth rate on GaAs (001) surface as mentioned in the previous section. Finally, the growth was terminated by closing the Sb and In fluxes followed by the As flux after a few minutes once the wafer had been cooled to a temperature where the surface was stable. All samples were grown with the same Sb composition and started with InAs stems followed by the InAsSb layer. The optimal growth conditions at T_S= 494 °C and 20 minutes growth of InAs stems followed by 1 hour of InAsSb NWs is expected to grow NWs containing an initial 400 nm InAs layer followed by 800 nm of InAsSb NWs, giving in total an average length of 1300 nm. The nucleation of the wires formed similarly to the InAs NWs when the adatoms diffuse on the surface until they get trapped in the holes within the oxide layer. The planar bulk InAs sample grown on an InAs substrate was also used as a comparison reference in this work. Further growth attempts were investigated for more understanding, for example, sample (QA392) was grown with an InAsSb stem instead of InAs, and (QA613) was grown with high Sb composition in order to

extend the wavelength emission. The effect of the diffusion growth rate and the direct incorporation of the impinging species on the growth with the effect of adding the Sb will be explained later in the text. Table 3 summarized the InAsSb NW samples used in this work with growth temperature, the wire length and PL peak energies.

Figure 5.17 (a) and (b) show scanning electron microscope (SEM) images of InAsSb nanowires grown with this pattern that are on average about 1.3 μm in length and 80 nm in diameter and the area fraction occupied by the nanowires is approximately 10%.

Sample no.	Pattern	Seed	Tg	Wire length	InAsSb PL peak energy (eV)
QA399	1	InAs	494	1300 nm	0.380
QA392	1	InAsSb	494		0.375
QA393	1	InAs	480	500 nm	0.394
QA397	1	InAs	465	400 nm	0.381
QA613	2	InAs	494		0.320
QA587	2	InAs	509	86 nm	No PL emission
QA601	2	InAs	487	600 nm	No PL emission
QA602	2	InAs	501	100 nm	No PL emission

Table 3: summary of the grown InAsSb NWs samples, at different growth temperatures at the range of (465- 509 ºC). All the samples have Sb composition of X= 6%, except the sample QA613 with Sb composition of x~ 15 %.

From SEM analysis of various samples, we have found that, in cases where a nanowire fails to grow, nearby wires have a greater length variation (circular outline in Figure 5.17 (a)) and are typically longer because of proximity effects. This is due to the small pitch of the patterned array being less than twice the diffusion length of indium adatoms on SiO_2, which is estimated to be ~750 nm[27]. As a result, each nanowire is within the capture area of nearby wires. When a hole is not fully etched and no nanowire grows at that location, the indium adatoms diffuse to neighbouring nanowires leading to an increase in their growth rate. In regions of more successful growth the wire length is more uniform as seen in the square outline in Figure 5.17 (a). For uniform length distribution in dense arrays, it is therefore crucial that all holes are cleanly etched. For device applications, it is important that the nanowire is grown directly onto the substrate to provide electrical contact and avoid any series resistance due to the presence of an oxide layer between the nanowire and the substrate.

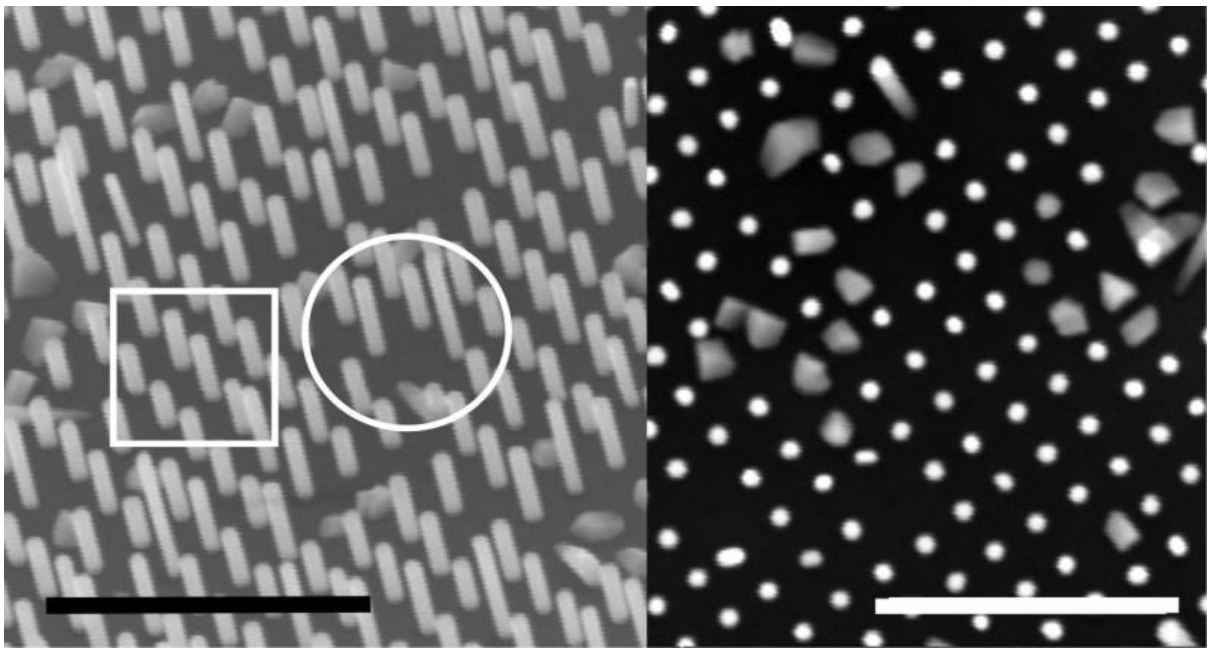

Figure 5.17. (a) SEM image with 30° tilt of InAsSb nanowires grown in the holes in the oxide layer. The square and circular outlines indicate regions of uniform and nonuniform growth. Scale bar: 2 μm. (b) Top view SEM image of patterned InAsSb nanowires with highly uniform nanowire diameter. Scale bar: 2 μm.

5.9. Structural analysis

Low and high magnification ADF-STEM analysis have been performed on InAsSb nanowire grown on silicon substrate. Figure 5.18 (a) shows a low magnification ADF-STEM image of an InAsSb NWs with 80 nm diameter and consist of InAs stems and InAsSb layer. Figure 5.18 (b) shows a high magnification ADF-STEM image of the interface between the InAs nanowire and the Si substrate which indicates that the nanowire has grown directly on the substrate. Furthermore, the InAs has the characteristic mix of WZ and ZB phases[28], the polytype phase seen in InAs NWs can lead to unwanted uncontrollable heterostructures due to the different bandgaps of the ZB and WZ phases.

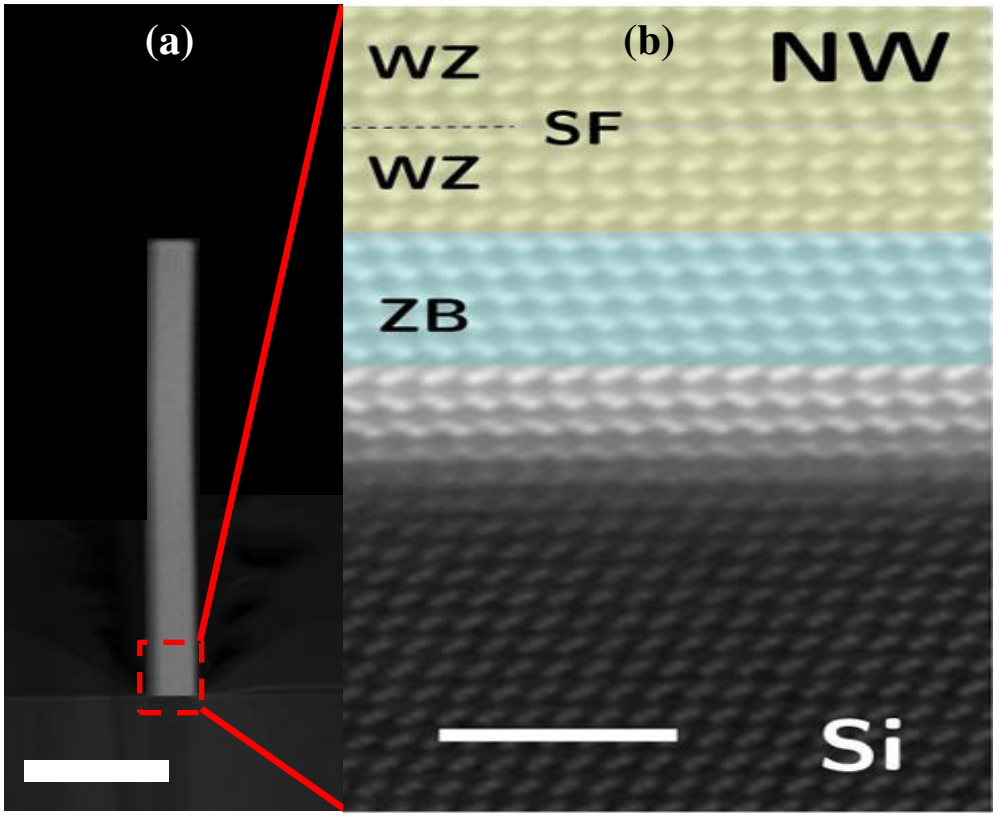

Figure 5.18. Structural characterization of InAsSb nanowires. (a) Low magnification ADF-STEM image of InAsSb nanowire. Scale bar: 500 nm. (b) High magnification ADF-STEM image corresponding to the InAs nanowire/Si interface shows that the nanowires have grown directly onto the substrate. The InAs section shows a mix of WZ (with stacking fault (SF) indicated by the dashed line) and ZB regions. Scale bar: 2 nm.

Figure 5.19 (b) shows the same low magnification ADF-STEM image of an InAsSb NWs with high magnification ADF-STEM images of the InAsSb NWs at different areas within the NW, Figure 5.19 (a) shows an area in the top of the wire and Figure 5.19 (c) shows an area in the middle of the wire. The InAsSb NW shows a characteristic of ZB, as expected for InAsSb with 6 % Sb. The addition of Sb forces a ZB phase with ortho twins which do not change the polarity of the crystal along the nanowire. The NWs are formed mainly by twinned ZB segments with stacking faults highlighted in brown in the figure. The multi twinned ZB areas were observed in different areas of the nanowire even far away from the interface with the silicon substrate, also the top area contains fewer stacking faults compared to the area in the middle of the wire. The twinning is mainly on {111} planes parallel to the surface growth. Compositional analysis (see Figure 5.20) along the length of an InAsSb nanowire revealed that the base of the wire contains a 20 nm section of polytype InAs suggesting that the incorporation of Sb is suppressed during the early formation of the nanowire. The reason for this is not yet understood.

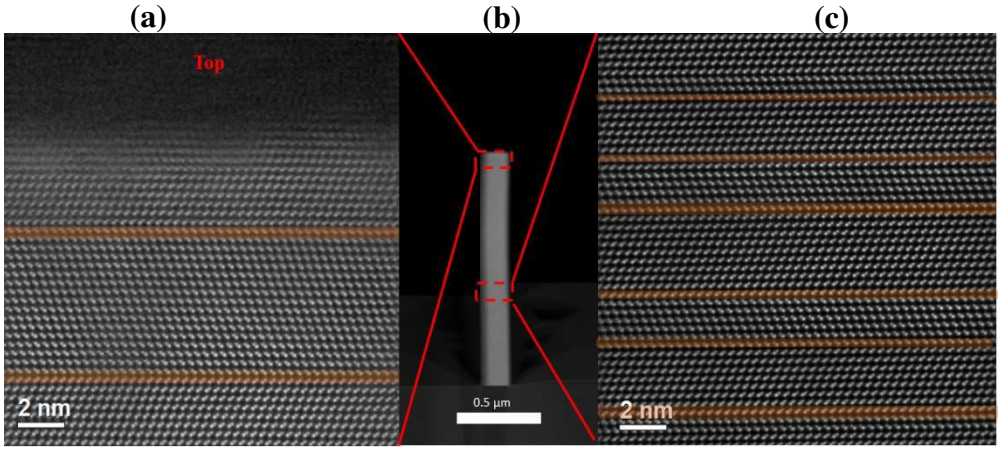

Figure 5.19. Structural characterization of InAsSb nanowires. (b) Low magnification ADF-STEM image of InAsSb nanowire. Scale bar: 500 nm. (a) The top of the nanowire is flat and shows the multi twinned ZB structure of the InAsSb. Scale bar: 2 nm. (c) High magnification ADF-STEM image corresponding to the area in the middle of the NW shows that the nanowires are formed mainly by twinned ZB segments with stacking fault (SF) indicated by brown highlighted lines. The twinning is mainly on {111} planes parallel to the surface growth. Scale bar: 2 nm.

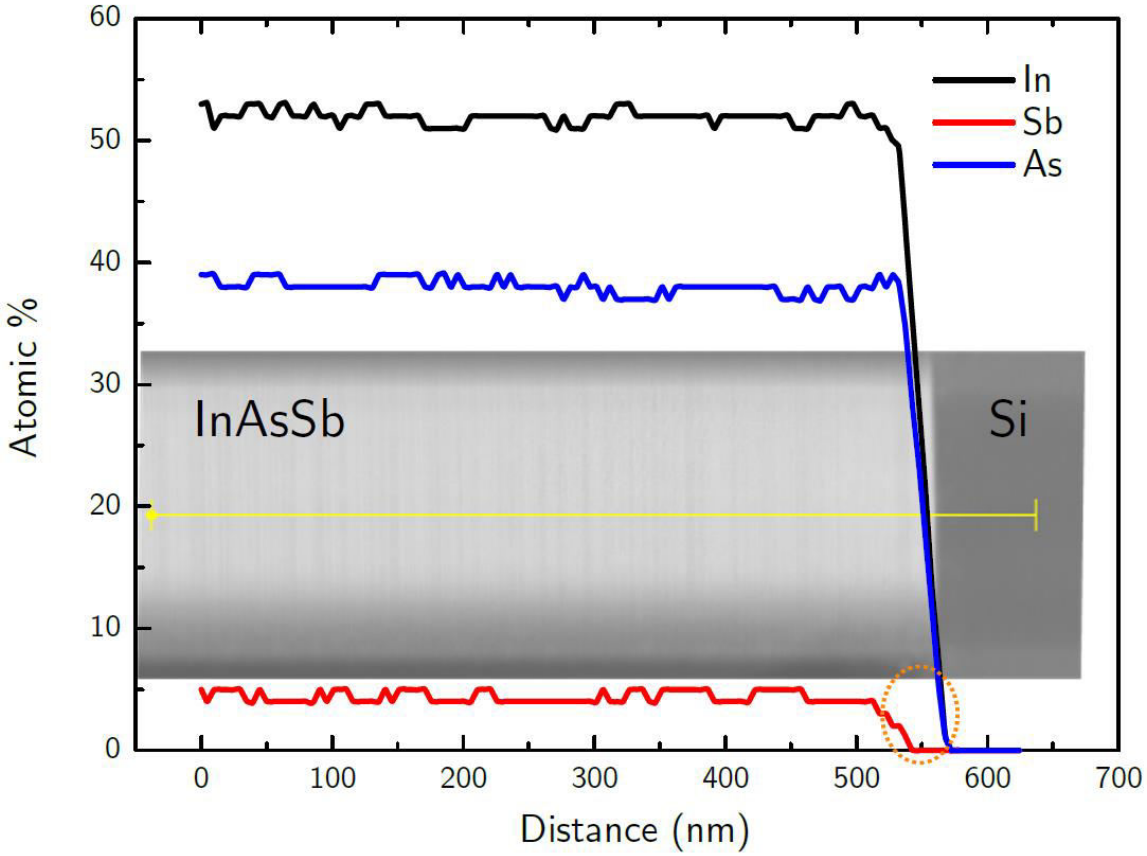

Figure 5.20. Compositional (STEM) analysis along the length of an InAsSb nanowire, showing that the Sb is not incorporated in the first few nanometres of the wire.

5.10. X-Ray Diffraction of InAsSb NWs

A Bede QC200 XRD double crystal rocking system was used to determine the composition of the InAs1−xSbx nanowires by performing a 2θ−ω scan of the (111) reflection of the as-grown sample (see Figure 5.21). The peak position corresponds to an Sb composition of x = 0.07 which is calculated using the position of the InAsSb peak relative to the substrate peak and is in good agreement with the results from photoluminescence. To ensure that the XRD peak originates from nanowires and not surface growth, several scans with different θ offsets were performed showing only a slight decrease in intensity (see inset of Figure 5.21). Due to the small diameter of the nanowires, their diffraction peaks have a larger in-plane broadening

compared to surface growth for which only a small θ offset is sufficient to decrease the intensity considerably.

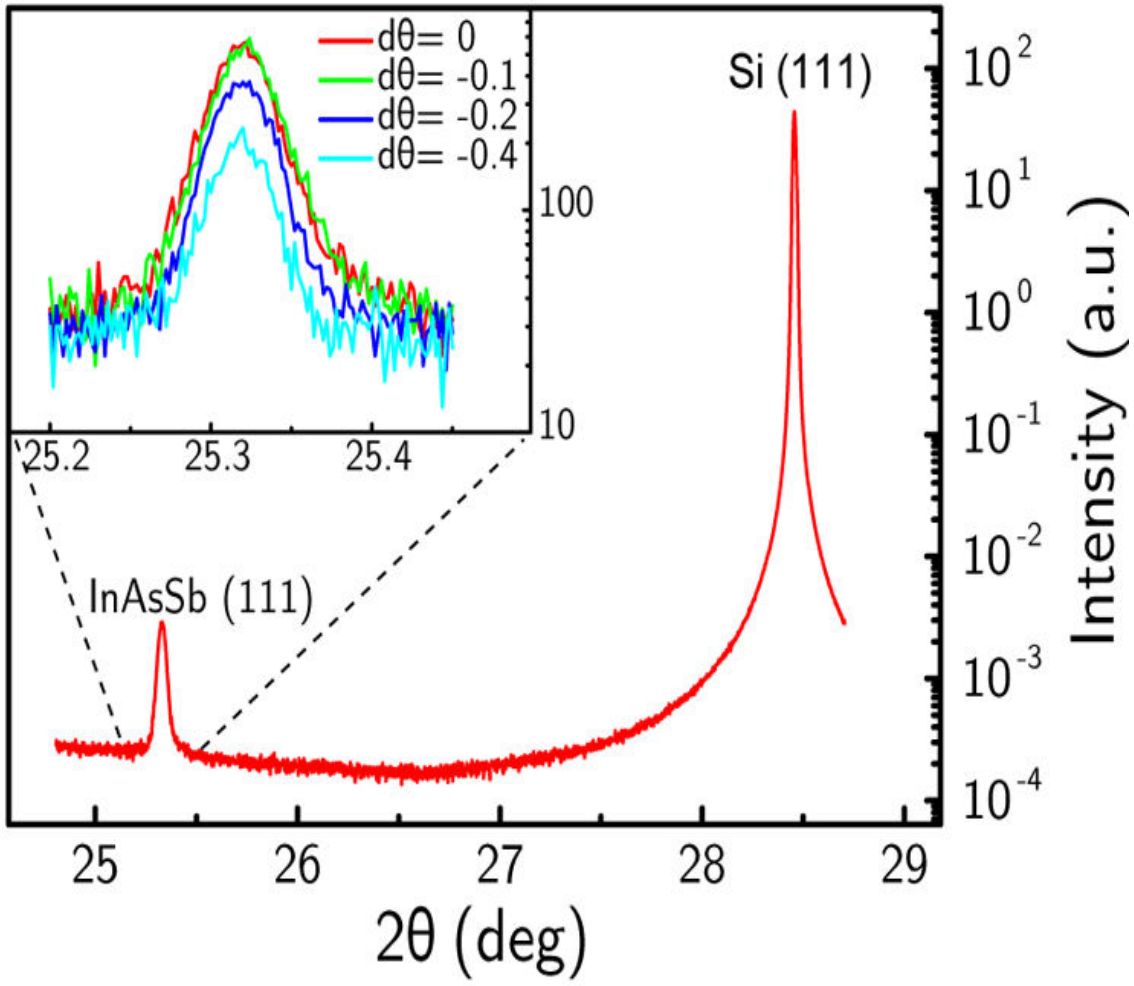

Figure 5.21. XRD rocking curve of $InAs_{0.93}Sb_{0.07}$ nanowires on (111) Si substrate. Inset: The InAsSb peak for different θ offsets which shows only a slight decrease in intensity indicating that the peak originates from the nanowires and not from planar material.

5.11. The effect of the growth temperature on the PL intensity

Figure 5.22 presents the 4K PL spectra for InAsSb NWs grown at different growth temperatures in the same range used in the previous section. All the NWs investigated here are grown with InAs stems followed by InAsSb except one sample grown at the optimal growth temperature (QA392). In general, the PL spectra should consist of two main peaks,

InAs and InAsSb. At the lower growth temperature, there are clearly two peaks for the InAs at 0.410 eV and the InAsSb at 0.385 eV, increasing the growth temperature to 540 ^{o}C improved the PL intensity. The FWHM was increased in this sample due to random fluctuations in the composition[6]. Most notably, the InAs gives brighter PL with respect to the InAsSb. This may suggest that the Sb is not fully incorporated at lower growth temperature. With increasing the growth temperature to 494 ºC, the NWs exhibited strong InAsSb and InAs PL peaks at 0.380 eV and 0.421 eV respectively. The FWHM was found to be relatively narrower at this growth temperature, as the wires exhibited better uniformity in length and diameter. A single peak is observed at 0.382 eV for sample QA392 without any emission from the InAs. Although this sample was grown at a higher growth temperature, the PL intensity is comparable to the lower growth temperature. This may indicate that the InAs stems improved the subsequent growth. Figure 5.23 shows the PL intensity as a function of the growth temperature, were the InAsSb PL intensity increased gradually to the maximum intensity.

5.12. The effect of the growth temperature on the average NW length

Growth temperature has a marked effect on nanowire properties. Figure 5.24 illustrates the morphological changes that take place with different growth temperatures. At lower temperature, namely T_g = 465 ºC and T_g = 480 ºC, the NWs are short and have wide bases (400 nm and 500 nm respectively) see SEM images in Figure 5.25 and Figure 5.26. This can be related to an increase of radial growth rate, with few clusters and deposition between the wires.

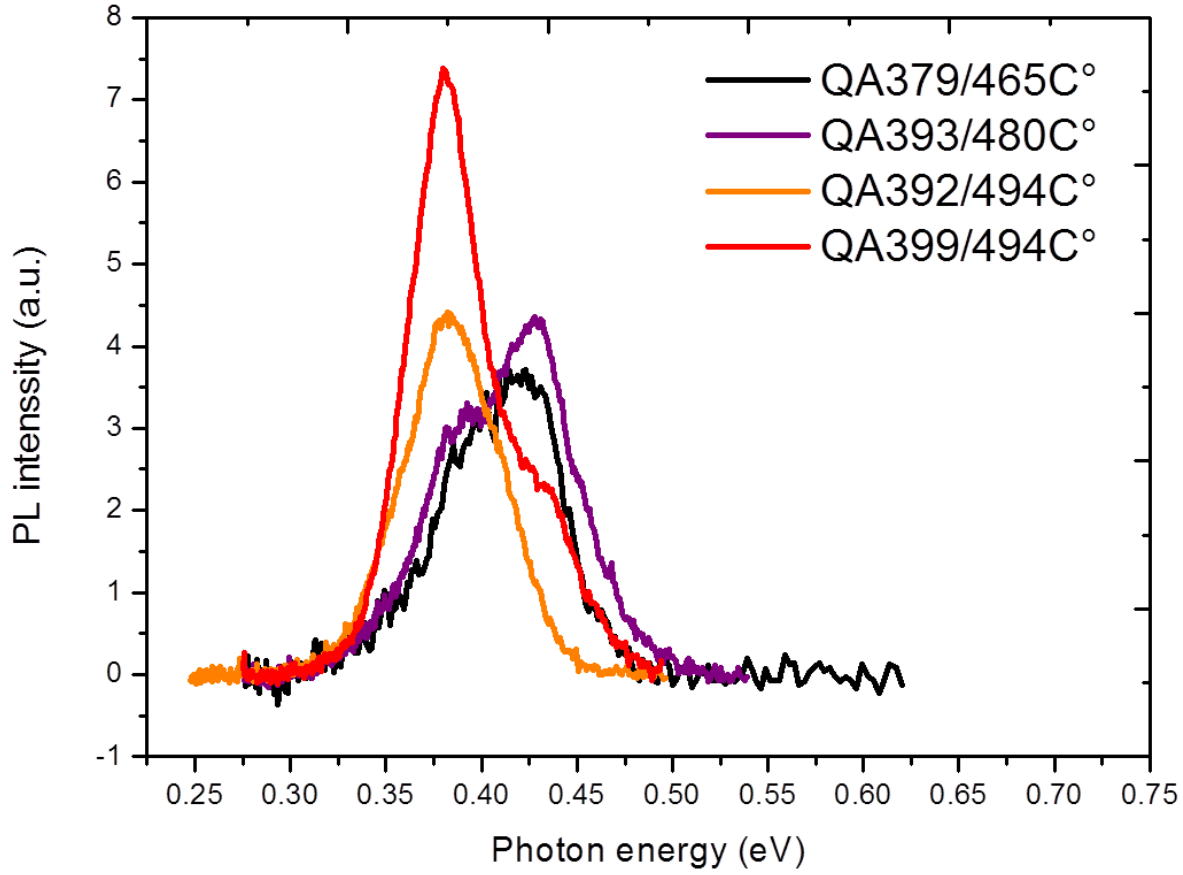

Figure 5.22. PL spectra at 4 K for InAsSb NWs. (a) PL emission for different NW growth temperatures in the range (465, 480 and 494 ºC).

This can be explained by the surface migration length of In adatoms on SiO_x/Si (111) which is rather low resulting in higher sticking coefficient and extensive cluster formation. Increasing the temperature to T_g = 478 ºC, the NWs are taller with 600 nm length, and have lots of clusters between the grown wires see SEM images in Figure 5.27. This occurs because, as the substrate temperature is increased, the rate of Sb_2 precursor decomposition increases and the adatom diffusion length increases. Another possibility is that the roughness of the substrate surface and the lower temperature causes the adatoms to diffuse along the surface surrounding the NWs. Hence, the incorporation of adatoms at the top facet of the NWs will be negligible for the wires especially at the first stage of the growth.

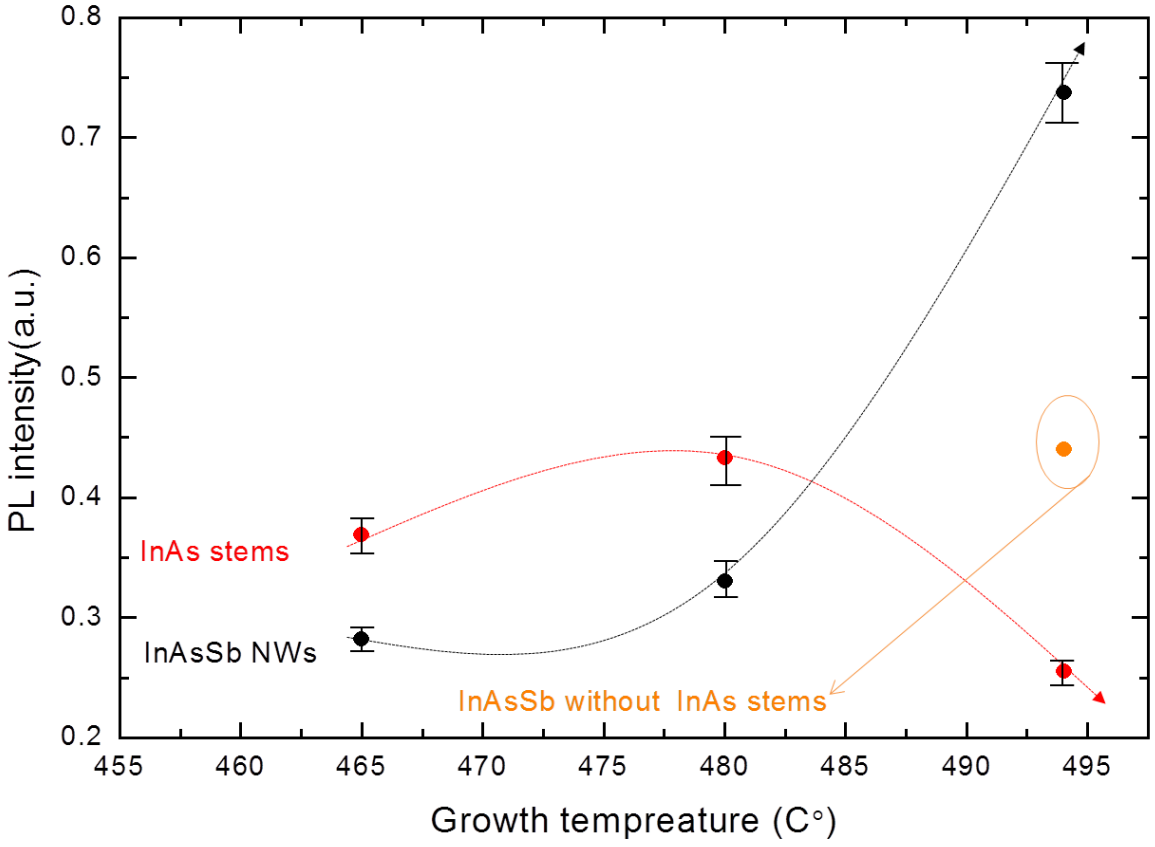

Figure 5.23. The PL intensity as a function of the growth temperature showing that the InAsSb NWs increased to the maximum at the optimal growth temperature while the InAs stems intensity reduced compared to the InAsSb NWs.

In this case, it is expected that the length will be reduced when the temperature is not high enough. As temperature is further increased to T_g = 494 ºC (see SEM images in Figure 5.28), the wire length increases to a maximum of 1300 nm, with the formation of a few clusters on the substrate, and with proximity effects as explained before leading to an increase in the growth rate. At this growth temperature, more Sb adatoms are available for both axial and radial growth, while longer surface migration lengths can be maintained. Furthermore, the probability of Sb incorporation into the NW was also enhanced, which results in longer NWs. Consequently, at the highest growth temperatures T_g = 501 and 509 ºC (the SEM images in Figure 5.29 and in Figure 5.30), the nanowires are short ~100 nm and 86 nm in length

respectively. At these temperatures, there are no clusters formed on the oxide layer. However, droplets were formed in the holes instead of wires, as observed for the InAs NWs, hence the desorption of As and In is enhanced with increasing temperature. Thus, 494 ^{o}C is concluded to be the optimal growth temperature for well controlled uniformity and successful selective growth of InAsSb NW arrays.

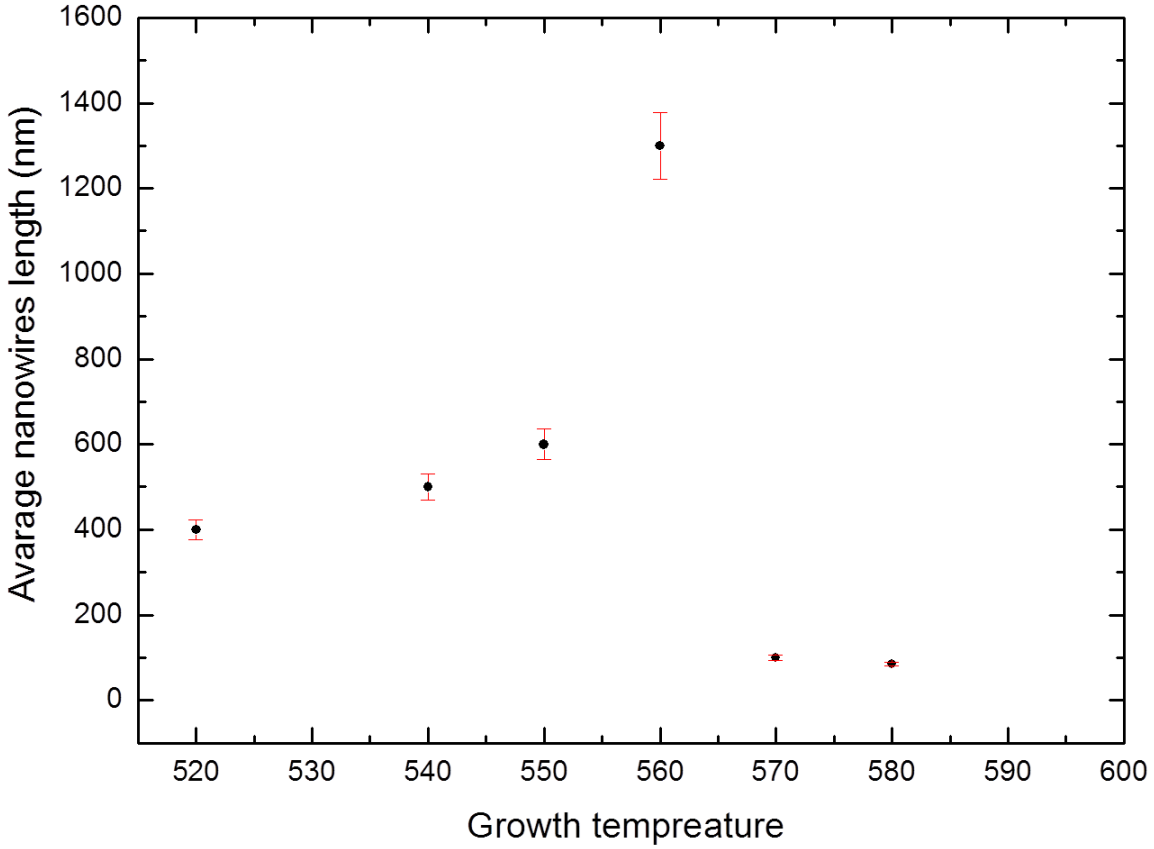

Figure 5.24. Structural analysis for the InAsSb NWs samples. (a) Showing the average wire length as a function of the growth temperature.

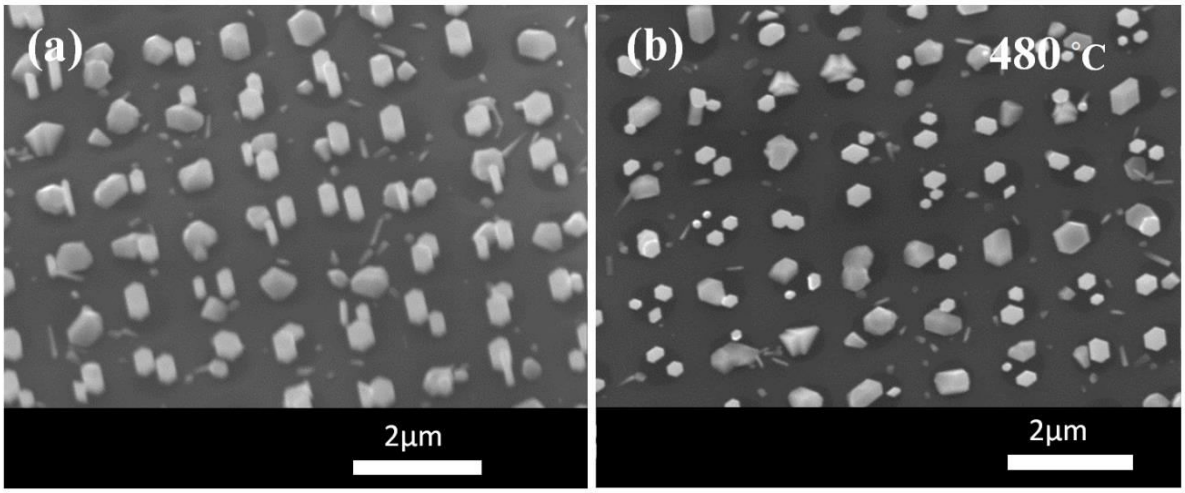

Figure 5.25. Structural analysis for the InAsSb NWs samples. InAsSb NWs at growth temperature of 465 °C with 400 nm wire length, (a) 30° tilted SEM images, (b) top view SEM images.

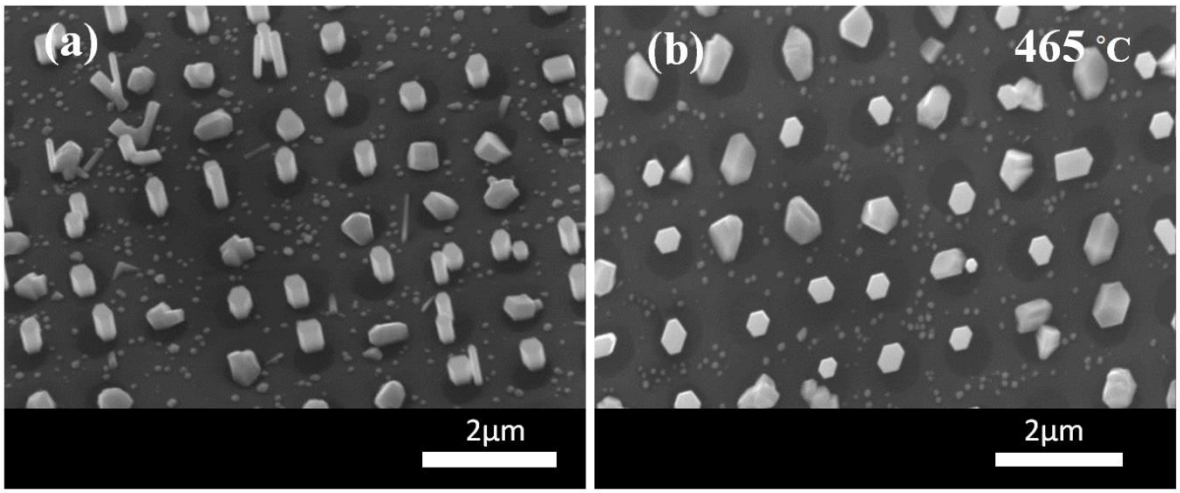

Figure 5.26. Structural analysis for the InAsSb NWs samples. InAsSb NWs at growth temperature of 480 °C with 500 nm wire length, (a) 30° tilted SEM images, (b) top view SEM images.

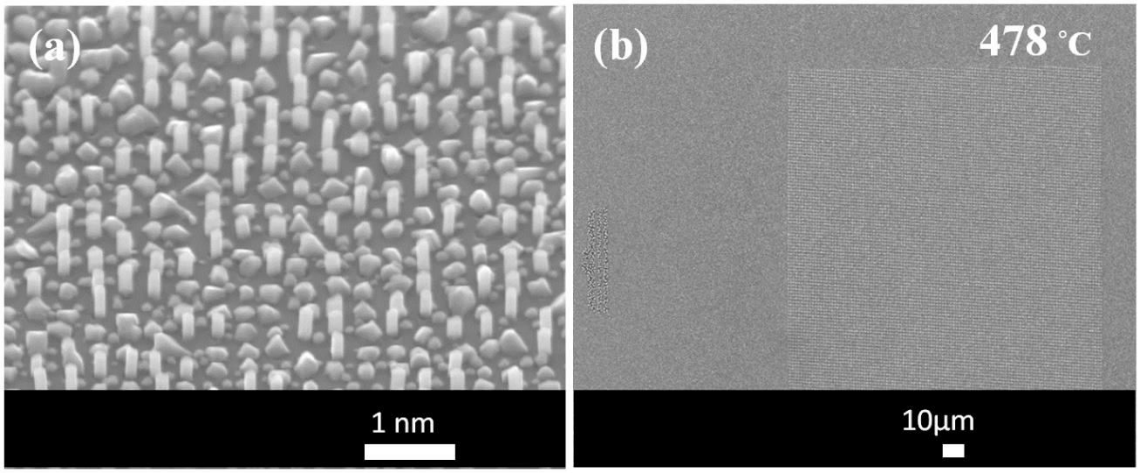

Figure 5.27. Structural analysis for the InAsSb NWs samples. InAsSb NWs at growth temperature of 478 °C with 600 nm wire length, (a) 30° tilted SEM images, (b) top view SEM images.

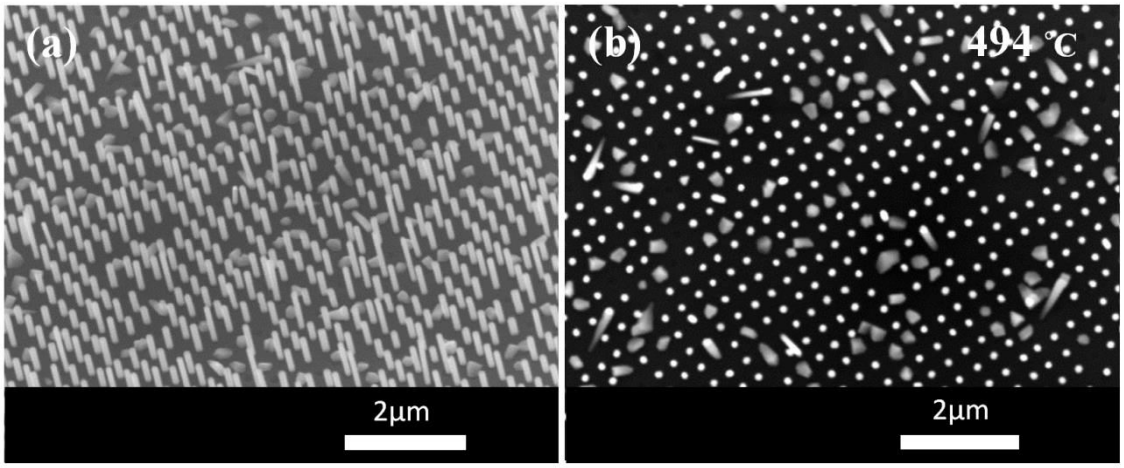

Figure 5.28. Structural analysis for the InAsSb NWs samples. InAsSb NWs at growth temperature of 494 °C with 1300 nm wire length, (a) 30° tilted SEM images, (b) top view SEM images.

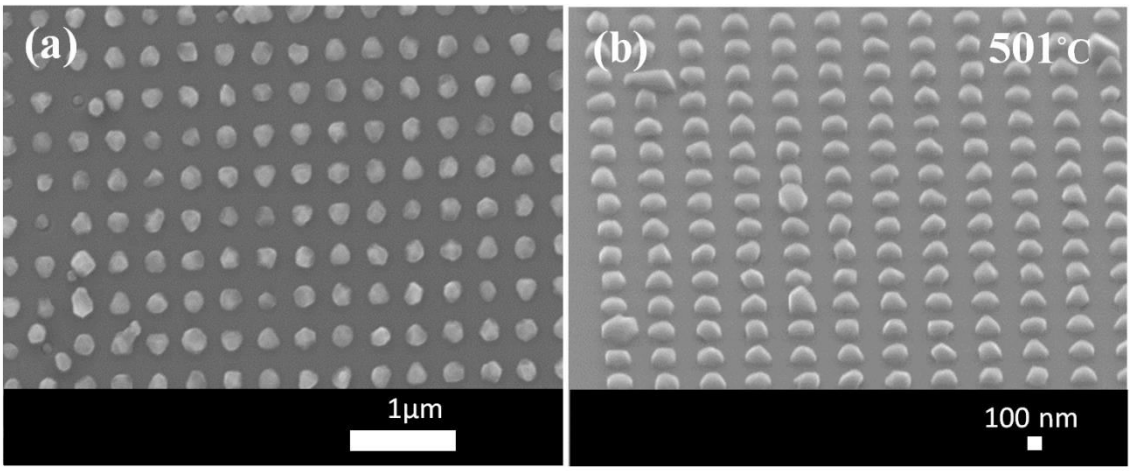

Figure 5.29. Structural analysis for the InAsSb NWs samples. InAsSb NWs at growth temperature of 501 °C with 100 nm wire length, (a) 30° tilted SEM images, (b) top view SEM images.

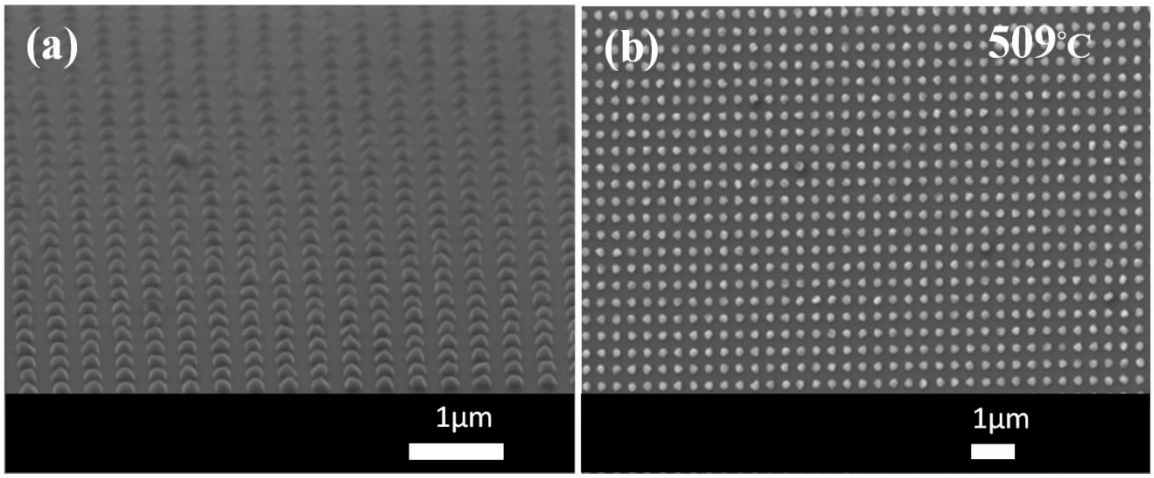

Figure 5.30. Structural analysis for the InAsSb NWs samples. InAsSb NWs at growth temperature of 509 °C with 86 nm wire length, (a) 30° tilted SEM images, (b) top view SEM images.

5.13. The effect of the Sb flux on the InAsSb nanowires

Two NW samples (QA399 and QA613) were grown under the same growth conditions with varying the Sb content. The Sb fractional flux was increased from 0.36 to 1.15 at growth temperature of 480 ^{o}C. From XRD we know that the sample (QA399) with 0.36 Sb flux corresponds to 6-7% Sb incorporated into the wires. The Sb content incorporated into the

wires with Sb flux around 1.15 is estimated to be around 10%. However, with increasing the Sb, NWs become much shorter around 500 nm (see SEM images in Figure 5.31 (a) and (b)).

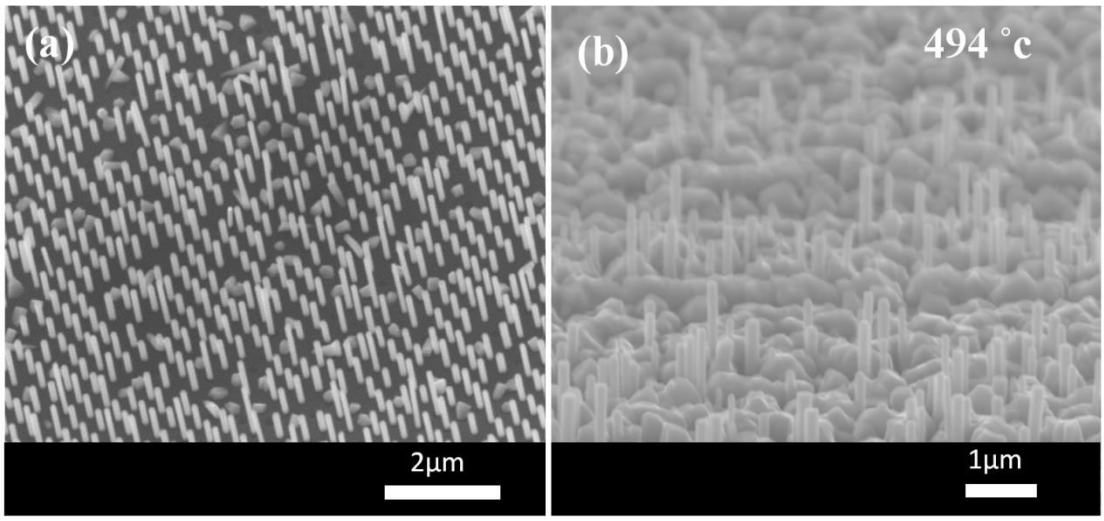

Figure 5.31. (a) SEM images for the sample QA399 correspond to 6%, (b) and SEM images for the sample QA613 corresponding to ~15% Sb.

Additionally, clusters start to develop which may result in formation of a thin 2-D InAsSb layer growth on the substrate. Sourribes et al reported that, at Sb fractional flux above 1.3, the antimony incorporation starts to saturate at around 8%. Thus, due to this saturation growing NWs at this growth temperature will not be successful. However, a 15% or even higher incorporation can be achieved by decreasing the growth temperature to 450°C. In contrast, antimony atoms diffuse more slowly at 450°C than at 480°C which will increase the formation of clusters even more on the surface. Our results are in good agreement with the results reported by Sourribes et al. PL measurements reveal the effect of the Sb fractional flux on NW optical properties. Figure 5.32 shows 4K PL spectra at 1.2×10^4 Wcm^{-2} excitation power. Two samples are plotted corresponding to 6% and ~15% Sb compositional. The PL peaks are fitted with two Gaussian peaks for the InAsSb NWs and the InAs stems. The peak energy for the lower fractional flux was found to be centred at 0.380 eV, while for the higher

Sb fractional flux the peaks red shifts by 60 meV to be centred at 0.327 eV. The peak position for the sample QA613 is in good agreement with the results reported by Ferall et al[6] for ~15% Sb incorporated into the wires.

The PL emission intensity is reduced for the sample with higher Sb content, maybe because of fewer wires are grown on the sample, and when the wires are not formed perfectly in the holes, clusters grow on the surface instead. However, theses clusters do not contribute to the PL emission and are associated with poor material quality which cannot give PL emission. Another reason could be the poor signal due to misalignment of the μ-PL setup. The InAs peak is present in the spectra for both samples at 0.420 eV.

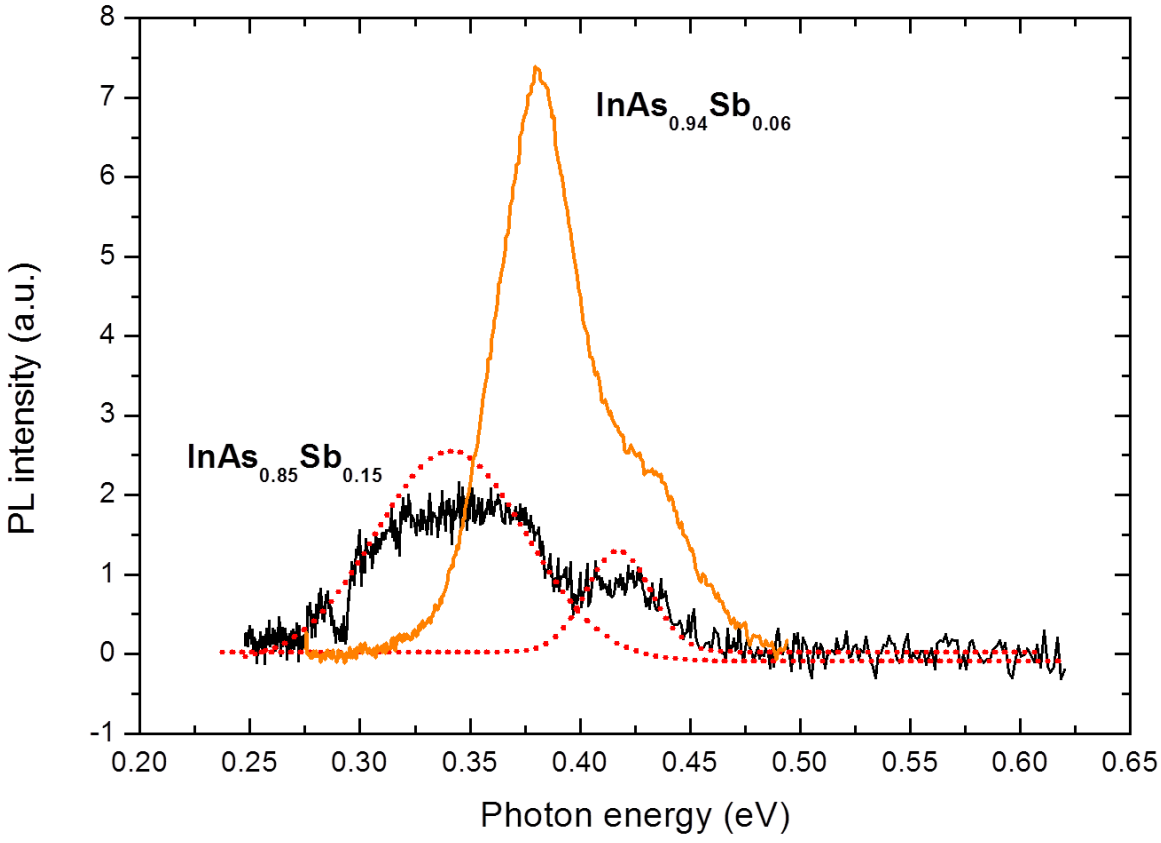

Figure 5.32. 4K PL spectra for InAsSb NWs at two different Sb compositions, high and low Sb composition with PL peaks at 0.320 eV and 0.380 eV respectively.

5.14. 4K PL analysis for QA399

For PL measurements, undoped nanowires were used to perform the experiment. Figure 5.33 shows a comparison between the PL peak for the bulk reference sample and InAsSb NWs. The InAsSb bulk used in this comparison was grown onto a GaSb with 6~7% Sb. The overall PL peak consists of emission from both the InAs and InAsSb sections at ~0.421 and 0.380 eV, respectively. The emission from the InAs is blue-shifted from the expected wavelength by around 5 meV which is consistent with confinement in an 80 nm 1-D quantum wire. Assuming similar confinement for the bulk InAsSb NW the fraction of antimony incorporated was calculated to be 6 -7 %, these results are in good agreement with the XRD measurements. The InAsSb NWs exhibited a FWHM of 45 meV at $1.2x10^4$ Wcm^{-2}. These wires are 13meV broader than the InAsSb bulk and 18 meV boarder than the InAs bulk with FWHM= 32 and 27 meV for the InAsSb and InAs bulk respectively. Ferrell et al reported that the NWs FWHM is 10 meV broader than planar InAsSb on InAs reference due to random fluctuation in composition.

5.15. PL power dependence

Excitation power intensity measurements performed on sample QA399 at 4K are shown in Figure 5.34. The main peak energy blue shifted from 0.380 eV under low excitation $1.2x10^4$ Wcm^{-2} to 0.390 eV under high excitation $2.6x10^4$ Wcm^{-2}. The intensity was found to increase linearly with increasing laser power. Also, a blue shift of 10 meV is observed with increasing laser power, which is similar to that obtained by others and is associated with band filling, as shown clearly in Figure 5.35.

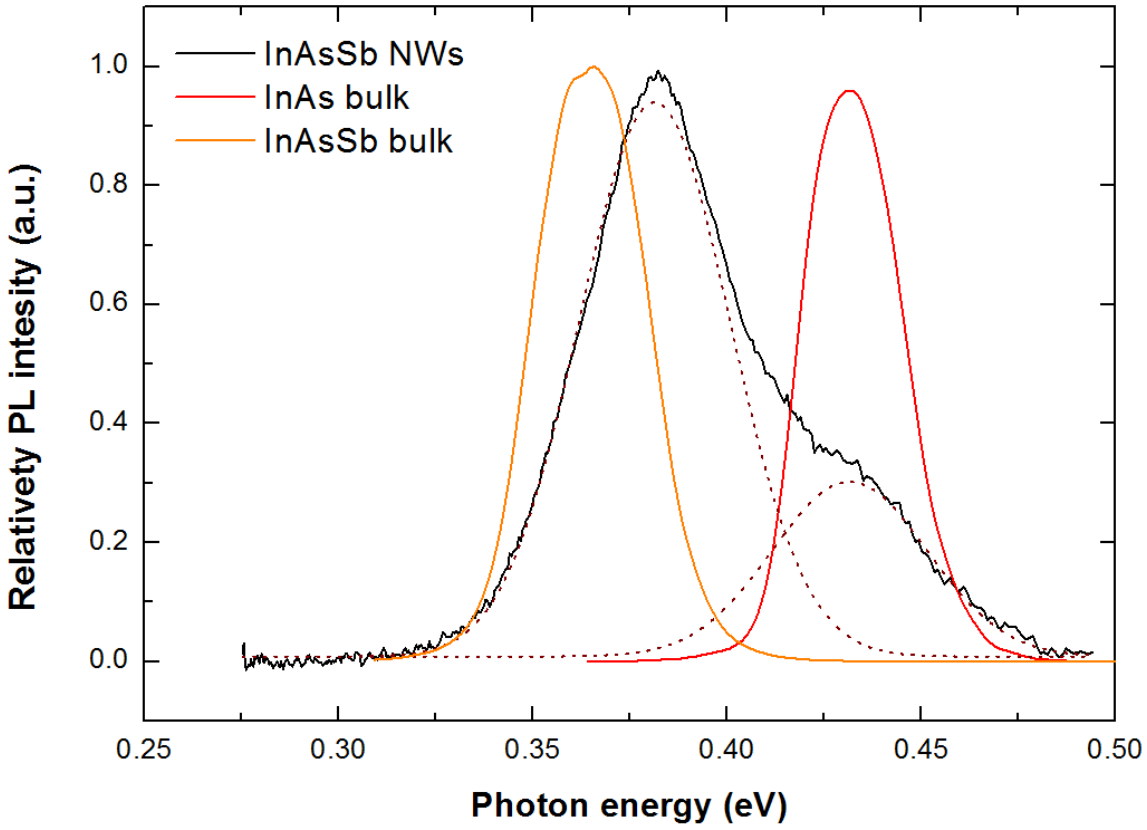

Figure 5.33. Micro-PL spectra obtained at 4 K. comparison of the PL emission spectra measured from InAsSb NWs, InAsSb bulk and InAs bulk at ($1.2x10^4$ Wcm^{-2}). The dotted lines represent Gaussian fits to theInAsSb NWs.

In order to determine the type of recombination, the k values were calculated from plotting the integrated intensity and the laser power, as shown in Figure 5.36. The InAsSb peak had a k value of 0.56 which corresponds to free- and bound exciton transitions. The K value suggests that maybe more impurity-like recombination processes (surface states recombination) are involved in InAsSb NWs compared to the InAs only NWs. Although it has been reported that adding the Sb supressed the twins and stacking faults density in the wires[29], the PL emission only marginally improved[6] since the band-edge perturbations introduced by these defects do not strongly influence non-radiative recombination.

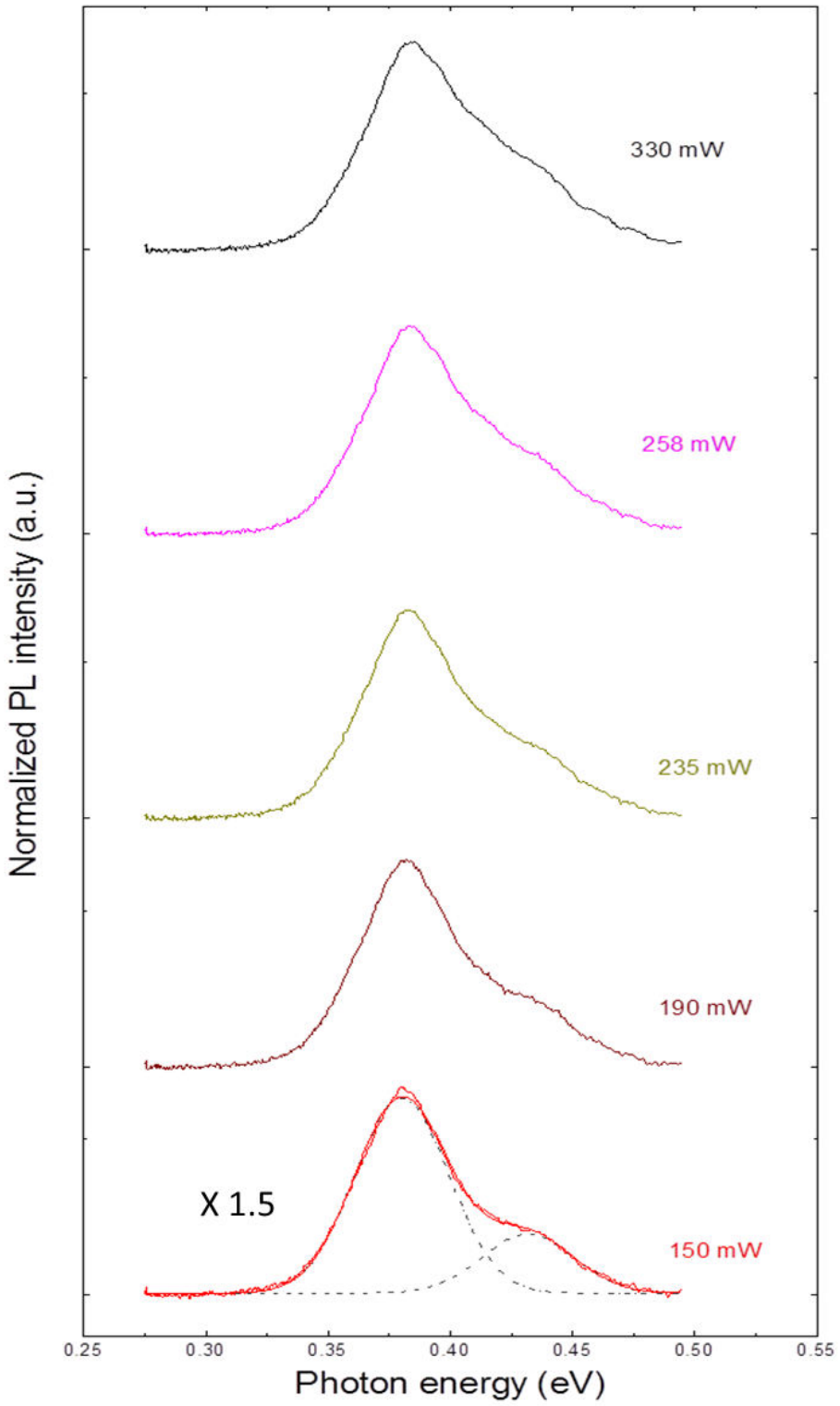

Figure 5.34. Excitation power dependence for the InAsSb NWs in the range of 1.2×10^4 Wcm^{-2} –2.6×10^4 Wcm^{-2}. The dotted lines represent Gaussian fits to the InAs stems and InAsSb NWs.

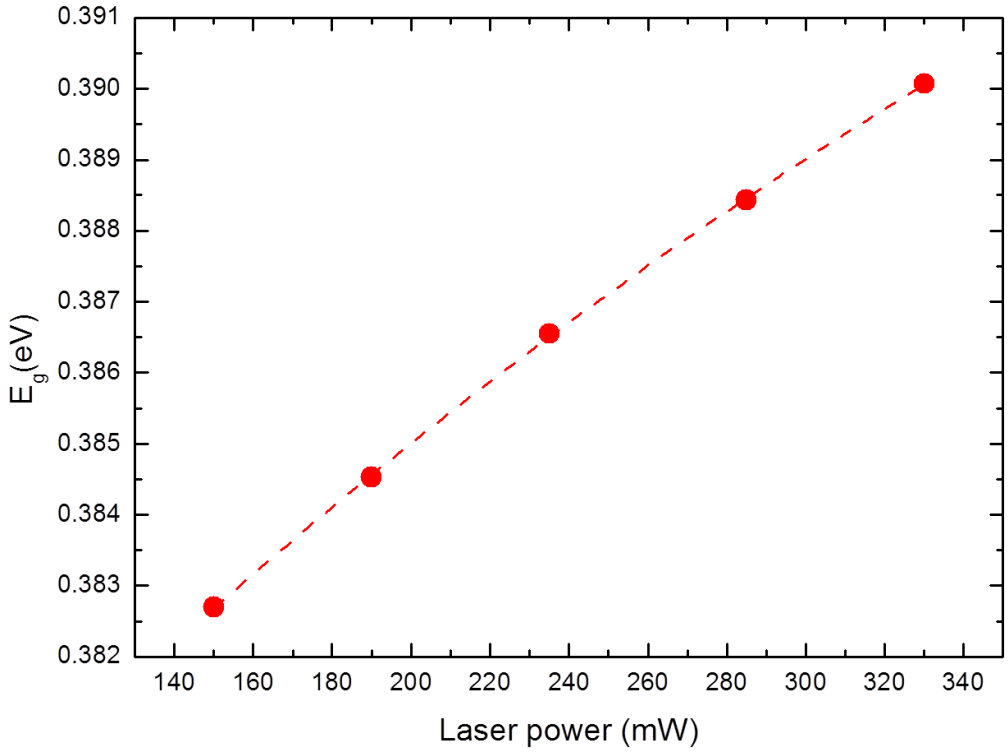

Figure 5.35. The energy gap as a function of the laser power with a 10meV shift for the InAsSb NWs in the range of ($1.2x10^4$ Wcm^{-2} – $2.6x10^4$ Wcm^{-2}).

5.16. PL temperature dependence

PL spectra obtained at different temperatures for sample QA399 are shown in Figure 5.37. The wires exhibit similar behaviour to the InAs NWs with a strong PL emission obtained at 4 K before quenching at 150 K. This indicates that radiative recombination occurs near to surface regions, in a similar manner to InAs NWs, the surface state recombination plays a role in the thermal quenching processes within the wires. Figure 5.38 shows a clear increase in the PL peak intensity of the InAs luminescence by three times at 4K compared to the InAsSb NWs. This maybe demonstrates that the nonradiative Auger recombination and the surface state recombination increased in InAsSb which results in reduction of the PL peak intensity.

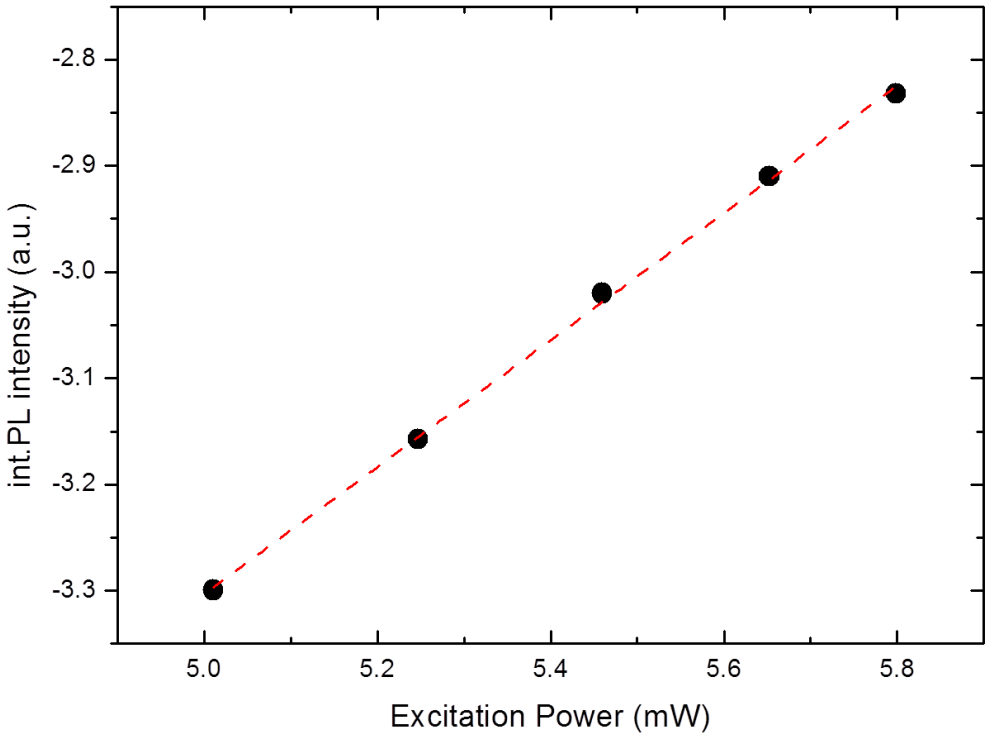

Figure 5.36. The integrated PL intensity as a function of the excitation power for the InAsSb NWs. The extracted K value = 0.56.

The evolution of the PL peak energy as a function of temperature is further shown in Figure 5.39, where E_g is corrected by $k_BT/2$. The dotted lines represent fitting of the results using the empirical Varshni equation. Notably, the InAsSb NWs have a weak dependence on the temperature with around 10 meV shift. Similar dependence has been observed for InAsSb NWs in the literature ~ 27 meV shift with increasing temperature[6].

Figure 5.40 shows the integrated PL intensities as a function of 1/kT (Arrhenius plot) for the InAsSb NWs and bulk reference in the measured temperature range (4 –150K). The Arrhenius dependency can be expressed by the relation (2.18) mentioned in chapter 2. Best fitting of data for the NWs gives thermal activation energies of E_a =34 meV for the high-T region and E_b =1.7 meV for the low-T region, respectively.

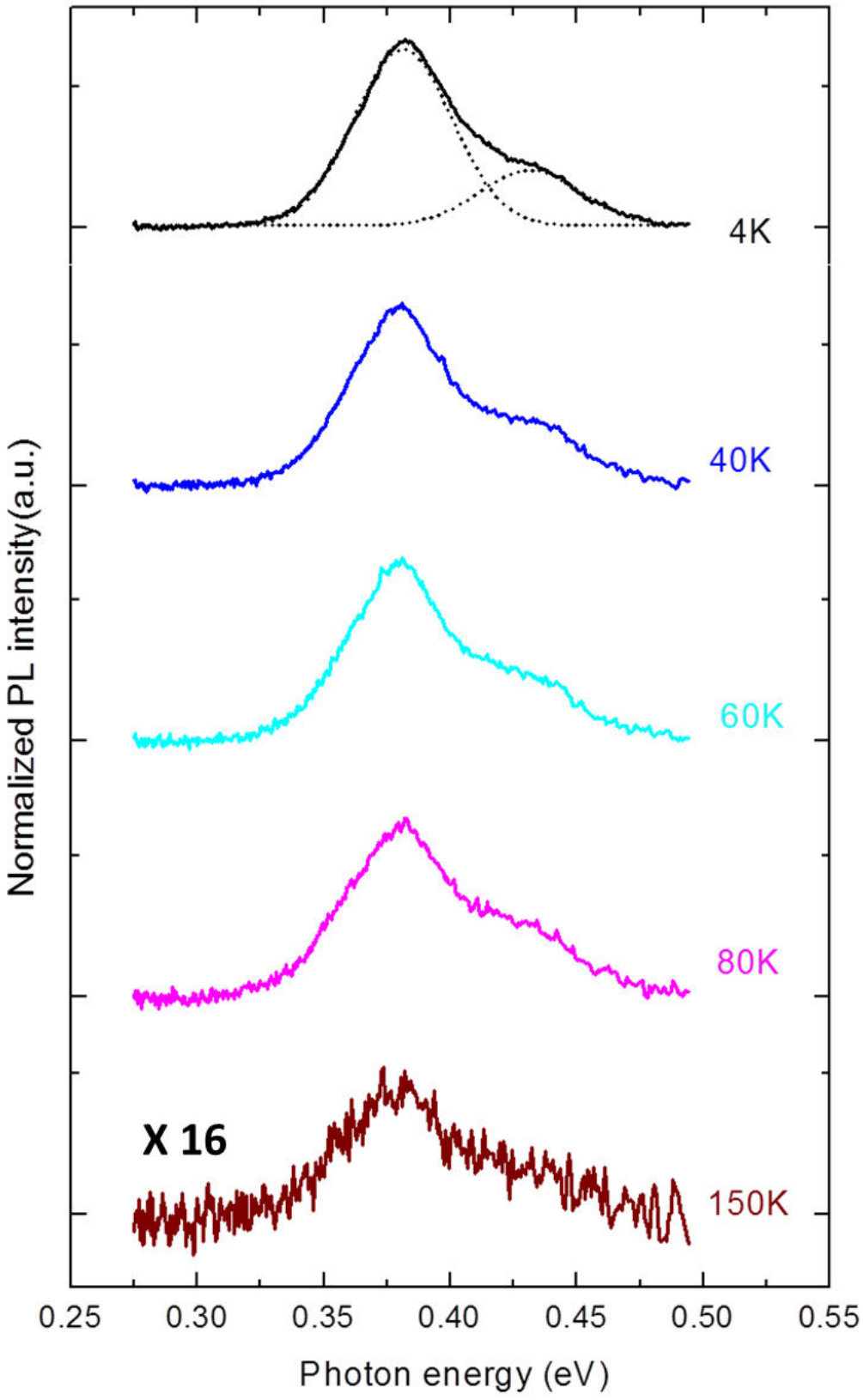

Figure 5.37. Temperature dependence of the PL emission from InAsSb NWs. Emission spectra measured over the range 4-150 K. Above 150 K the emission intensities fell below our measurement noise floor.

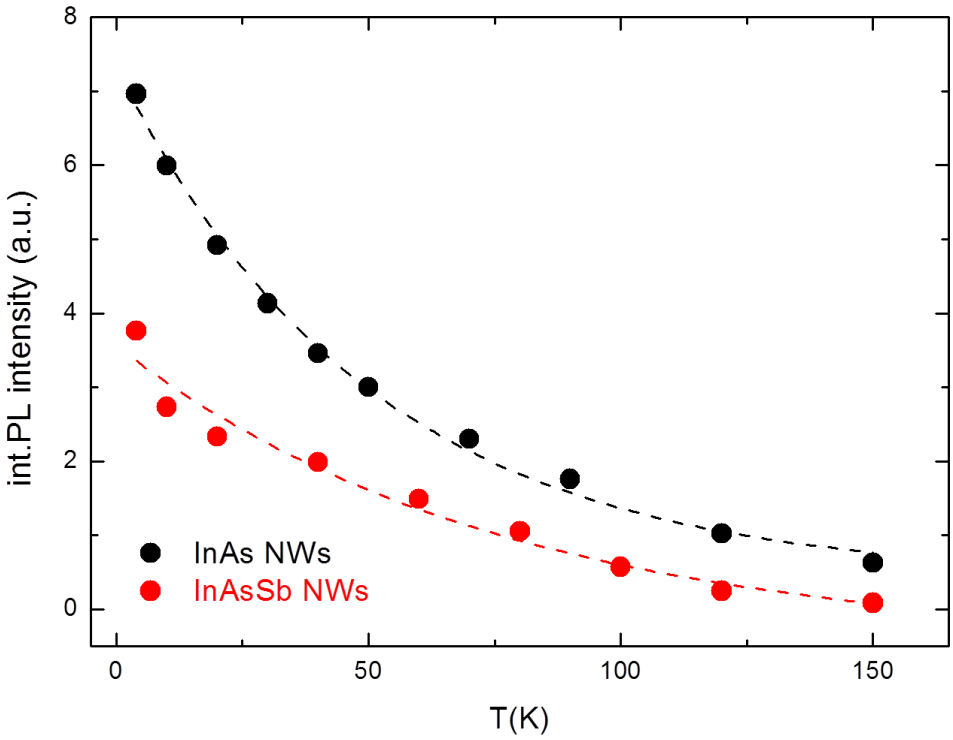

Figure 5.38. (a) the integrated PL intensity as a function of the temperature showing the PL emission up to 150 K, for InAs in black dots and InAsSb NWs in red dots.

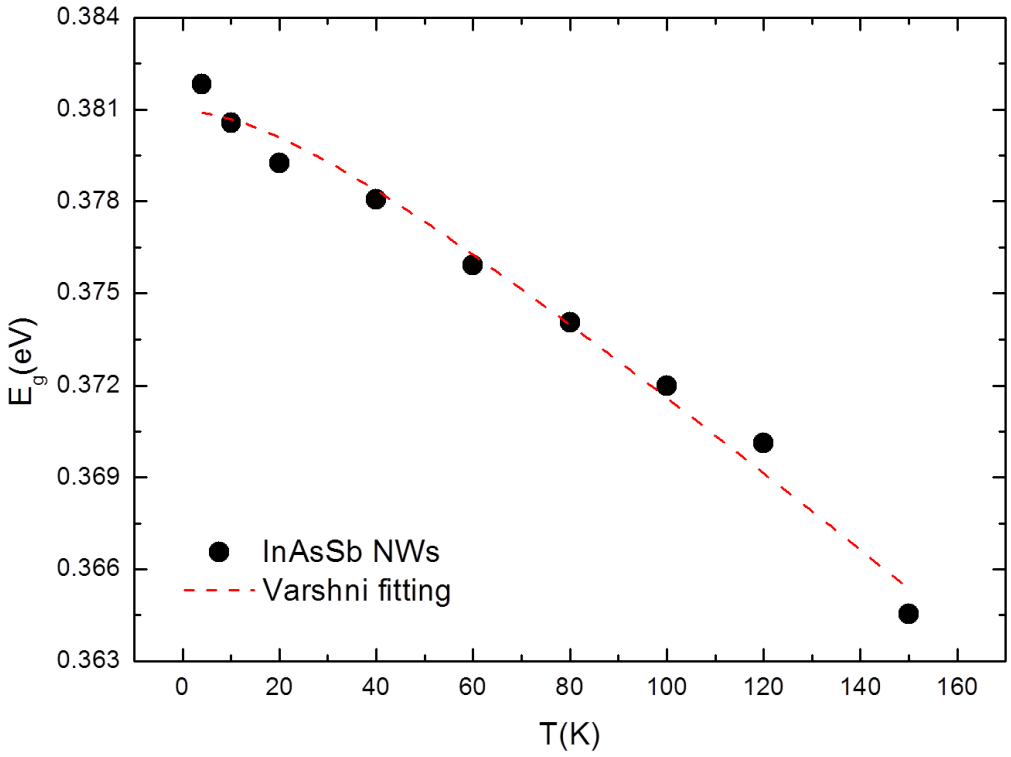

Figure 5.39. Varshni fitting of the transition energy of QA399 as a function of temperature, the temperature dependence of the PL peak emissions (points), used to fit the Varshni relationships (solid lines) and extract the associated coefficients, for the NW sample.

	E_0 (eV)	α (meV/K)	β (K)
InAs NWs	0.494	0.126	47
InAsSb NWs	0.380	0.133	42
InAs bulk	0.417	0.276	93
InSb bulk	0.235	0.320	170

Table 4: Table showing the extracted Varshni fitting parameters E_0, α and β from Varshni fits for InAsSb (QA399), compared with InAs NWs and published parameters for bulk InAs and InSb[19].

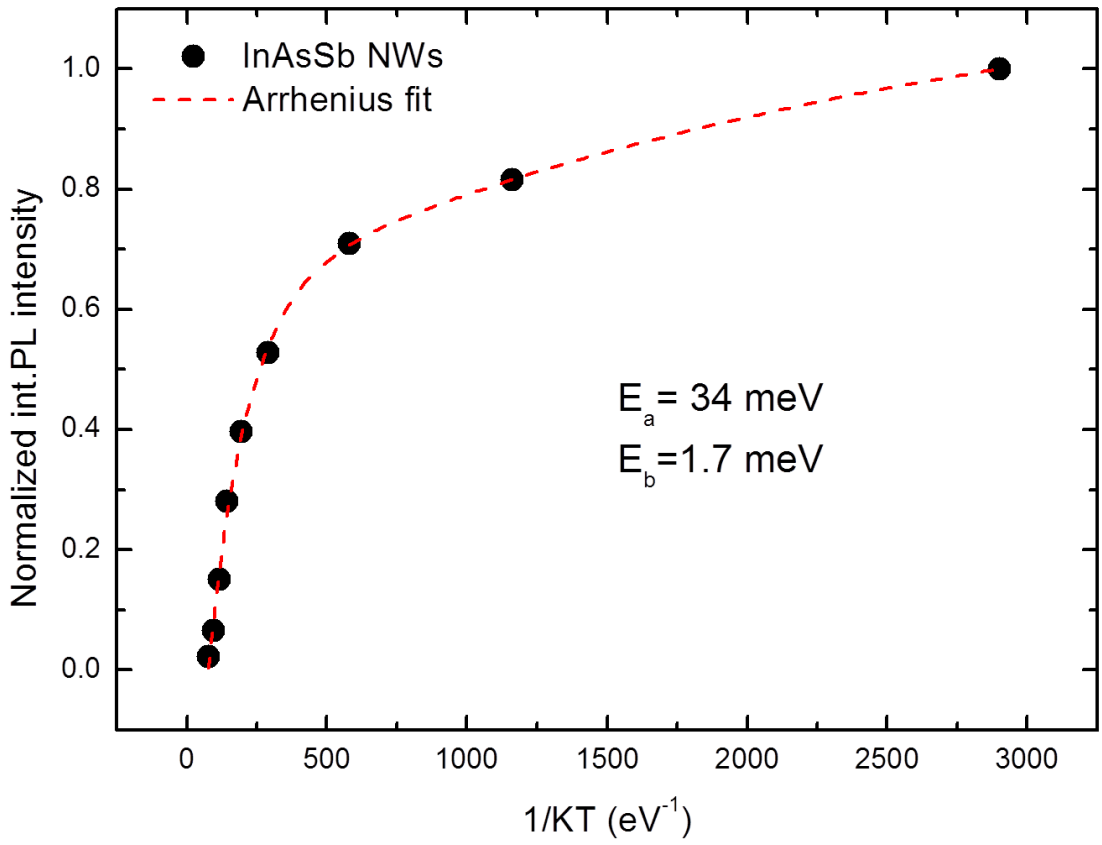

Figure 5.40. Arrhenius plot for QA399, plotting the normalized PL integrated intensity, giving activation energy of 34 meV from the high temperature region and ~1.7 meV for the low temperature region.

5.17. Conclusion

In this work, a catalyst-free formation of site-controlled InAs(Sb) NWs demonstrated by SA-MBE growth on patterned (111) Si substrates. Uniform NW arrays with a diameter of 80 nm and length around 700 nm were obtained for the InAs NWs and enhanced to be around 1.3 µm for the InAsSb due to enhancement in the growth rate a result of introducing the Sb to the wires which thus increase the length of the grown wires due to adatoms diffusion on the surface. The growth temperature ranges were investigated under V/III ratio of 25, with maximum temperature close to 501°C for InAs and 509 °C for InAsSb NWs. The growth temperature significantly affected the axial growth rate in the range between 473 -501°C for InAs NWs and 456 -509 °C for InAsSb NWs. However, the ideal axial growth rate was achieved at 494 °C for both wires. Decrease NWs growth rate at very high growth temperatures was limited by excess In desorption from the Sio_2 on the Si (111) surface. TEM studies of InAs NWs shows that the wurtzite (WZ) crystal phase structure is dominating and the addition of Sb drives a change to a zinc-blende (ZB) phase with 6% - 7% Sb. The NWs exhibited strong PL at low temperatures with PL peak in the range assigned for the WZ InAs at 0.473 eV, the addition of Sb shifts the energy towards lower energy gaps at 0.380 eV. A blue shift of ~5 meV is observed due to confinement in the NWs. PL emission persist up to 150 K from InAs and InAsSb NWs, the addition of small amounts of Sb has been shown to suppress lattice defects, including twinning and stacking faults in InAsSb NWs. However, the PL quenching behaviour is only marginally improved since the band-edge perturbations introduced by these defects do not strongly influence non-radiative recombination. The results presented here lay the groundwork for developing high-performance InAsSb nanowire-based infrared photodetectors and nanoelectronic devices.

5.18. References

[1] Sun, M.; Leong, E.; Chin, A.; Ning, C.; Cirlin, G.; Samsonenko, Y.; Dubrovskii, V.; Chuang, L.; Chang-Hasnain, C. Photoluminescence Properties of InAs Nanowires Grown on GaAs And Si Substrates. Nanotechnology, 2010, 21, 335705.

[2] Koblmüller, G.; Vizbaras, K.; Hertenberger, S.; Bolte, S.; Rudolph, D.; Becker, J.; Döblinger, M.; Amann, M.; Finley, J.; Abstreiter, G. Diameter Dependent Optical Emission Properties of InAs Nanowires Grown on Si. Applied Physics Letters, 2012, 101, 053103.

[3] Joyce, H.; Gao, Q.; Hoe Tan, H.; Jagadish, C.; Kim, Y.; Zou, J.; Smith, L.; Jackson, H.; Yarrison-Rice, J.; Parkinson, P. et al. III–V Semiconductor Nanowires for Optoelectronic Device Applications. Progress in Quantum Electronics, 2011,35, 23-75.

[4] Thelander, C. et al. Electron transport in InAs nanowires and heterostructure nanowire devices. Solid State Commun. 2004, 131, 573-579.

[5] Aharonovich, I., Englund, D. & Toth, M. Solid-State Single-Photon Emitters. Nat. Photon. 2016, 10, 631-641.

[6] Farrell, A.; Lee, W.; Senanayake, P.; Haddad, M.; Prikhodko, S.; Huffaker, D. High-Quality InAsSb Nanowires Grown by Catalyst-Free Selective-Area Metal–Organic Chemical Vapor Deposition. Nano Letters, 2015, 15, 6614-6619.

[7] Potts, H.; Friedl, M.; Amaduzzi, F.; Tang, K.; Tütüncüoglu, G.; Matteini, F.; Alarcon Lladó, E.; McIntyre, P.; Fontcuberta i Morral, A. From Twinning to Pure Zincblende Catalyst-Free InAs(Sb) Nanowires. Nano Letters 2016, 16, 637-643.

[8] E. Fadaly. Molecular Beam Epitaxy of Catalyst-Free InAs Nanowires on Si (111). PhD thesis, Chalmers University of Technology Gothenburg, Sweden 2015.

[9] Dick, K.; Thelander, C.; Samuelson, L.; Caroff, P. Crystal Phase Engineering in Single InAs Nanowires. Nano Letters 2010, 10, 3494-3499.

[10] J. D. Heber and C. C. Philips, InAs/InAsSb emitters for the mid-infrared region, Chapter in "III-V Semiconductor Heterostructures: Physics and Devices", ed. by W. Z. Cai, Keraia: Research Signpost, 2003, pp. 140-167.

[11] Thompson, M., Alhodaib, A., Craig, A., Robson, A., Aziz, A., Krier, A., Svensson, J., Wernersson, L., Sanchez, A. and Marshall, A. Low Leakage-Current InAsSb Nanowire Photodetectors on Silicon. Nano Letters. 2016, 16(1), pp.182-187.

[12] Rota, M. et al. Bandgap Energy of Wurtzite InAs Nanowires. Nano Lett. 2016, 16, 5197-5203.

[13]Trägårdh, J.; Persson, A.; Wagner, J.; Hessman, D.; Samuelson, L. Measurements of The Band Gap of Wurtzite $InAs_{1-X}P_X$ Nanowires Using Photocurrent Spectroscopy. Journal of Applied Physics 2007, 101, 123701.

[14] Möller, M.; de Lima Jr, M.; Cantarero, A.; Chiaramonte, T.; Cotta, M.; Iikawa, F. Optical Emission of InAs Nanowires. Nanotechnology 2012, 23, 375704.

[15] A photoluminescence study of polycrystalline thin-film CdTe/CdS solar cells, D.P. HALLIDAY, J.M. EGGLESTON, K. DUROSE, Journal of Crystal Growth 186, 543-549 (1998)

[16] Midinfrared photoluminescence of InAsSb quantum dots grown by liquid phase epitaxy, A. KRIER, X.L. HUANG, A. HAMMICHE, Applied Physics Letters volume 77 number 23, 3791-3793 (2000).

[17] Low-temperature photoluminescence of epitaxial InAs, Y. LACROIX, C.A. TRAN, S.P. WATKINS, M.L.W. THEWALT, Journal of Applied Physics volume 80 number 11, 6416-6424 (1996).

[18] Excitonic photoluminescence in high-purity InAs MBE epilayers on GaAs substrates, P.J.P. TANG, C.C. PHILLIPS, R.A. STRADLING, Semiconductor Science and Technology 8, 2135-2142 (1993).

[19] Excitation-power dependence of the near-band-edge photoluminescence of semiconductors, T. SCHMIDT, K. LISCHKA, W. ZULEHNER, Physical Review B volume 45 number 16, 8989-8994 (1992)

[20] Schmidt, T.; Daniel, G.; Lischka, K. The Excitation Power Dependence of the Near Band Edge Photoluminescence of II-VI Semiconductors. Journal of Crystal Growth 1992, 117, 748-752.

[21] Schmidt T, Lischka K and Zulehner W 1992 Excitation power dependence of the near-band-edge photoluminescence of semiconductors Phys. Rev. B 45 8989–94.

[22] Tang P J P, Phillips C. C. and Stradling R. A. Excitonic photoluminescence in high-purity InAs MBE epilayers on GaAs substrates Semicond. Sci. Technol. 1993, 8 2135–42.

[23] Noguchi, M.; Hirakawa, K.; Ikoma, T. Phys. Rev. Lett. 1991, 66,2243.

[24] Olsson, L. O.; Andersson, C. B. M.; Hakansson, M. C.; Kanski, J.; Ilver, L.; Karlsson, U. O. Phys. Rev. Lett. 1996, 76, 3626.

[25] Olsson, L.; Andersson, C.; Håkansson, M.; Kanski, J.; Ilver, L.; Karlsson, U. Charge Accumulation at InAs Surfaces. Physical Review Letters 1996, 76, 3626-3629.

[26] Latkowska, M.; Kudrawiec, R.; Janiak, F.; Motyka, M.; Misiewicz, J.; Zhuang, Q.; Krier, A.; Walukiewicz, W. Temperature Dependence Of Photoluminescence From Innassb Layers: The Role of Localized and Free Carrier Emission In Determination of Temperature Dependence of Energy Gap. Applied Physics Letters 2013, 102, 122109.

[27] Hertenberger, S.; Rudolph, D.; Bichler, M.; Finley, J. J.; Abstreiter, G.; Koblmuller, G. Growth kinetics in position-controlled and catalyst-free InAs nanowire arrays on Si(111) grown by selective area molecular beam epitaxy. J. Appl. Phys. 2010, 108, 114316.

[28]Johansson, J.; Bolinsson, J.; Ek, M.; Caroff, P.; Dick, K. A. Combinatorial Approaches to Understanding Polytypism in IIIV Nanowires. ACS Nano 2012, 6, 6142−6149. PMID: 22681568.

[29] Sourribes, M. J. L.; Isakov, I.; Panfilova, M.; Liu, H.; Warburton, P. A. Mobility Enhancement by Sb-mediated Minimisation of Stacking Fault Density in InAs Nanowires Grown on Silicon. Nano Lett. 2014, 14, 1643−1650. PMID: 24502770

Chapter 6

Growth, Structural and Optical Analysis of

InAs/InAsSb MQW NWs

&

InAs/InAsSb SL NWs

6.1. InAsSb MQW NWs: Introduction

Early works have focused on exploiting the structural and optical properties of bulk InAs(Sb) NWs, in such a way that their application to photonics promises many transformational advantages. The principle challenge in this work is in achieving efficient light emission without the requirement for cryogenic cooling, which in turn necessitates incorporating quantum nanostructures into the NW. This chapter demonstrates the structural and optical properties of novel faceted, conical InAsSb multi-quantum well (MQW) and InAsSb superlattices (SLs) embedded within InAs NWs, exhibiting room temperature mid-infrared light emission.

6.2. The growth

InAsSb/InAs MQW have been grown on silicon (111) substrates, using selective area MBE as described previously in chapter 4. The MQW nanowire growth was initiated by impinging As flux followed by exposure of the sample to the In flux 20 seconds later. Following the growth of an initial pure InAs section for 1 hour, the MQW active region was grown as 10 repeats of InAs/$InAs_{1-x}Sb_x$ MWQs with growth durations of 180s and 27s respectively. This was expected to form 10 repeats of 25 nm InAs and 8 nm $InAs_{1-x}Sb_x$, giving a total active region thickness of 330 nm as shown in figure 6.1(a). Finally, the wires were finished with an InAs cap, grown for 10 minutes. All growths commenced with a pure InAs section and were finished with an InAs cap. The InAs NWs mentioned in chapter five were used for comparison (QA612), the wires were grown sequentially under the same growth conditions, with the only difference being the omission of the InAsSb quantum well layers. For further comparison, a planar bulk InAs sample was grown as a reference. The MQW NWs were grown in arrays of 50 nm diameter holes patterned in a 330 nm pitch square array defined

within a number of 200 µm x 200 µm areas, on each silicon substrate as mentioned before in chapter 4, the final hole diameter was ~80 nm due to lateral etching. From the SEM images, the MQW wires were on average ~1.5 µm in length and ~100 nm in diameter see figure 6.1 (b) and (c).

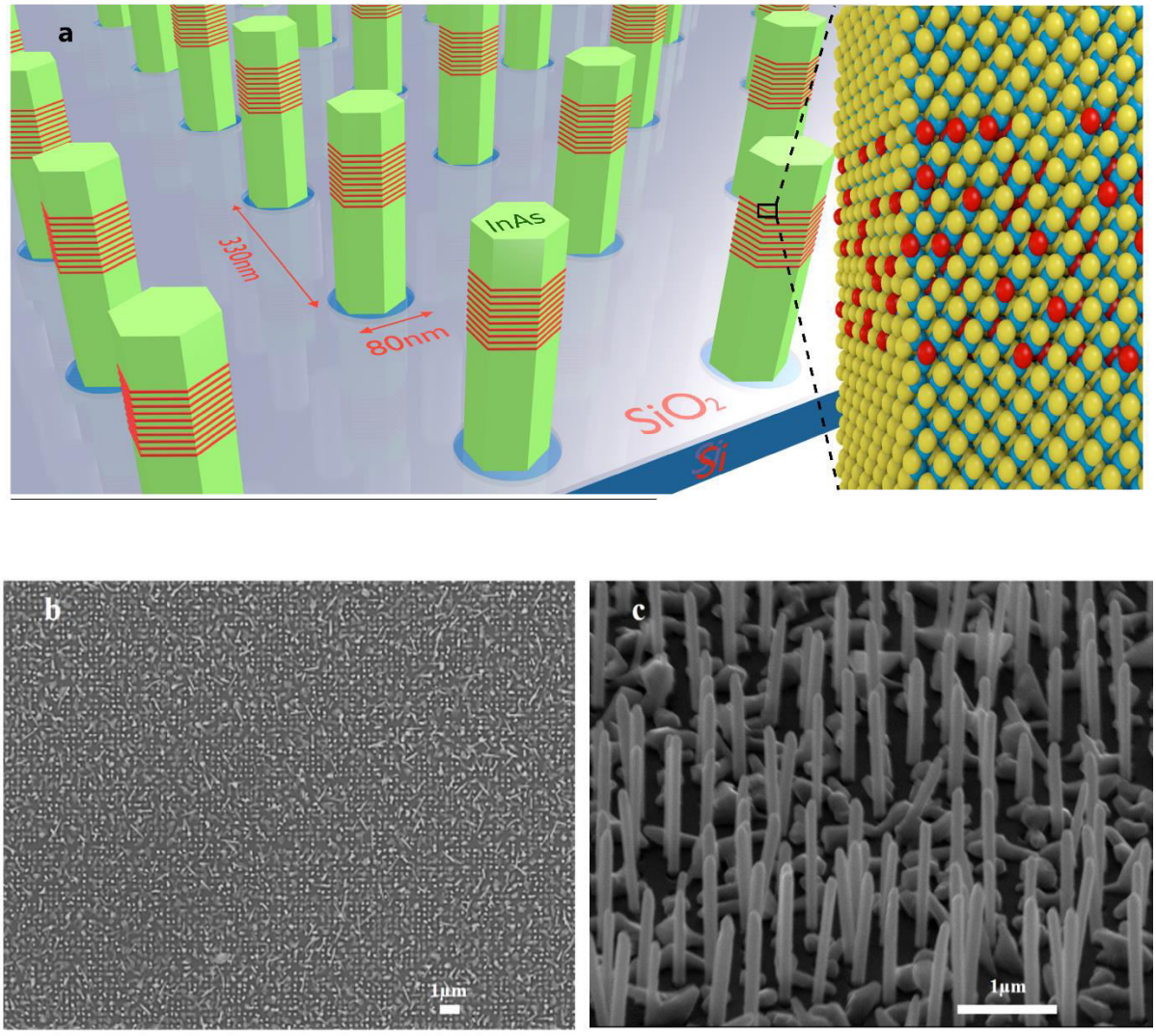

Figure 6.1. (a) Nanowire structural design and analysis. a, Schematic drawing of the InAsSb/InAs MQW within InAs NWs, grown in a 330 nm pitch square array patterned on a silicon substrate using a SiO_2 template with 80 nm diameter holes. Blue and yellow spheres represent In and As atoms respectively, while red spheres indicate the random incorporation of Sb within the quantum well region. (b) and (c) top view and tilted view SEM images respectively. The nanowires are viewed at an angle of 70˚. The scale bars in (b) and (c) are 1 µm.

6.3. Structural analysis

The lattice structure of the InAs/InAsSb MQW NWs was investigated using STEM. Close inspection of the high resolution STEM image in figure 6.2 shows a section of the NW with a QW in it. The image has 270 layers almost formed with a WZ phase structure with stacking faults and twins. One insert of a ZB segments (2-4 monolayers), has been observed in the analysed STEM image, this ZB insert is incidentally nowhere near the well and considered the smallest possible segment referred to by Caroff et al.[1]. However, if we consider these 2 monolayers as ZB, then 99.3% of the structure in the STEM image is WZ which is very close to a pure WZ structure. Figure 6.2 shows the different structures found in the MQW NWs, which are namely twinned WZ, ideal WZ, WZ with stacking faults, and the ZB segments (2 monolayers).

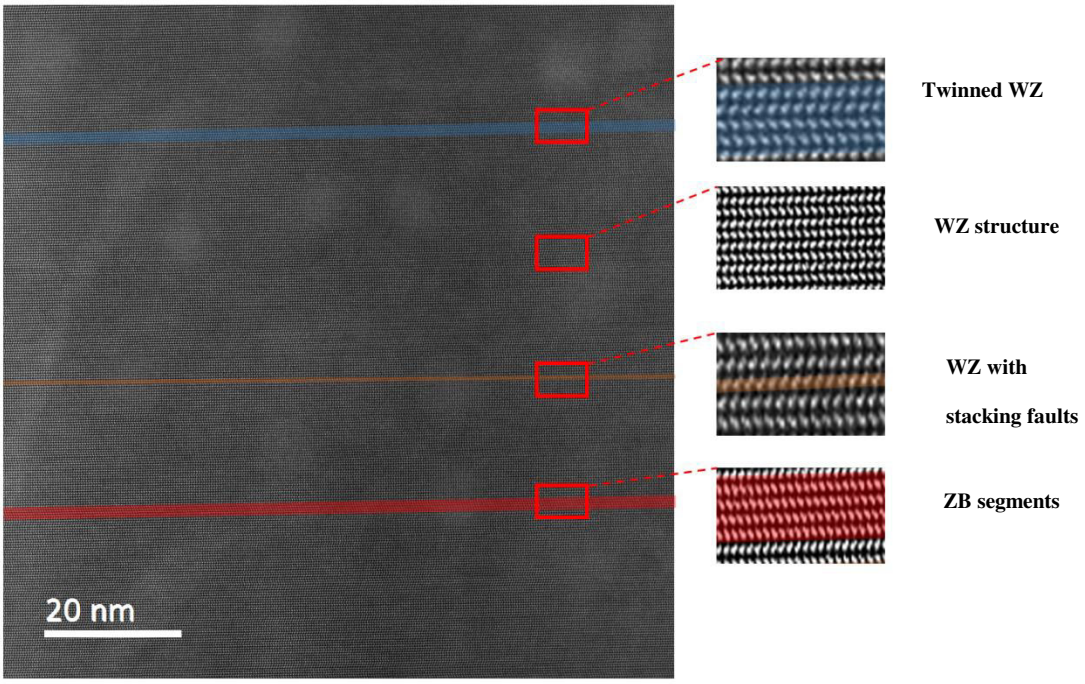

Figure 6.2. Nanowire structural analysis. High resolution STEM image of the InAsSb/InAs MQW within InAs NWs, grown in a 330 nm pitch square array patterned on a silicon substrate using a SiO_2 template with 100 nm wire diameter. Showing the different structures found in the grown NWs, twinned WZ, ideal WZ, and WZ with stacking faults and the ZB segments.

The nanowires had a regular hexagonal cross-section with $\{10\bar{1}0\}$ sidewalls, faceted tips and a twinned WZ crystal structure with stacking faults, which is a characteristic of InAs NWs[2, 3]. In common with other researchers we have found that the addition of Sb to form bulk InAsSb NWs forces a rotation in the layer stacking leading to a predominantly ZB structure with a flat top. Bulk InAsSb NWs grown under these conditions contained 6-7% Sb, in good agreement with earlier work that reports saturation at this concentration[4]. However, when the InAsSb growth is limited to nanoscale quantum wells, energy dispersive x-ray (EDXS) mapping revealed preferential incorporation of the Sb on specific crystal planes. This results in the formation of novel quantum wells having faceted, flat-topped, conical shape, with open or partially closed flat tops, as shown in figure 6.3 (a). It is noted that in other NW studies, authors have considered nanoscale axial heterostructures as both quantum dots (QDs) [5,6] and QWs[7,8,9]. The QD model is understandably favoured for lower wire diameters, however in light of our larger 100 nm diameter and the weak lateral conferment of the higher effective mass holes, we consider our heterostructures to be QWs.

Angular STEM analysis of the plane with preferential Sb incorporation shows it to be consistent with the $(10\bar{1}1)$ plane, since it matches the 62º angle expected for this plane from the WZ unit cell (see figure 6.3 (b)) rather than the $(1\bar{1}20)$ plane which has an angle of 73º. We expect that the tip of the InAs wire is faceted during growth such that when the InAsSb QW growth is initiated, the adatoms have a choice of incorporating on the (0001) or $(10\bar{1}1)$ planes. It appears that bonding onto the $(10\bar{1}1)$ facets is energetically favoured. Interestingly, close inspection of high resolution TEM images shows both the angled nature of the well and a continued WZ structure within the InAsSb well. Figure 6.4 shows a full diameter image of the wire together with a zoomed-in view, within which the lattice structure can be discerned. From the zoomed-in view it is clear that the structure of the InAsSb well does not change to

ZB, as it would do in a pure InAsSb NW, or an extended segment of growth. This is in contrast to the case with extended durations of $InAsSb_{0.07}$, and could suggest that the Sb fraction in the QW is less than the 6-7% seen in comparable bulk wires, because the phase is still WZ, but this is an overly simplistic view.

With extended growth on an InAs wire, a switch to the ZB phase is observed. Starting with the WZ structure, preferential incorporation on the $(10\bar{1}1)$ facets would lead to a flat-topped wire forming over time, enabling the required 60º rotation of the lattice around the (0001) axis, for the switch to ZB. However, in the case of the QWs, the short growth durations are insufficient to allow a flat top to form and so the WZ phase is maintained. Hence, the Sb fraction in the wells is currently best estimated at 6-7%, based on comparable bulk wires.

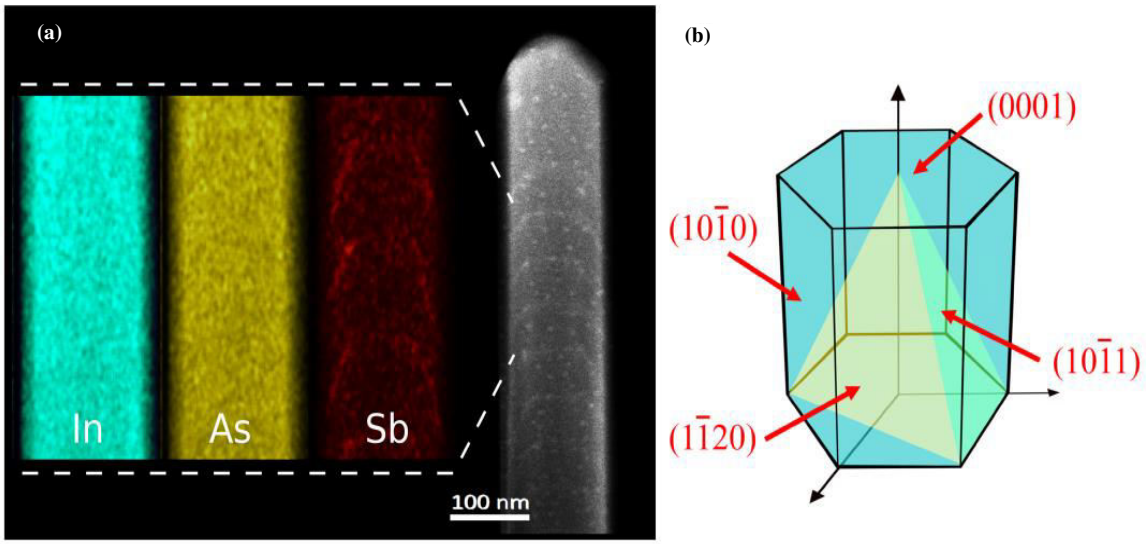

Figure 6.3. (a) STEM image showing the distribution of In, As and Sb obtained from 2D EDXS mapping and the resulting unusual facetted conical shape of the InAsSb MQW. (b) The unit cell of the WZ crystal structure showing the possible growth planes for the InAsSb MQW facets.

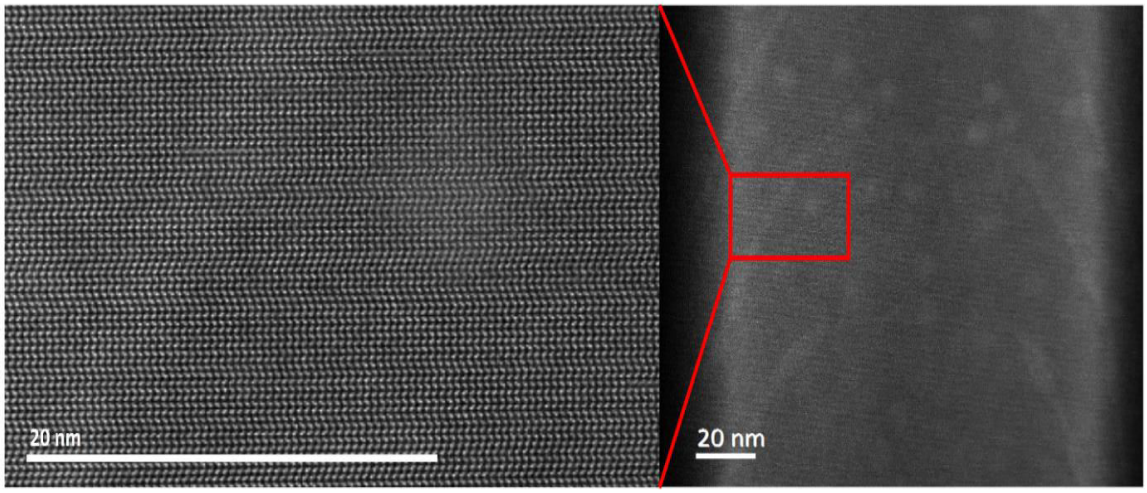

Figure 6.4. High resolution TEM analysis of the QW in NW. Cross-sectional TEM images, looking across a section of wire including a QW. The lattice structure is visible and the crystalline phase (WZ) is evidently continuous across the quantum well.

6.4. 4k Micro- PL measurements

The 4K PL emission from the MQW was studied using temperature dependent micro-photoluminescence spectroscopy. Introducing the InAsSb MQW significantly changes the PL emission characteristics of the NWs in a number of ways. A comparison of the spectra measured at 4 K from the InAsSb MQW NWs, bulk alloy InAsSb NWs and InAs NW samples is shown in figure 6.5. Emission from the bulk InAsSb NWs figure 6.5(c) deconvoluted into peaks at 0.380 eV corresponding to 6 % Sb with a dominant ZB phase in agreement with previous work[10], and a shoulder on the main peak originating from ZB InAs which appears as the dominant phase in the early stage of all our NW growths[11].

Emission from the InAs NWs peaks at 0.482 eV as shown in figure 6.5 (d), consistent with earlier work and a dominant WZ phase[3,12] (discussed previously in details in chapter 5).

Figure 6.5 (a) and (b) show the PL emission from the InAsSb MQW NWs at high and low excitation respectively, both exhibits a clear increase in peak emission energy with respect to the bulk alloy InAsSb NWs, due to the strong carrier confinement within the quantum wells. The InAsSb MQW NWs also exhibit increased emission intensity and superior temperature quenching behaviour compared with the bulk NWs as expected. Most notably the emission intensity is enhanced at all temperatures, due to the quantum confinement of electrons and holes. PL originates from type II spatially indirect recombination of electrons in the InAs layers with confined hole states in the InAsSb QWs, where the spatial separation helps to reduce non-radiative Auger recombination with a corresponding increase in radiative emission[13]. Single Gaussian fits were made to the spectra which reveal interference from characteristic atmospheric absorption by water vapour between 0.445 eV and 0.485 eV[14]. The spectra can be scaled to account for the reduced cross-sectional area of the nanowire samples, where only 7% of the surface area is covered by the NWs assuming a 100% nucleation yield in the mask sites. Accounting for this reduced active area allows the most direct comparison of emission intensity.

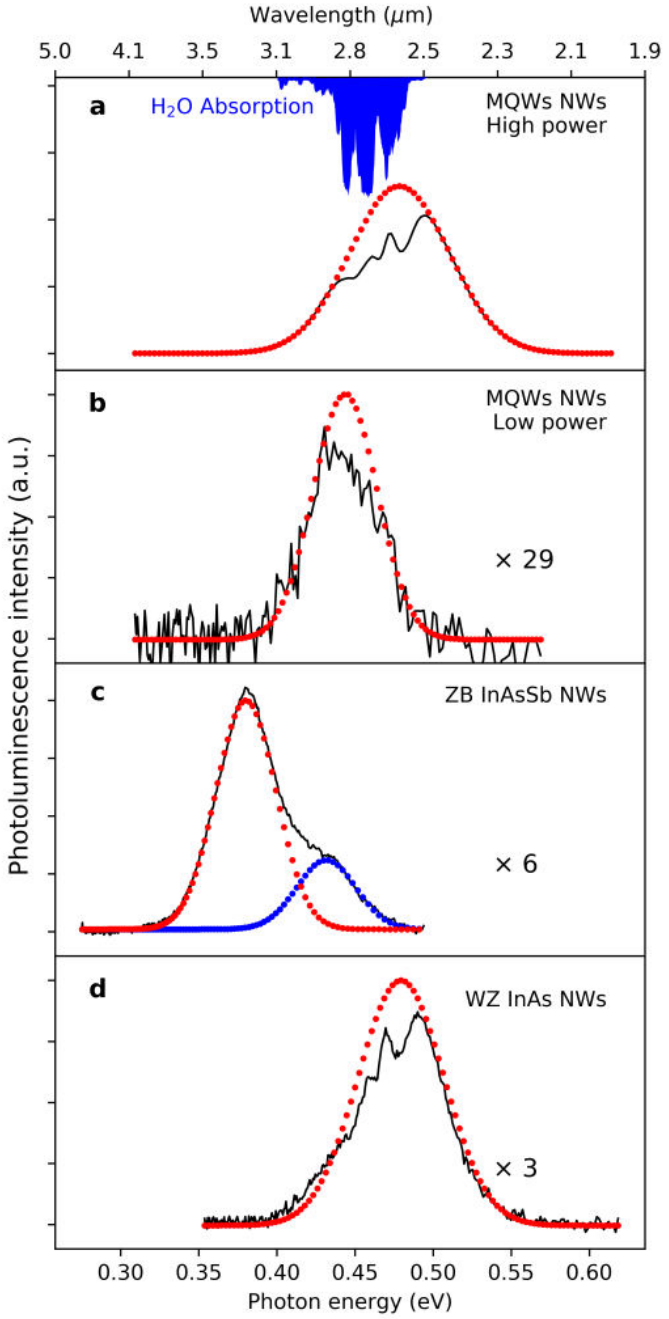

Figure 6.5. Micro-PL spectra obtained at 4 K. The emission spectra measured from a, InAsSb/InAs MQW NWs at high power (1.2×10^4 Wcm^{-2}), b, InAsSb/InAs MQW NWs at low power (80 Wcm^{-2}), c, InAsSb NWs at (1.2×10^4 Wcm^{-2}) and d, InAs NWs at (1.2×10^4 Wcm^{-2}). The dotted lines represent Gaussian fits to the spectra, which also reveal the atmospheric absorption from water vapour[15] in this spectral region, as shown in a.

We observed that at the low excitation (0.011 Wcm^{-2}) the MQW NW emission intensity is 4.2-fold enhanced with respect to a bulk InAs reference sample, compared to a 1.6-fold

enhancement from the InAs NWs (see figure 6.6). It must be noted that this comparison assumes direct area proportionality for the optical pumping efficiency. However, it has been shown that the efficiency of optical absorption in nanowire arrays exhibits a spectral dependence arising from mode guiding, due to the geometry of the wire and array, such that the peak field can occur either inside or outside the wires[16]. To a first order this effect is defined by the wire diameter and in prior work we reported a very similar effect from an array of InAsSb NWs in a photodetector[11], where the peak response was obtained at 1.5 µm with a FWHM of 320 nm. Consequently, there is non-optimal coupling with the 808 nm pump laser used in the present PL studies, and hence further enhancement of PL emission intensities are to be expected if the pump laser wavelength is correctly matched to the NW geometry.

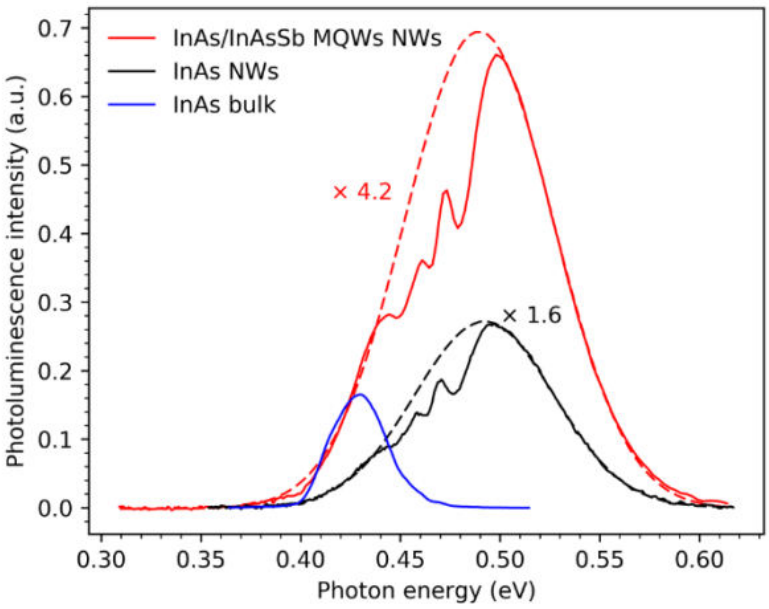

Figure 6.6. Comparison of emission intensities. PL spectra, under 3.2×10^4 Wcm^{-2} excitation, showing the relative emission intensities for MQW NWs, InAs NWs and an InAs bulk sample, scaled by active area.

6.5. Development of a band structure for the MQWs

Developing a band diagram for the InAs/InAsSb MQW NWs is not straightforward, due to limited data describing bandgaps and alignments for the Wurtzite phases. In particular, pure $InAs_{1-x}Sb_x$ nanowires take on a predominately zinc-blende structure for x > 4%, precluding the measurement of Wurtzite bandgaps at higher antimony fractions. In contrast, the $InAs_{1-x}Sb_x$ growth in this work maintains its Wurtzite structure due to the growth being on the $(10\bar{1}1)$ facets of the Wurtzite InAs wire. To approximate the band diagram in this absence of reported parameters, we start with the band alignment for a comparable zinc-blende structure, calculated taking account of the Sb fraction and the strain within a (111) orientated nanowire. The band gap of Wurtzite InAs is taken to be 60 meV greater than that for InAs zinc-blende (E_{Gwz}), with the noted caveat that there is a lack of consensus in the literature. The value of the band-gap for the wurtzite $InAs_{1-x}Sb_x$ can be calculated using the quadratic approximation

$$E_g\,(InAs_{1-x}Sb_x) = xE_{gWZ}\,(InAs) + (1-x)\,E_{gWZ}\,(InSb) + x\,(1-x)\,0.67 \qquad (6.1)$$

Where 0.67 is the bowing parameter for zinc-blende InAsSb and E_{gWZ} (InSb) is the bandgap of wurtzite InSb taken as 0.287 eV[17]. This gives $E_g\,(InAs_{0.93}Sb_{0.07})$ = 0.424 eV which is 63 meV greater than the known value for the zinc-blende phase. This also agrees with results by Farrell et al. who showed that for x=3.9% the bandgap of Wurtzite $InAs_{1-x}Sb_x$ was also ~60 meV greater than the known value for the zinc-blende phase.

The confined hole states were calculated using a six-band k.p solver in Nextnano. The first confined heavy hole state is calculated to be 8 meV above the band edge, as shown in the schematic energy band diagram in figure 6.8 (b) corresponding to a flat-band recombination transition energy, E_t, of 0.443eV.

6.6. PL Power dependence

Under low excitation conditions, bulk ZB InAs at 4 K normally exhibits characteristic emission from bound exciton and donor-acceptor transitions around 0.417 eV and 0.374 eV respectively[18]. The higher excitation intensity (~ 10^4 Wcm^{-2}) in our micro-PL experiments results in state filling so that a single InAs peak is observed at 0.425 eV. In the present case, the InAs NW emission is further blue-shifted with respect to the bulk ZB reference sample, due to the WZ crystal structure of the NW, with peak emission energy ranging from 0.469 eV under low excitation, to 0.485 eV under high excitation, as shown in figure 6.7. The bandgap for WZ InAs is known to be higher than that of ZB InAs and our result is consistent with earlier studies of WZ InAs NWs which reported bandgaps in the range 0.477 eV to 0.540 eV[12,19]. Quantum confinement induced blue-shifts have also been observed as the diameter of InAs NWs are reduced[14], however in our case, for 100 nm diameter wires, the shift is rather small ~5 meV. Hence, the emission observed from the InAs NWs grown in this work is in good agreement with earlier reports and we envisage modest size-related confinement effects in the InAsSb MQW NWs. The PL emission energy from the InAs NWs blue shifted by 21 meV over the range of pump powers used in our experiments, which is similar to that obtained by others[14], and is associated with band filling. The commensurate shift for the MQW NWs is much larger, at 45 meV (see figure 6.7). The majority of this blue shift occurs at low pump powers before the dependence becomes similar to that for pure InAs wires at higher powers.

The blue shift in the MQW nanowires arises due to band bending effects characteristic of type II QWs and originates from Coulomb attraction between localised holes in the InAsSb quantum well attracting electrons from the adjacent InAs barrier forming triangular quantum wells.

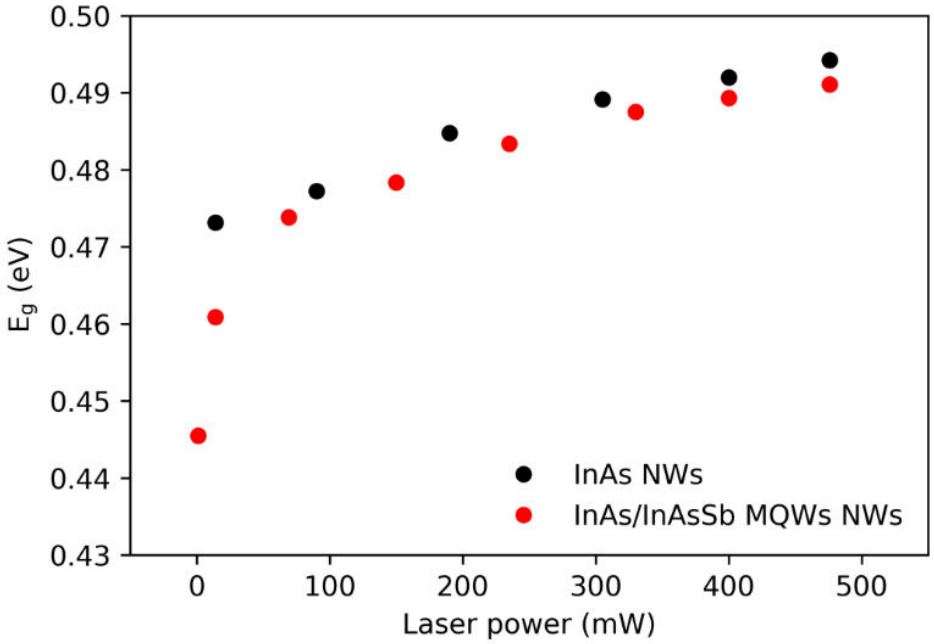

Figure 6.7. Power dependence of PL emission. The dependence of the peak emission energy on the power of the pump laser incident on the sample, for InAs and InAsSb/InAs MQW NWs. Showing the difference in the blue shift between the pure InAs NW, with minimal quantum confinement effects and the MQW NW, with strong quantum confinement and charging effects.

An increase in excitation intensity will raise the steepness of the confining potential and consequently the electron quantization energy E, with a typical $\Delta E \sim L^{1/3}$ behaviour discussed in details in chapter 2. Accordingly, the flat band transition energy of the InAsSb/InAs MQW can be extracted from the intercept of figure 6.8 (a) - the PL peak position versus $L^{1/3}$. Consequently, the flat band transition energy for the InAs/InAsSb MQW NWs is obtained as 0.438 eV which is in good agreement with the calculated transition energy of 0.443 eV, as shown in the schematic band diagram in figure 6.8 (b).

Further power dependence analysis for the MQW NWs demonstrating the calculated k value obtained from plotting the integrated intensity and laser power, as shown in figure 6.9. The MQWs had a k value of 0.75 which corresponds to free- and bound exciton transitions as discussed in chapter 2. This value suggests that impurity-like recombination processes are

involved, similar to what mentioned for the InAs and InAsSb NWs in chapter five, because of the large surface charge density, the Fermi level for InAs is pinned in the conduction band. The surface Fermi level pinning and associated band bending at the surface may result in spatially separated electrons near the surface and holes confined rather in the centre of the NW.

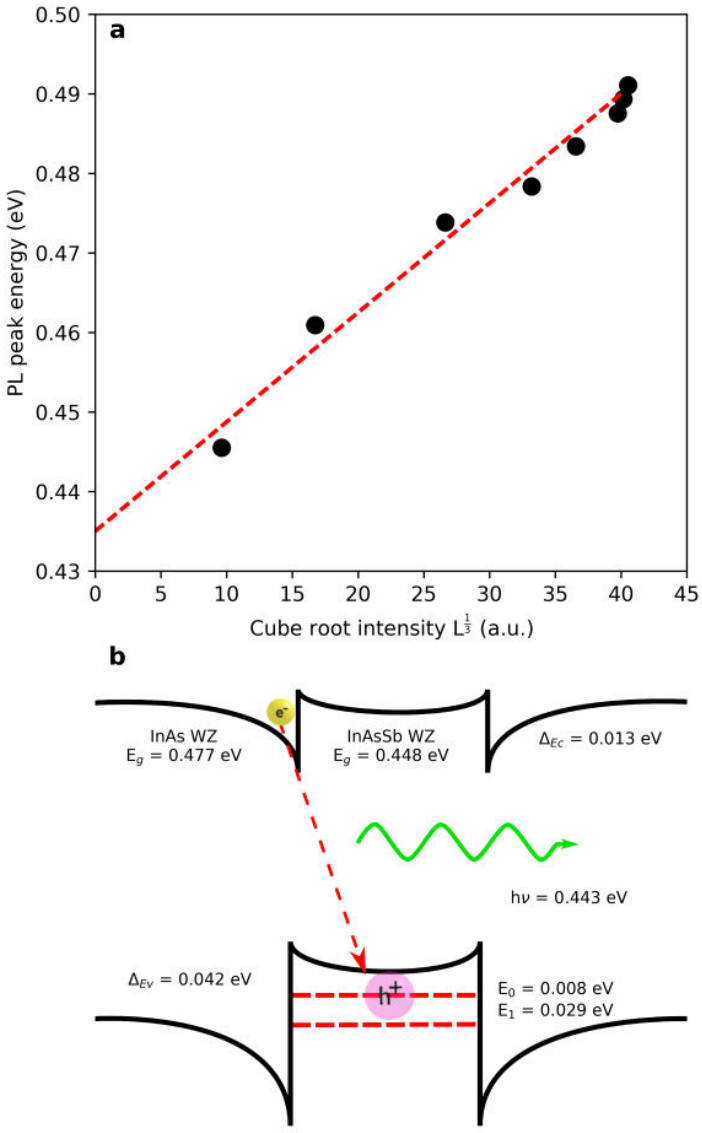

Figure 6.8. Determination of the flat band transition energy at the QW. a, PL peak energy vs cube root of integrated PL intensity, elucidating the charging of the type II QW and allowing the flat band transition energy to be identified. b, the calculated band diagram for the InAsSb/InAs QW and photon energy, showing the band bending and triangular well formation.

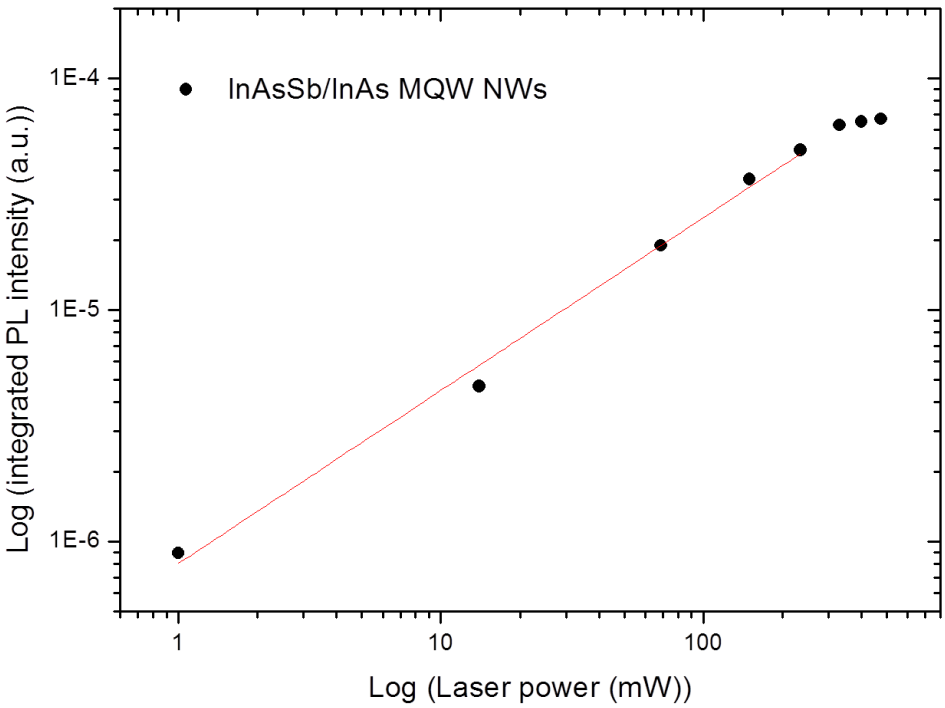

Figure 6.9. Excitation power dependent PL spectra recorded at 4K showing the K value of 0.75 for the InAs/InAsSb NWs.

6.7. PL temperature dependence

PL spectra obtained at different temperatures for the InAsSb MQW NWs are shown in figure 6.10. Although the wires are not capped or passivated they exhibit strong PL emission which persists up to room temperature. This indicates that radiative recombination occurs primarily in the MQW away from the near surface regions, which in InAs NWs are known to be accumulated due to Fermi level pinning resulting in a low efficiency for radiative emission[20]. In our case, the quantum confinement of the MQWs allows room temperature emission to be observed without passivation. The PL spectra are inhomogeneously broadened due to length variations in the NWs which also result in thickness variations of the QWs. The atmospheric water vapour absorption is again evident near 2.7 μm (0.459 eV) in all the spectra.

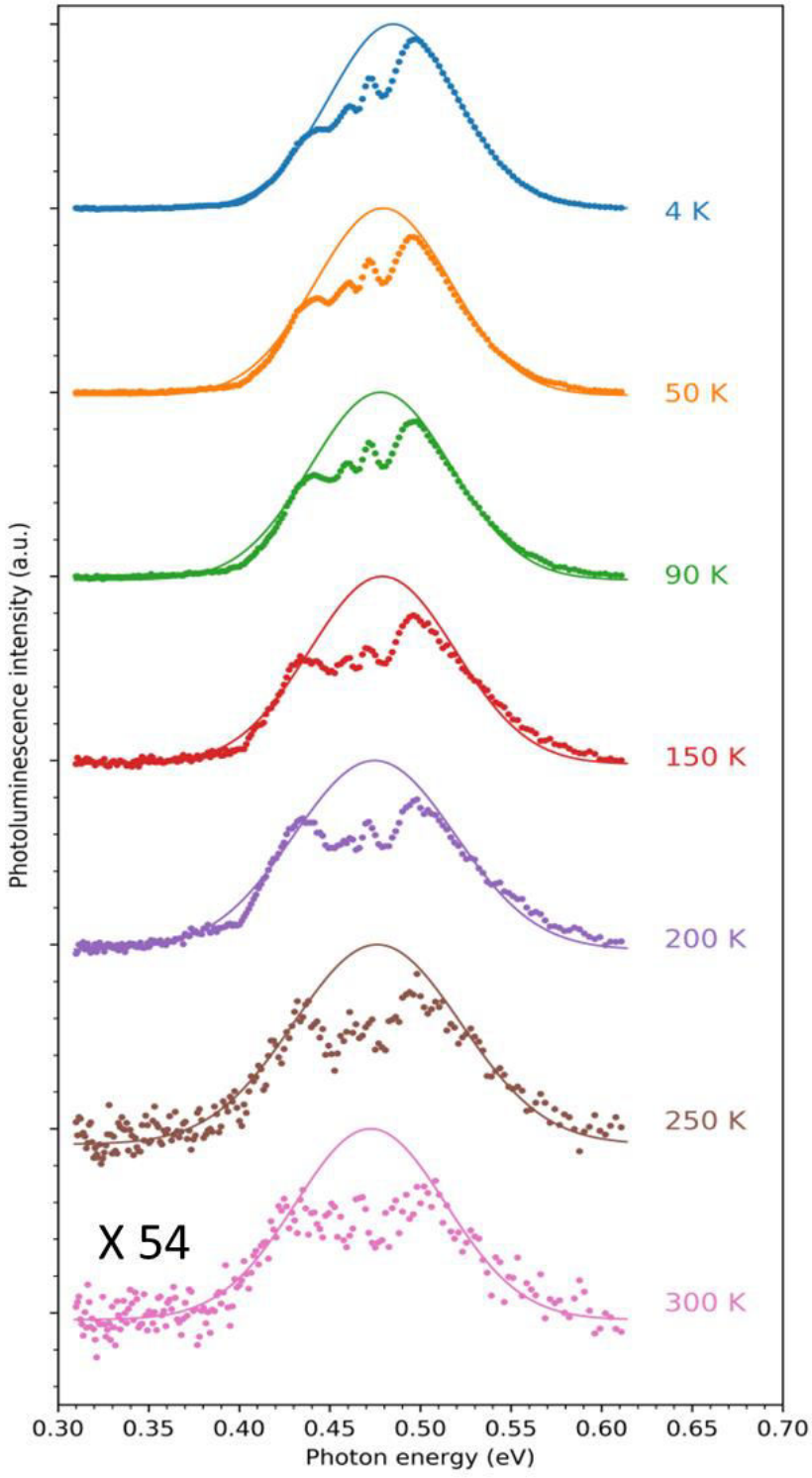

Figure 6.10. Temperature dependence of the PL emission spectra obtained from the InAsSb MQW NWs. Emission spectra measured over the range 4-300 K using high excitation (2.6×10^4 Wcm^{-2}), showing the room temperature emission required for future practical NW infrared emitters. The dotted lines indicate Gaussian fits used to extract the peak emission wavelength. Atmospheric water vapour absorption is again evident in all the spectra.

Figure 6.11 presents a comparison of the temperature quenching of the NW samples, where the superior performance of the InAsSb MQW NWs is clearly evident due to the increase in the radiative emission rate and suppression of Auger recombination.

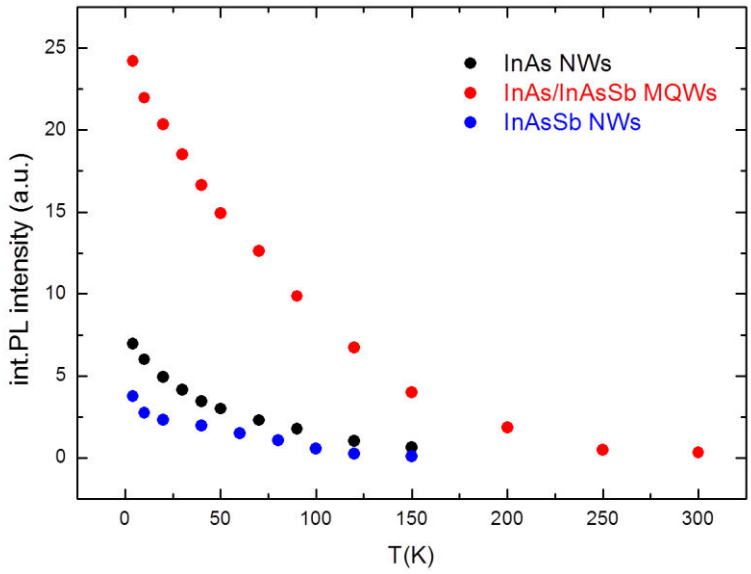

Figure 6.11. Temperature dependent analysis of PL data from the InAsSb/InAs MQWs, InAsSb and InAs NW samples, showing the integrated PL intensities as a function of temperature, showing the quenching behaviour of the three NW sample.

The temperature dependence of the peak energies for the NWs is shown in figure 6.12. The dotted lines represent fitting of the results using the empirical Varshni equation. The values obtained for the fitting parameters (E_g (0), α and β) are given in the table along with reference values for bulk InAs, both the InAs and the InAsSb MQW NWs have a WZ crystal structure and consequently have a weaker dependence of bandgap on temperature (lower value of α) than the corresponding bulk ZB materials.

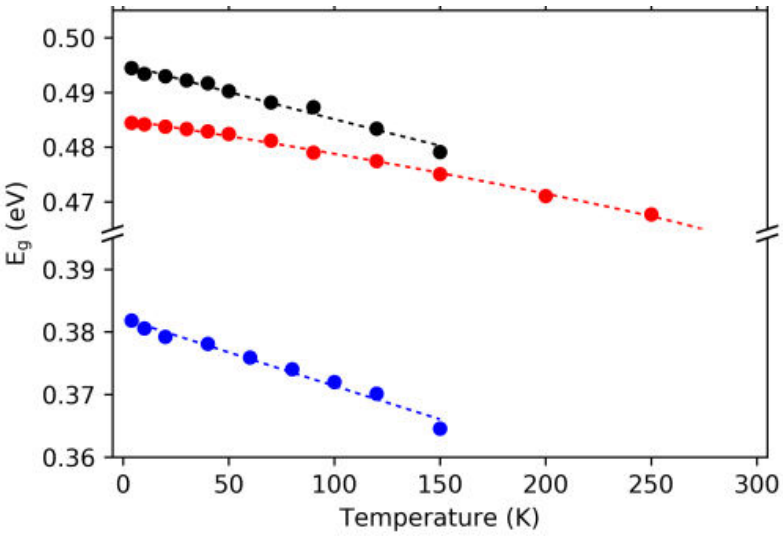

Figure 6.12. Temperature dependent analysis of PL peak from the InAsSb/InAs MQWs, InAsSb and InAs NW samples. The temperature dependence of the PL peak emissions (points), used to fit the Varshni relationships (solid lines) and extract the associated coefficients, for the three NW samples.

	E_0 (eV)	A (meV/K)	β (K)
InAs NWs	0.494	0.126	47
InAsSb NWs	0.380	0.133	42
InAsSb/InAs MQWs	0.484	0.099	97
InAs bulk	0.417	0.276	93
InSb bulk	0.235	0.320	170

Table1: Comparison of Varshni parameters. The fitted Varshni parameters E_0, α and β for the NW samples, compared with published parameters for bulk InAs and InSb[21].

An Arrhenius plot is shown in figure 6.13 for the InAsSb MQW NWs from which an activation energy of 49 meV was obtained from the high temperature region and ~5 meV for the low temperature region. This is in approximate agreement with the confinement energy for thermal excitation of holes out of the QW (hole localisation energy of 34 meV) and electrons from the interface triangular QWs (< 13 meV localisation energy) respectively.

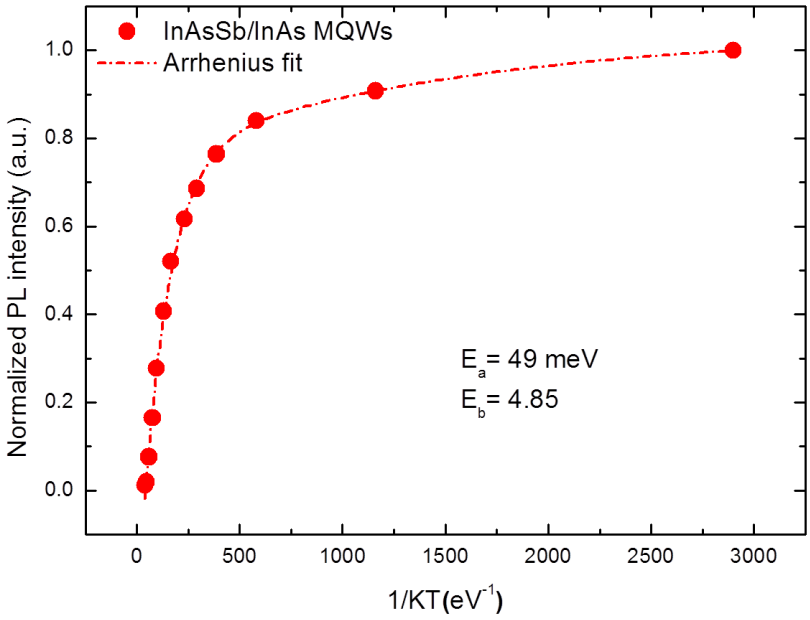

Figure 6.13. Temperature dependent analysis of PL emission intensity from the InAsSb/InAs MQWs sample shows an Arrhenius plot of integrated PL intensity as a function of inverse temperature for the InAsSb/InAs MQW NWs, used to extract activation energies for the mechanisms driving thermal quenching.

The InAsSb MQW NWs exhibit increased emission intensity and superior temperature quenching behaviour compared with the bulk NWs as expected. Most notably the emission intensity is enhanced at all temperatures, due to the quantum confinement of electrons and holes. PL originates from type II recombination of electrons in the InAs layers with confined hole states in the InAsSb QWs, where the spatial separation helps to suppress Auger recombination. The activation energy of ~49 meV obtained from the Arrhenius plot is consistent with

quenching due to carriers escaping confinement rather than Auger recombination and so provides indirect evidence for Auger suppression.

In type II QWs the Auger rate is determined by the overlap integral (between initial and final electron states at small transferred momentum) which is a minimum when the valence band offset is about three times the conduction band offset. Meanwhile, the radiative rate does not depend on the final state of any excited carrier, since it is a two body process, so the radiative rate can remain comparable with that in a type I QW[22].

6.8. The effect of Sb flux on MQWs

Two MQW NW samples (QA608 and QA615) have been grown under the same growth conditions with varying the Sb content in order to extend the emission wavelength through the Midinfrared range required for many applications. The Sb fractional flux was reduced from 0.360 ML/S in the sample (QA608) to 0.169 ML/S in the sample (QA615) at growth temperature of 480°C. From previous work we assumed that the sample (QA608) with 0.36 Sb flux corresponds to 6-7% Sb incorporated into the wires as confirmed by XRD for comparable bulk InAsSb NWs grown under the same growth conditions. The PL peak for QA608 is at 0.443 eV and QA615 is found to be at 0.457 eV. The PL emission is shifted towards higher energies by 14 meV with respect to the sample QA608. This maybe indicated that we have lower Sb content in the sample as expected from the PL, but it is not straight forward to confirm exactly how much Sb has been incorporated in to the wells. Ferrell et al reported an InAsSb NWs PL peak emission at ~ 0.445 eV corresponding to Sb content of x= 0.039, that would suggested that the Sb content in the sample QA615 is around ~ 4%[23]. In principle for type II QWs were the recombination occurs between electrons in the InAs layers

with confined hole states in the InAsSb QW, the QW PL should shifts to longer wavelengths as the Sb content is increased from 4 to 6 % as clear in figure 6.14. The PL peak intensity decreases at low excitation powers (80 Wcm^{-2}) for QA608 with 6% Sb, which is mainly due to the decrease in the wavefunction overlap as the Sb content increases in the well. As the band edge offset between the InAs and InAsSb increases, the overlap of electrons in the InAsSb and holes in the InAs decreases and thus the PL signal decreases.

6.9. The effect of changing the wells thickness

The critical thickness h_c is schematically the minimum thickness necessary for an epilayer to adapt its lattice constant to that of an underlying layer. It is thus thought to be the thickness above which dislocations will be generated at the interface between the two layers[24]. Assuming that the misfit dislocation generation is solely determined by the balance between the interfacial energy and the areal strain energy density, the critical thickness h_c can be expressed as:

$$h_c \approx \left(\frac{1-\nu}{1+\nu}\right)\left(\frac{1}{16\pi\sqrt{2}}\right)\left(\frac{b^2}{a(x)}\right)\left[\left(\frac{1}{f^2}\right)\ln\left(\frac{h_c}{b}\right)\right] \qquad (6.2)$$

where ν is Poisson's ratio, b the slip distance, $a(x)$ the lattice constant of the material function of x the element fraction in the alloy, f the misfit (see (2.31)). Poisson's ratio is defined as $\nu = \frac{C_{12}}{C_{11}+C_{12}}$ where C_{11} and C_{12} are tabulated elastic constants of the material. A layer thinner than h_c is considered fully strained in XRD analysis. A layer thicker than the critical thickness is subject to strain relaxation, misfit and thread dislocations[25] .

Varying the thickness of the InAsSb MQWs with a fixed Sb flux has been investigated in this work to study the influence of changing the well thickness on the MQW NWs. Three samples with well thickness of 4nm, 8nm and 16 nm have been grown by MBE growth techniques and under the same growth conditions used for the sample QA608 with 8nm thickness. In general, when growing a strained heteroepitaxial layer on a substrate, the layer will grow to a certain thickness without the formation of misfit dislocations. After a certain thickness, which depends on the lattice mismatch between the substrate and the epitaxial layer, the epitaxial layer will relax by forming misfit dislocations.

These crystal defects can have negative effects on the electrical and optical properties of the crystal, as they reduce the carrier mobility due to increased scattering[4] and can act as non-radiative recombination centres. Figure 6.15 shows that the PL intensity appears to increase with increasing the well thickness from 4 to 8 nm, then reduced for 16 nm, this reduction of the intensity is possibly due to exceeded of the critical thickness.

The thickness of our samples is far away from the critical thickness reported by Carrington et al. around 1000 nm for a planer layer with comparable Sb composition in the wells[26]. The best explanation for these PL results is that reducing the well thickness in type II band system should increase the heavy-hole splitting in the wells, thus the PL intensity will be reduced at lower thickness, this explains the 4nm wells with respect to the 8nm wells. Furthermore, a shift in the energy gap for the three thicknesses is observed as seen in figure 6.15. The energy gap is found to be at 0.487, 0.491 and 0.486 eV for the thickness of 4, 8 and 16 nm respectively. The sample with 8 nm thicknesses is shifted by 4 and 5 meV with respect to the other two samples with 4 and 16 nm thicknesses respectively, this shift is considerably low for changing the thickness. More investigations are required to study the wells thickness influence in these MQW NWs.

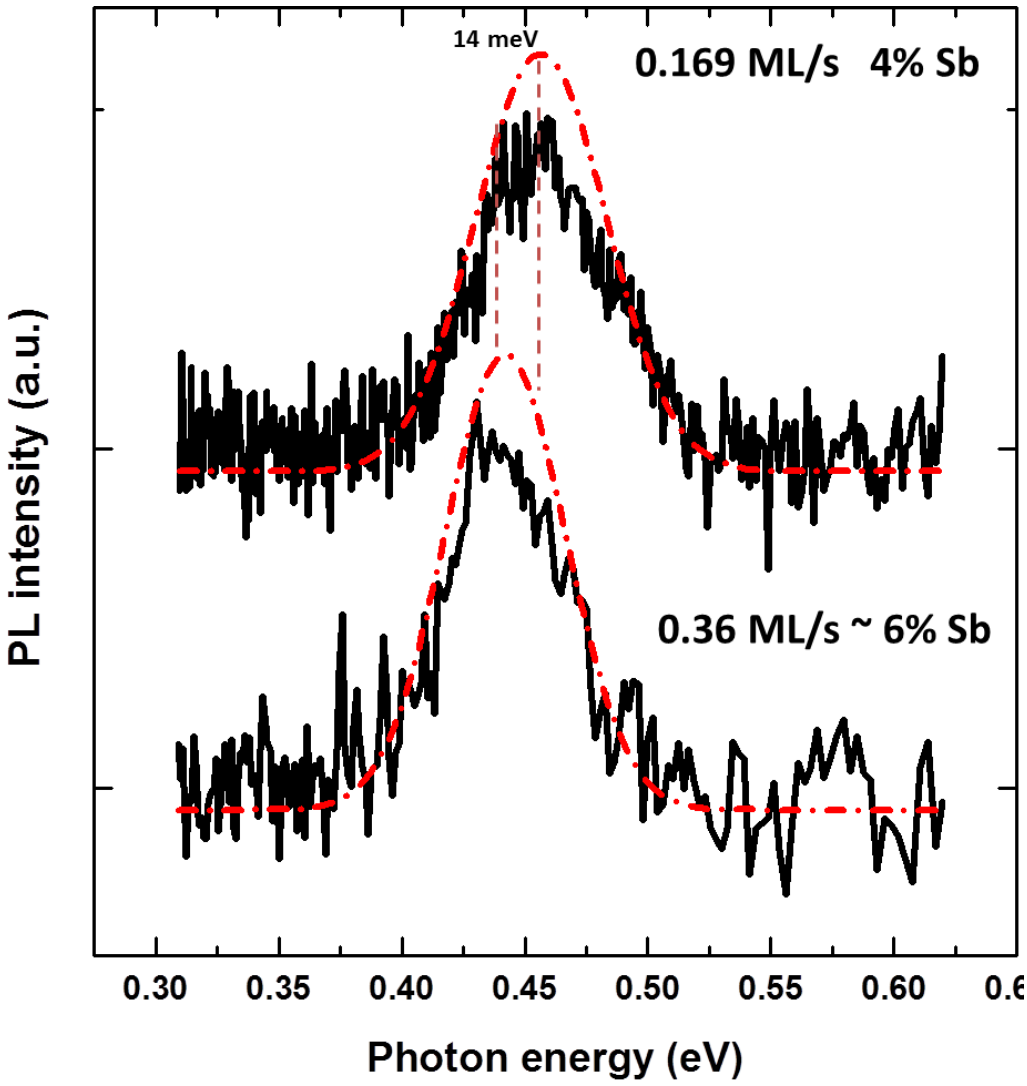

Figure 6.14. Micro-PL spectra obtained at 4 K. The emission spectra measured from InAsSb/InAs MQW NWs at low and high Sb content in the wells 4% and 6% respectively. The dotted lines represent Gaussian fits to the spectra, which also reveal the atmospheric absorption from water vapour in this spectral region.

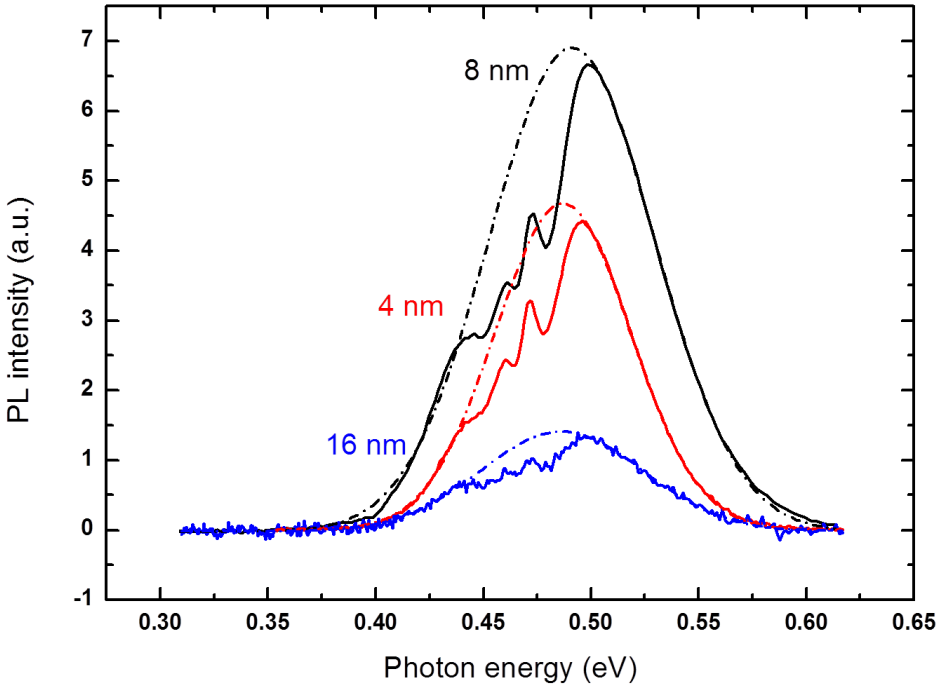

Figure 6.15. Micro-PL spectra obtained at 4 K. The emission spectra measured from InAsSb/InAs MQW NWs at different well thickness 4,8 and 16 nm respectively. The dotted lines represent Gaussian fits to the spectra, which also reveal the atmospheric absorption from water vapour in this spectral region.

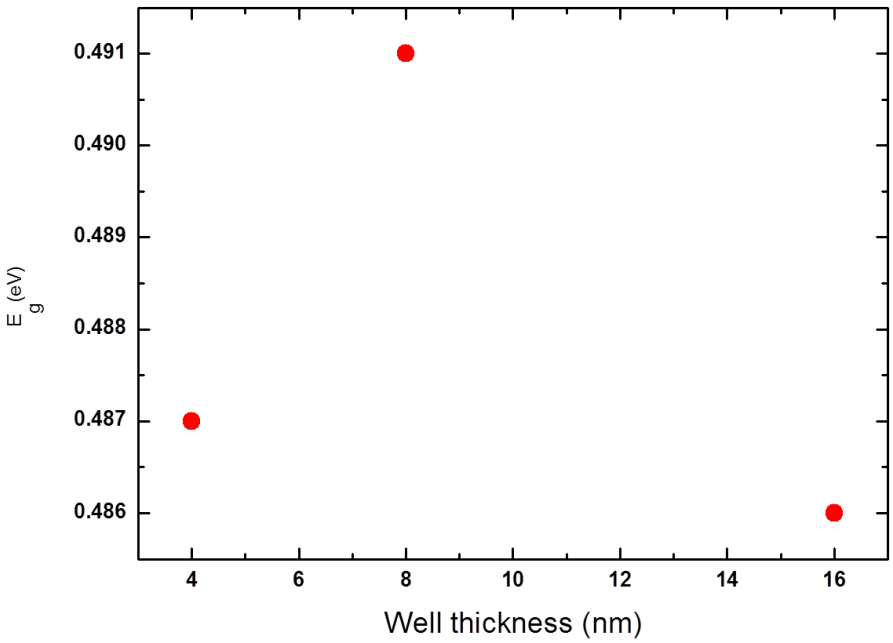

Figure 6.16. The energy gab for the InAsSb/InAs MQWs sample at different well thickness, 4, 8, 16 nm.

6.10. Organic coating

InAs NWs suffer from large densities of electrons at the surface because of Fermi level pinning above the conduction band which affected the luminescence efficiency[27]. Consequently, since the surface to volume ratio in nanowires is very large, the effect of surface states is greatly enhanced. Therefore, alternative methods have been used to reduce the surface states in InAs NWs, e.g. using a passivation technology[28,29]. One example is sulfide passivation, where the sulfidization forms bonds between sulfur atoms and surface atoms of the semiconductor, which help to prevent the oxidation of the surface and for long-time stability in the atmosphere, required for development of device applications. Sun et al[30] reported a recovery for the band edge emission in WZ and ZB InAs NWs by surface passivation where the PL peaks become much narrower and stronger and the deep level surface states in the band gap were eliminated for both NWs. In our experiment, we tried to extend this approach by coating with organic compounds in a way to improve the optical performance for our NWs. We performed the experiment on the InAs/InAsSb MQW NWs (QA608). This sample had the brightest PL at 4 K among our samples along with emission persisting up to room temperature, which would be a perfect candidate for this experiment.

6.10.1. Coating and rinsing processes

The sample was coated by 2, 6-Diaminoanthraquinone, an organic compound which is a good electron acceptor that binds to the surface via the amino (NH_2) group. The deposition was from 1mg/ml solution in THF (Tetrahydrofuran) in water. Then the solution was pipetted onto the sample and allowed to dry completely. The sample was then washed with pure THF

and the deposition repeated. Figure 6.17 (a) shows a schematic diagram of the organic coating process sequence for the MQW NWs sample.

6.10.2. PL measurements before and after the coating

PL measurements were carried out on the MQWs sample using the micro-PL setup at 4K. The procedure for the experiment was employed by first taking PL spectra for the as grown sample, then coating the sample using the organic compound and taking PL spectra for the coated sample, before finally rinsing excess molecules off the sample and taking PL spectra of the rinsed sample.

Figure 6.17 (c) shows the PL peaks for the InAs/InAsSb MQWs for each step of the coating treatment process, as grown, as coated and as rinsed. The PL emission was obtained for the as grown sample at 0.475 eV with FWHM of 84.09 meV (black line in figure 6.17(c)), however, after the coating, the PL emission was blue shifted by 4 meV with respect to the emission before the treatment, giving a PL peak at 0.479 eV (red line in figure 6.17(c)) along with an increase in the FWHM ~96.73 meV. After rinsing, the PL emission was found to be at 0.470 eV and slightly red shifted, in particular, the high energy edge (see orange line in figure 6.17(c)) with respect to the As grown sample. The PL peak becomes narrower with a FWHM around 75.47 meV. InAs surfaces in particular are known to possess a high concentration of donor-type surface states[31], which results in an electron accumulation layer and Fermi level pinning located above the conduction band. Most of the changes to the PL peaks happened at the high energy tail of the emission, as the tail corresponds to the surface state emission. In the case of coating the wires, it is been found that the PL emission shifts toward higher energies, with broadening in the FWHM. We anticipate that with coating the nanowires, the

molecules of the organic compound from a disordered layer multiple molecules thick (see the middle schematic on figure 6.17(b)), which could have an associated accumulation of positive charge surrounding the nanowire. The observed blue shift in the PL spectra can be due to these positive charges near the wire surface which then will attract the electrons towards the wire surface, increasing the surface charge accumulation layer near the surface. As a result the band bending increases, causing a blue shift in the PL emission.

After rinsing the sample, most of the organic molecules will be removed, leaving only a few tightly bonded and electrically connected acceptor molecules on the InAs(Sb) surface (see the right schematic on figure 6.17 (b)), some electrons in the surface accumulation layer can then move into the electron acceptor molecules, causing a slight red shift to the emission, thus a reduction in the band bending is expected in this case. This further confirms that organic coating has affected the surface states. However, to accurately determine the effect of this treatment future work is essential, including a study on bulk InAs NWs which is less complicated than the MQWs sample (the full structural details of which have not been considered here).

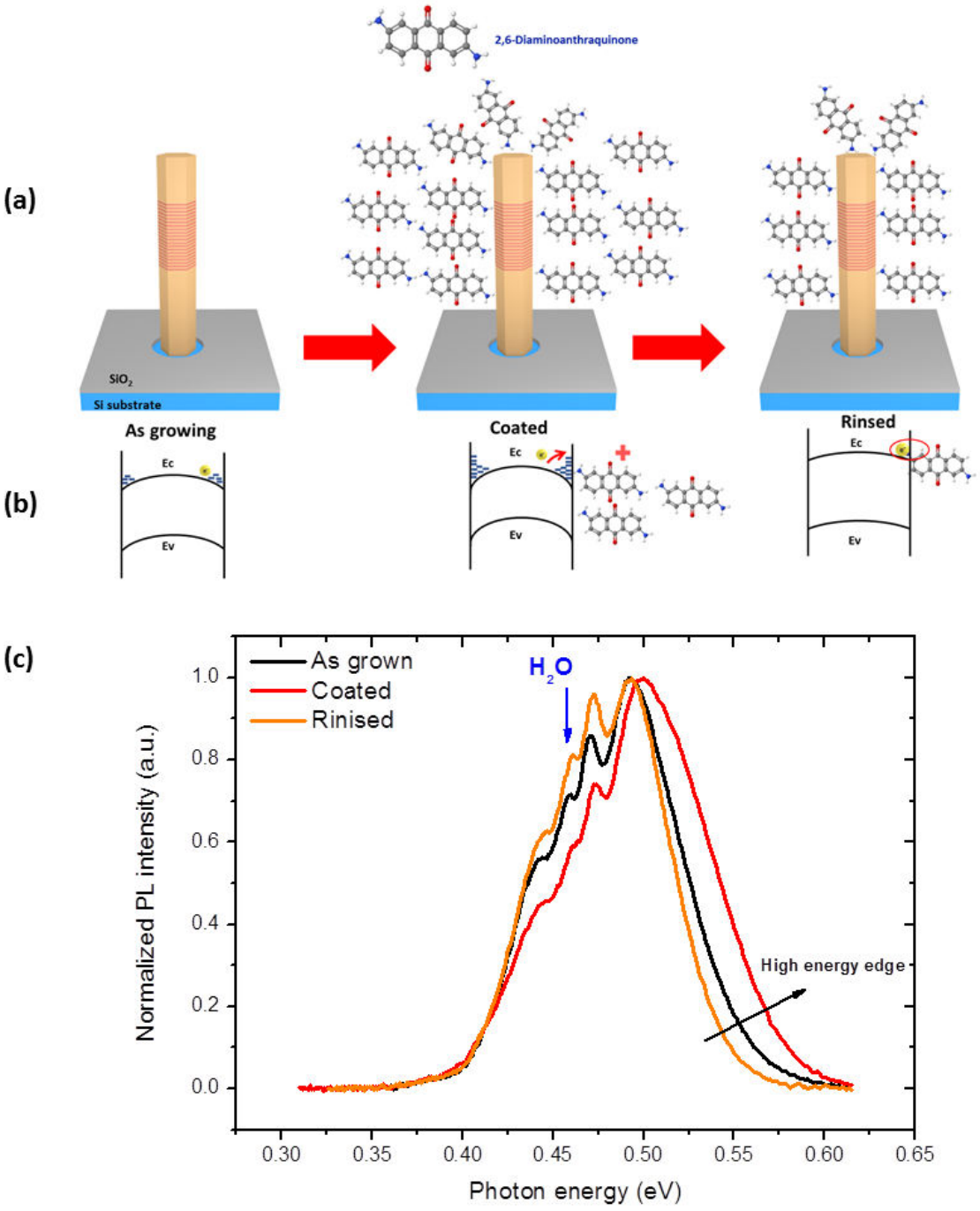

Figure 6.17. (a) A schematic diagram of the organic coating process sequence for the MQW NWs sample, (b) A schematic diagram of the band energy of the treatment sequence for the MQW NWs sample, (c) Micro-PL spectra obtained at 4 K for the organic coating process. The emission spectra measured from InAsSb/InAs MQW NWs at high power ($1.2x10^4$ Wcm^{-2}) for the sample: as grown, as coated and as rinised.

6.11. InAs/InAsSb SLS NWs: Introduction

InAs/InAsSb superlattices enable bandgap engineering which can result in greater Auger suppression, giving the potential to reach longer wavelength and to operate at higher temperatures. This work demonstrates novel SL structures within NWs which revealed mid-infrared light emission for the first time and which persists up to room temperature. The growth and structural properties of InAsSb/InAs SL embedded in InAs (Sb) NWs were investigated in this work, using STEM and PL analysis.

6.12. The growth

The substrates were annealed in the growth chamber at 600°C for 10 minutes to remove any contamination and then cooled to the growth temperature of 480°C. The SLs nanowire growth was initiated by impinging As flux followed by expose the sample to the In flux 20 seconds later. The growth started by an initial bulk InAs section for 20 minutes, followed by an InAsSb layer grown for 20 minutes. The thicknesses of these first two layers were approximately 180 and 370 nm respectively. The growth finished by deposition of the SL structure with an active region which consists of 100 repeats of InAs/$InAs_{1-x}Sb_x$ and growth durations of 180s and 27s respectively within each repeat. This was expected to form 100 repeats of 7 nm InAs and 3.5 nm $InAs_{1-x}Sb_x$, giving a total SL active region thickness of ~1.1 µm as shown in figure 6.18 (a). For comparison, the same InAs nanowires and the planar bulk InAs sample mentioned before were also used as a reference in this experiment. The nanowires were grown in arrays defined within a number of 200 µm x 200 µm areas, on each silicon substrate. From the SEM images in figure 6.18 (b) the SLs wires are longer with respect to the MQW NWs and the bulk NWs, with an average of ~2 µm in length and 100 nm in diameter.

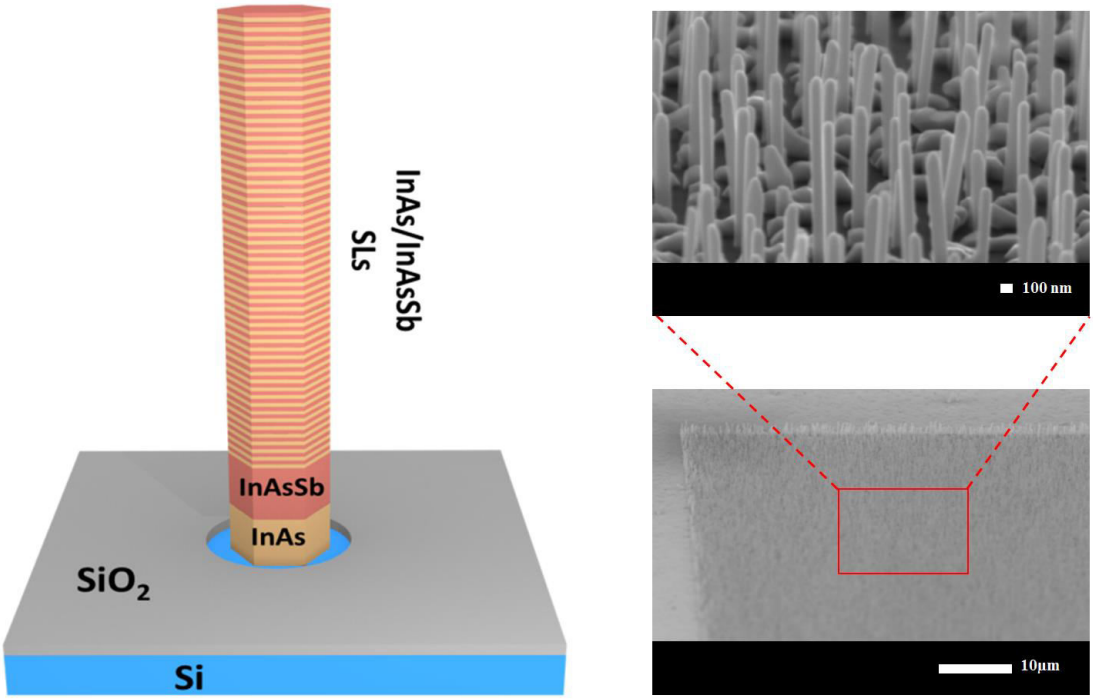

Figure 6.18. Nanowire structural design and SEM images. (a) Schematic drawing of the InAsSb/InAs SL within InAs NWs, grown in a 330 nm pitch square array patterned on a silicon substrate using a SiO_2 template with 100 nm diameter holes. (b) SEM image showing the SL NWs.

6.13. Structural analysis

The lattice structure of the InAs/InAsSb SL NWs was investigated using STEM measurments. The nanowires had a regular hexagonal cross-section formed by a polytype like structure, with multiple stacking faults on (0001)/ (111) planes for the WZ and the ZB structure respectively. The first few nanometres of the NW consist of a polytype structure, with ZB and WZ segments, commonly observed for InAs NWs. Figure 6.19 (a) represents a High magnification TEM image of the NW interface demonstrate that the NW grows directly on the Si substrate . A relatively higher concentration of Sb at ~5% was observed between 500 nm and 1µm from the Si substrate, which corresponds to the InAsSb section grown after the InAs section (see figure 6.19 (c)). Figure 6.19 (b) looking across a section of the SL in the

wire which is also formed by a polytype structure, that could be an InAs or InAsSb section of the SL period structure with the polytype like structure. However, compositional analysis did not reveal the SLs structure of the wire, due to the very thin period.

From earlier reports we found that the MQW NWs sample is almost entirely formed by WZ structure with twin and stacking faults, and the Sb preferential incorporation is consistent with the $(10\bar{1}1)$ plane or the $(1\bar{1}20)$ plane, with the 62º or 73º angle respectively, which is expected for these planes from the WZ unit cell, see figure 6.20 (a). The poly type structure in the SL case is further complicating the analysis, thus, we tried to estimate the structure based on measuring the angle on the top of the SL which is equal to 73º. It is been found that the SL is possibly grown as a ZB and WZ structure with the same angle 73º which is consisting with the $(1\bar{1}1)$ planes in the ZB unit cell (see figure 6.20), and with the $(1\bar{1}20)$ facets from the WZ unit cell (see figure 6.20 (a)).

The short growth durations are insufficient to allow a flat top to be formed as seen in comparable InAsSb NWs, and thus ending with a faceted top of the WZ $(1\bar{1}20)$ facet, or on the ZB planes $(1\bar{1}1)$ plane. However, more STEM atomic analysis are required for the whole length of the wire to support this study.

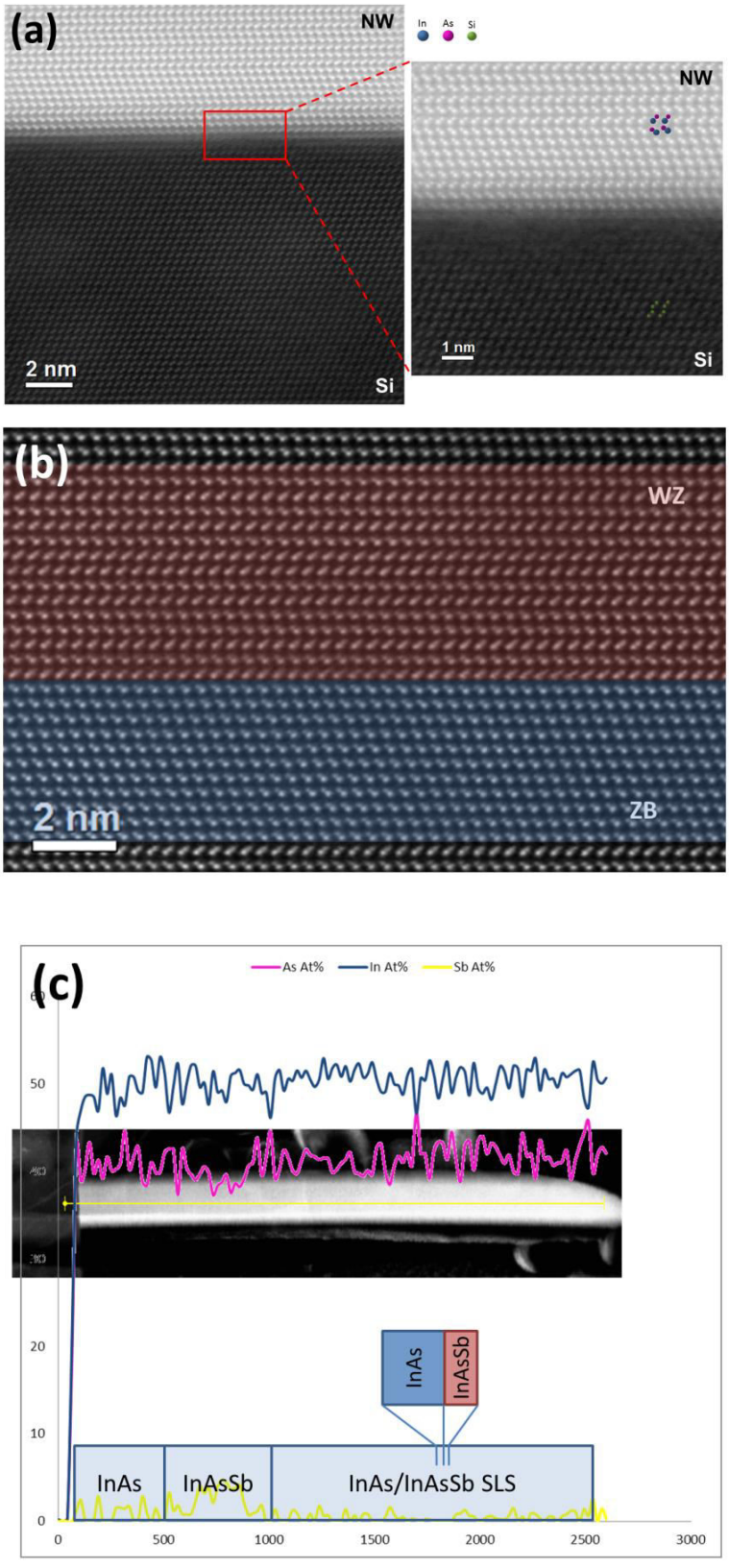

Figure 6.19. High resolution TEM analysis of the SL in NW. (a) High magnification TEM images of the interface NW/Si demonstrate that the NW grows directly on the Si substrate (left), (b) Cross-sectional TEM images, looking across a section of the SL period formed by a polytype structure with multiple stacking faults on (111)/ (0001) planes, (c) Compositional analysis of the wire showing the Presence of Sb at ~5 % between 500 nm and 1μm from the Si substrate, the SL structure is not visible in this analysis.

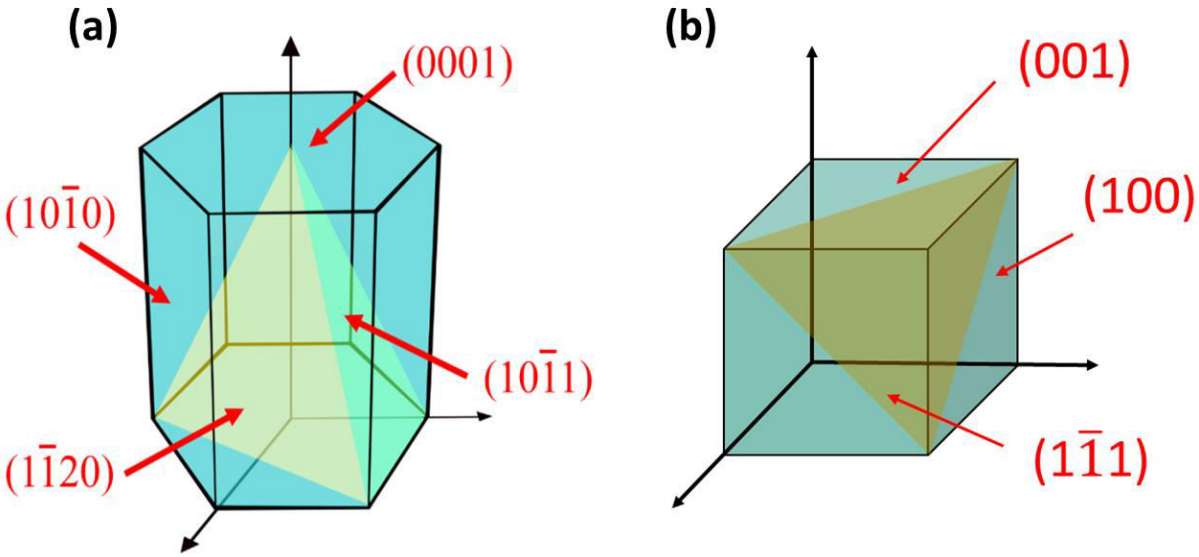

Figure 6.20. The unit cell of the WZ crystal structure showing the possible growth planes for the InAsSb SLs facets, (b) the unit cell of the ZB crystal structure showing the possible growth planes for the InAsSb SLs.

6.14. 4K PL for the sample

The optical properties of the SL NWs were studied to understand the significant changes in PL emission characteristics which occur as a result of adding 100 periods of InAsSb/InAs SL within the NWs. A comparison of the spectra measured at 4 K from the InAsSb SL NWs and InAs NW samples is shown in figure 6.21.

A shoulder on the main peak can be observed originating from WZ InAs which appears as the dominant phase in the early stage of the wires growths[11] mentioned before. Two Gaussian fits were made to the overall PL peak which reveals the spectra from the InAsSb NWs on the lower energy side at 0.38 eV and SLs emission at 0.43 eV.

The SLs emission exhibit a clear increase in peak emission energy with respect to the bulk alloy InAsSb NWs, consistent with the strong carrier confinement within the SLs. The InAsSb SL NWs also exhibit increased emission intensity and superior temperature quenching behaviour compared with the bulk NWs as expected. Most notably the emission intensity is enhanced at all temperatures, due to the quantum confinement of electrons and holes (and or much higher wave function overlap due to the significantly smaller period). PL originates from type II recombination of electrons in the InAs layers with confined hole states in the InAsSb SLs periods, where the spatial separation helps to enhance the radiative recombination[24].

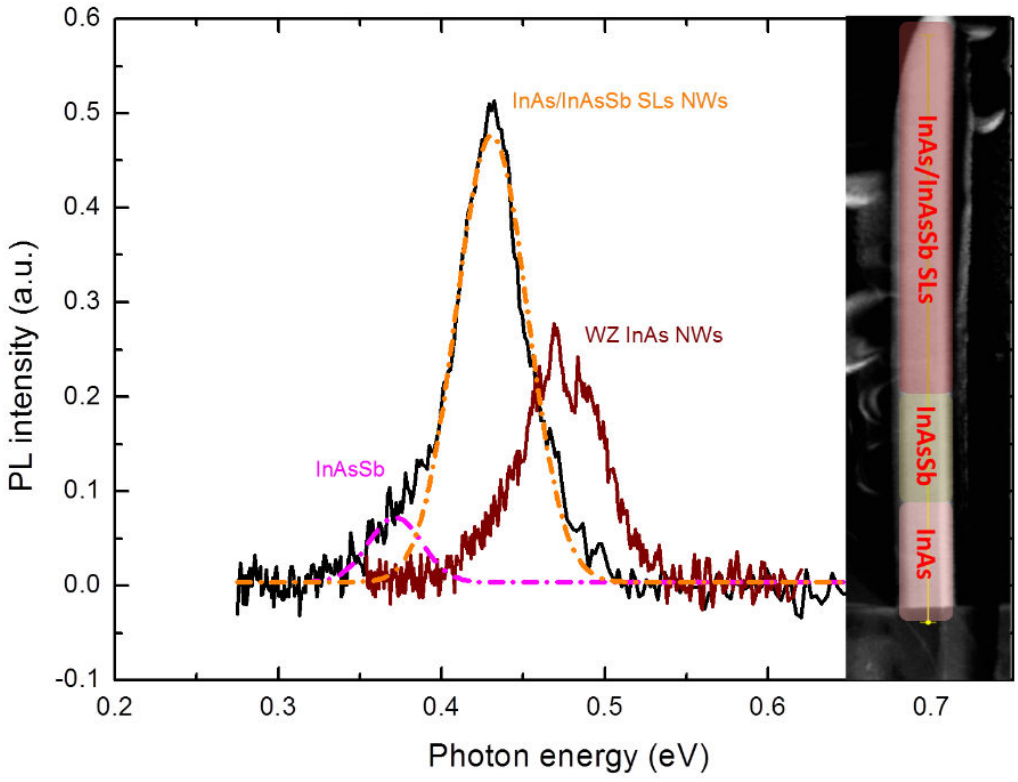

Figure 6.21. Micro-PL spectra obtained at 4 K. The emission spectra measured from a, InAsSb/InAs SL NWs and InAs NWs at low power (80 Wcm^{-2}). The dotted lines represent Gaussian fits to the spectra.

6.15. Development of a band structure for the SLs

Although the alignments are well known for (100) ZB, the InAsSb/InAs SL NWs has a phases changes and it is not in this orientation, thus describing the bandgaps and alignments for such structures is not straightforward. However, based on the band alignment used in previous work considering the Sb fraction and the strain within a (111) orientated nanowire. We suggested three possible cases; both ZB for InAs and InAsSb see figure 6.22 (a), WZ InAs with ZB InAsSb figure 6.22 (b) and both WZ for InAs and InAsSb figure 6.22 (c). The confined hole states were calculated using a six-band k.p solver in Nextnano. Considering 3nm well and 7 nm barrier, the first confined heavy hole state is calculated to be 23.7 meV above the band edge, corresponding to a flat-band recombination transition energy E_t of 0.406, 0.427 eV and 0.487 eV respectively for the three cases. The best fit for this work corresponding to the PL results is either in the first case or the second case.

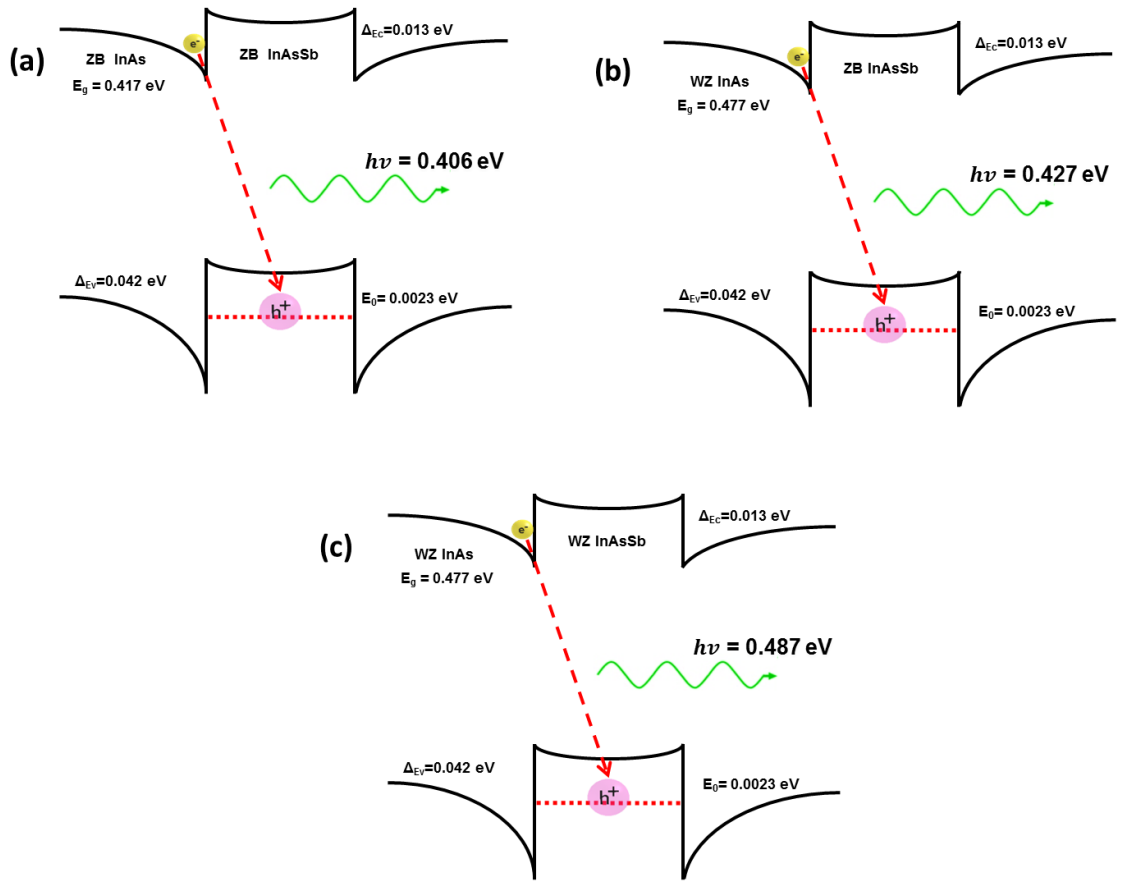

Figure 6.22. The calculated band diagram for the InAsSb/InAs SL and photon energy, showing the band bending and triangular well formation for the three cases: (a) for ZB InAs and InAsSb, (b) for WZ InAs and ZB InAsSb, (c) WZ InAs and InAsSb.

6.16. PL power dependence

As mentioned previously the higher excitation intensity (~ 10^4 Wcm^{-2}) in our micro-PL experiments results in state filling. However, the SL has a very similar dependence to the MQW NWs, with peak emission energy ranging from 0.421 eV under low excitation, to 0.453 eV under high excitation, as shown in figure 6.23. The PL emission energy from the InAs NWs blue shifted by 21 meV and is associated with band filling, the shift for the MQW NWs is much larger, at 45 meV, however, the shift for the SL at 32 meV is between the InAs and the MQWs (see figure 6.23). This blue shift is very similar to MQWs where most of it

happens at low pump powers then the dependence becomes similar to that for bulk InAs wires at higher powers. We believe that the blue shift in the SL nanowires arises due to band bending effects characteristic of type II QWs and originates from Coulomb attraction between localised holes in the InAsSb quantum well attracting electrons from the adjacent InAs barrier forming triangular quantum wells. The flat band transition energy of the InAsSb/InAs SLs is extracted from the intercept of figure 6.24 (c) - the PL peak position versus $L^{1/3}$. Consequently, the flat band transition energy for the InAsSb/InAs SL NWs is obtained as 0.4095 eV which is in good agreement with the calculated transition energy of 0.406 eV, as shown in the schematic band diagram in figure 6.24 (a), this value also agree with the calculated transition energy of 0.427 eV (figure 6.24 (b)). Which is likely the case from our estimated structure, further analysis are going on to support this point.

The power dependence of the MQW NWs shows that it is following the typical $\Delta E \sim L^{1/3}$ behavior where L is integrated PL intensity, which been previously analyzed in a bulk QWs system. The SL NWs have the same power dependence which is due to self-consistent charging QWs, where the carriers are localized at the interface, the holes are confined in the quantum well, and the electrons are attracted toward the interface. Although there is uncertainty about this value, the calculated values are well agreed with the predicted ones.

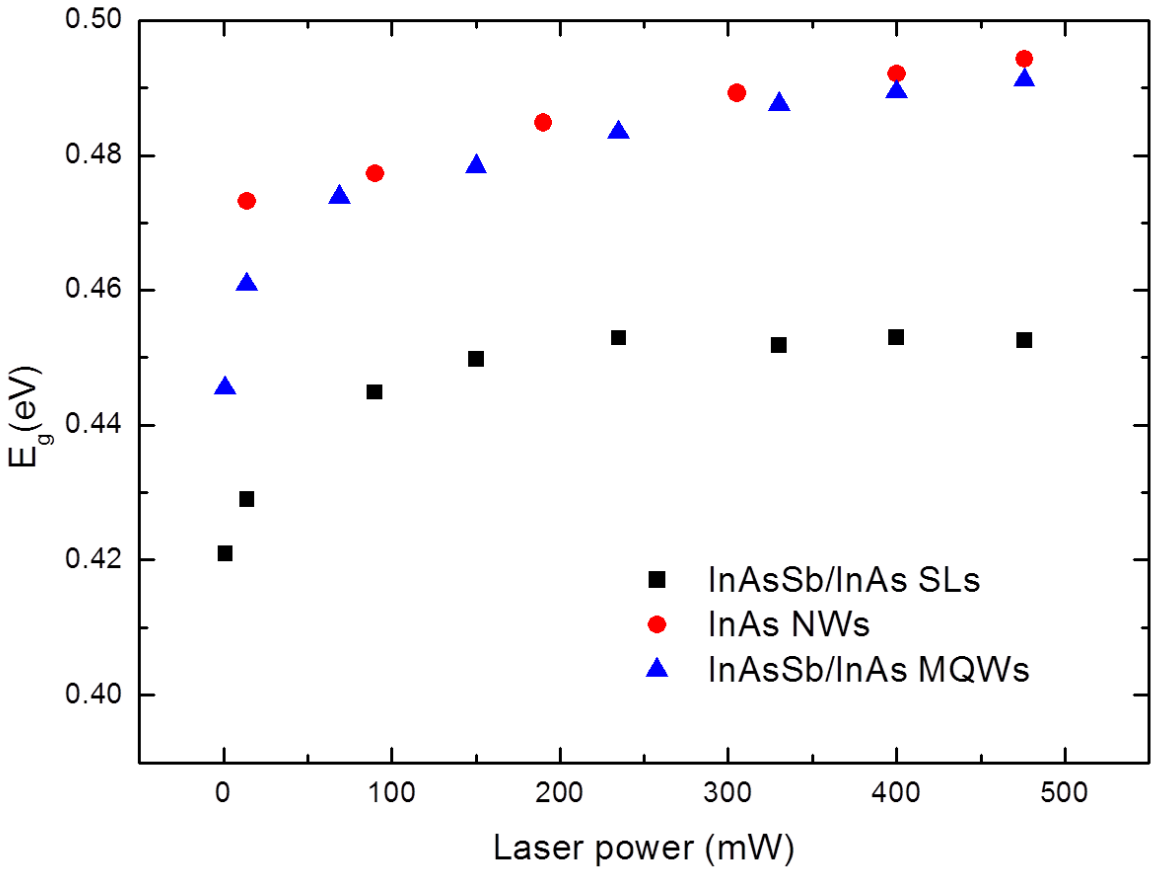

Figure 6.23. Power dependence of PL emission. The dependence of the peak emission energy on the power of the pump laser incident on the sample, for InAs, InAsSb/InAs MQW and InAsSb/InAs SLs NWs. Showing the difference in the blue shift between the three NWs, with minimal quantum confinement effects and the SLs NW, with strong quantum confinement and charging effects.

The k value was calculated from plotting the integrated intensity and laser power, as shown in figure 6.25 (see chapter 2). The SLs had a k value of 0.75 which is the same value for the MQWs and corresponds to free- and bound exciton transitions[32]. Having the same K value as the MQWs would suggests that impurity-like recombination processes are also involved, similar to what mentioned for the InAs and InAsSb NWs in chapter five, because of the large surface charge density, the Fermi level for InAs is pinned in the conduction band.

The surface Fermi level pinning and associated band bending at the surface may result in spatially separated electrons near the surface and holes confined rather in the centre of the NW.

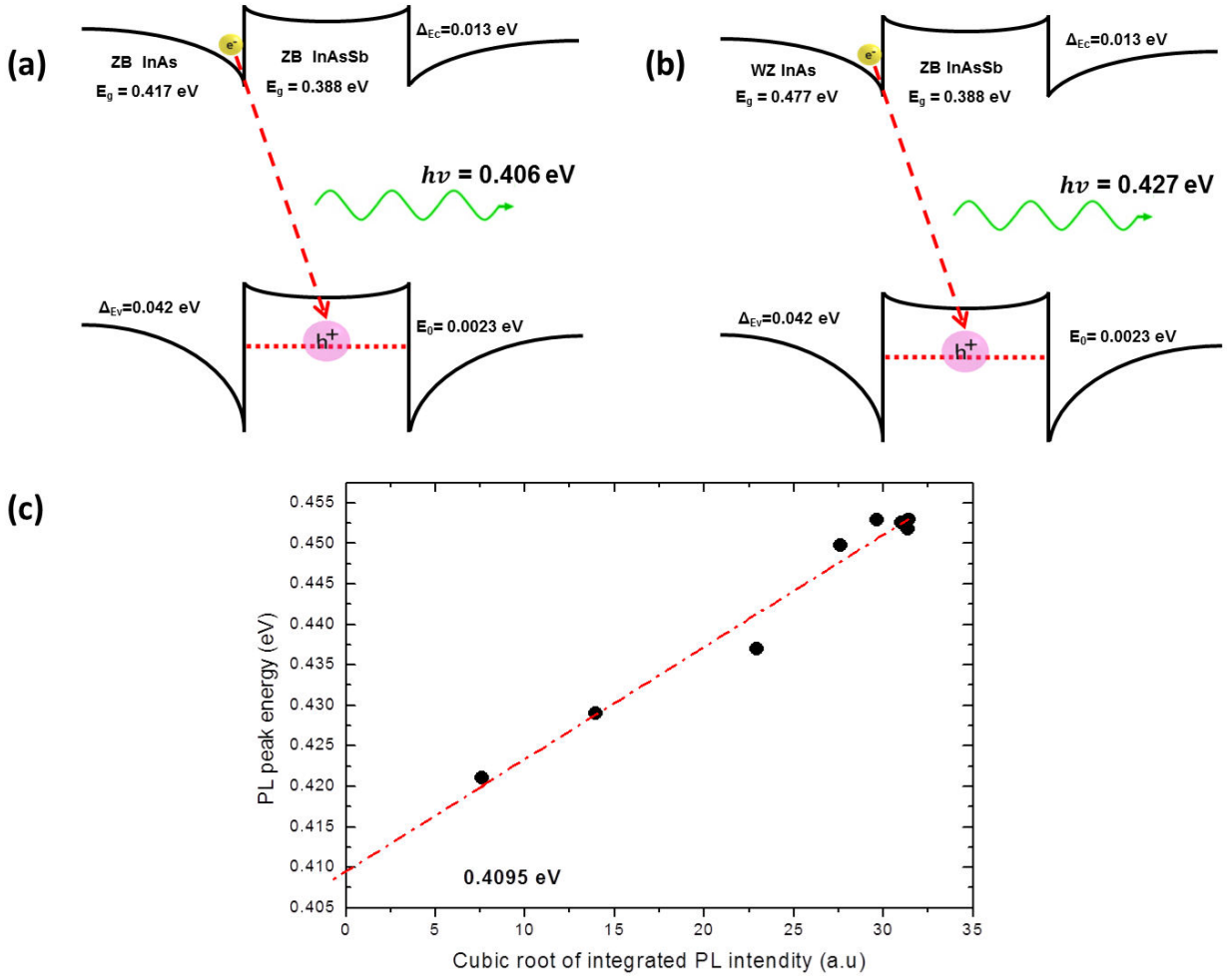

Figure 6.24. Determination of the flat band transition energy at the SL. (a) the calculated band diagram for the InAsSb/InAs SL and photon energy for ZB InAs and InAsSb, showing the band bending and triangular well formation, (b) the calculated band diagram for the InAsSb/InAs SL and photon energy for WZ InAs and ZB InAsSb, showing the band bending and triangular well formation, (c) PL peak energy vs cube root of integrated PL intensity, elucidating the charging of the type II QW and allowing the flat band transition energy to be identified.

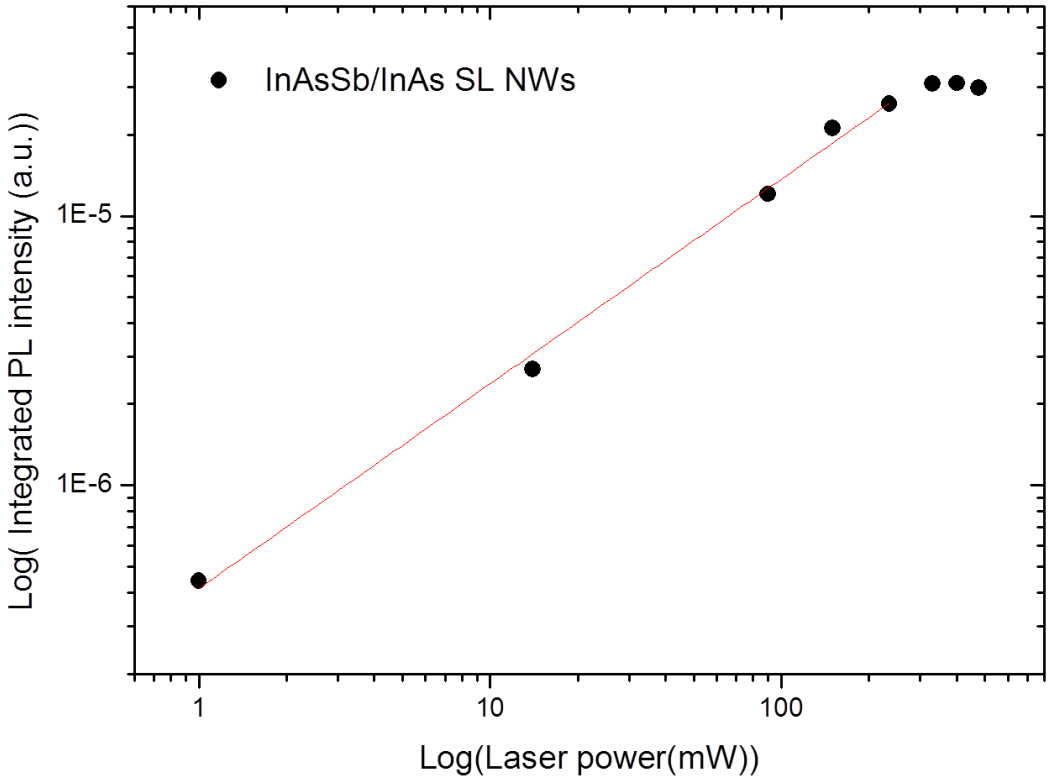

Figure 6.25. Excitation power dependent PL spectra recorded at 4K for the InAs/InAsSb NWs, showing K value of 0.75 for the InAs/InAsSb NWs.

6.17. PL temperature dependence

The PL spectra for the InAsSb SLs NWs are obtained at different temperatures and are shown in figure 6.26. The wires exhibit strong PL emission which persists up to room temperature. This may indicate a similar result to the MQWs where radiative recombination ensued mostly in the SLs and not near the wires surface, which is typically for InAs NWs to be accumulated due to Fermi level pinning as discussed before[33]. In this case, the quantum confinement of the SLs enables room temperature emission to be observed without passivation. All the samples follow a similar trend with respect to the inhomogeneous broadening in the PL spectra due to

length variations in the NWs which in turn causes variations of the SLs thickness. The atmospheric water vapour absorption is again evident near 2.7 μm (0.459 eV) in all the spectra.

Figure 6.27 presents a comparison of the temperature quenching of the samples. Although the QWs has the brightest PL emission, the SLs has better quenching which is clearly evident due to the increase in the radiative emission rate and suppression of Auger recombination in both samples with respect to bulk NWs. The PL intensity is enhanced compared to the InAs NWs, however, it is lower in intensity with respect to the MQW NWs. This can be attributed to the band bending effect in the MQWs which would then act to localize the electrons at the interface and increase the e-h wave function overlap, thus the PL intensity increased. However, in the SLs case, the separation of electron wave function into the InAsSb wells caused by the very thin barriers (7nm) and the low conduction band offset (13meV), should also improves the e-h wave function overlap but it is not the case here as the PL intensity reduced. All the PL measurements for the MQWs and the SLs have been done consistently, thus measurements faults are unlikely a reason for reducing the PL intensity. Further investigations are going on for better understanding.

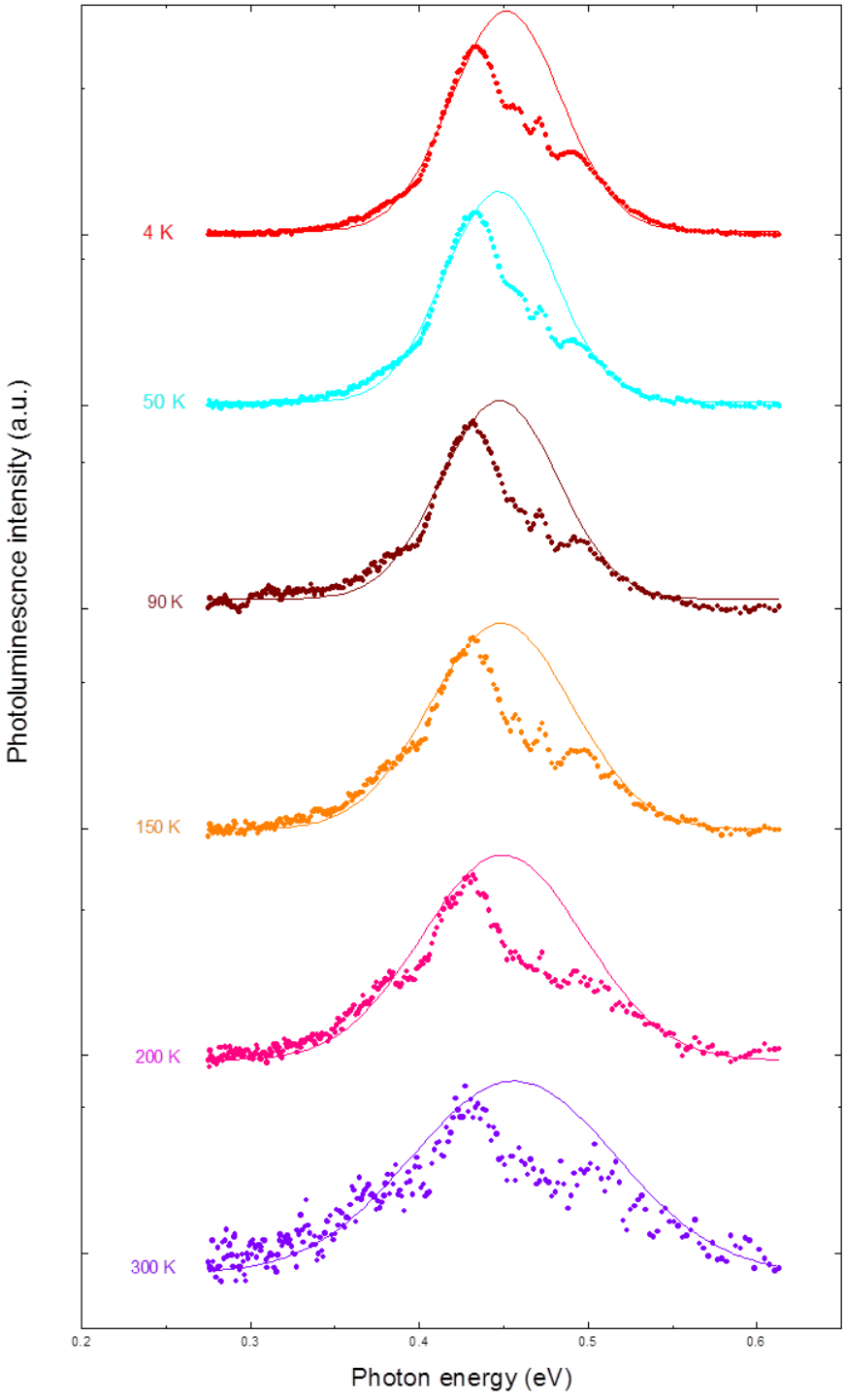

Figure 6.26. Temperature dependence of the PL emission spectra obtained from the InAsSb SL NWs. Emission spectra measured over the range 4-300 K using high excitation (2.6×10^4 Wcm^{-2}), showing the room temperature emission required for future practical NW infrared emitters. Dotted lines indicate Gaussian fits used to extract the peak emission wavelength. Atmospheric water vapour absorption is again evident in all the spectra.

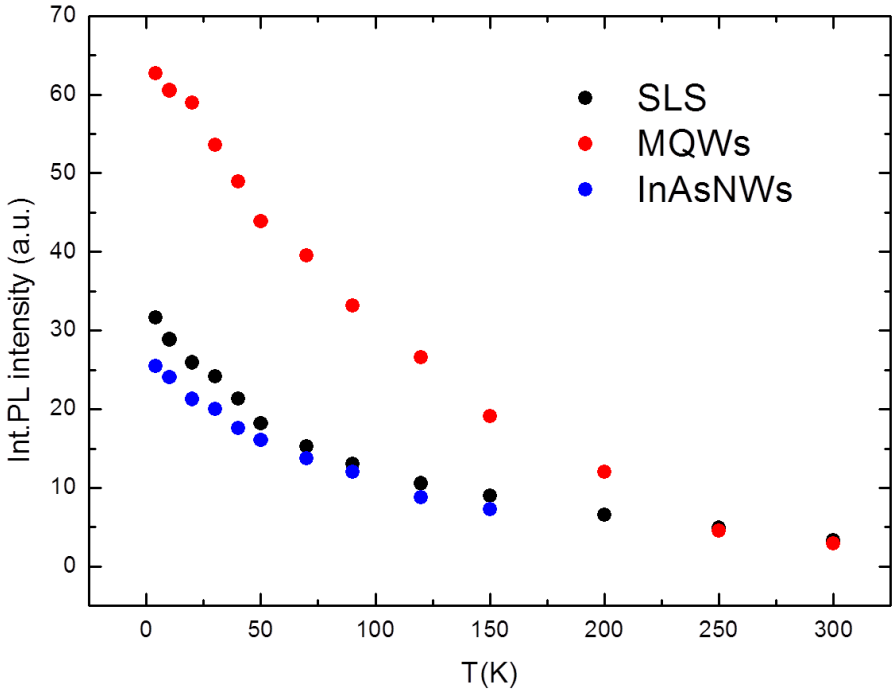

Figure 6.27. Temperature dependent analysis of PL emission for InAs, InAsSb/InAs MQW and InAsSb/InAs SL NWs, represent the integrated PL intensities as a function of temperature, which shows the quenching behaviour of the three NW sample.

The temperature dependence of the peak energies for the NWs is shown in figure 6.28. The SL is following an unusual temperature dependence which does not follow the Varshni equation with an almost liner fit. The grown SLs have a complicated structure which could be a possible reason for the unusual behaviour of the wires. The SLs type structure contains an InAs layer at the bottom of the wires followed by InAsSb layer then the SLs structure at the top of the wire, each layer of this structure should obey different temperature dependence, hence different Varshni parameters. Another reason could be a disorder of Sb fluctuation in the SLs. Further analyses are required for more understanding of this dependence.

An Arrhenius plot is shown in figure 6.29 for the InAsSb SL NWs from which an activation energy of 15 meV was obtained from the high temperature region and ~1.86 meV for the low temperature region. This is approximately in agreement with the confinement

energy for thermal excitation of holes out of a single (3nm) QW in the SL (hole localisation energy of 19 meV) and electrons from the interface triangular QWs (< 13 meV localisation energy) respectively.

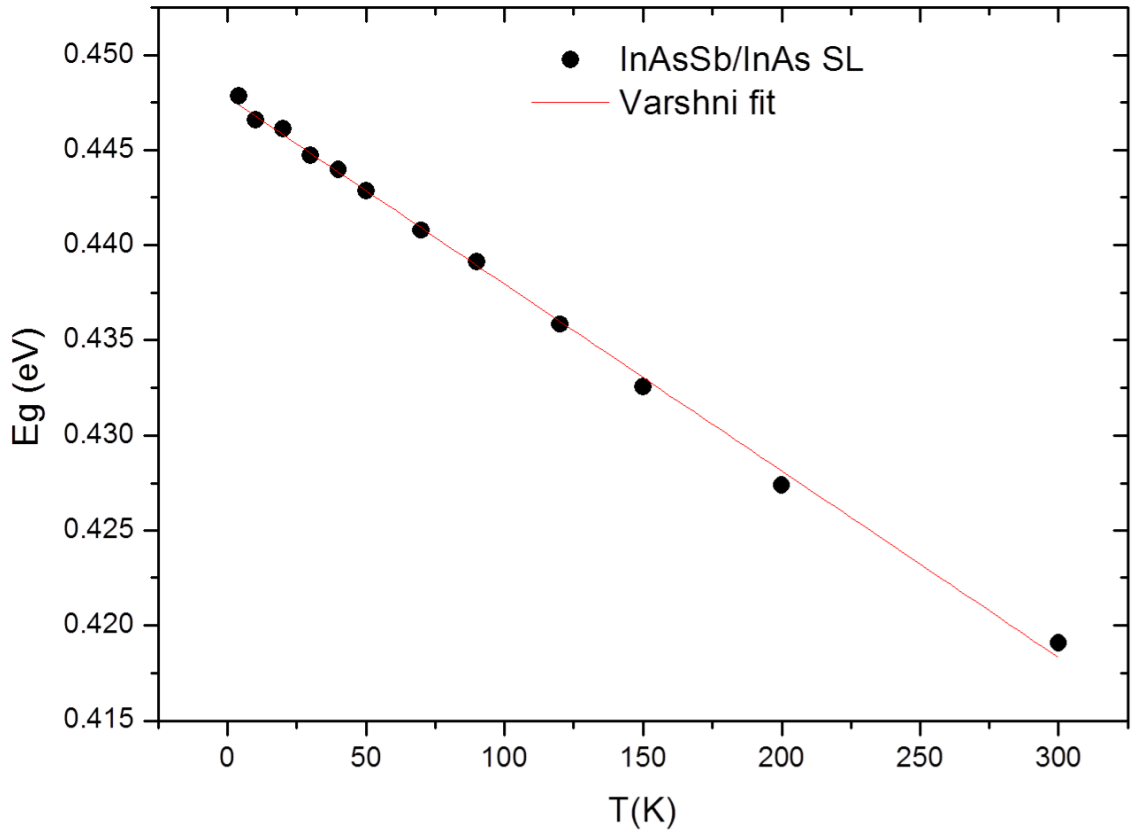

Figure 6.28. Temperature dependent analysis of PL data from the InAsSb/InAs SL, sample. The temperature dependence of the PL peak emissions (points), which is not following the Varshni relationships.

	E_0 (eV)	α (meV/K)	β (K)
InAs bulk	0.417	0.276	93
InSb bulk	0.235	0.320	170
InAs NWs	0.494	0.126	47
InAsSb NWs	0.380	0.133	42
InAsSb/InAs MQW NWs	0.484	0.099	97
InAsSb/InAs SL NWs	0.447	0.981	$4.4e^{-5}$

Table 2: Comparison of Varshni parameters. The fitted Varshni parameters E_0, α and β for the NW samples, compared with published parameters for bulk InAs and InSb[21].

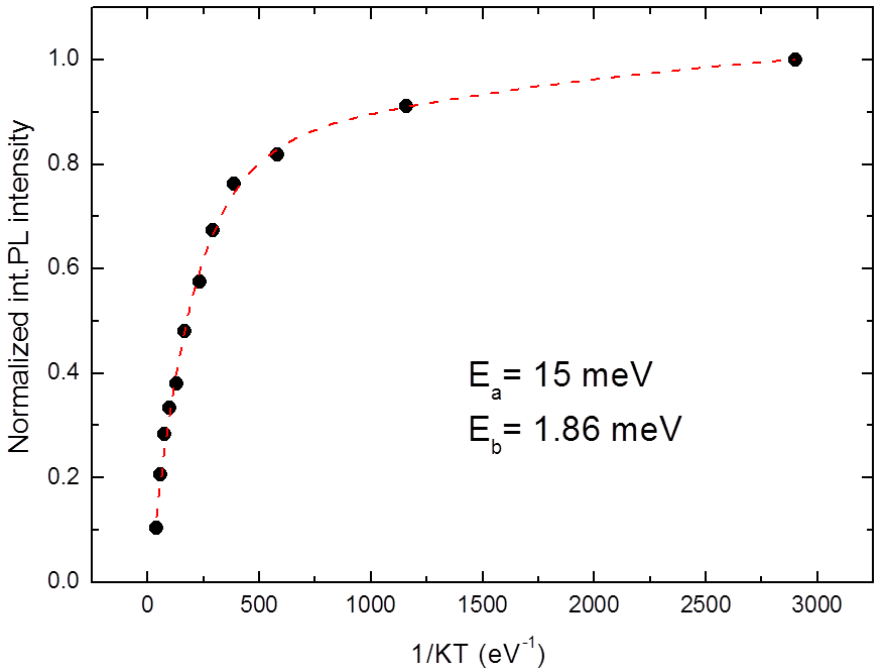

Figure 6.29. Temperature dependent analysis of PL data from the InAsSb/InAs SLs sample shows an Arrhenius plot of integrated PL intensity as a function of inverse temperature used to extract activation energies for the mechanisms driving thermal quenching.

6.18. Conclusion

Development of quantum structures in NWs systems have shown their applicability to extend the concept of bandgap engineering not only to be used as building blocks for such systems, but also to be integrated further into the leading CMOS technology, providing a promising future for nanotechnology in optics and electronics. In this work, we have demonstrated novel InAsSb MQWs and InAsSb SLs structures within NWs which exhibit mid-infrared emission at room temperature for the first time. Type II QWs provide quantum confinement, spatial localisation of the carriers and Auger suppression, resulting in enhanced PL emission. Both structures exhibited enhanced PL emission with respect to the bulk InAs NWs. However, even though the MQWs is 5 times enhanced compared to the SLs, both

structures have PL emission which persists up to room temperature. Furthermore, having characterised the effect of charging on the type II QW, the flat band transition energy is found to be in good agreement with calculations for both samples. These new quantum structured NWs will allow novel nano-photonic and quantum light sources to be developed for the technologically important mid-infrared spectral range. They can exploit both the general advantages of site controlled NWs, such as integration with silicon substrates, and also enhance light-matter coupling based on their dimensions and geometry, opening the way for a wide range of applications.

6.19. References

[1] Caroff, P.; Dick, K.; Johansson, J.; Messing, M.; Deppert, K.; Samuelson, L. Controlled Polytypic and Twin-Plane Superlattices in III–V Nanowires. Nature Nanotechnology 2008, 4, 50-55.

[2] Johansson, J.; Bolinsson, J.; Ek, M.; Caroff, P.; Dick, K. A. Combinatorial Approaches to Understanding Polytypism in IIIV Nanowires. ACS Nano 2012, 6, 6142−6149. PMID: 22681568

[3] Dick, K.; Thelander, C.; Samuelson, L.; Caroff, P. Crystal Phase Engineering in Single InAs Nanowires. Nano Letters 2010, 10, 3494-3499.

[4] Sourribes, M., Isakov, I., Panfilova, M., Liu, H. & Warburton, P. Mobility Enhancement by Sb-Mediated Minimisation of Stacking Fault Density in InAs Nanowires Grown on Silicon. Nano Lett. 2014, 14, 1643-1650.

[5] Wu, J.; Ramsay, A.; Sanchez, A.; Zhang, Y.; Kim, D.; Brossard, F.; Hu, X.; Benamara, M.; Ware, M.; Mazur, Y. et al. Defect-Free Self-Catalyzed GaAs/GaAsP Nanowire Quantum Dots Grown on Silicon Substrate. Nano Letters 2015, 16, 504-511.

[6] Reimer, M.; Bulgarini, G.; Akopian, N.; Hocevar, M.; Bavinck, M.; Verheijen, M.; Bakkers, E.; Kouwenhoven, L.; Zwiller, V. Bright Single-Photon Sources in Bottom-up Tailored Nanowires. Nature Communications 2012, 3, 737.

[7] Yang, L.; Motohisa, J.; Takeda, J.; Tomioka, K.; Fukui, T. Size-Dependent Photoluminescence of Hexagonal Nanopillars With Single InGaAs⁄GaAs Quantum Wells Fabricated by Selective-Area Metal Organic Vapor Phase Epitaxy. Applied Physics Letters 2006, 89, 203110.

[8] Ra, Y.; Navamathavan, R.; Park, J.; Lee, C. High-Quality Uniaxial $In_xGa_{1-X}N$/GaN Multiple Quantum Well (MQW) Nanowires (NWs) on Si (111) Grown by Metal-Organic Chemical Vapor Deposition (MOCVD) and Light-Emitting Diode (LED) Fabrication. ACS Applied Materials & Interfaces 2013, 5, 2111-2117.

[9] Armitage, R.; Tsubaki, K. Multicolour Luminescence from InGaN Quantum Wells Grown Over GaN Nanowire Arrays by Molecular-Beam Epitaxy. Nanotechnology 2010, 21, 195202.

[10] Farrell, A.; Lee, W.; Senanayake, P.; Haddad, M.; Prikhodko, S.; Huffaker, D. High-Quality InAsSb Nanowires Grown by Catalyst-Free Selective-Area Metal–Organic Chemical Vapor Deposition. Nano Lett. 2015, 15, 6614-6619.

[11] Thompson, M.; Alhodaib, A.; Craig, A.; Robson, A.; Aziz, A.; Krier, A.; Svensson, J.; Wernersson, L.; Sanchez, A.; Marshall, A. Low Leakage-Current InAsSb Nanowire Photodetectors on Silicon. Nano Lett 2016, 16, 182-187.

[12] Rota, M.; Ameruddin, A.; Fonseka, H.; Gao, Q.; Mura, F.; Polimeni, A.; Miriametro, A.; Tan, H.; Jagadish, C.; Capizzi, M. Bandgap Energy of Wurtzite InAs Nanowires. Nano Lett. 2016, 16, 5197-5203.

[13] Carrington, P.; Zhuang, Q.; Yin, M.; Krier, A. Temperature Dependence of Mid-Infrared Electroluminescence in Type II InAsSb/InAs Multi-Quantum Well Light-Emitting Diodes. Semiconductor Science and Technology 2009, 24, 075001.

[14] Koblmüller, G.; Vizbaras, K.; Hertenberger, S.; Bolte, S.; Rudolph, D.; Becker, J.; Döblinger, M.; Amann, M.; Finley, J.; Abstreiter, G. Diameter Dependent Optical Emission Properties of InAs Nanowires Grown on Si. Appl. Phys. Lett. 2012, 101, 053103.

[15] Lord, S.D., NASA Tech. Memo. 103957 (1992).

[16] Svensson, J.; Anttu, N.; Vainorius, N.; Borg, B.; Wernersson, L. Diameter-Dependent Photocurrent in InAsSb Nanowire Infrared Photodetectors. Nano Lett 2013, 13, 1380-1385.

[17] Predicted band structures of III-V semiconductors in the wurtzite phase A. De and Craig E. Phys. Rev. B. 2011, 84, 239907.

[18] J. D. Heber and C. C. Philips, InAs/InAsSb emitters for the mid-infrared region, Chapter in "III-V Semiconductor Heterostructures: Physics and Devices", ed. by W. Z. Cai, Keraia: Research Signpost, 2003 pp. 140-167.

[19] Möller, M.; de Lima Jr, M.; Cantarero, A.; Chiaramonte, T.; Cotta, M.; Iikawa, F. Optical Emission of InAs Nanowires. Nanotechnology 2012, 23, 375704.

[20] Olsson, L.; Andersson, C.; Håkansson, M.; Kanski, J.; Ilver, L.; Karlsson, U. Charge Accumulation at InAs Surfaces. Physical Review Letters 1996, 76, 3626-3629.

[21] Latkowska, M. et al. Temperature Dependence of Photoluminescence from InNAsSb Layers: The Role of Localized and Free Carrier Emission in Determination of Temperature Dependence of Energy Gap. Appl. Phys. Lett. 2013, 102, 122109.

[22] Zegrya G.G. and Andreev A.D. Mechanism of suppression of Auger recombination processes in type II heterostructures, Appl. Phys. Lett. **1995**, 67(18) 2681.

[23] Farrell, A.; Lee, W.; Senanayake, P.; Haddad, M.; Prikhodko, S.; Huffaker, D. High-Quality InAsSb Nanowires Grown by Catalyst-Free Selective-Area Metal–Organic Chemical Vapor Deposition. Nano Lett. 2015, 15, 6614-6619.

[24] R. People, J.C. Bean, Calculation of critical layer thickness versus lattice mismatch for Ge_xSi_{1-x}/Si strained-layer heterostructures, Applied Physics Letters 47(3), 322-324 (1985).

[25] Dominating nucleation of misfit dislocations from the surface in GeSi/Si(0 0 1) films with a stepwise composition grown by means of molecular-beam epitaxy, Yu.B. Bolkhovityanov, A.S. Deryabin, A.K. Gutakovskii, M.A. Revenko, L.V. Sokolov, Journal of Crystal Growth 293, 247-252 (2006).

[26] Carrington, P.; Zhuang, Q.; Yin, M.; Krier, A. Temperature Dependence of Mid-Infrared Electroluminescence in Type II InAsSb/InAs Multi-Quantum Well Light-Emitting Diodes. Semiconductor Science and Technology 2009, 24, 075001.

[27] Sun, M.; Leong, E.; Chin, A.; Ning, C.; Cirlin, G.; Samsonenko, Y.; Dubrovskii, V.; Chuang, L.; Chang-Hasnain, C. Photoluminescence Properties of InAs Nanowires Grown on GaAs and Si Substrates. Nanotechnology, 2010, 21, 335705.

[28] Petrovykh, D.; Yang, M.; Whitman, L. Chemical and Electronic Properties of Sulfur-Passivated InAs Surfaces. Surface Science 2003, 523, 231-240.

[29] Shu, H.; Cao, D.; Liang, P.; Jin, S.; Chen, X.; Lu, W. Effect Of Molecular Passivation on The Doping f InAs Nanowires. The Journal of Physical Chemistry C 2012, 116, 17928-17933.

[30] Sun, M.; Joyce, H.; Gao, Q.; Tan, H.; Jagadish, C.; Ning, C. Removal of Surface States And Recovery of Band-Edge Emission in InAs Nanowires Through Surface Passivation. Nano Letters 2012, 12, 3378-3384.

[31] Halpern, E.; Elias, G.; Kretinin, A.; Shtrikman, H.; Rosenwaks, Y. Direct Measurement of Surface States Density and Energy Distribution in Individual InAs Nanowires. Applied Physics Letters 2012, 100, 262105.

[32] Schmidt, T. and Lischka, L. Phys Rev B, 1992, 45 8989.

[33] Olsson, L.; Andersson, C.; Håkansson, M.; Kanski, J.; Ilver, L.; Karlsson, U. Charge Accumulation at InAs Surfaces. Physical Review Letters 1996, 76, 3626-3629.

Chapter 7

InAsSb Nanowire Photodetectors on Silicon

7.1. Introduction

This chapter is focused on utilising nanowires for optoelectronic applications. A low leakage current and high photoresponse is obtained at room temperature from a simple photodiode structure. Interestingly, the measured dark current for the fabricated photodetector is significantly below the best results reported for large area InAs photodiodes, ~100 mA/cm^2, which typically also suffer from high levels of surface leakage. This paves the way towards realizing efficient nanowire based photodetectors in the mid infrared range at room temperatures.

7.2. Detector growth

The nanowires were grown on boron-doped (111) orientated Si substrates with a known oxide thickness of 25 nm using selective area catalyst free growth. The catalyst free method used in this work is favoured to avoid metal incorporation[1], this is because metals such as gold can form trap states in silicon that limit the efficiency of the fabricated photodetectors[2]. In addition, growing on Si substrates provides opportunities in monolithic integration of III-V optoelectronic technology on the widely industrially used electronic material[3]. Following the preparation process mentioned earlier, the substrate was immediately loaded into the MBE reactor to start the growth. The substrate was then heated up to 600 °C to remove any contaminants, before being cooled to the growth temperature of 480 °C. The same growth conditions mentioned in the chapter five for the InAs(Sb) NWs were kept constant for the sample used in this work. The samples grown in this work have an Sb composition of 6-7 %. Dopant cell temperatures were set according to the measured concentrations in 2D InSb grown at a rate of 1µm/hr of 7×10^{17} cm^{-3} for Be and 5×10^{17} cm^{-3} for Te.

7.3. Photodetector fabrication

The main idea behind growing such NWs structures is to use them for improving the performance of NW based mid-infrared photodetector devices compared to those of bulk materials. Despite the challenges, such improvements can solve technical problems related to large lattice mismatch[4], as the growth mechanism for the nanowire gives a natural way for relaxing the lattice strain at the interface and achieves high crystal quality by reducing the potential lattice faults within the structures [5]. However, from earlier TEM analysis, the grown NWs have few lattice faults, such as twin defects, stacking faults and zinc-blende wurtzite polytypism structure. The existence of the twin defects and stacking faults could be a reason for electron scattering[6], which increases the resistivity. Also, the polytype phase as seen in InAs stems can lead to unwanted uncontrollable heterostructures due to the different bandgaps of the ZB and WZ phases[7]. However, as discussed earlier the addition of Sb forces a ZB phase with ortho twins which do not change the polarity of the crystal along the nanowire. Thus, maintaining this crystalline quality which we believe is high enough to obtain a high efficiency device, the nanowire photodetectors were fabricated by growing a 2µm pitch array of NWs with axial p−i−n junctions. The structure of the NWs consisting of 250 nm p-type (Be doped) InAs followed by 500 nm p-type InAsSb, 500 nm undoped InAsSb, and finally 500 nm n-type (Te doped) InAsSb. The schematic of a finished device is shown in Figure 4Figure 7.1 which highlights the different sections of the nanowire. Next, the fabrication process of the photodetectors was completed by spin coating the wires with 2 µm thick SU-8 and flood exposing with UV light, to harden the resist. The resist was then etched back using reactive ion etching in CF_4 and O_2 to expose the tips of the wires. The wire tips were then contacted using an optically opaque Ti/Au (30 nm Ti and 200 nm Au) while 200 nm Al was deposited on the back of the substrate as shown in Figure 7.2.

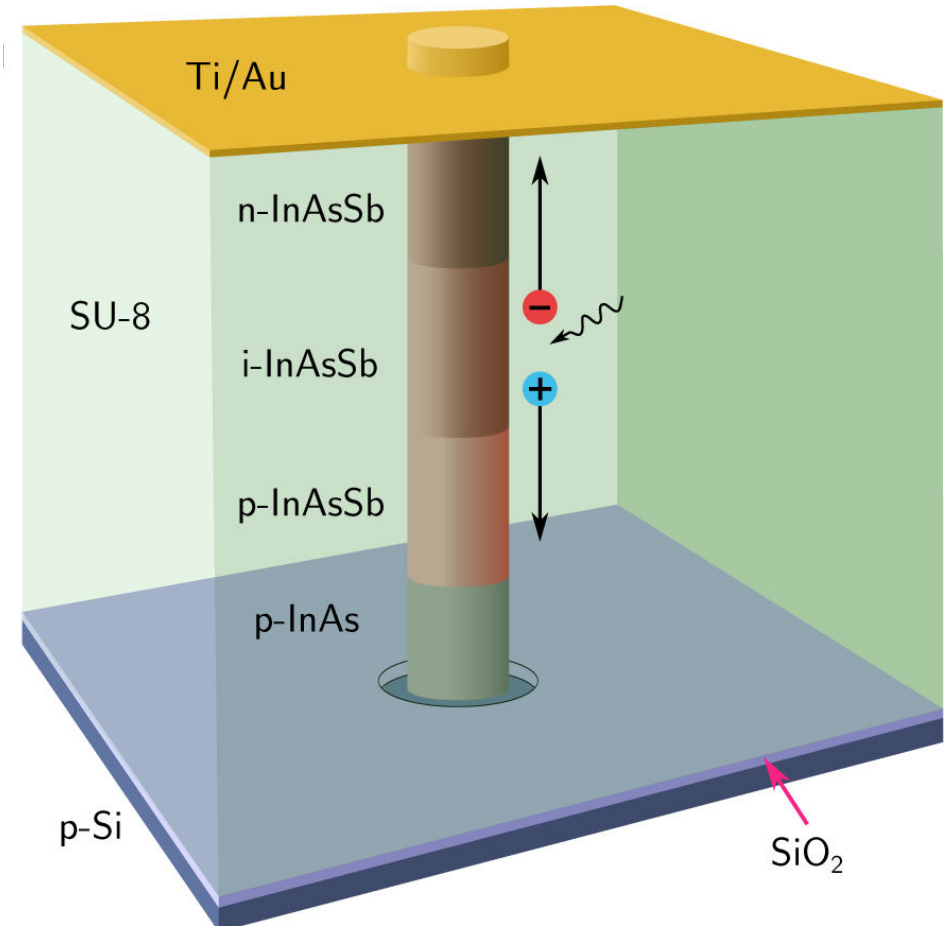

Figure 7.1. Schematic of p−i−n InAsSb nanowire photodiode. (a) The nanowire consists of a 200 nm Be doped InAs stub followed by 500 nm Be doped InAsSb, 500 nm undoped InAsSb and 500 nm Te doped InAsSb.

Figure 7.3 is a band diagram at zero bias for the full structure. In devices where the junction occurs at the interface between the nanowire and the substrate, the band offsets between the nanowire and silicon can obstruct the movement of the carriers. By growing a p−i−n structure, the voltage drop principally occurs across the intrinsic region of the nanowire, where the photogenerated carriers can drift easily into the majority carrier regions. Subsequent conduction across the NW to Silicon interface is then by majority carrier movement through a heavily doped interface.

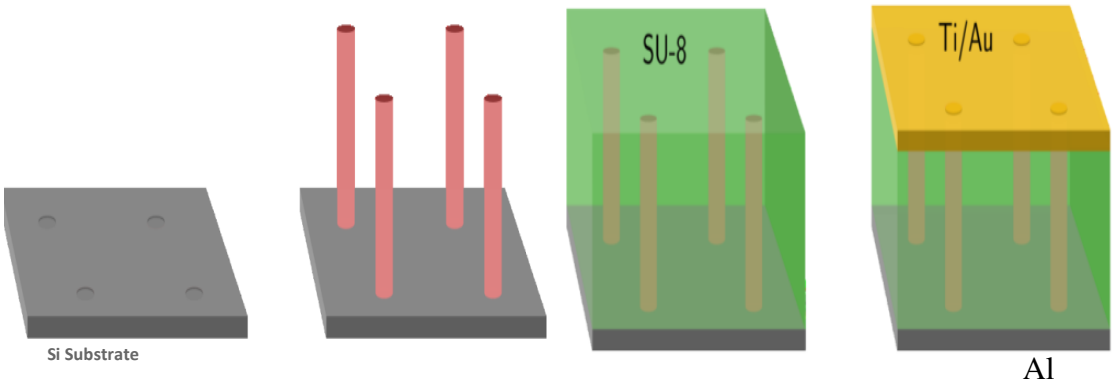

Figure 7.2. The Photodetector fabrication steps. The nanowire is encapsulated by cross-linked SU-8, with Ti/Au forming the top contact and Al on the back of the substrate forming the back contact.

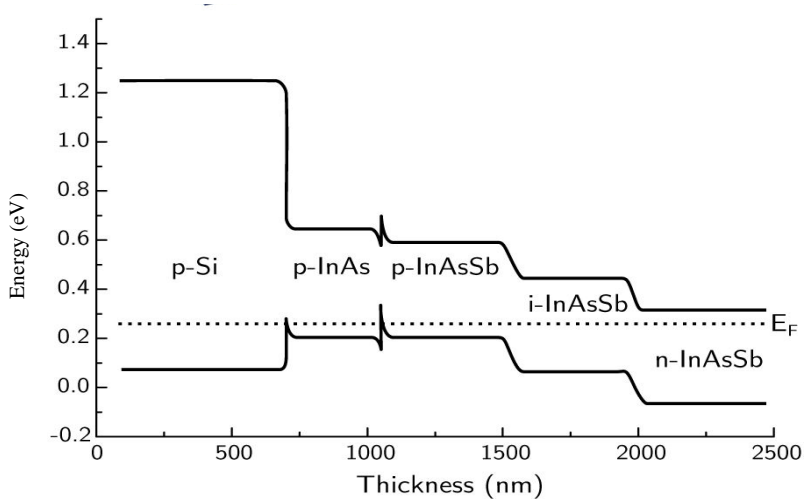

Figure 7.3. Band diagram of the p−i−n photodiode at zero bias. Showing the band offsets between the nanowire and silicon.

A microscope image of the processed sample is shown below in Figure 7.4. The dark squares are nanowire arrays with different pitches and diameters. The light grey areas are resist windows which will define Ti/Au contacts of exactly the same area. It should be noted that at this research stage we did not have a customised contact pattern to use, hence another device's contact pattern is used to make contact to some wires.

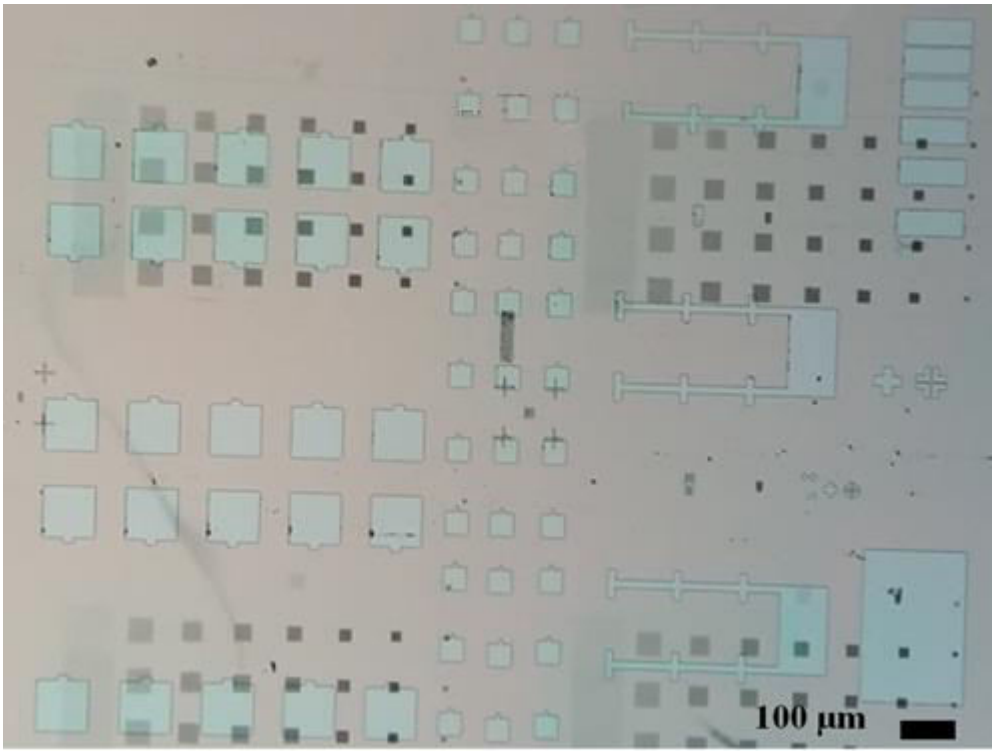

Figure 7.4. The pin nanowires with contact pattern defined with 1500 wires positions defined within it, to give an indication of wire density.

For a direct comparison of the current density with large-scale area structures the total number of the wires contacted by gold must be estimated. We imaged areas of the sample that were not covered by metal to determine what fraction of the wires was exposed after etching back the SU-8. Figure 7.5 shows an SEM image of some of the exposed wires. On average, around 15 % of the wires were exposed and contacted by the metal. Taking this into account we estimated that approximately 200 nanowires were contacted by metal in the device reported in detail below.

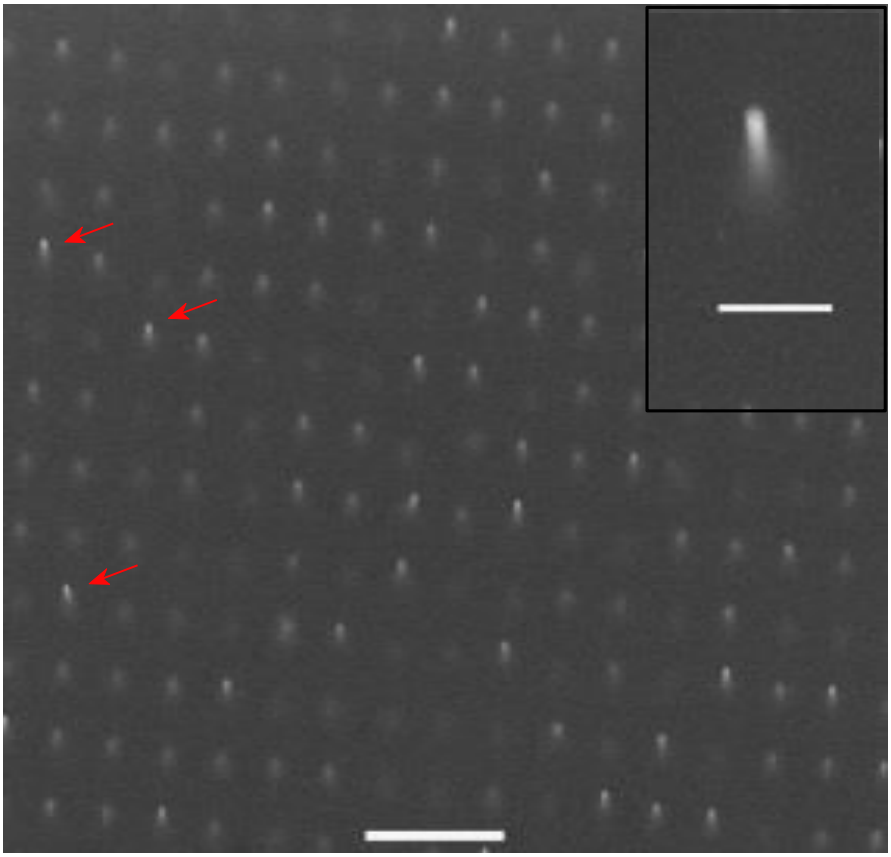

Figure 7.5. SEM image with 30° tilt of nanowires covered with SU-8. The resist has been etched back to expose the tops of several nanowires, three of which are indicated by the red arrows. Scale bar: 5µm. Inset: close-up of a single exposed nanowire. Scale bar: 1µm.

Once the sample had been fully processed, room temperature leakage current and spectral response measurements were carried out, the results will be explained in the next section.

7.4. Current Voltage Measurements

The leakage current measured at room temperature is shown in Figure 7.6. At a typical detector operational bias of −0.1 V, the reverse leakage current was 18 pA, which corresponds to a current density below 2 mA/cm^2 for the 200 nanowires contacted by the metal. Interestingly, the measured dark current for the fabricated photodetector is significantly below the best results reported for large area InAs photodiodes, which typically suffer from high levels of surface leakage and exhibit ~100mA/cm^2. However, this is unexpected since InAsSb has a smaller band gap than InAs and the wires have a very large surface area, both factors which would typically increase the current density compared with conventional devices. This result also shows the nanowire photodetector to have significantly lower noise due to leakage current compared to conventional InAs(Sb) detectors, despite being grown on a heavily mismatched substrate. The forward bias current can be fitted well as an ideal diode, with an ideality factor of 1.4, and a simple series resistance. This indicates that the current−voltage characteristic is dominated by a single type-junction. Furthermore, the series resistance fitted is 2 orders of magnitude lower than the dynamic resistance in reverse bias, at −0.1 V, confirming that it cannot be the cause of the exceptionally low reverse leakage current density. Photocurrent was measured under illumination by a 14 mW 1.55 μm laser; however, due to the continuous, optically opaque top contact covering the nanowire array, this was not directly incident on the nanowires. Instead it was fibre coupled onto an area adjacent to the edge of the contact, where a small fraction was coupled into the wires through scattering and interface reflections. As seen in Figure 7.6, a photocurrent was detected which indicates that the nanowires are optically active; however, due to the optically opaque top and bottom contacts, the nanowires can only be indirectly illuminated at this time, and hence it is not yet possible to determine the quantum efficiency. Prior studies have been

made of InAsSb nanowires with higher Sb fractions, configured for infrared photodetection. Without any type-junction these photoconductive wires showed some response; however, despite cooling to 5 K, leakage remained in the mA range for ~8000 wires.[8]

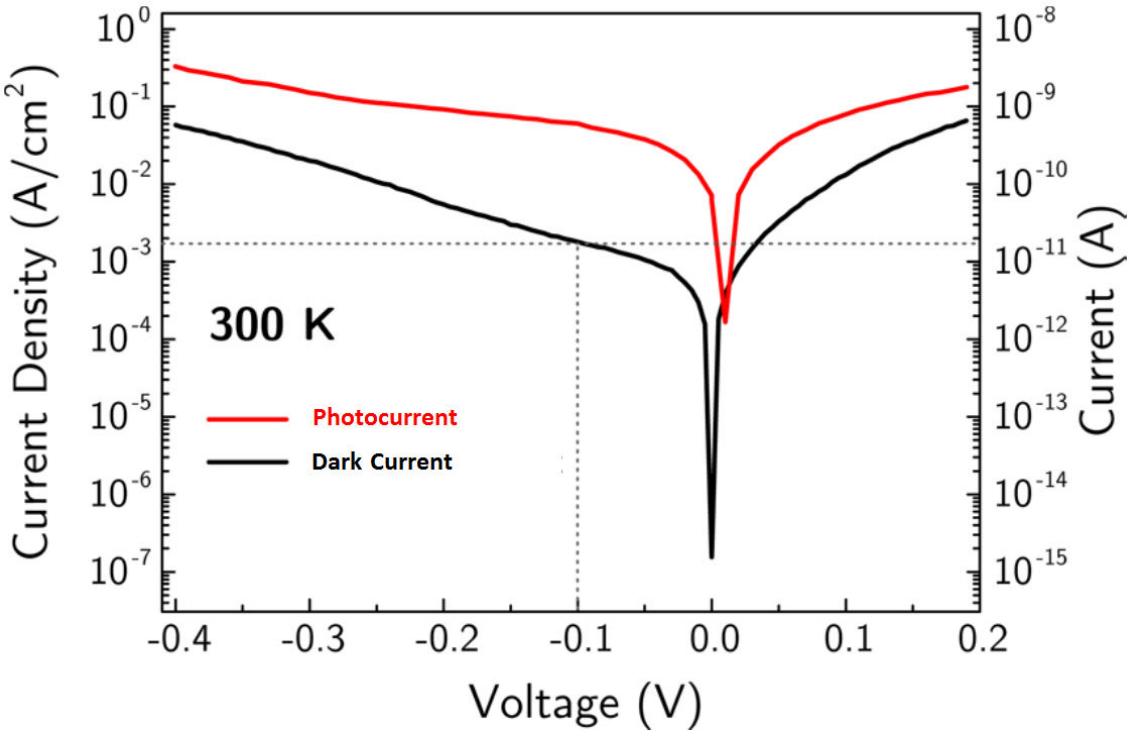

Figure 7.6. Semi log current−voltage characteristic of $InAs_{0.93}Sb_{0.07}$ p−i−n photodiode at 300 K with a nanowire diameter of 80 nm and a length of 1.7 µm. The black and red plots show the leakage current and photocurrent density, respectively, for 200 contacted nanowires. At a typical operational bias of −0.1 V the leakage current is 18 pA which corresponds to a leakage current density around 2 mA/cm^2. For photocurrent measurements, illumination was provided by a 1.55 µm laser.

7.5. Spectral Response Measurements

Spectral response measurements on the photodetectors were performed using a Bruker Vertex FTIR at room temperature and a bias of −0.1 V. The 300 K peak spectral response in **Error! Reference source not found.** is significantly shorter than the photoluminescence (PL) peak. The optical properties of micro and nano structures are particularly dependent on their

physical dimensions[9]. However, it has been shown that the efficiency of optical absorption in nanowire arrays exhibits a spectral dependence arising from mode guiding, due to the geometry of the wire and array, such that the peak field can occur either inside or outside the wires[8]. The peak response was obtained at 1.5 µm with a FWHM of 320 nm, which we to the wavelength and the wire diameter dependence of the HE_{11} mode in the nanowires[8].

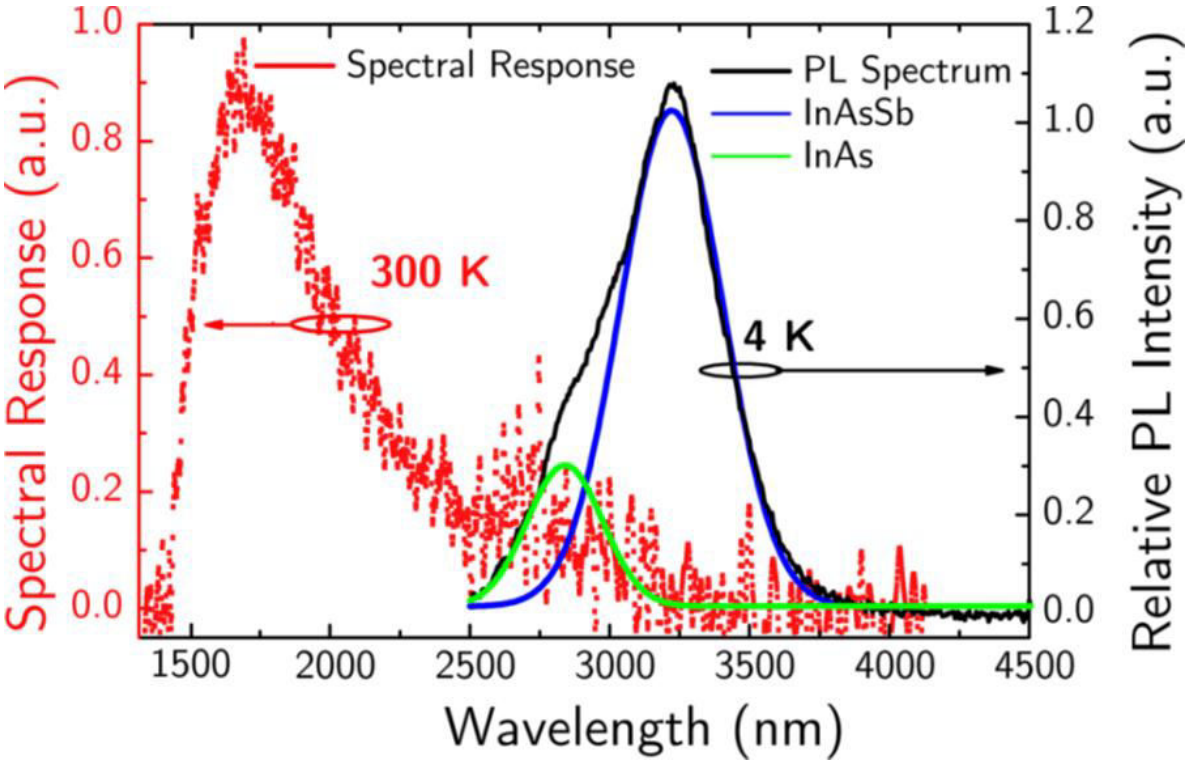

Figure 7.7. Spectral response at 300 K and −0.1 V bias (red) and 4 K photoluminescence spectrum (black) of $InAs_{0.93}Sb_{0.07}$ nanowires. The PL spectrum is deconvoluted using two Gaussian peaks to show the contributions of the InAs (green) and InAsSb (blue) sections of the wire. The noise in the spectral response between 2500 and 3000 nm is an artifact of the system response correction due to atmospheric absorption.

For the PL comparison, the sample QA399 used is mentioned in chapter 5. The noise in the spectral response between 2500 and 3000 nm is an artifact of the system response correction due to atmospheric absorption. The emission from the InAs is blue-shifted from the expected

wavelength by around 5 meV which is consistent with confinement in an 80 nm 1-D quantum wire[10].

Optimisation of the length and diameter of InP nanowires has been shown to increase the absorbance of nanowire arrays to levels which equal planar devices despite having only a fraction (10%) of the volume[11]. Assuming equal absorbance, 10% nanowire coverage, and the observed leakage current density reduction of 50 times, InAsSb nanowire photodetectors could increase the SNR by up to 500 times over conventional InAs(Sb) photodetectors. InAs based photodiodes have long been known to suffer from high levels of surface leakage originating from an electron accumulation layer, such that, as the perimeter to area ratio increases, surface leakage tends to dominate the total leakage current[12] . The perimeter/area ratio of the nanowires in this work is extremely high at 5×10^5 cm^{-1}. Ker et al. separated surface and bulk leakage in InAs photodiodes and reported them as a function of temperature[12]. Comparison with these results shows that conventional InAs photodiodes with the nanowires dimensions would indeed be strongly dominated by surface leakage. Only by cooling to 125 K would this surface leakage current fall to the levels of the total leakage measured in these nanowires at 300 K. Defining a mesa diode requires the removal of material through chemical etching, which disrupts the lattice and allows impurities to be introduced. By using monolithically grown nanowires to define the detecting volume, the surfaces remain unmodified and defect free which we believe leads to a reduction in the surface contribution to the overall leakage current. Even if surface leakage is neglected, cooling to 230 K would be required for the best InAs photodiodes to match the leakage current density measured in the nanowires at 300 K.

Bulk leakage current density is closely associated with the crystalline quality of the detector material and hence it is inferred that the nanowire material exceeds the quality of conventional epitaxial InAs(Sb).

This is supported by TEM analysis, which shows twinning of the zinc-blende lattice, but an absence of threading defects. The nanoscale diameter of the wires ensures that any 60° threading dislocations originating from the interface with the (111) Si reach a sidewall and terminate within the lower 150 nm of the wire. Hence the crystalline structure of the wire in the region of the p−i−n junction is expected, and observed, to be entirely free from any leakage-causing defects.

7.6. Conclusion

In summary, we have fabricated shortwave infrared photodetectors, using site-controlled nanowires on silicon, with unprecedentedly low leakage current at room temperature. Not only has this allowed for high quality shortwave infrared photodetectors to be grown on silicon substrates, but surprisingly, the leakage current density is almost 2 orders of magnitude lower than state of the art InAs(Sb) photodiodes. The unique design also allows for electrical conduction through the substrate which simplifies many aspects of the fabrication and expands the opportunities for integration. Although the nanowires occupy only a small fraction of light collection area, optimization of the length and diameter[11,6] can significantly increase the absorbance up to that of planar films[13,11]. Combined with the reduction in leakage current density over InAs(Sb), this should provide more than 2 orders of magnitude increase in SNR over state of the art InAs(Sb) devices. This result is the first reported InAsSb nanowire photodiode and the lowest leakage current density reported for any InAs(Sb) photodiode at 300 K. We believe that this represents a major step toward high-performance mid-infrared photodetectors compatible with silicon technologies and which can be integrated with other photonic systems. Hence NWs are good at trapping light, increasing the absorption strength for longer wavelengths can be achieved by optimizing the nanowire

diameter to get absorption up to 90% and reflection reduced below 5%. Since our aim is to detect in the mid-infrared, this will be the focus of future work.

7.7. References

[1] Wang, D , Aplin, D. P. R., Ding, Y., Wang, Z.-L., Bando, Y., Sun, K., Li, C., Wei, W., Bao, X., and Jing, Y. "Catalyst-free Heteroepitaxial MOCVD growth of InAs Nanowires on Si substrates". J. Phys. Chem. C, 2014, 118 (3), 1696–1705.

[2] Li, X , Wu, D., Tang, X., Yoon, H., Wang, K., and Olivier, A. "MOCVD growth of high-quality and Density-Tunable GaAs Nanowires on ITO catalyzed by au Nanoparticles deposited by centrifugation", Nanoscale research letters. 2015, 1(10).

[3] Mori, H., Sugo, M. and Itoh, Y. "Heteroepitaxy of InP on Si substrates', Advanced Materials", 1993, 5(3), 208–209.

[4] Koblmuller, G.; Hertenberger, S.; Vizbaras, K.; Bichler, M.; Bao,F.; Zhang, J.-P.; Abstreiter, G. "Self-induced growth of vertical freestanding InAs nanowires on Si(111) by molecular beam epitaxy". Nanotechnology. 2010, (21), 365602.

[5] Potts, H., Friedl, M, Amaduzzi, F., Tang, K., Tütüncüoglu, G., Matteini, F., Alarcon L. E., Paul C. l., and Morral, A." From Twinning to Pure Zincblende Catalyst-Free InAs(Sb) Nanowires" Nano Lett. 2016, (16) 637−643.

[6] Foldyna, M.; Yu, L.; Roca i Cabarrocas, P. Theoretical short-circuit current density for different geometries and organizations of silicon nanowires in solar cells. Sol. Energy Mater. Sol. Cells 2013, 117, 645−651. Dye Sensitized Solar Cells, Organic, Hybrid Solar Cells and New Concepts Dye Sensitized Solar Cells, Organic, Hybrid Solar Cells and New Concepts.

[7] Murayama, M.; Nakayama, T. Chemical trend of band offsets at wurtzite/zinc-blende heterocrystalline semiconductor interfaces. Phys. Rev. B: Condens. Matter Mater. Phys. 1994, 49, 4710−4724.

[8] Svensson, J.; Anttu, N.; Vainorius, N.; Borg, B. M.; Wernersson, L.-E. Diameter-Dependent Photocurrent in InAsSb Nanowire Infrared Photodetectors. Nano Lett. 2013, 13, 1380−1385. PMID: 23464650.

[9] K. Seo, M. Wober, P. steinvurzel, E. Schonbrun, Y. Dan, T. Ellenbogen and K. B. Crozier, "Multicolored Vertical Silicon Nanowires,'' J. Nano letters. 2011, 11, 1851-1856.

[10] Koblmüller, G.; Vizbaras, K.; Hertenberger, S.; Bolte, S.; Rudolph, D.; Becker, J.; Döblinger, M.; Amann, M.; Finley, J.; Abstreiter, G. Diameter Dependent Optical Emission Properties Of Inas Nanowires Grown On Si. Applied Physics Letters 2012, 101, 053103.

[11] Anttu, N.; Abrand, A.; Asoli, D.; Heurlin, M.; Aberg, I.; Samuelson, L.; Borgstrom, M. Absorption of light in InP nanowire arrays. Nano Res. 2014, 7, 816−823.

[12] Ker, P.; Marshall, A.; Krysa, A. B.; David, J.; Tan, C. H. Temperature Dependence of Leakage Current in InAs Avalanche Photodiodes. IEEE J. Quantum Electron. 2011, 47, 1123−1128.

[13] Sourribes, M. J. L.; Isakov, I.; Panfilova, M.; Liu, H.; Warburton, P. A. Mobility Enhancement by Sb-mediated Minimisation of Stacking Fault Density in InAs Nanowires Grown on Silicon. Nano Lett. 2014, 14, 1643−1650. PMID: 24502770.

Chapter 8

Conclusion and future work

8.1. Summary

This thesis focuses on the development and synthesis of novel InAs- based NWs structures as a significant step towards viable nano and quantum optoelectronic devices. Due to the unique optical properties of NWs, they can have great potential for the development of emitters and photodetectors operating in the mid-infrared spectral range. In particular, the selective area growth technique on Si is an attractive technology to realize high performance and low cost optoelectronic devices. In this work we developed the growth of InAs NWs and report the optical properties for the grown wires, while mainly aiming at improving their poor optical efficiency by reducing nonradiative surface and Auger recombination, which will results in enhanced emission at room temperature for realising practical applications. The next step was in introducing the Sb to the InAs NWs, as it was found that the addition of small amounts of Sb has been shown to suppress lattice defects, including twinning and stacking faults in InAsSb NWs. However, the PL quenching behaviour is only slightly improved since the band-edge perturbations introduced by these defects do not strongly influence non-radiative recombination. Developing quantum structures into the NWs systems was one of the main challenges in this work to achieve efficient light emission without the requirement for cryogenic cooling, in addition to illuminate the poor optical efficiency in the InAs(Sb) NWs. As a consequence advanced novel structures have been developed by growing InAsSb MQWs and InAsSb SLs embedded within InAs NWs on Si(111) substrate using selective area growth. This gives quantum confinement and localisation of the carriers on the nanoscale, suppressing loss and allowing for the tuning of the emission wavelength. As a result enhanced PL emission intensity up to room temperature operation was demonstrated for both structures, along with enhancement in the PL intensity emission with respect to the InAs NWs. Finally, the final goal of realising proof of principle

InAsSb nanowire based photodetectors was achieved with the lowest leakage current density by almost 2 orders of magnitude lower than state of the art InAs(Sb) photodiodes.

The following is a summary of the achievements in this work:

- Developed a catalyst-free formation of site-controlled InAs(Sb) NWs by SA-MBE growth on patterned (111) Si substrates.
- Designed novel heterostructures MQWs and SLs embedded within InAs(Sb) NWs containing type II QWs that provide quantum confinement, spatial localization of the carriers and Auger suppression, resulting in enhanced PL emission. Also the effect of type II QW charging on the flat band transition energy is found to be in good agreement with calculations for both samples.
- The first demonstration of novel mid-infrared light room temperature emission from InAsSb MQWs and InAsSb SLs embedded within InAs NWs, with bright PL room temperature emission at 0.459 eV for the MQWs and at 0.443 eV for the SLs NWs, with enhancement in the PL emission with respect to bulk InAs NWs,
- The first demonstration of pin junctions in InAsSb NWs and photodetectors having the lowest leakage current density reported for any InAs(Sb) photodiode at 300 K with a spectral response peak at room temperature.

8.2. InAs(Sb) NWs

A catalyst-free formation of site-controlled InAs(Sb) NWs was demonstrated by SA-MBE growth on patterned (111) Si substrates. Uniform NWs arrays with a diameter of 80 nm and length around 700 nm were obtained for the InAs NWs and enhanced to be around 1.3 µm for the InAsSb NWs. This is due to the enhancement in the growth rate as a result of introducing the Sb to the wires. Increase in the length of the grown wires was explained by the adatoms diffusion on the surface. The growth temperature ranges were investigated under V/III ratio of 25 for the InAs and 42:2 for the InAsSb, with maximum temperature close to 501°C for InAs and 509 °C for InAsSb NWs. The growth temperature significantly affected the axial growth rate in the range between 473-501°C for InAs NWs and 456-509 °C for InAsSb NWs. However, the ideal axial growth rate was achieved at 494 °C for both types of nanowires. The decrease in NWs growth rate at very high growth temperatures was limited by excess In desorption from the SiO_2 on the Si (111) surface. TEM studies of InAs NWs show that the wurtzite (WZ) crystal phase structure dominates and the addition of Sb drives a change to a zinc-blende (ZB) phase. Both structures have stacking faults along the growth direction. XRD analysis confirmed that 6-7% Sb is incorporated into the InAsSb NWs. The NWs exhibited strong PL emission at low temperatures with PL peak in the range assigned for the WZ InAs at 0.473 eV, the addition of Sb shifts the energy towards lower energy gaps at 0.380 eV and a blue shift of ~5 meV is observed due to confinement in the NWs. The PL emission persisted up to 150 K for both InAs and InAsSb NWs, the addition of small amounts of Sb has been shown to suppress lattice defects, including twinning and stacking faults in InAsSb NWs. However, the PL quenching behaviour is only marginally improved since the band-edge perturbations introduced by these defects do not strongly influence non-radiative

recombination. The results presented here lay the groundwork for developing high-performance InAsSb nanowire-based infrared photodetectors and nanoelectronic devices.

8.3. InAsSb/InAs MQW NWs and InAsSb/InAs SL NWs

Development of quantum structures in NWs systems have shown their applicability to extend the concept of bandgap engineering not only to be used as building blocks for such systems, but also to be integrated further into the leading CMOS technology, providing a promising future for nanotechnology in optics and electronics. In this thesis, novel structures have been grown by developing InAsSb MQWs and SLs embedded within InAs NWs on Si(111) substrate using selective area growth.

From the STEM analysis, the MQWs were mainly formed in the WZ phase crystal structure with stacking faults and twins where only one insert of ZB segments (2-4 monolayers) has been observed in the analysed STEM image. This ZB insert is incidentally nowhere near the well and considered the smallest possible segment that cannot form a phase. The SLs case is further complicated, as it has a poly type structure and the grown InAsSb layer could be a reason for forming more ZB segments within the SLs structure. Angular STEM analysis of the plane with preferential Sb incorporation shows that the $(10\bar{1}1)$ facets are energetically favoured for the MQWs with 62º angle, in comparison to the $(1\bar{1}20)$ facets favoured for the SLs with the 73º angle, assuming that the structures are mainly WZ. In the SLs case, growing an InAsSb layer on top of the InAs and impinging Sb during the SLs growth, would suggest that it contains more ZB phases and possibly Sb incorporation on the same angle of ZB (111) facets, hence the SLs grows on top of a ZB InAsSb layer. Extending the growth further on an InAs or InAsSb wire for both structures would switch the structures into the ZB phase with flat-topped wires formed over time as reported earlier. However, in this case, the short

growth durations are insufficient to allow a flat top to be formed, thus ending with a faceted top.

Optical measurments have been performed on both samples containing type II QWs that exhibit mid-infrared emission at room temperature. Type II QWs design gives quantum confinement and spatial localization of the carriers and Auger suppression, resulting in enhanced PL emission intensity, persistent up to the technologically vital room temperature operation point. The MQWs structure is 5 times enhanced compared to the SLs, and both of them exhibited enhanced PL emission with respect to the bulk InAs(Sb) NWs. Furthermore, having characterized the effect of charging on the type II QW, the flat band transition energy was found to be in good agreement with the calculated values for both samples.

These novel quantum structures NWs will allow novel nano-photonic and quantum light sources to be developed for the technologically important mid-infrared spectral range. They can exploit both the general advantages of site controlled NWs, such as integration with silicon substrates, and also enhance light-mater coupling based on their dimensions and geometry, opening the way for a wide range of applications.

8.4. InAs(Sb) NWs photodetectors

Shortwave infrared photodetectors have been fabricated using site-controlled nanowires on silicon, with significant low leakage current and high photoresponse obtained at room temperature. Interestingly, the measured dark current for the fabricated photodetector is below the best results reported for large area InAs photodiodes, which typically suffer from high levels of surface leakage ~100mA/cm^2. This paves the way towards realizing efficient nanowire based photodetectors in the mid infrared spectral range at room temperature. These results allow for high quality shortwave infrared photodetectors to be grown on silicon

substrates. Also the unique design allows for electrical conduction through the substrate which simplifies many aspects of the fabrication and expands the opportunities for integration. Although the nanowires occupy only a small fraction of the light collection area, optimization of the length and diameter can significantly increase the absorbance up to that of planar films. Combined with the reduction in leakage current density over InAs(Sb), this should provide more than 2 orders of magnitude increase in SNR over state of the art InAs(Sb) devices. This result is the first reported InAsSb nanowire photodiode and the lowest leakage current density reported for any InAs(Sb) photodiode at 300 K.

8.5. Suggestions for future work

8.5.1. Improving the wires seeding and yield

We have shown that MBE growth of InAs(Sb) NWs occurs within certain temperature windows, where NW nucleation and growth increase with increase in temperature, reaching a maximum, then decreasing, and stop. The ability to control the axial growth was achieved, however, the radial growth of the NWs diameter was self-limited between 80 -100 nm, despite the hole diameter variation in the template mask and the spacing between the wires. Further studies are required to optimize the radial growth and improve the yield of nanowires which requires an improvement in EBL patterning.

8.5.2. Change the Sb flux and increase the Sb composition

Another challenge in this work was in achieving higher Sb composition in the NWs. Therefore, an attempt to grow InAsSb bulk NWs was performed to grow wires with higher Sb flux. However, the NWs become much shorter and instead clusters start to develop which

may result in formation of a thin 2-D InAsSb layer growth on the substrate. A 15% or even higher Sb incorporation can be achieved by decreasing the growth temperature to 450°C. Considering that the antimony atoms will diffuse even more slowly at 450°C than at 480°C, the increase in the formation of clusters may affect the surface. However, monitoring and controlling the Sb incorporation in the wires is essential to get silicon- based NWs optoelectronics operating in the entire mid- to long infrared wavelength ranges.

8.5.3. X-Ray Diffraction Measurments of the NWs

X-ray measurement is a good method besides PL to determine the Sb composition within the grown wires. X-ray measurements performed on InAsSb NWs (namely QA399) in Lund University have shown that the Sb content was approximately 6-7%, which is in good agreement with our PL results. Considering that the MQWs are grown at the same growth conditions, the Sb content should be equal to 6-7% as well. However, x-ray measurements have been performed on both the MQWs and the SLs in Lancaster University, but haven't been fully interpreted due to limited time available in this project.

8.5.4. Change the Wells and barriers width in the MQWs

Growth attempts have been made to vary the QWs thickness in the MQWs sample. Three samples have been grown with different InAsSb well thickness of 4nm, 8nm and 16nm. The PL intensity appears to increase with increasing the well thickness from 4 to 8 nm, then further reduces for the 16nm thickness as mentioned in chapter 6. However, this reduction of the intensity is probably due to exceeding the critical thickness. There is a slight variation in the PL energy gap which can be attributed to the Sb incorporation in the wires. Thus, further study is also required to eliminate this effect on the grown wires.

8.5.5. Organic coating studies on MQW NWs

Preliminary experimants have been performed on the MQW NWs in order to study the influence of the organic coating and how the chemical treatment affects the MQWs surface. As mentioned previously, InAs NWs suffer from large densities of surface states because of Fermi level pinning above the conduction band which affected the luminescence efficiency. A preliminary study was performed on the MQWs at 4 K and room temperature. The results have shown a clear red shift in the PL spectra after the organic treatment that has been attributed to charge accumulation at the surface. However, to accurately determine the effect of this treatment further work is essential. This should begin with a study of bulk InAs NWs for which growth is less complicated than the MQW sample used for this experiment.

8.5.6. Photodetector development

Since NWs are good at trapping light, increasing the absorption strength for longer wavelengths can be achieved by optimizing the nanowire diameter to get up to 90% absorption and reduce reflection to below 5%.

However, since our aim is to obtain photodetection in the mid-infrared range, the photonic coupling of the light determined by the geometry of the NW array needs to be carefully reconsidered to extend the spectral response - this should be an important focus of future work. Growing such unique narrow gap NW pin structures is a major step toward high-performance mid-infrared photodetectors and emitters compatible with silicon technologies and which could be integrated with other photonic systems. The growth has been performed for two preliminary samples and the processing steps for these samples should be similar to the pin InAsSb photodetectors mentioned previously in chapter 7. However, due to the

limited time, the processing and characterization of these samples was started but needs to be followed up in future work.

Appendix

- **The origin of the equation** $E_e = \left(\frac{9\pi}{8}\right)^{2/3}\left(\frac{\eta^2}{2m_e}\right)^{1/3} F^{2/3} \propto N^{2/3} \propto L^{1/3}$

In type II quantum well structures holes are confined in the quantum well and the electrons are attracted toward the interface. An increase in excitation intensity will produce additional charges which raise the steepness of the confining potential for electrons and create a triangular quantum well (with electron quantization energies). The flat-band energy of the quantum well can then be extracted from the power dependence of the PL.

The energies within single quantum well or multiple quantum well of the electrons are quantized in the step like density of states. Therefore many carriers can be put in the channel with a narrower dispersion of energies.

Electron wave inside well is

$\Psi = \sum e^{jk\alpha} u_{ck}(r)\Psi_n$ This is Kane model.

Where x is the growth direction and k is the transverse electron wave vector.

$u_{ck}(r) =$ block wave form and Ψ_n is the envelope wave function which is the solution of

$$\left[-\frac{h^2}{2m^*(x)}\frac{\partial^2}{\partial x^2} + V_c(x)\right]\Psi_n(x) = \varepsilon_n \Psi_n(x)$$

Where $m^*(z)$ is the effective is mass, $V_c(z)$ is the potential and ε_n is the confinement energy of carriers.

Boundary conditions are $x_n(x)$ and $\frac{1}{m^*(x)}\frac{\partial x^n}{\partial x}$ should be continuous at the interfaces.

The triangular potential well is shown in Fig 1 below.

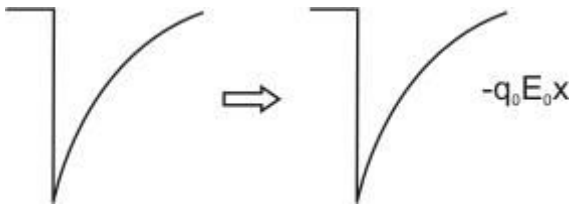

The triangular quantum well Potential $V(X)$ is linear for $x > 0$ and ∞ at x = 0

The Schrödinger equation is

$$-\frac{h^2}{2m}\frac{d^2\psi_n(x)}{dx^2} + qE_o x\psi_n(x) = E_n\psi_n(x)$$

The boundary condition is $\psi_n(0) = 0$

The above equation has two independent solutions.

One solution that is nonsingular at $x \to \infty$ is AIRY function (Ai), so the resulting wave function is $\psi_n(x) = Ai\left[\left(\frac{2m_n^*}{\hbar^2 q^2 E_o^2}\right)(qE_o x - E_n)\right]$.

The quantized energy levels are

$$E_n = -\left(\frac{\hbar^2 q^2 E_o^2}{2m_n^*}\right)^{\frac{1}{3}} a_n$$

Where, a_n is the nth zero of Ai(x), hence

$$a_n \cong -\left[\frac{3\pi}{2}\right]\left(n+\frac{3}{4}\right)^{\frac{2}{3}} \qquad n = 0,1,2.....$$

So

$$E_n \cong \left(\frac{\hbar^2}{2m}\right)^{\frac{1}{3}}\left[\frac{3\pi qE_o}{2}\left(n+\frac{3}{4}\right)\right]^{\frac{2}{3}}$$

Assuming that before the charge transfer the potential is flat band. After charge transfer of N_s electrons the electric field in the potential well created can be taken as constant to first order and is given by

$$E_o = \frac{qN_s}{\epsilon_o \epsilon_2}$$

Gauss' Electrostatic potential is given by

$$\phi(x) = -E_o x \qquad \text{for} \quad x > 0$$

Hence the Schrödinger equation for the electron envelope wave function is

$$\left[\frac{p^2}{2m^*} - q\phi(x)\right]\psi(x) = E\psi(x)$$

The energy level in infinite triangular potential well for the ground state $(n = 0)$ is

$$E_1 = \left(\frac{\hbar^2}{2m_n^*}\right)^{\frac{1}{3}}\left(\frac{\frac{9}{8}\pi q^3 N_s}{\epsilon_o \epsilon_2}\right)^{\frac{2}{3}}$$

$$= \gamma N_s^{2/3}$$

Where $\gamma = \left(\frac{\hbar^2}{2m_n^*}\right)\left[\frac{\frac{9}{8}\pi q^3}{\epsilon_o \epsilon_2}\right]^{\frac{2}{3}}$ and is usually determined experimentally[1,2].

The triangular quantum well originates from an electric field F, which is proportional to the charge carrier density n_w and the integrated PL intensity L is proportional to the integrated spontaneous emission rate which is proportional to n_w squared, as we can see from equation (2.6). The strongly localized holes form a charged plane and produce an approximately triangular quantum well with electric-field strength of F

$$F = \frac{\pi\, q\, N_S}{\varepsilon\, \varepsilon_0}$$

Where N_S is the charge carrier density in the triangular well.

The integrated PL intensity *L* is proportional to the integrated spontaneous emission rate as described in the following formula:

$$L = \gamma B N_S^{\,2}$$

B is the radiative recombination coefficient and γ is the collection efficiency.

N_S will be proportional to the square root of L. The ground electron state energy is given by this equation and will be proportional to n to the power of 2 divided by 3 and will be in proportional to the cubic root of L. The electron charge carrier density N_S is:

$$N_S = \sqrt{\frac{L}{\gamma B}} \propto L^{1/2}$$

The ground electron state in such a well is given by:

$$E_e = \left(\frac{9\pi}{8}\right)^{2/3}\left(\frac{\eta^2}{2m_e}\right)^{1/3} F^{2/3} \propto N^{2/3} \propto L^{1/3}$$

Thus, an increase in excitation intensity will raise the steepness of the confining potential and consequently the electron quantization energy E, with a typical $\Delta E \sim L^{1/3}$ behavior where L is integrated PL intensity[3].

- **Monochromator grating**

The reflective blazed diffraction grating has a sawtooth cross-section, as shown in Figuer1. As light that passed through an adequately fine slit is diffracted, light reflected from an adequately fine sawtooth surface is also diffracted. There are 500 to 2000 serrations per millimeter. The sawtooth face of a commercially produced diffraction grating is the replica of a master grating. A thin synthetic-resin replica is stuck onto a glass sheet and coated with aluminum. The master was traditionally produced using a machine tool, but now the surface is formed by an ion beam or using laser beam photolithography. A smooth surface reduces stray light (light at unwanted wavelengths). The basic expression governing diffraction gratings is:

$m\lambda = d\ (\sin I + \sin\theta)$

Where, d is the groove (serration) spacing, i is the angle of incidence, θ is the diffraction angle (positive if the incident light and diffracted light are on the same side of the normal to the diffraction grating surface, negative if they are on opposite sides of the normal), λ is the wavelength, and m is the order. This means that when d, m, and i are fixed, light of wavelength λ is diffracted in direction θ.

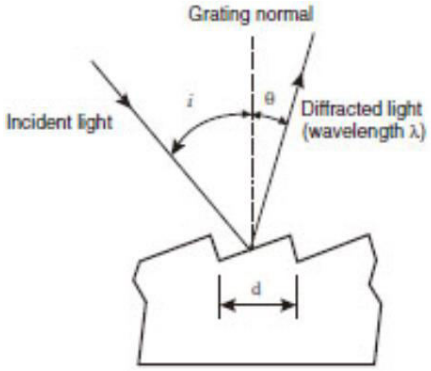

[1] Bohm, D. *Quantum Theory*; Dover Publications, 2012.
[2] Park, D. Introduction to the Quantum Theory; Dover Publications, 2012.
[3] Ledentsov, N.; Böhrer, J.; Beer, M.; Heinrichsdorff, F.; Grundmann, M.; Bimberg, D.; Ivanov, S.; Meltser, B.; Shaposhnikov, S.; Yassievich, I. et al. Radiative States in Type-II GaSb/GaAs Quantum Wells. Physical Review B 1995, 52, 14058-14066.